# Structure and function of trimeric intracellular cation channels (TRIC) and ryanodine receptors (RyR)




Jianshu Hu

Linacre College

University of Oxford

A thesis submitted for the degree of

*Doctor of Philosophy*

Michaelmas 2021

# Acknowledgement

I would like to sincerely thank my supervisor, Prof. Rebecca Sitsapesan for her guidance, inspiration, and encouragement throughout three years of my DPhil. Her enthusiastic and meticulous attitude in academic research has shown me how to think and behave better in science. If scientific research is like exploring in the dark mist, her guidance is like the light from the lighthouse, revealing the shrouded and helping me find the direction.

Thank you to everyone in the Sitsapesan's Lab for help and advice during my research. In particular, thank you to Dr Elisa Venturi for guiding me on how to perform single-channel experiments and membrane fraction preparations. Thank you to Dr Charalampos Sigalas for teaching me in the animal experiments and mentoring me during the difficult time together with Prof Paolo Tammaro as well as thanks to Tom Humberstone sharing opinions and discussing with me about academic and fancy life here, Dr Abigail Wilson teaching and helping me in the PCR and western blot and Dr Chris Lindsay helping me in the laboratory all the time. Also, thanks to lovely friends in the department, Lara Scofano, Ria Dinsdale, Claire Pearson and Kathryn Acheson. It is enjoying having coffee and cakes with everyone.

I would like to thank the support from the Pharmacology department and Linacre College during my life in Oxford. Thanks also to my friends, Weikang Gong, Zongqi Liu, Meng Lyu for spending an enjoyable time with you guys.

Thanks to my family, Mum and Dad, who have been loving and supporting me all the time.

*Scientia ērudītiōnem sempiternam meruit.*

# Abstract

Controlled $Ca^{2+}$-release from the sarcoplasmic reticulum (SR) during excitation-contraction coupling (EC-coupling) is essential for cardiac and skeletal muscle contraction. $Ca^{2+}$ is released through ryanodine receptors (RyR) in the SR membrane but there are other, different types of ion channels in the SR with unclear physiological roles, and some of these channels have not been identified. In this thesis, I have investigated the structural and biophysical properties of certain ion channels found in the SR, including SR $K^+$ channels, trimeric intracellular cation channels (TRIC-A and B) and RyR.

The gating and single-channel conductance of SR ion channels was examined after incorporation of vesicles of SR into planar phospholipid bilayers under voltage-clamp conditions. In the search for a ligand that binds to the SR $K^+$ channel, I found that ebselen irreversibly inhibited the channel and that dithiothreitol could partly reverse this effect suggesting the ebselen modified cysteine residues on the channel.

It is suggested that TRIC-A or TRIC-B could be the SR $K^+$ channel and so I investigated this by characterising the biophysical properties of the ion channels observed after incorporating membrane vesicles obtained from HEK293 cells co-expressing RyR2 plus TRIC-A or RyR2 plus TRIC-B into bilayers. My results indicated that TRIC-A and TRIC-B are non-selective ion channels, permeable to both $Cl^-$ and $K^+$, and therefore are unlikely to be SR $K^+$ channels which are highly selective for monovalent cations. I also found that co-expression of TRIC-A or TRIC-B with RyR2 altered the response of RyR2 to cytosolic $Ca^{2+}$ suggesting that both TRIC-A and TRIC-B interact with RyR2 to regulate RyR2 gating.

I established a cardiac-specific *Tric-a* knockout (*Tric-a*-cKO) mouse colony as a platform to explore the physiological roles of TRIC channels in the heart. The colony was validated by mRNA and protein levels of other ion channels present in mice hearts.

Using homology modelling, I also studied the putative structural changes to RyR2 caused by the mutations V2475F and R2474S that are associated with the lethal arrhythmic disease, catecholaminergic polymorphic ventricular tachycardia type 1 (CPVT1). The predicted models suggested that there are significant conformation changes to the RyR2 helical domain1, thus providing new information regarding the relationship between structural and function in CPVT1.

# Contents

**List of Figures** ..... *v*
**List of Tables** ..... *x*
**List of Abbreviations** ..... *xi*
**Table of Contributions** ..... *xv*

**CHAPTER 1 INTRODUCTION** ..... **1**

1.1 $Ca^{2+}$ signalling and contraction in cardiac and skeletal muscle ..... 2
1.2 Excitation contraction coupling ..... 2
1.3 Single channel recording ..... 5
1.4 Ryanodine receptors ..... 7
*1.4.1 The cardiac RyR (RyR2)* ..... *8*
*1.4.2 Other physiological and pharmacological regulators of RyR2* ..... *10*
*1.4.3 Catecholaminergic polymorphic ventricular tachycardia* ..... *12*
1.5 Counter-ion current across the SR membrane ..... 20
*1.5.1 Trimeric intracellular cation channels* ..... *20*
*1.5.2 Interactions between TRIC and RyR channels* ..... *24*
*1.5.3 The SR $K^+$ channel* ..... *25*
*1.5.4 Ebselen as a potential ligand that binds to the SR $K^+$ channel* ..... *30*
1.6 Aims of this thesis ..... 32

**CHAPTER 2 METHODOLOGY** ..... **34**

2.1 Isolation of membrane fractions ..... 35
*2.1.1 Sheep skeletal muscle* ..... *35*
*2.1.2 Mouse heart and skeletal muscle* ..... *35*
*2.1.3 HEK-293 cells* ..... *36*
*2.1.4 Preparation of mixed membrane and sarcoplasmic reticulum vesicles* ..... *36*
*2.1.5 Mixed membrane from HEK 293 cells* ..... *37*
2.2 The planar phospholipid bilayer set up ..... 38
*2.2.1 Lipid bilayer apparatus* ..... *38*
*2.2.2 Lipid bilayer painting* ..... *39*
*2.2.3 Electrical equipment set up for measurement and acquisition* ..... *41*
*2.2.4 Voltage-clamp approach* ..... *43*
2.3 Fusion of vesicles with the lipid bilayer ..... 44
*2.3.1 Bilayer detection and estimation of the area* ..... *46*
*2.3.2 Experimental solutions and choice of permeant ion* ..... *47*
2.4 Data acquisition and analysis process ..... 48
*2.4.1 Data acquisition* ..... *48*
*2.4.2 Analysis of the single-channel recordings* ..... *49*
2.5 Cardiac TRIC-A KO mouse colony ..... 58
*2.5.1 Genotyping via Polymerase chain reaction (PCR):* ..... *58*
*2.5.2 mRNA level validation with real-time polymerase chain reaction (RT-qPCR) protocol* ..... *59*
*2.5.3 Delta-delta cycle threshold (Ct) method ($\Delta\Delta$Ct method) analysis* ..... *61*

2.6 Homology modelling method ..... 62
2.7 Statistics ..... 65
*2.7.1 Statistical test ..... 65*
*2.7.2 Models for linear and non-linear regression ..... 67*

**CHAPTER 3 THE EFFECTS OF EBSELEN ON THE SR $K^+$ CHANNEL ..... 69**

3.1 Introduction ..... 70
3.2 Results ..... 70
*3.2.1 Effects of ebselen on SR $K^+$ channel gating ..... 70*
*3.2.2 Investigation into the mechanism of the inhibitory effect of ebselen on SR $K^+$ channel gating 79*
3.3 Discussion ..... 87

**CHAPTER 4 EFFECT OF CO-EXPRESSING TRIC-CHANNELS ON RYR2 IN HEK293 CELLS 91**

4.1 Introduction ..... 92
4.2 Result ..... 93
*4.2.1 Effect of co-expressing TRIC-channels with RyR2 in HEK293 cells on RyR2 single-channel function 93*
*4.2.2 Effect of co-expression of TRIC channels on RyR2 single-channel conductance ..... 95*
*4.2.3 Effect of TRIC-A and TRIC-B on the response of RyR2 to changes in cytosolic $Ca^{2+}$ .... 98*
*4.2.4 Effect of co-expression of TRIC-A and TRIC-B on the voltage-dependence of RyR2 gating 102*
*4.2.5 Sub-conductance state of RyR channels with TRIC-A or TRIC-B co-expressed ..... 108*
*4.2.6 Investigation into the ion permeability of channels from the HEK cell preparations of co-expressed TRIC-A or TRIC-B ..... 109*
*4.2.7 Current fluctuation comparison between the channels incorporated from TRIC-A/TRIC-B co-expressed RyR2 HEK293 cells and normal SR $K^+$ channel ..... 114*
4.3 Discussion ..... 116

**CHAPTER 5 DEVELOPMENT OF A CARDIAC-SPECIFIC *TRIC-A* KNOCK OUT MICE COLONY 121**

5.1 Introduction ..... 122
5.2 Methods & Results ..... 123
*5.2.1 Breeding mouse colony with Cre-Lox recombination system ..... 123*
*5.2.2 Tamoxifen induced knock-out (KO) in the mouse heart ..... 129*
5.3 Discussion ..... 133

**CHAPTER 6 HOMOLOGY MODELLING OF RYR2 CPVT1 MUTATIONS ..... 136**

6.1 Introduction ..... 137
6.2 Results ..... 138
*6.2.1 Homology modelling models on RyR2 CPVT1 mutations ..... 138*
*6.2.2 Clustering and structural analysis of homology modelling results ..... 142*
6.3 Discussion ..... 149

**CHAPTER 7 CONCLUSIONS ..... 160**

**REFERENCES**.....165

**APPENDIX**.....178

# List of Figures

Figure 1.1 Representation of EC-coupling process in cardiac muscle ..... 3

Figure 1.2 CPVT mutations on the linear sequence of RyR2 (Jiang et al. 2005)..... 13

Figure 1.3 Electrocardiographs from RyR2 R4496C$^{+/-}$ ventricular cardiac myocytes, illustrating delayed after depolarizations (DADs). (Ruan, Liu, and Priori 2009)..... 15

Figure 1.4 Likelihood of formation of RyR2 tetramers with different compositions of V2475F mutated monomers. ..... 17

Figure 1.5 Sequences and structures of the RyR2 channel ..... 19

Figure 1.6. Structure of vertebrate TRIC-A and TRIC-B structures from Wang et al. 2019 (Wang et al. 2019) ..... 22

Figure 1.7 Structure of decamethonium and hexamethonium ..... 27

Figure 1.8 An example of current-fluctuations of full open and sub-conductance state gating events from the SR $K^+$ channel of mouse skeletal muscle. Figure is from Matyjaszkiewicz et al. 2015. ..... 29

Figure 1.9 The chemical 2D-structure of ebselen ..... 31

Figure 2.1 A diagram of the lipid bilayer experimental block ..... 41

Figure 2.2 A diagram of electrical equipment for single channel recording ..... 42

Figure 2.3 A diagram of a simplified circuit of an ion channel in a bilayer ..... 43

Figure 2.4 Fusion of vesicles under the osmotic gradient across the bilayer membrane. ..... 45

Figure 2.5 Gaussian curve fitting to current amplitude and compiling the amplitude histogram in QuB ..... 55

Figure 2.6 A diagram of work-flow of the homology modelling method ..... 63

Figure 3.1 The typical effects of ebselen on the gating of SR $K^+$ channels ..... 72

Figure 3.2 Ebselen shows inhibitory effect in experiments where only one SR $K^+$ channel in the bilayer for visualisation of the full open and sub-conductance open states..... 73

Figure 3.3 The conductance of the SR $K^+$ single-channel full open state is not altered by ebselen ..... 75

Figure 3.4 Time-dependent effects of ebselen on the Po of the full open state and sub-conductance open states of the SR $K^+$ single-channel ..... 76

Figure 3.5 The irreversible inhibitory effects of ebselen on the Po of the full and sub-conductance open states of the SR $K^+$ channel..... 77

Figure 3.6 The effects of ebselen on the Po of the full and sub-conductance open states of the SR $K^+$ channel expressed as a percentage of the total Po ..... 78

Figure 3.7 Diagram of the proposed mechanism for ebselen's effect on the SR $K^+$ channel and the proposed validation method of the mechanism..... 80

Figure 3.8 Effects of cytosolic and luminal ebselen and DTT treatments on the gating of SR $K^+$ channels, showing a recovery of channel gating from the inhibitory effect of ebselen when treated with DTT ..... 83

Figure 3.9 Effects of a range of ebselen concentrations followed by DTT treatment on the Po of SR $K^+$ channel from cytosolic and luminal side. ..... 84

Figure 3.10 Time-dependent effects on the Po of the SR $K^+$ channel showing the inhibition by ebselen and the partial recovery by DTT..... 85

Figure 3.11 Comparison of cytosolic and luminal additions of ebselen and DTT on the

Po of the full and sub-conductance open states of the SR $K^+$ channel expressed as a percentage of the total Po ..... 86

Figure 4.1 Western blot of RyR2 over-expressing HEK293 cells transfected with TRIC-A or TRIC-B by Dr Takashi Murayama's group ..... 94

Figure 4.2 Effects of co-expressing TRIC-A or TRIC-B with RyR2 on the gating of RyR2 channels incorporated into bilayers at 2 µM free $Ca^{2+}$ ..... 96

Figure 4.3 The co-expression of TRIC-A or TRIC-B with RyR2 does not affect RyR2 single-channel conductance ..... 97

Figure 4.4 Effect of co-expressing TRIC-A or TRIC-B with RyR2 on the gating of incorporated RyR2 channels at increased cytosolic $[Ca^{2+}]$ ..... 100

Figure 4.5 Effect of co-expressing TRIC-A or TRIC-B with RyR2 on the response of RyR2 to increasing cytosolic $[Ca^{2+}]$ ..... 101

Figure 4.6 The co-expression of TRIC-A or TRIC-B with RyR2 affects RyR2 Po over a range of cytosolic $[Ca^{2+}]$ at -30 mV ..... 103

Figure 4.7 Voltage-dependent inactivation of multiple RyR2 channels at +30 mV .... 106

Figure 4.8 Co-expressing TRIC-A or TRIC-B with RyR2 increases the rate of voltage-dependent inactivation of RyR2 channels ..... 107

Figure 4.9 Effect of co-expressing TRIC-A or TRIC-B with RyR2 on sub-conductance frequency ..... 111

Figure 4.10 Typical current fluctuation of channels from HEK cell preparations co-expressing TRIC-A or TRIC-B with RyR2 by voltage ramps ..... 112

Figure 4.11 Effects of co-expressing TRIC-A or TRIC-B with RyR2 on the Erev of the

currents elicited by voltage ramps..... 113

Figure 4.12 Comparison of mouse skeletal SR $K^+$ single-channel events with those derived from HEK293 cell vesicles co-expressing TRIC-A or TRIC-B with RyR2..... 115

Figure 5.1 Structure of the *Tric-a* gene coding, *Tmem38a*, and a schematic of gene editing on the gene..... 125

Figure 5.2 Genotyping of the targeted, Flp deleted, and wild-type gene..... 126

Figure 5.3 Schematic diagram of the breeding strategy for the cardiac-specific *Tric-a* KO mouse ..... 127

Figure 5.4 Genotyping gel of Cre and Flox on the colony ..... 128

Figure 5.5 RT-qPCR result of TRIC-A mRNA expression level..... 130

Figure 5.6 Western-blot of TRIC-A protein expression level (from Dr E. Venturi).... 131

Figure 5.7 RT-qPCR analysis of Tric-a, Tric-b, and RyR2 mRNA expression level... 132

Figure 6.1 Sequences and structures of the RyR2 channel ..... 140

Figure 6.2 Structure of the HD1 and alignment of the corresponding wild-type and mutated HD1 amino acid sequences of RyR2 from pig and human..... 141

Figure 6.3 Using root-mean-square deviation (RMSD) to quantify structural similarities between WT and mutant models..... 143

Figure 6.4 Effects of the R2474S and V2475F mutations on the structure of the HD1 ..... 146

Figure 6.5 Cartoon of effects of the R2474S and V2475F mutations on the HD1 conformation ..... 147

Figure 6.6 Structural details of the interactions around the mutation site..... 148

Figure 6.7 Overall view of the homology modelling results aligned with the original cryo-EM pRyR2 structure..... 150

Figure 6.8 Typical gating of native RyR2 channels derived from the hearts of WT and V2475F(+/-) mice and effects of the V2475F mutation on the response of RyR2 channels to cytosolic $Ca^{2+}$..... 152

Figure 6.9 Effects of the V2475F mutation on the population frequency of high Po RyR2 channels in mouse cardiac muscle. ..... 153

Figure 6.10 Effect of cytosolic $Mg^{2+}$ on WT and V2475F channels..... 154

Figure 6.12 CaM-RyR2 domain interactions illustrating the shift of the RyR2 binding site for CaM at different $Ca^{2+}$ concentrations from (Gong et al. 2019) ..... 159

Figure 7.1 Schematic showing the effects of ebselen and DTT on the SR $K^+$ channel162

Figure 7.2 $Ca^{2+}$-release-related ion pathways on the SR..... 163

# List of Tables

Table 2-1 Primers of Flox pairs and Cre pairs ..... 56

Table 2-2 Target gene and corresponding Taqman assay (Thermo Fisher Scientific, UK) ..... 57

Table 2-3 Master Mix table ..... 58

# Abbreviation List

**A/D converter** - Analogue to digital converter

**ANOVA** - Analysis of variance

**ARVD2** - Arrhythmogenic right ventricular dysplasia type 2

**ATP** – Adenosine-5'-triphosphate

**CaM** - Calmodulin -

**CaMKII** - Calmodulin-dependent kinase II

**CASQ** - Calsequestrin –

**CICR** - $Ca^{2+}$-induced-$Ca^{2+}$-release

**cKO** – cardiac-specific knock-out

**CPVT -** Catecholaminergic polymorphic ventricular tachycardia

**Ct** - Cycle threshold

**CTT** - Carboxyl-terminal tail

**DAD** - Delayed after depolarisations

**DCM** - Decamethonium

**DHPR** - Dihydropyridine receptor

**DTT** - Dithiothreitol

**EC-coupling** – Excitation and contraction coupling

**ECG** - Electrocardiogram

**EDTA** - 2,2′,2″,2‴-(ethane-1,2-diyldinitrilo)tetraacetic acid

**EGTA** - Ethylene glycol-bis(β-aminoethyl ether)-N,N,N',N'-tetraacetic acid

$\mathbf{E_{rev}}$ - Reversal potential

**EtBr** - Ethidium bromide

**FKBP** - FK506-binding protein

**flox** - Flanking/flanked by LoxP

**HD1** – Helical domain 1

**HEK293** - Human embryonic kidney 293 cells

**HEPES** - 4-2-hydroxyethyl-1-piperazineethanesulfonic acid

**IC50 -** Half maximal inhibitory concentration

**IP3R** - Inositol trisphosphate receptor

**KDE** - Kernel density estimation

**KO** – Knock-out

**LJP** - Liquid junction potential

**LoxP** - Locus of X-over P1

**LSR** – Light sarcoplasmic reticulum

**LTCC** - L-type $Ca^{2+}$ channel

**mRNA** - Messenger ribonucleic acid

**NaCl** - Sodium chloride

**NaF** - Sodium fluoride

**NCX1** - $Na^{+}$-$Ca^{2+}$ exchanger 1

**NTC** - Non-template control

**PCR** - Polymerase chain reaction -

**PDB** – Protein Database Bank

**PE -** Phosphatidylethanolamine

**PIPES -** 1,4-Piperazinediethanesulfonic acid

**PKA -** Protein kinase A

**PLB** - Phospholamban

**PMCA** - Plasma membrane $Ca^{2+}$ ATPase

**PMSF** - Phenylmethylsulphonic fluoride

**Po** – Open probability

**QuB** - Quantify Unknown Biophysics

**R2475S** - Arginine amino acid at position 2475 mutated to serine residue

**RT-qPCR** - Quantitative reverse transcription PCR

**RyR** – Ryanodine receptor

**RyR1** – Skeletal isoform ryanodine receptors / ryanodine receptor isoform 1

**RyR2** – Cardiac isoform ryanodine receptors / ryanodine receptor isoform 2

**SD** - Standard deviation

**SDS** - Sodium dodecyl sulphate

**SEM** - Standard error of the mean

**SERCA** - Sarco/endoplasmic reticulum $Ca^{2+}$-ATPase

**SKM -** Segmental k-means algorithm

**SR** - Sarcoplasmic reticulum

**TAM** - Tamoxifen

**TRIC** – Trimeric intracellular cation channel

**TRIC-A** – Trimeric intracellular cation channel subtype A

**TRIC-B** – Trimeric intracellular cation channel subtype B

**Tris** - Tris(hydroxymethyl)aminomethane

**T-tubules** - Transverse tubules

**V2475F** - Valine amino acid at position 2475 mutated to phenylalanine residue

**VDCR** - Voltage-dependent-$Ca^{2+}$-release

**WT** - Wild type

# Table of Contributions

| **Figure number** | **Contributor(s)** | **Work contributed/ Contribution** |
|---|---|---|
| Figure 1.2 | Cite from article: Jiang, Dawei, Ruiwu Wang, Bailong Xiao, Huihui Kong, Donald J Hunt, Philip Choi, Lin Zhang, and SR Wayne Chen. 2005. 'Enhanced store overload–induced $Ca^{2+}$ release and channel sensitivity to luminal $Ca^{2+}$ activation are common defects of RyR2 mutations linked to ventricular tachycardia and sudden death', Circulation research, 97: 1173-81. | The original figure was cited to illustrated CPVT mutations in RyR2 |
| Figure 1.3 | Cite from article: Ruan, Yanfei, Nian Liu, and Silvia G Priori. 2009. 'Sodium channel mutations and arrhythmias', Nature Reviews Cardiology, 6: 337-48. | The original figure was cited to illustrate DADs |
| Figure 1.4 | A laboratory effort | The illustration figure for CPVT mutation combinations in RyR2 |
| Figure 1.6 | Cite from article: Wang, Xiao-hui, Min Su, Feng Gao, Wenjun Xie, Yang Zeng, Delin Li, Xue-lei Liu, Hong Zhao, Li Qin, and Fei Li. 2019. 'Structural basis for activity of TRIC counter-ion channels in calcium release', Proceedings of the National Academy of Sciences, 116: 4238-43. | The original figure was adapted to illustrate structure of TRIC channels |
| Figure 1.7 | Cite from article: Matyjaszkiewicz, Antoni, Elisa Venturi, Fiona O'Brien, Tsunaki Iida, Miyuki Nishi, Hiroshi Takeshima, Krasimira Tsaneva- | The original figure was adapted to illustrate current-fluctuation of sub-conductance state of SR $K^+$ channel |

| | | |
|---|---|---|
| | Atanasova, and Rebecca Sitsapesan. 2015. 'Subconductance gating and voltage sensitivity of sarcoplasmic reticulum $K^+$ channels: a modelling approach', Biophysical journal, 109: 265-76. | |
| Figure 3.9 and Figure 3.11 | Dr Elisa Venturi | 3 recordings of ebselen and DTT treatment experiments on SR $K^+$ channel from luminal side<br>3 recordings of ebselen and DTT treatment experiments on SR $K^+$ channel from cytosolic side |
| Figure 4.1 | Dr Takashi Murayama's group | Western blot figure was generated by Dr Takashi's group |
| Figure 4.5 and 4.6 | Dr Elisa Venturi | 4 recordings of $Ca^{2+}$ response experiments on RyR2+TRIC-A HEK293 cells<br>6 recordings of $Ca^{2+}$ response experiments on RyR2+TRIC-B HEK293 cells |
| Figure 4.11 | Dr Elisa Venturi | 2 recordings of $E_{rev}$ measurement in ramp-voltage experiments on RyR2 only HEK cells<br>7 recordings of $E_{rev}$ measurement in ramp-voltage experiments on RyR2+TRIC-A HEK cells<br>6 recordings of $E_{rev}$ measurement in ramp-voltage experiments on RyR2+TRIC-B HEK cells |
| Figure 5.2 | Dr Ben Davies' group | The build-up and validation of $Tmem38a^{tm1.1}$ were performed by Dr Ben Davies' group |
| Figure 5.6 | Dr Elisa Venturi | The western blot experiments and the analysis figure were |

| | | |
|---|---|---|
| | | performed and generated by Dr Elisa Venturi |
| Figure 6.8, 6.9 and 6.10 | Dr Abigail Wilson | Figures from published paper (Wilson et al. 2021) |
| Figure 6.11 | Cite from article:<br>Gong, Deshun, Ximin Chi, Jinhong Wei, Gewei Zhou, Gaoxingyu Huang, Lin Zhang, Ruiwu Wang, Jianlin Lei, SR Wayne Chen, and Nieng Yan. 2019. 'Modulation of cardiac ryanodine receptor 2 by calmodulin', Nature, 572: 347-51. | Original figure was adapted and cited to illustrate interactions between CaM/apo-CaM and RyR2 |

# Chapter 1 Introduction

## 1.1 $Ca^{2+}$ signalling and contraction in cardiac and skeletal muscle

$Ca^{2+}$ is one of the most important second messengers in the cell signalling process and plays an important role in many vital cellular processes, including muscle contraction, neurotransmitter release, energy consumption, protein synthesis and transcriptional regulation (Bers 2008). The absolute necessity of extracellular $Ca^{2+}$ for contractile function of the heart was first discovered in 1883 by Ringer (Ringer 1883) and this highlights an important difference between cardiac and skeletal muscle which, in comparison, can contract for a while without extracellular $Ca^{2+}$ (Armstrong, Bezanilla, and Horowicz 1972). Nevertheless, the mechanisms underlying contraction of skeletal and cardiac muscle bear many similarities and $Ca^{2+}$ plays an important role in both types of muscle. Many of the key proteins involved in the control of cardiac and skeletal muscle contraction are similar and the ultra-structure of cardiac and skeletal muscle shares many similarities as discussed below. In this thesis, I have studied the properties of two types of proteins that play a role in muscle contraction and are found in both cardiac and skeletal muscle, namely the ryanodine receptor $Ca^{2+}$-release channel (RyR) and the trimeric intracellular ion channels (TRIC).

## 1.2 Excitation contraction coupling

Contraction of cardiac and skeletal muscle is initiated by an action potential that is propagated throughout the sarcolemmal membrane, including the transverse tubules (T-

tubules), which are invaginations of the plasma membrane (Franzini-Armstrong and Jorgensen 1994) (see Figure 1.1), At certain regions of the T-tubules, the sarcoplasmic reticulum (SR) lies very close to the T-tubule membrane and these portions of the SR are called the junctional SR (Costello et al. 1986; Franzini-Armstrong and Jorgensen 1994). The SR acts as a $Ca^{2+}$-store containing millimolar levels of $Ca^{2+}$ that can be released as required for muscle contraction (Bers 2002; Peachey 1965).

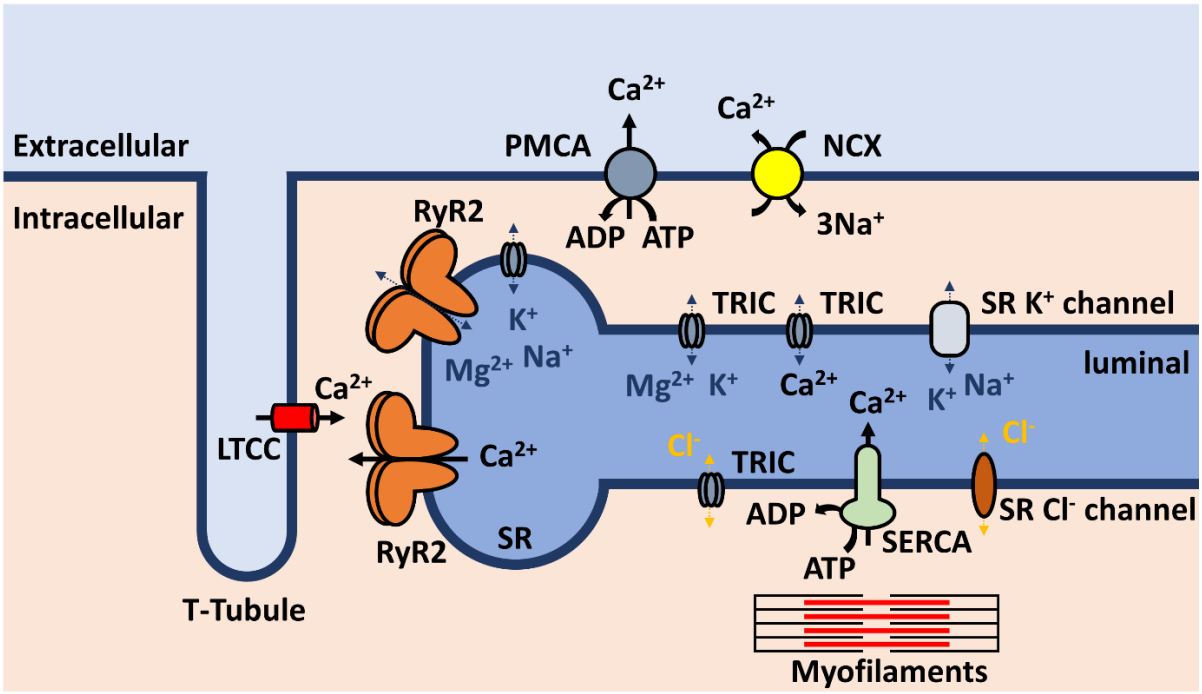



**Figure 1.1 Representation of EC-coupling process in cardiac muscle**

The diagram shows a T-tubule and SR membranes containing the main proteins involved in CICR. Membranes are shown in deep blue. The ion channels and molecules are as follows: LTCC — L-type calcium channel; PMCA — plasma membrane $Ca^{2+}$ ATPase; NCX — $Na^+/Ca^{2+}$ exchanger; RyR — cardiac ryanodine receptor; TRIC — trimeric intracellular cation channel; SERCA — sarcoplasmic/endoplasmic reticulum $Ca^{2+}$-ATPase; ATP — adenosine triphosphate; ADP — adenosine diphosphate; The flow of $Ca^{2+}$ is indicated by black arrows and flow of other ions, like $Na^+$, $K^+$ and $Cl^-$ are illustrated by dashed dark-blue arrows.

The EC-coupling process in skeletal muscle is referred to as voltage-dependent $Ca^{2+}$ release (VDCR). In skeletal muscle, EC-coupling is triggered by the depolarization of the sarcolemmal membranes, which results in the activation of voltage-sensitive L-type $Ca^{2+}$ channels (LTCC), the dihydropyridine receptors (DHPRs) (Tanabe et al. 1988; Flucher, Takekura, and Franzini-Armstrong 1993; Ríos and Pizarro 1991). The DHPRs locate on the T-tubule invaginations and directly couple to the skeletal isoform of RyR (RyR1) in the SR (Tanabe et al. 1988; Block et al. 1988; Ríos, Ma, and González 1991; Tanabe et al. 1990; Schneider 1994). RyR is a high molecular mass membrane-spanning protein introduced in the later paragraph in this chapter (Meissner 1975; Kawamoto, Brunschwig, and Caswell 1988). Depolarisation of the T-tubule membrane causes a conformational change in the voltage-sensing DHPRs which induces opening of those RyR1 channels with which they are in physical contact with, thus initiating rapid $Ca^{2+}$ flux from SR (Ríos and Pizarro 1991; Tanabe et al. 1990; Schneider 1994; Takeshima et al. 1994). The subsequent rise in intracellular $[Ca^{2+}]$ results in the activation of cellular contractile proteins, causing the contraction of skeletal muscle cells.

The EC-coupling process in cardiac muscle is referred to as $Ca^{2+}$-induced calcium release (CICR) (Fabiato 1985) and Figure 1.1 shows the important components of this process. EC coupling in cardiac muscle begins with the action potential which causes depolarization of the sarcolemmal membranes including the T-tubule membranes, which contain high quantities of the L-type calcium channel (LTCC) (Bean 1985; Bers 2001). Depolarization causes activation of the LTCC and allows a small amount of $Ca^{2+}$ to flow into the tiny cytosolic space between the LTCCs in the T-tubule membrane and the

clusters of cardiac ryanodine receptors (RyR2) situated in the junctional sarcoplasmic reticulum (SR) membranes (Carl et al. 1995; Sun et al. 1995). The $Ca^{2+}$ that enters the cell in this manner is not enough to activate the contractile proteins, however, the free $[Ca^{2+}]$ in the cytosolic cleft region between the LTCC and RyR2 channels can rise to levels as high as $10 - 100$ μM (Despa et al. 2014) and is thought to activate each cluster of RyR2. As the RyR2 channels in each cluster are activated, $Ca^{2+}$ floods out of the SR and results in activation of the myofilaments, causing synchronous contraction of the cardiac muscle cells. Nabauer et al. 1989 showed that extracellular $Ca^{2+}$ is required for triggering this $Ca^{2+}$ release process from cardiac SR, by providing an inward $Ca^{2+}$ current through LTCCs (Nabauer et al. 1989).

Following contraction of both skeletal and cardiac muscle cells, intracellular $Ca^{2+}$ levels are re-equilibrated primarily by the action of the sarco-/endoplasmic reticulum $Ca^{2+}$-ATPase (SERCA) pumping $Ca^{2+}$ back into the SR, and the $Na^{+}/Ca^{2+}$ exchanger (NCX) and plasma membrane $Ca^{2+}$ ATPase (PMCA) which pump $Ca^{2+}$ out of the cell (Bassani, Bassani, and Bers 1994; Bassani, Bassani, and Bers 1992; Bers and Bridge 1989).

## 1.3 Single channel recording

In the pursuit of a detailed characterisation of the function of the SR ion channels, numerous studies have employed single-channel recordings, an electrophysiological method that allows extensive control of the cytosolic and luminal environment of specific ion channels when monitoring their activity (Miller 1978). In these experiments, an artificial phospholipid bilayer is used for the incorporation of vesicles from SR membrane

preparations that contain the target ion channels (further details of the membrane preparation and vesicle fusion are described in the Methodology Chapter).

During the recording process, both sides across the phospholipid bilayer are filled with a combination of ion solutions specifically designed to allow ion passing through the target type of channels. With a setup of electrical equipment (2.2.3 in Methodology Chapter), the current passing through the membrane will be amplified and recorded on a computer upon the application of a voltage and/or chemical stimulus.

The recorded traces can then be analysed to study the gating and conductance properties of the ion channels. For example, when incorporated ion channels are not gating there will be no currents passing through the membrane and the amplitude will be close to 0 pA, which defines the baseline of the recording. In contrast, when incorporated ion channels open, they allow the passage of currents through the membrane, which for certain channels can be stable, giving a plateau amplitude called the full conductance open state (or often open state). In some cases, ion channel current can pass at a reduced level between the baseline and the full conductance open state, which reflects gating at a sub-conductance state (further details in 1.5.3 of this Chapter). Sub-conductance states may have more complicated properties, such as multiple amplitude levels, unstable currents, and larger signal to noise ratio. To analyse the properties of sub-conductance states specialised software is used, such as QuB as described in detail in Methodology Chapter. To briefly describe the process of this analysis, QuB uses a multiple-normal-distribution curve fitting on the current amplitude of the recorded trace and the mean of each distribution reflects a gating level.

The most common way of characterising channel activity in single channel recordings is to calculate the open probability ($P_O$), which reflects the overall average channel opening during a given period time (the calculation of Po is given in the 2.4.2 of Methodology Chapter). There are other aspects of ion channel gating behaviour, including the mean duration of open and closed events, distributions of open and closed event lifetimes, permeability ratios of different types of cations or anions, channel conductance and channel block, the details of which are described in the Methodology Chapter.

While the method of single-channel recording provides the means to measure the biophysical characteristics of an ion channel in a controllable and simplified environment, it also has limitations. For example, it is often difficult to match the recording conditions to the physiological conditions that exist in a cell, such as the presence of important regulators which are not isolated together with the ion channels in the SR preparations. Also, there are hardware limitations that can restrict the minimum duration of opening or closing events that can be accurately resolved. These factors require us to design our experiments carefully avoiding possible bias on the characterization of ion channel gating and conductance properties.

## 1.4 Ryanodine receptors

Ryanodine receptors (RyR) are a family of $Ca^{2+}$ release channels essential for EC-coupling and are found on the sarcoplasmic or endoplasmic reticulum membranes (Franzini-Armstrong and Protasi 1997; Takeshima et al. 1989). The channels have been termed 'ryanodine receptors' because ryanodine, a plant alkaloid, binds specifically and

with high affinity to them causing the channels to enter irreversibly into a low conductance open state (Lai et al. 1988). RyR proteins are homotetrameric channels with ~5000 amino-acid residues (> 2,000 kDa) (Takeshima et al. 1989). There are three mammalian isoforms of RyR channels, known as the skeletal isoform (RyR1) (Takeshima et al. 1989), the cardiac isoform of RyR (RyR2) (Otsu et al. 1990; Valdeolmillos et al. 1989) and the type3 isoform which expressed in skeletal muscle and brain and many other tissues at low levels (Perez, López, and Allen 2005; Murayama and Ogawa 1996).

### 1.4.1 The cardiac RyR (RyR2)

In this thesis, I have studied certain structural and functional properties of RyR2. As EC-coupling in cardiac muscle is triggered by the inward flux of a small amount of $Ca^{2+}$ into the cell, it is not surprising that the primary activator of RyR2 is cytosolic $Ca^{2+}$. The resting free cytosolic [$Ca^{2+}$] in cardiac cells is 100 nM and, at this concentration, the open probability (Po) of RyR2 is extremely low. However, low micromolar concentrations of cytosolic $Ca^{2+}$ activate RyR2 (Ashley and Williams 1990) and Po peaks at approximately 100 μM (Sitsapesan and Williams 1994b; Laver et al. 1995; Copello et al. 1997). With cytosolic $Ca^{2+}$ as the sole activating ligand, peak Po values are close to 0.5 and do not open fully to Po values of 1 (Ashley & Williams, Sitsapesan). Thus, cytosolic $Ca^{2+}$ acts as a partial agonist and additional ligands together with cytosolic $Ca^{2+}$ are required before RyR2 can be fully opened (Rousseau, Smith, and Meissner 1987; McGarry and Williams 1994; Kermode, Williams, and Sitsapesan 1998). Mechanistically, this is because activation of RyR2 by cytosolic [$Ca^{2+}$] alone occurs predominantly by an

increased frequency of channel opening events and very little increase in the duration of openings occurs (Saftenku, Williams, and Sitsapesan 2000). There are high-affinity activation sites and low-affinity inhibitory sites for $Ca^{2+}$ on the cytosolic side of RyR2 (Chu et al. 1993; Sitsapesan and Williams 1994b; Laver et al. 1995; Meissner 2017). It is important that $Mg^{2+}$ binds to both of these sites and can compete with $Ca^{2+}$ for the binding sites (Smith, Coronado, and Meissner 1986; Meissner, Darling, and Eveleth 1986) and thus can regulate the channel physiologically (Ashley and Williams 1990; Laver, Baynes, and Dulhunty 1997). $Mg^{2+}$ is an antagonist of RyR2. It binds to the closed state of the channel without opening it and by competing with cytosolic $Ca^{2+}$ can reduce channel opening (Laver, Baynes, and Dulhunty 1997).

It has been demonstrated that luminal $Ca^{2+}$ regulates single RyR2 channels incorporated into bilayers [$Ca^{2+}$] (Sitsapesan and Williams 1994a; Györke et al. 2004). Ching et al. 2000 found that tryptic digestion of the luminal side of RyR2 abolished the activating effects of luminal $Ca^{2+}$ on RyR2 via a (Ching, Williams, and Sitsapesan 2000). RyR2 is sensitive to micromolar level of luminal $Ca^{2+}$ causing an increment in Po in sheep cardiac (Ching, Williams, and Sitsapesan 2000). However, it was then found that RyR2 was not stimulated by luminal $Ca^{2+}$ until treated by millimolar level of luminal $Ca^{2+}$ (Loaiza et al. 2013). Additionally, it has been shown that the optimum effects of luminal $Ca^{2+}$ activation require the presence of activating cytosolic [$Ca^{2+}$] as well as other channel activators, such as ATP or caffeine (Sitsapesan and Williams 1994a; Lukyanenko, Györke, and Györke 1996). It is important to note, that unlike cytosolic $Ca^{2+}$ which can open RyR channels in the absence of other ligands, luminal $Ca^{2+}$ is a regulator, not a trigger

and does not activate RyR channels in the absence of other activators (Sitsapesan & Williams 1994a). Luminal $Ca^{2+}$ also induces no change in RyR2 Po if cytosolic $Ca^{2+}$ is the only activating ligand (Sitsapesan and Williams 1994a; Lukyanenko, Györke, and Györke 1996). Bassini et al. 1995 measured the release and uptake of SR $Ca^{2+}$ and found that SR $Ca^{2+}$ content regulates fractional SR $Ca^{2+}$-release in cardiac myocytes (Bassani, Yuan, and Bers 1995). The SR $Ca^{2+}$ content and free SR $[Ca^{2+}]$ have been found to be correlated with potentiation of EC-coupling, suggesting that luminal $Ca^{2+}$ plays important role in the $Ca^{2+}$-release process (Shannon, Ginsburg, and Bers 2000). Thus, cellular experiments also suggest that luminal $Ca^{2+}$ is a powerful regulator of RyR2 Po in the cardiac cell.

### 1.4.2 Other physiological and pharmacological regulators of RyR2

In addition to cytosolic $Ca^{2+}$, $Mg^{2+}$ and luminal $Ca^{2+}$, there are many other drugs and physiological ligands that can alter the Po or single-channel conductance of RyR2 (Meissner 2017; Pessah, Cherednichenko, and Lein 2010). Caffeine and ryanodine, for example, are both used as tools to manipulate RyR2 Po in cellular experiments or to identify the presence of RyR channels in a tissue (McGarry and Williams 1994; Elison and Jenden 1967; Bassani, Bassani, and Bers 1992). ATP is an important physiological regulator of RyR2 that activates the channel in synergy with $Ca^{2+}$ (Kermode et al. 1998; Kermode, Williams, and Sitsapesan 1998), enabling RyR2 Po to increase to high levels as $Ca^{2+}$ enters the cell through L-type $Ca^{2+}$ channels (LTCC). The large macromolecular

structure of RyR also allows RyR2 to act as a scaffolding protein where many other proteins bind. The proteins calmodulin (CaM), calsequestrin (CASQ), junctin, junctophilin, triadin and the FK506-binding proteins (FKBP12 and FKBP12.6) bind tightly and have been shown to affect RyR2 function (Timerman et al. 1996; Jeyakumar et al. 2001; Ahern, Junankar, and Dulhunty 1997; Cheung 1980; Qin et al. 2008; Galfre et al. 2012; Venturi et al. 2014; Munro et al. 2016).

There are also several post-translational modifications that can occur to RyR2, and which are thought to be important in the regulation of RyR2 (Denniss, Dulhunty, and Beard 2018). Protein kinases, such as protein kinase A (PKA) and calmodulin-dependent protein kinase II (CaMKII), closely and indirectly associate with RyR2 and regulate its activity (Marx et al. 2000; Camors and Valdivia 2014; Carter, Colyer, and Sitsapesan 2006) There many potentially important phosphorylation sites on RyR2, among which S2030, S2808 and S2814 have been most extensively studied due to the availability of antibodies for the phosphorylation sites. PKA and CaMKII both phosphorylate the S2808 residue while the S2030 residue is targeted by PKA and the S2814 residue is targeted by CaMKII (Rodriguez, Bhogal, and Colyer 2003; Wehrens et al. 2004; Xiao et al. 2006). It has been suggested that the phosphorylation of RyR2 plays an important role in the pathophysiological mechanisms of cardiac disease (Denniss, Dulhunty, and Beard 2018). Carter et al 2006 researched PKA phosphorylation of site S2808 and showed that the basal levels of phosphorylation of RyR2 are at 75% of maximum S2808 levels while Po is low (Carter, Colyer, and Sitsapesan 2006). However, both hyperphosphorylation to the maximal level and dephosphorylation to near 0% level of

S2808 will cause an increase in Po of the channel, showing a biphasic effect of PKA phosphorylation on the regulation of channel gating (Carter, Colyer, and Sitsapesan 2006). It also has been further shown that the hyperphosphorylated levels of phosphorylation by PKA result in the RyR2 channel becoming unregulated by cytosolic $Ca^{2+}$ regulation such that the channels open even in the absence of cytosolic $Ca^{2+}$ (Carter et al. 2011).

### 1.4.3 Catecholaminergic polymorphic ventricular tachycardia

Catecholaminergic polymorphic ventricular tachycardia (CPVT) is a disease with a phenomenon of adrenergically (exercise or emotional stress) mediated bidirectional and/or polymorphic ventricular tachycardia without cardiac pathology. In 2001 (Kapiloff, Jackson, and Airhart 2001), CPVT related mutations were found in the cardiac ryanodine receptor (RyR2) and in cardiac calsequestrin (CASQ2) and CPVT was categorized into two major types. CPVT type 1 (CPVT1) is caused by single-point mutations to the RyR2 $Ca^{2+}$ release channel and is autosomal dominant (Priori et al. 2001), whereas CPVT2 refers to mutations to proteins associated with RyR2 such as CASQ2. Figure 1.2 shows the 'hotspot' locations of CPVT1 mutations that cluster in certain regions of the human RyR2 together with the relative positions of binding sites for certain closely associated proteins of RyR2 and mapped onto the RyR2 amino-acid sequence.

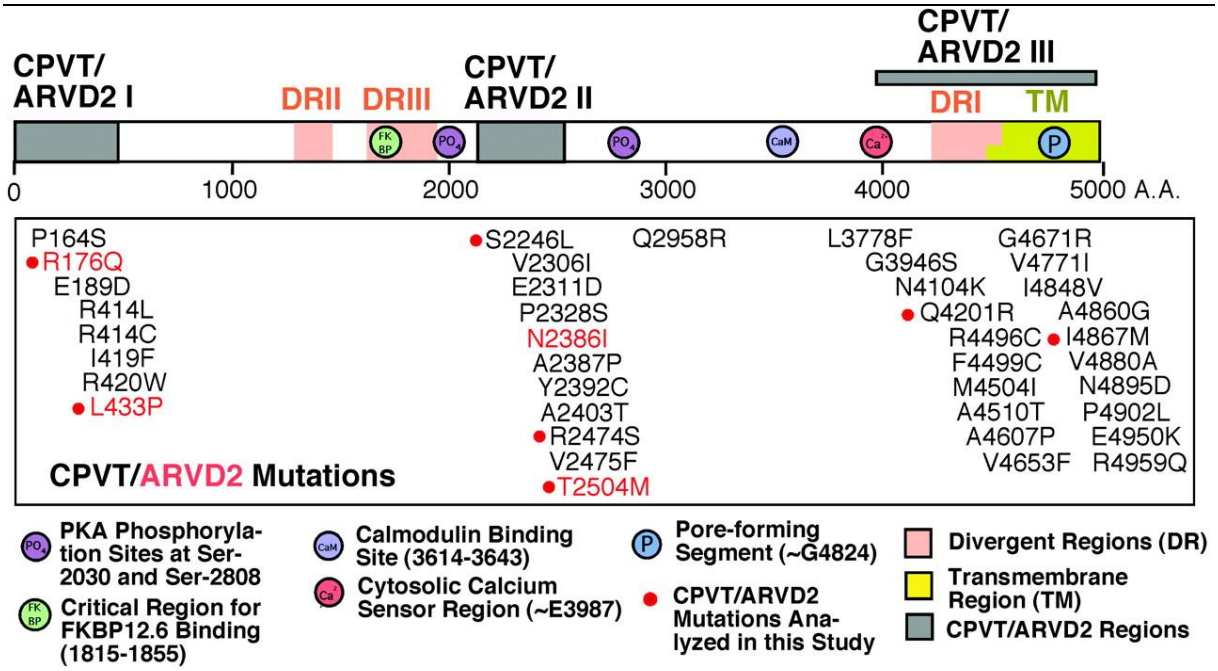



**Figure 1.2 CPVT mutations on the linear sequence of RyR2 (Jiang et al. 2005)**

The 'hotspot' regions of CPVT1 mutations in human RyR2 are shown (together with arrhythmogenic right ventricular dysplasia (ARVD)). The FKBP12.6 binding site, CaM binding site and PKA sites are labelled in green, light purple, and dark purple, respectively. Different regions containing CPVT mutations are also labelled in pink, grey and yellow (Jiang et al. 2005). The lists of CPVT1 mutations are not exhaustive and since publication of this review, more CPVT1 mutations have been detected.

CPVT1 is usually observed in children and young adults and results in life-threatening arrhythmias due to abnormalities in sarcoplasmic reticulum (SR) $Ca^{2+}$ release (Priori et al. 2001). Patients with CPVT have a normal QT interval (approximates to the time for the cardiac ventricles starting to contract to finishing relaxing), and structural heart disease is also not observed, yet polymorphic ventricular tachycardia can be induced by physical exertion or emotional stress (Napolitano, Priori, and Bloise 2016; Priori et al. 2001). As described above, RyR2 plays an important role in CICR wherefore it is not surprising that mutations, which affect the function of RyR2, will produce adverse effects on cardiac cellular $Ca^{2+}$ handling and contractile behaviour. Indeed, many CPVT1-RyR2 mutations have been shown to cause arrythmogenic changes in the $Ca^{2+}$-release process (Jiang et al. 2004; Liu et al. 2006; Uehara et al. 2017). Many CPVT1-associated RyR2 mutations appear to cause increased sensitivity of RyR2 to cytosolic $Ca^{2+}$ and increase the likelihood of $Ca^{2+}$-release during diastole, independent of the depolarization-stimulated $Ca^{2+}$ release described previously (Jiang et al. 2004; Priori et al. 2001). This abnormal, spontaneous release of SR $Ca^{2+}$ during diastole can lead to a type of arrhythmia called a delayed afterdepolarization (DAD), which can trigger an additional action potential that is elicited before the action potential has fully repolarized (Marban, Robinson, and Wier 1986; Loaiza et al. 2013). This happens because the extra release of SR $Ca^{2+}$ is sufficient to produce enough inward current through NCX (3 x $Na^{+}$ into the cell for every $Ca^{2+}$ out) to produce depolarization of the cell (Mohamed, Napolitano, and Priori 2007). Figure 1.3 shows an example of DADs observed in a patient with CPVT1.

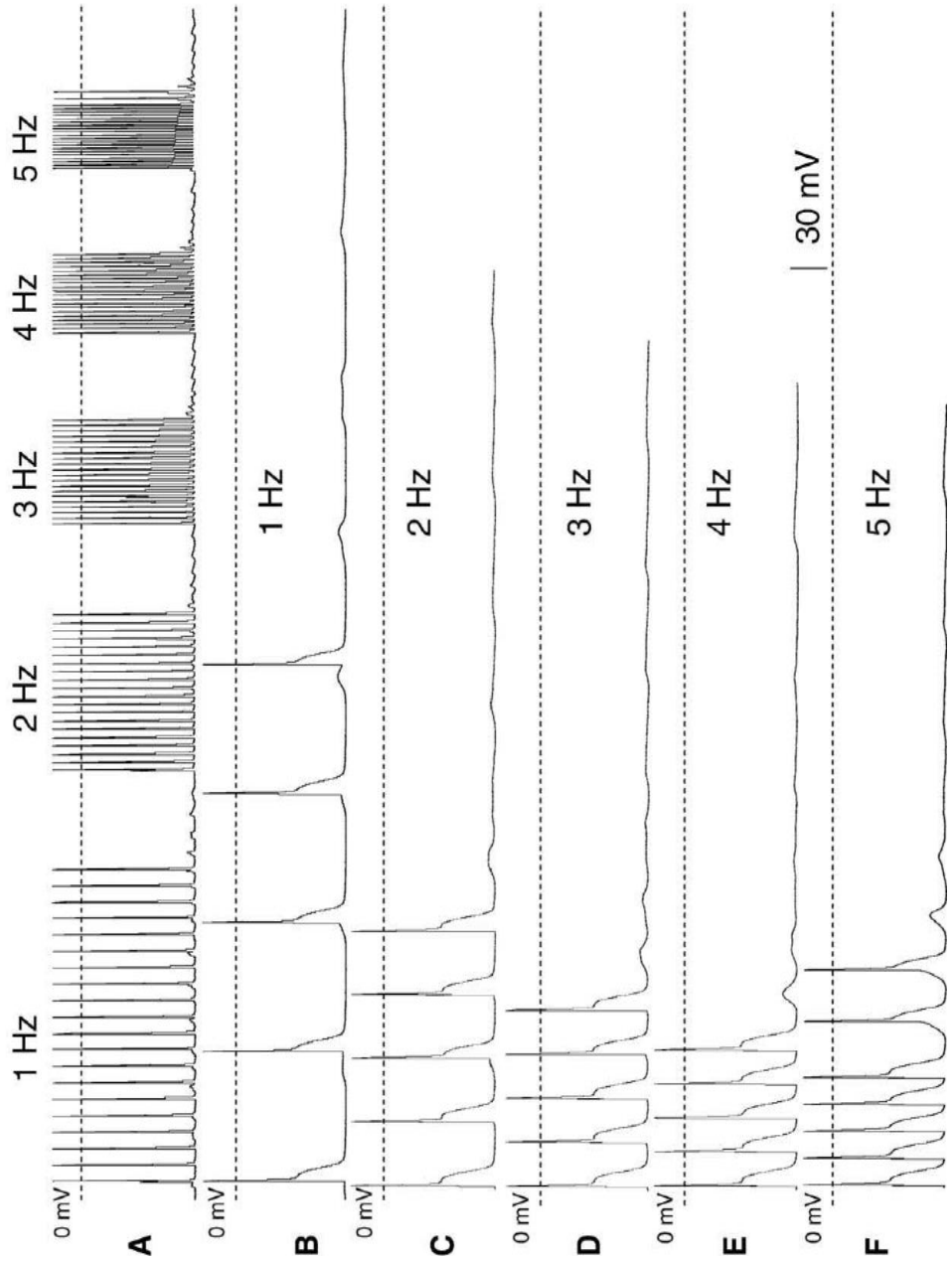



**Figure 1.3 Electrocardiographs from RyR2 R4496C$^{+/-}$ ventricular cardiac myocytes, illustrating delayed after depolarizations (DADs). (Ruan, Liu, and Priori 2009)**

(A) Action potentials recorded from an RyR2 R4496C$^{+/-}$ ventricular cardiac myocyte, stimulated at 1 to 5 Hz. DADs develop when pacing is interrupted.

(B to F) The last five driven action potentials at each pacing frequency. DADs and triggered activity developing when pacing is discontinued are shown. The amplitude of DADs increases and DAD coupling interval decreases at faster pacing frequencies.

It can be seen that DADs can develop when pacing is interrupted and that the likelihood of DADs can increase at higher frequencies of stimulation. Figure 1.3F illustrates two action potentials triggered by DADs at 5Hz. Although it is known that CPVT1-RyR2 mutations can increase the spontaneous release of $Ca^{2+}$ during diastole and result in a recognized type of arrhythmia, surprisingly, most of the CPVT1 mutations have either not been studied in detail, or have not been studied at all, at the single-channel level. To a large extent due to the enormous size of RyR2, it also remains unclear how the structural changes caused by the various CPVT1 mutations cause the dysfunctional properties of RyR2 and thereby lead to the pathogenesis of CPVT1.

The number of cases detailing the clinical phenotypes associated with mutations to RyR2 is increasing (Priori and Chen 2011). In recent studies, other RyR2 mutation-related symptoms were found in addition to the adrenergic stress-induced ventricular arrhythmias, such as the supra-ventricular arrhythmias (Sy et al. 2011). This suggests that different mutations in RyR2 may cause different functional changes to the gating behaviour and/or conductance properties of RyR2 channels. Thus, rather than all CPVT patients being treated in the same way, it is likely that treatments may need to be tailored to individual patient needs. Another source of variability in CPVT phenotypes comes from the fact that RyR2 channels consist of four monomers. CPVT is an autosomal dominant condition and reported CPVT patients are heterozygous for the mutation. Figure 1.4 illustrates the expected likelihood of different compositions of RyR2 subunits in the tetramer structure.

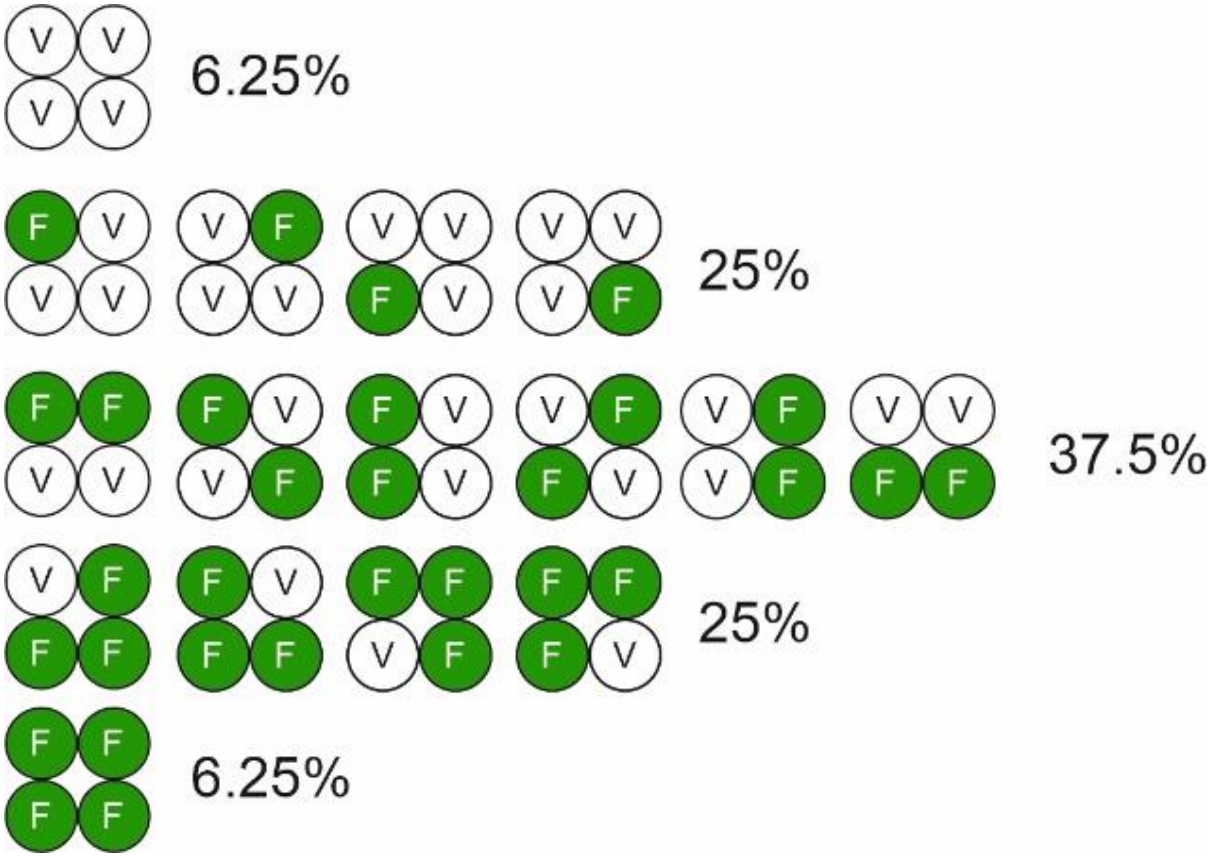



**Figure 1.4 Likelihood of formation of RyR2 tetramers with different compositions of V2475F mutated monomers.**

White (V) and green (F) circles represent WT and V2475F mutated monomers, respectively. Assuming random assembly and identical surface expression, the probabilities of tetramers with the indicated numbers of mutant or WT subunits per tetrameric RyR2 channel is indicated as a percentage (%).

It can be seen that only a small portion of RyR2 channels have all mutated sequences. Thus, patients have a variable number of mutated monomers in each RyR2 homotetramer found in the heart, and it will be important in future research to investigate the significance of this. Not only this, but some compositions of mutated RyR2 tetramers, for example, may not form viable ion channels or be trafficked correctly to the SR membrane so that there may be loss of RyR2 ion channels in the junctional SR.

Using a mouse model, the Sitsapesan lab is researching the functional changes to single RyR2 channels caused by the human CPVT1 mutation V2475F (Tester et al. 2005; Loaiza et al. 2013). In this thesis I describe parallel experiments where I used molecular modelling techniques in an attempt to relate the functional changes in single-channel function to possible structural changes at the molecular level. Another severe CPVT1 patient mutation is the R2474S mutation (Lehnart et al. 2008; Loaiza et al. 2013; Salvage et al. 2019), which is located on a neighbouring amino acid. Thus, I focused on comparing the putative structural changes with these two mutations. Figure 1.5A shows the domain organization of the RyR2 channel and highlights the domain containing the V2475F and R2474S mutations. I applied a molecular homology modelling approach to generate models of the RyR2 region containing these mutations in the human RyR2 Helical Domain 1 (HD1, residues 2111 to 2679), using the solved pig HD1 structure as the template with a resolution at 4.20 Å. Figure 1.5B shows the location and relative position of HD1 within the whole structure of the RyR2 channel.

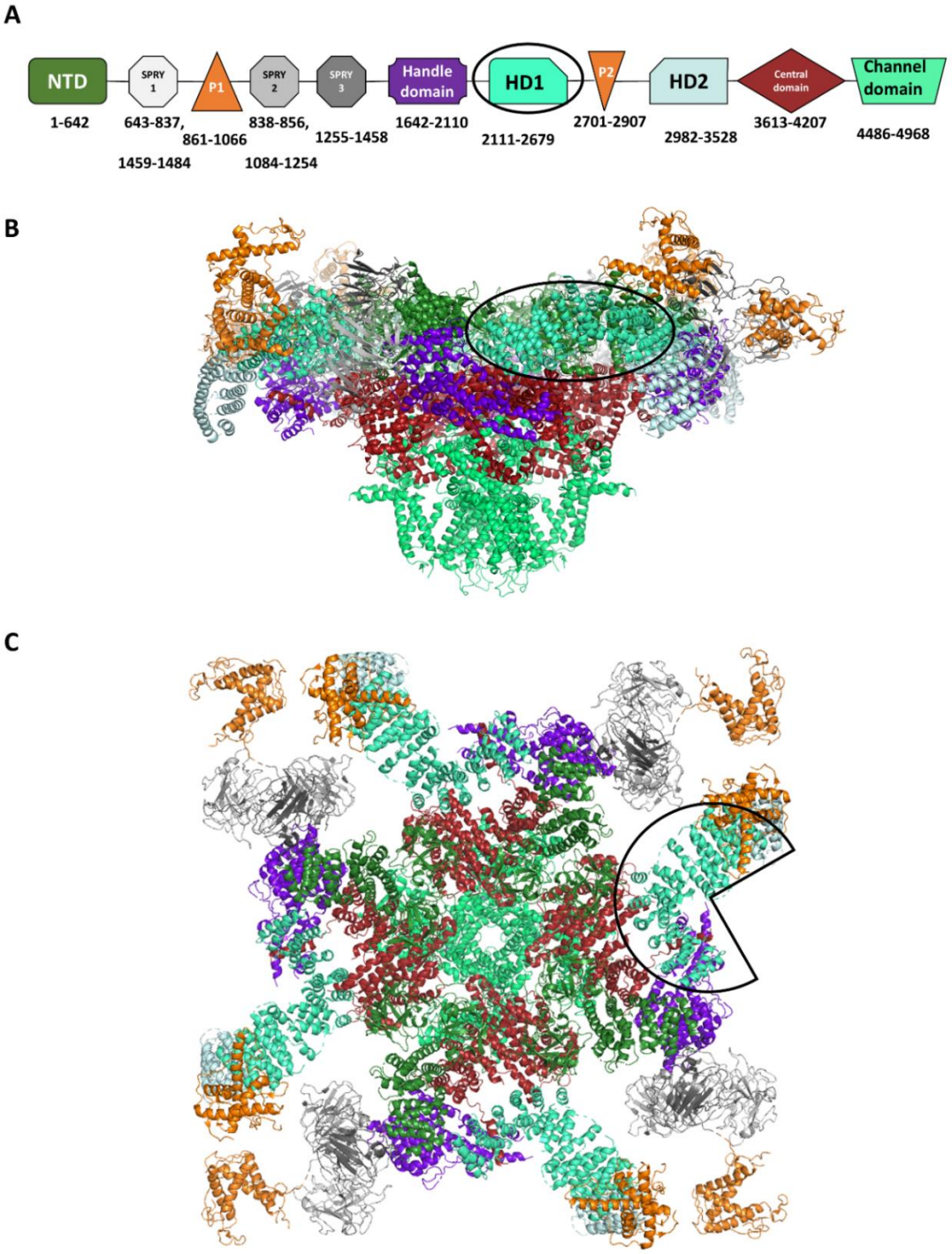



**Figure 1.5 Sequences and structures of the RyR2 channel**

**(A)** Domain organisation of the RyR2 channel and **(B)** Side-view of the cryo-EM RyR2 structure (PDB ID: 5GOA as a demonstration with a resolution at 4.20 Å). The helical domain-1 (HD1) is circled by black lines. **(C)** Cytosolic-view of the cryo-EM RyR2 structure. HD1 is circled by black lines.

## 1.5 Counter-ion current across the SR membrane

As described above, during EC-coupling in cardiac and skeletal muscle, a large and rapid release of $Ca^{2+}$ release from the SR stores is required to produce muscle contraction. To maintain this release, a mechanism is required to prevent accumulation of negative charge within the SR, otherwise the reversal potential ($E_{rev}$) for $Ca^{2+}$ would be rapidly reached, preventing $Ca^{2+}$ flux through the RyR channels even when they are open. Modelling studies indicate that while RyR channels can provide a proportion of their own counter-ion current (Zsolnay, Fill, and Gillespie 2018), other counter-ion pathways are required. It is thought that ionic flow through other ion-channels, such as SR $K^+$ and $Cl^-$ channels could provide the counter-current flux required to balance the loss of positive charge that occurs during the $Ca^{2+}$-release process (Miller 1978; Garcia and Miller 1984; Miller and Rosenberg 1979).

### 1.5.1 Trimeric intracellular cation channels

Yazawa et al. (2007) discovered the trimeric intracellular cation channel (TRIC) proteins on the endo-/sarco- plasmic reticulum (ER/SR) and nuclear membranes, identifying two sub-types, TRIC-A and TRIC-B (Yazawa et al. 2007). Cross-linking studies and electron microscopy indicated that TRICs were a novel type of ion channel being trimeric in structure (Yazawa et al. 2007). TRIC-A is abundant among excitable tissues, the brain and cardiac and skeletal muscles, while TRIC-B is expressed at lower levels in many kinds of tissues (Yazawa et al. 2007). Yazawa et al found that incorporation of purified TRIC-A into artificial membranes led to the appearance of $K^+$ and $Na^+$ conductances

and gave rise to the idea that TRICs were cation channels. There are studies in determining the structural features of TRIC channel from different sources including various prokaryotic and eukaryotic sources (Kasuya et al. 2016; Ou et al. 2017; Su et al. 2017; Wang et al. 2019; Yang et al. 2016). Recent solved vertebrate TRIC-A and TRIC-B structures from X-ray diffraction with a resolution at 3.29 Å are shown as the following Figure:

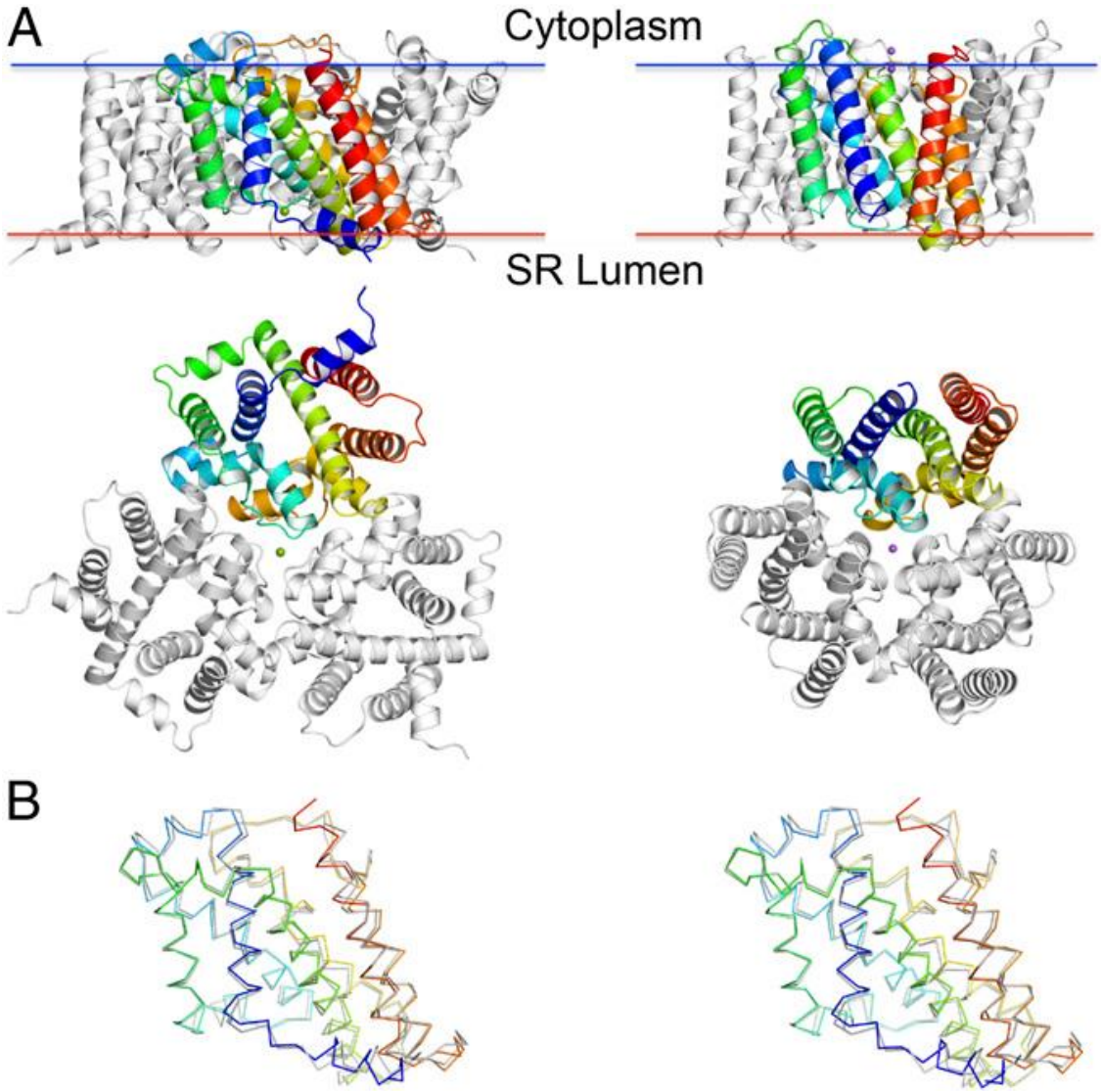



**Figure 1.6. Structure of vertebrate TRIC-A and TRIC-B structures from Wang et al. 2019 (Wang et al. 2019)**

(A)Side-view and cytosolic view of TRIC-A (left) from *gallus gallus* (chicken) and TRIC-B (right) from *xenopus laevis* (frog). Structures are obtained with a resolution at 3.29 Å (PDB ID: 6IZ6). One protomer of each channel is labelled from blue to red representing N terminus to C terminus, respectively.

(B)Superimposition of the protomer structure of TRIC-A and TRIC-B in the same orientation as in (A)

As for properties, characterisation of the functions of different TRIC channels has lagged. Purified TRIC proteins have always been reported to be permeable to $K^+$ but without a rigorous examination of their permeability or conductance properties (Kasuya et al. 2016; Ou et al. 2017; Pitt et al. 2010; Su et al. 2017; Venturi et al. 2013; Wang et al. 2019). During the characterisation on the reconstitution of purified TRICs into bilayers, the channels give rise to frequent brief currents of many varied amplitudes making the conventional single-channel untenable. There are similarities between the current fluctuation amplitudes of this rapid gating behaviour and the sub-conductance gating from the SR $K^+$ channel (described later on section (1.5.3 The SR $K^+$ channel)) (Coronado and Miller 1980; Miller 1978) while the exact gating behaviours of full open channel conductance between purified TRICs and SR $K^+$ channel were never observed as shown in the Figure 1.8 in 1.5.3 section. In view of the irregular TRIC channel behaviour and uncertain role of TRIC channels as SR $K^+$ channel, we would like to investigate the channel properties of TRICs via incorporated channels from co-expressed TRICs channel in RyR2 induced HEK293 cell in this thesis.

There have been some pathology studies using *Tric* knock-out (KO) channel mouse models (Yazawa et al. 2007; Yamazaki et al. 2009; Yamazaki et al. 2011; Zhao et al. 2010). Abnormal $Ca^{2+}$ release and over-loaded ER/SR stores is observed in these mouse models (Yazawa et al. 2007; Yamazaki et al. 2009; Yamazaki et al. 2011; Zhao et al. 2010). The *Tric-a* KO mouse survives until adulthood, however, the ability of its skeletal muscle cells to respond to stress is defective, and the $Ca^{2+}$ release process is unstable (Yamazaki et al. 2011; Zhao et al. 2010). *Tric-b* KO mice exhibits inadequate $Ca^{2+}$-

release from overloaded ER stores in alveolar epithelial cells and dies of respiratory failure after birth (Yamazaki et al. 2009). *Tric* double KO (*Tric-a* and *Tric-b* KO) mouse shows swollen and $Ca^{2+}$ overloaded SR in the heart and embryonic cardiac failure at embryonic day E9.5 (Yazawa et al. 2007). It has been found that the *Tric-a* KO mouse develops a hypertension phenotype affecting $Ca^{2+}$-release in vascular smooth muscle cells and *Tric-b* genetic mutations are correlated with osteogenesis imperfecta (Zhou et al. 2020; Shaheen et al. 2012; Rubinato et al. 2014; Zhao et al. 2010). Thus, an aim of this thesis is to investigate the physiological role and effect of *Tric-a* gene in the heart.

### 1.5.2 Interactions between TRIC and RyR channels

As previously mentioned, $Ca^{2+}$ release occurs primarily through RyR1 channels in skeletal muscle and through RyR2 in cardiac muscle (Bers 2001; Franzini-Armstrong and Protasi 1997; Takeshima et al. 1989). There is now emerging evidence that TRIC-A, in addition to providing monovalent cation flux during SR $Ca^{2+}$ release process, may also interact directly with RyR channels to modulate single-channel gating (El-Ajouz et al. 2017; Zhou et al. 2020). El-Ajouz et al 2017 found that knock-out of the *Tric-a* gene in mice caused alteration in the single-channel behaviour of RyR1. The Po of RyR1 channels derived from the skeletal muscle of *Tric-a* KO mice, in the presence of key physiological regulators, was markedly lower than that of RyR1 channels from WT mice, suggesting that there may be direct physical interactions between TRIC-A and RyR1 (El-Ajouz et al. 2017). Furthermore, it has been suggested that there is stimulation between TRIC-A and RyR2, where flexible carboxyl-terminal tail (CTT) portion of TRIC-A could activate

RyR2 whereas the CTT of TRIC-B does not exhibit the same effect (Zhou et al. 2020). It is suggested that TRIC-A may bind directly to RyR2 via the CTT domain and the CTT of TRIC-A and TRIC-B are located on the cytosolic channel side. The CTT domain is potentially responsible for interactions between TRIC channels and other types of channel such as RyR.

### 1.5.3 The SR $K^+$ channel

The SR $K^+$ channel was first observed and identified by Miller after incorporation of skeletal muscle SR membranes into artificial phospholipid bilayers in 1978 (Miller 1978). Based on the later characterisation study of the permeability and selectivity properties of the SR $K^+$ channel, it was found that the channel is selective for monovalent cations and impermeable to $Ca^{2+}$ (Coronado, Rosenberg, and Miller 1980) and anions. The SR $K^+$ channel is thus considered to provide a pathway for $K^+$ flowing into SR lumen to balance charge changes caused by $Ca^{2+}$ release (McKinley and Meissner 1978). The SR $K^+$ channel was found to be permeable to monovalent ions in the sequence of $K^+ > NH_4^+ > Rb^+ > Na^+ > Li^+ > Cs^+$ but not to divalent cations like $Ca^{2+}$ (Coronado, Rosenberg, and Miller 1980). The SR $K^+$ channel is described as a voltage-sensitive channel (Miller 1978). Under voltage-clamp conditions, the Po of the channel is higher at positive potentials than at negative potentials (Miller and Rosenberg 1979; Matyjaszkiewicz et al. 2015). The SR $K^+$ channel also exhibited sensitivity to acidic conditions, where the conductance of channel was reduced at pH 5.0 with $K^+$ as permeable ions (Miller 1978). Further studies of Dr Eberhardt from Prof. Sitsapesan's group illustrated that the Po of SR $K^+$

channel was significantly reduced under high pH from the luminal side (pH=9.2) at positive potentials in a manner whereby the contribution of full open states was significantly inhibited (Eberhardt 2018). It has been found that the SR $K^+$ channel is blocked by $Ca^{2+}$ (Miller 1978; Uehara, Yasukochi, and Imanaga 1994). Dr Eberhardt illustrated the detailed effect of $Ca^{2+}$ on the SR $K^+$ channel, where the Po of the channel was largely reduced by luminal $Ca^{2+}$ (1 mM) at positive potentials (David Eberhardt, PhD thesis, (Eberhardt 2018)). The Po contribution and mean event gating time of the SR $K^+$ channel full open state were inhibited by 1 mM luminal $Ca^{2+}$. In contrast, cytosolic $Ca^{2+}$ did not affect the Po and gating events of SR $K^+$ channel as efficiently the luminal $Ca^{2+}$ treatment.

The nature of the conduction pathway of the SR $K^+$ channel was investigated by Coronado and Miller 1980 using large ammonium organic cations, such as tetraethylammonium, decamethonium (DCM) and hexamethonium (Coronado and Miller 1980, 1982). It was suggested by Coronado and Miller that the conducting pathway of the SR $K^+$ channel was composed of a long, narrow pore with constriction area from 50 $Å^2$ to 20 $Å^2$ (Coronado and Miller 1980, 1982). Two positively-charged, cholinergic drugs, decamethonium and hexamethonium, were found to exhibit blocking effects on the current of the SR $K^+$ channel (Coronado and Miller 1980).

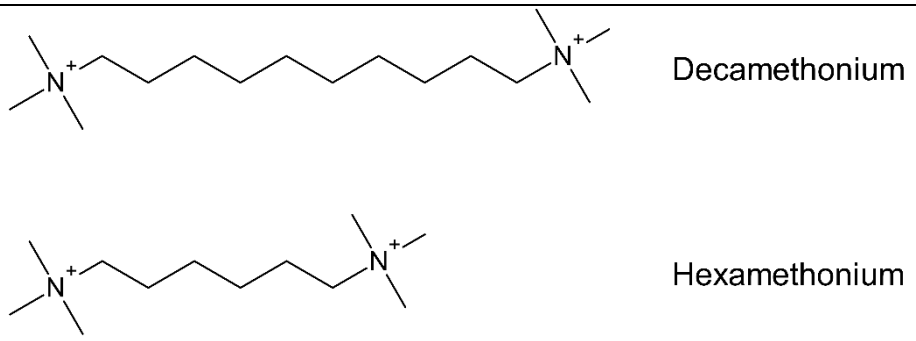



**Figure 1.7 Structure of decamethonium and hexamethonium**

On a close inspection, decamethonium caused a voltage-dependent block, affecting the channel in a 'flickery' way where the full open and blocked states could be clearly identified, while the hexamethonium caused a 'smooth' block, resulting in a reduced conductance of the open state. It was proposed that the differences between these two blocking effects resulted from the dissociation rates of the two different drugs (Coronado and Miller 1980). The fast dissociation of hexamethonium from the SR $K^+$ channel pore was not properly resolved under the filtering conditions of the experiment and so a lower conductance open state was observed, the so-called 'smooth' blocking effect, while the slow dissociation of decamethonium exhibited apparent gating events between the blocked and fully open states ('flickery block') of the channel (Coronado and Miller 1980). From the aspects of the chemical structure, it can be seen that the only difference between decamethonium and hexamethonium is two extra methylene chain groups in the decamethonium molecule (Figure 1.7). Miller (1982) then conducted a series of ammonium blocking experiments with two quaternary ammonium groups, as in decamethonium and hexamethonium, but with different lengths of methylene chain groups (Miller 1982). It was shown that the voltage-dependence was correlated with the length of the methylene chain group and that flicker blocking effects can be observed

and recognized among the series of bis-quaternary ammonium compounds with 8 or more methylene chain groups at a resolution of gating events at 1 ms (Miller 1982). The process of the blocking effect was explained by the structural conformation difference between the long- and short-chain bis-quaternary ammonium compounds, where the long-chain compounds approached a 'bent-over' configuration during binding to the SR $K^+$ channel (Miller 1982).

There are different sub-conductance states reported between the levels of full open and closed states of the SR $K^+$ channel observed by different researchers. The sub-conductance state gating was first observed in 1981, where the identified sub-conductance state was at 30% of the full open state of the SR $K^+$ channel from frog-leg skeletal muscle (Labarca and Miller 1981). The later single-channel studies (Fox 1985; Tomlins and Williams 1986; Labarca and Miller 1981) revealed more detailed characterisations of the sub-conductance SR $K^+$ channel in mammalian skeletal muscles, where a 60-70% sub-conductance level of the full open state was observed and the probabilities of the transitions between the sub-conductance and full open state were equal (Fox 1985; Tomlins and Williams 1986). Hill Jr et al. 1900 also illustrated a ~60% (57.7%) sub-conductance level of the full open state in canine cardiac SR (Hill Jr, Coronado, and Strauss 1990). A more recent study revealed more details of the sub-condutance states with a greater resultion of the single-channel events (Matyjaszkiewicz et al. 2015). Figure 1.8 shows that the SR $K^+$ channel gated to sub-conductance level at 30%, 60%, 80% of the full open state and also a rapid gating between states (Matyjaszkiewicz et al. 2015).

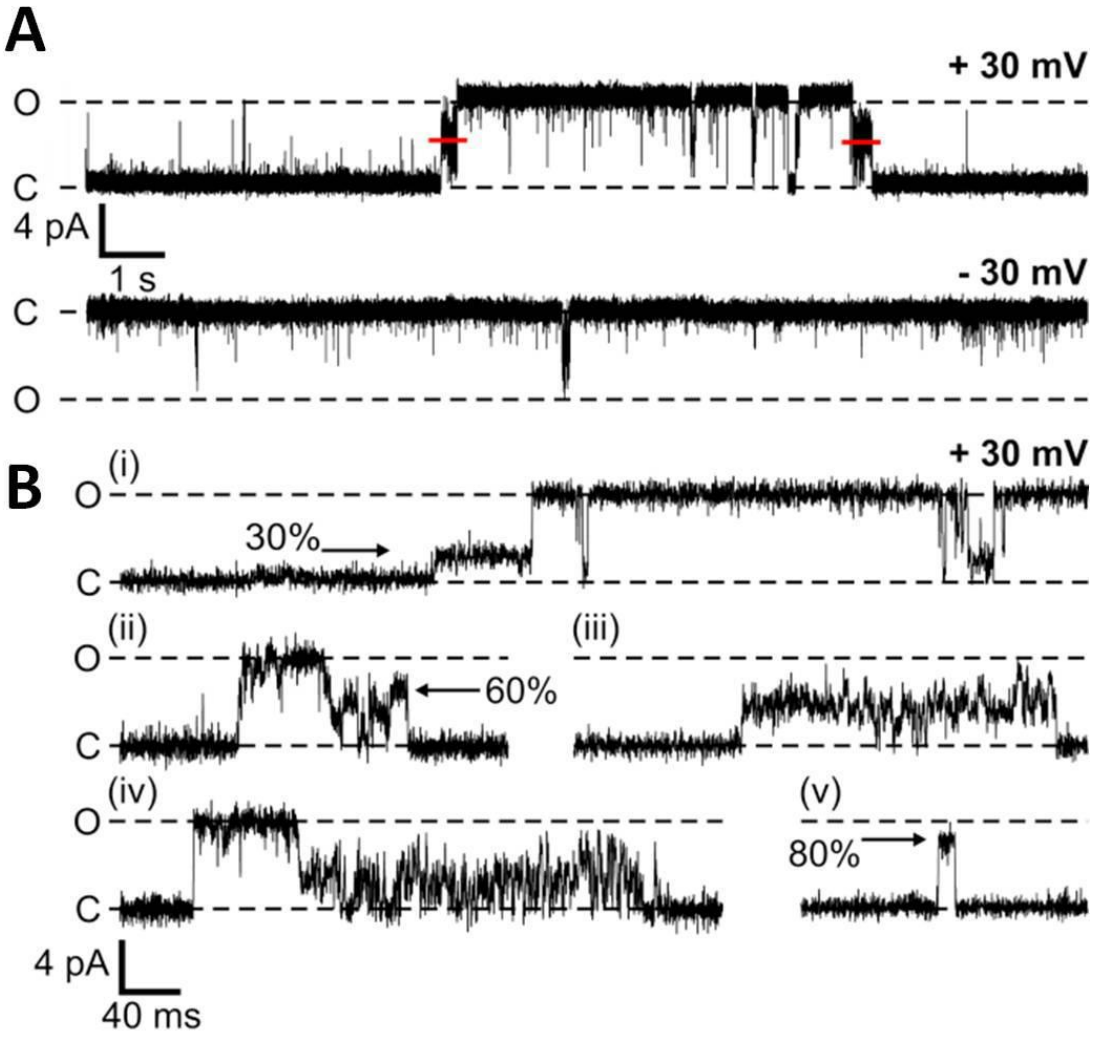



**Figure 1.8 An example of current-fluctuations of full open and sub-conductance state gating events from the SR $K^+$ channel of mouse skeletal muscle. Figure is from Matyjaszkiewicz et al. 2015.**

(A) Gating events of the SR $K^+$ channel in symmetrical 210 mM KPIPES at holding potentials of +30 mV and -30 mV with sub-conductance states indicated by red lines.

(B) When the timescale of single-channel traces is expanded, it can be seen that what appears to be a single noisy sub-conductance level in (A), can be seen to be multiple sub-conductance levels at 30% (i), 60% (ii) and 80% (v), and rapid gating between states (iii and iv). Closed and full open states are indicated by C and O, respectively.

### 1.5.4 Ebselen as a potential ligand that binds to the SR $K^+$ channel

Ebselen (2-phenyl-1,2-benzisoselenazol-3[2H]-one) is a selenium organic compound showing glutathione peroxidase-like activity (Müller et al. 1984; Nakamura et al. 2002). There are several papers suggesting that ebselen has anti-oxidant effects (Nakamura et al. 2002; Sharpley et al. 2020; Yamaguchi et al. 1998). Clinical trials reveal that ebselen can improve the outcome of acute ischemic stroke, serving as a neuroprotective agent (Yamaguchi et al. 1998). However, ebselen has not been reported to be used as a drug on the treatment of acute ischemic stroke yet. This may be due to its poor solubility in water and raise problems in ADME process (absorption, distribution, metabolism, and excretion). It also has been suggested in clinical trials that ebselen is a potential prophylactic and anti-manic treatment in bipolar disorder (Sharpley et al. 2020). Later, a series of clinical trials of ebselen were carried out on patients with Meniere's disease, subsequent studies for Phase 2 clinical trials suggested ebselen had effectiveness on treatment of Meniere's disease and ebselen was carried out in further Phase 3 of trials (Kil, Harruff, and Longenecker 2022). These clinical trials are still under processing and the results haven't been released or published yet. The structure of ebselen is shown below:

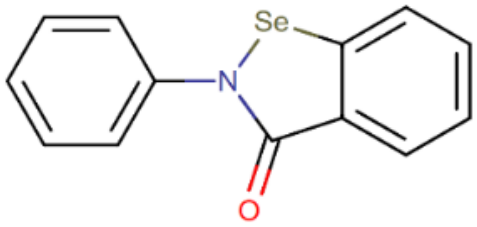



**Figure 1.9 The chemical 2D-structure of ebselen**

Ebselen can modify cysteine residues due to its reaction activity with the thiol group in the cysteine residues. It has been found that ebselen can interact with cysteine residue in proteins such as metallothionein (Ghoshal et al. 1998), glutathione-S-transferase (Nikawa et al. 1994), and the IP3 receptor (Dimmeler, Brüne, and Ullrich 1991). It has also been found that ligand-gated ion channels containing cysteine residues that can be modified by redox-active compounds, including the nicotinic acetylcholine receptor (Karlin and Bartels 1966), the γ-aminobutyric acid receptor type A (GABAA) (Castro-Lopes et al. 1995), and the N-methyl-D-aspartate (NMDA) subtype of glutamate receptor (Aizenman, Lipton, and Loring 1989; Tang and Aizenman 1993).

Interestingly, Yarotskyy, V and R. T. Dirken 2016 found ebselen exhibiting a high-affinity inhibitory effect (100 nM) on the nuclear monovalent cation channel when they screened a chemical compound database to measure $K^+$-currents in the inner membrane of skeletal muscle nuclei using patch-clamp (Yarotskyy and Dirksen 2016; Mak et al. 2013). The nuclear monovalent cation channel observed by Yarotskyy, V. and R. T. Dirksen 2014 shows a $K^+$ selective permeability and other properties similar to SR $K^+$ channels (Yarotskyy and Dirksen 2014). Thus, we speculated that the nuclear cation channel could be the same protein as the SR $K^+$ channel (neither have been identified) and TRIC

proteins have been found in the nucleus (Takeshima, Venturi, and Sitsapesan 2015) and that ebselen may also inhibit the SR $K^+$ channel. As mentioned earlier, no ligand selectively binds to SR $K^+$ channels (positively charged channel blockers such as decamethonium block many other cation channels) and by investigating the effect of ebselen on SR $K^+$ channel we could find a possible agent that binds to the SR $K^+$ channel. This might provide us with clues for developing a more specific ligand and would help in researching the identity and physiological roles of the SR $K^+$ channel.

## 1.6 Aims of this thesis

In Chapter 3 of this thesis, I have investigated the effects of ebselen on the SR $K^+$ channel from sheep skeletal muscle by a single-channel voltage-clamp approach. In order to understand the mechanism of the unique inhibitory effect, I designed a series of experiments to explore the reaction mechanism of ebselen's effect on the SR $K^+$ channel. As described in the introduction, it is important to understand the roles of RyR and TRIC channels in SR $Ca^{2+}$-release in cardiac and skeletal muscle cells. In Chapter 4, I therefore investigated the potential interaction effects between TRIC and RyR2 channels by co-expressing TRIC-A or TRIC-B in RyR2-induced HEK293 cells and then incorporating the channels into planar lipid bilayers. I measured and characterised the influence of co-expression of TRIC-A or TRIC-B channels on the conductance and open probability (Po) of RyR2.

As described in the introduction, the *Tric-a* KO mouse exhibits $Ca^{2+}$ signalling dysregulation in vascular cells and develops hypertension due to insufficient RyR-

mediated $Ca^{2+}$ sparks. I therefore developed a cardiac specific-*Tric-a* knock-out (KO) mouse colony in Chapter 5, to investigate the changes in cardiac function while avoiding any secondary cardiac changes that might arise to due to the effect of knocking out TRIC-A in blood vessels.

In Chapter 6, the work centres on investigating the potential structural changes to RyR2 that result from the V2475F CPVT mutation. Based on the available structural and genetic information, I performed a homology modelling of the RyR2-CPVT mutation. The models predicted the structural and conformation changes to the RyR2 HD1 domain caused by this and the neighbouring CPVT mutation, R2474S, providing a better understanding of the relationships between structure and function of RyR2 in CPVT.

# Chapter 2 Methodology

## 2.1 Isolation of membrane fractions

The membrane fractions used in the experiments were prepared from different tissues, including sheep skeletal muscle, mouse skeletal muscle and HEK293 cells.

### 2.1.1 Sheep skeletal muscle

Sheep skeletal muscle was obtained from sheep legs acquired from a local abattoir (Long Compton Abattoir, Warwickshire, UK). The tissue was collected and immediately kept in cold cardioplegic solution at 4°C. The cardioplegic solution contains 100 mM NaCl, 16 mM $MgCl_2$, 29 mM Na-Lactate, 2.4 mM $CaCl_2$, 21.4 mM KCl, and 1 mM procaine. The muscle was snap-frozen in liquid nitrogen and subsequently stored at -80°C until use.

### 2.1.2 Mouse heart and skeletal muscle

Mouse hearts and all the skeletal muscle from the leg were obtained from mouse colonies, including C57BL/6J (collected in Oxford University), WT mice (collected in laboratory of Hiroshi Takeshima, Kyoto University, Japan) (Yazawa et al. 2007) derived from the TRIC-A germline deletion/knock-out (KO) colony and MYTA (a cardiac-specific TRIC-A knock-out mice colony developed in Oxford). 8-weeks old mice and were randomly picked for each group and were sacrificed following the ARRIVE guidelines. The relevant tissues were collected, snap-frozen and stored in liquid nitrogen until use. 10 mouse hearts or approximately 3 legs were used for the isolation of membrane fractions from

cardiac or skeletal muscle, respectively.

### 2.1.3 HEK-293 cells

We obtained transfected HEK-293 cell pellets from Hiroshi Takeshima (Kyoto University, Kyoto, Japan). These cell lines were separately transfected with RyR2 only, RyR2 with TRIC-A, and RyR2 with TRIC-B (Uehara et al. 2017). The cell pellets were stored at -80°C in the freezer.

### 2.1.4 Preparation of mixed membrane and sarcoplasmic reticulum vesicles

**Heavy SR and light SR vesicles isolation from sheep skeletal muscles**

The whole procedure for isolating heavy and light SR membrane fractions was carried out at in a cold room at 4°C. The frozen tissues were broken into small pieces using a mortar and pestle. The pieces of tissue were then poured into a pre-cooled solution A (300 mM sucrose, 20 mM PIPES, 300 nM aprotinin, 1 μM leupeptin, 1mM benzamidine with 1 mM phenylmethylsulphonic fluoride (PMSF) and 2.5 mM dithiothreitol (DTT) at pH 7.2), homogenised with a blender (Braun GmbH, Kronberg, Germany) and further triturated with a high-speed homogenizer (Ultra-Turrax, IKA-Werke GmbH & Co. KG, Staufen, Germany). After homogenization, the mixture was centrifuged at 6,500 x g (F12S-6x500y) in a SORVALL RC 6 Plus centrifuge (Thermo Scientific, US) for 20 minutes. The supernatant was collected and centrifuged at 100,000 x g (Rotor: Type 45Ti-11E2098, Optima XPN-80 Ultracentrifuge, Beckman Coulter, California, United

States) for 1 hour. The resulting supernatant from the second spin was discarded while the pellet containing the mixed membrane fraction was homogenised using a glass homogenizer (Dounce tissue grinder set, Sigma-Aldrich, Missouri, USA) in solution B (400 mM KCl, 0.1 mM $CaCl_2$, 0.1 mM $MgCl_2$, 0,1 mM EGTA, 5 mM PIPES, pH 7.2) with 10% w/v sucrose. The mixed membranes were loaded onto a discontinuous sucrose gradient of 20%, 30%, and 40% w/v in solution B from top to bottom in a 30 ml centrifuge tube and spun at 100,000 x g (SW32Ti-11U2955 rotor) for 2 hours.

Different membrane fractions were separated by the sucrose interfaces. The membrane fraction found at the 20-30% sucrose interface was collected and resuspended with a buffer containing 400 mM KCl, 10 mM PIPES solution at pH 7.2. This is the fraction that contains light SR membrane vesicles. The heavy SR fraction between the 30-40% sucrose interface was collected and resuspended in the same way (Jones et al. 1979; Sitsapesan et al. 1991). The suspended light SR and heavy SR membrane vesicles were ultra-centrifuged at 100,000 x g (Type 45Ti-11E2098 rotor) for 1 hour to remove the high-density sucrose solution. The light SR and heavy SR pellets were finally separately resuspended in a minimum volume of 400 mM sucrose, 5 mM HEPES at pH 7.2 (with Tris) solution. The mixture was, then, aliquoted, snap-frozen in liquid nitrogen, and stored at -80°C (Sitsapesan et al. 1991).

### 2.1.5 Mixed membrane from HEK 293 cells

The cell pellets (collected from ten 150 mm culture dishes, around 5 mL) were removed from -80°C storage and put on ice in the cold room at 4°C. All the procedures in this

preparation need to be performed in the cold room or on ice.

The HEK cell pellets were put into HEPES (10 mM) with EDTA (1 mM), pH 7.2 with fresh 5 mM NaF, 2.5 mM DTT and 1 mM PMSF. The mixture was manually homogenized with a small glass homogenizer (Dounce tissue grinder set, Sigma-Aldrich, Missouri, USA). The cell homogenate was transferred to a 40 mL centrifuge tube and mixed in a 1:1 ratio with 500 mM sucrose, 10 mM HEPES, with 1mMEDTA in pH 7.2 solution. The mixture was then balanced and centrifuged at 6,500 x g for 20 minutes (SW32Ti-11U2955 rotor, Optima XPN-80 Ultracentrifuge, Beckman Coulter, California, United States). The supernatant was collected and centrifuged at 100,000 x g for 1 hour (SW32Ti-11U2955 rotor). The pellet from the second spin was collected and resuspended with a minimum volume (less than 1 mL to concentrate proteins) in 250 mM sucrose, 10 mM HEPES, 1 mM EDTA at pH 7.2 (by Tris) solution. The resuspended mixture was homogenized 10 times using a 3 mL glass homogenizer and rod. The mixture was aliquoted, snap-frozen in liquid nitrogen, and stored at -80°C.

## 2.2 The planar phospholipid bilayer set up

The artificial planar bilayer method is based on Miller's method (Miller 1978).

### 2.2.1 Lipid bilayer apparatus

The bilayer set up consisted of a Delrin (acetyle resin) cup (Warner Instrument, Hamden, USA) with an aperture of 150-200 μm, and a Perspex block (Warner Instrument, Hammden, USA). The cup is inserted into the block to form two chambers, the *cis*

chamber from the cup with a volume for 1 mL solution and the *trans* chamber from the block with same volume to balance the height of solution avoiding the mechanical gradients. The block has a transparent glass front as shown in Figure 2.1. There were two smaller chambers as shown in Figure 2.1A and Figure 2.1C, containing 3 M LiCl solution and housing the Ag/AgCl electrodes from the headstage. The smaller chambers were connected to the *cis* and *trans* chamber separately with agar bridges (3 M LiCl with 2% w/v agar), electrically connecting the LiCl solutions and the recording solutions in the *cis*/*trans* chambers (Figure 2.1C) (Alvarez 1986; Miller 1978). The bilayer experiments were conducted under room temperature at 21±1°C.

### 2.2.2 Lipid bilayer painting

Artificial bilayers were formed from phosphatidylethanolamine (PE) or a 1:1 mixture of PE and phosphatidylserine (PS) (Avanti Polar Lipids, Alabama, USA). The lipids were stored as a 50 mg/mL solution in chloroform at -80°C. Before the experiment, the lipid solution was dried with nitrogen gas and dissolved in decane at a concentration of 35 mg/mL for PE lipid or 10 mg/mL PE and 10 mg/mL PS for PE/PS lipid.

The aperture of a Delrin cup (Warner Instruments LLC, Hamden, USA) was firstly primed to form a surface on which a bilayer could form (White 1986), with PE lipid mixture on the interior side by painting with a plastic painting stick fashioned from a disposable plastic pipette. Then, a thumb was used to apply a gentle pressure to the top of the cup to push the lipid through the aperture. After drying of the lipids, another priming of PE was applied and dried. The cup was then inserted into a Delrin block to

form the *cis* (with respect to SR and RyR incorporation (Sitsapesan and Williams 1994b) this corresponds to the cytosolic side of the membrane) and *trans* (luminal side of membrane) compartments in the cavity of the block. The relevant lipids used in the experiments (PE or PE/PS) were then painted over the aperture of the cup under the symmetrical solutions of 210 mM KPIPES, pH 7.2, 2 μM free $Ca^{2+}$. The lipid covered the aperture, disrupting the current flow between the chambers. The lipid initially formed an artificial phospholipid layer of micrometre scale thickness, which was not a bilayer. However, the centre of the lipid membrane becomes thinner naturally under a number of different forces (Miller 1992) until it can be considered a bilayer. In brief, the lipid forms a thick torus around the rim of the circular aperture, and the central portion thins out as a result of the Plateau-Gibbs border suction force (Miller 1992). As the pressure at the thinnest point of membrane is greatest, the surrounding solution from either cytosolic or luminal side of membrane is pushed to the rim of the aperture and causes the membrane to become thinner. When a small region thins to a bilayer, Van der Waals forces between the aqueous phases in each solution of chamber increase the pressure on thinner areas of the membrane resulting in additional thinning of the bilayer (Parsegian 1975). In the end, steric repulsion prevents the bilayer membrane from thinning further and the Van der Waals forces counteract the Plateau-Gibbs border suction force. The forces, thus, equilibrate allowing the formation of a stable lipid bilayer membrane.

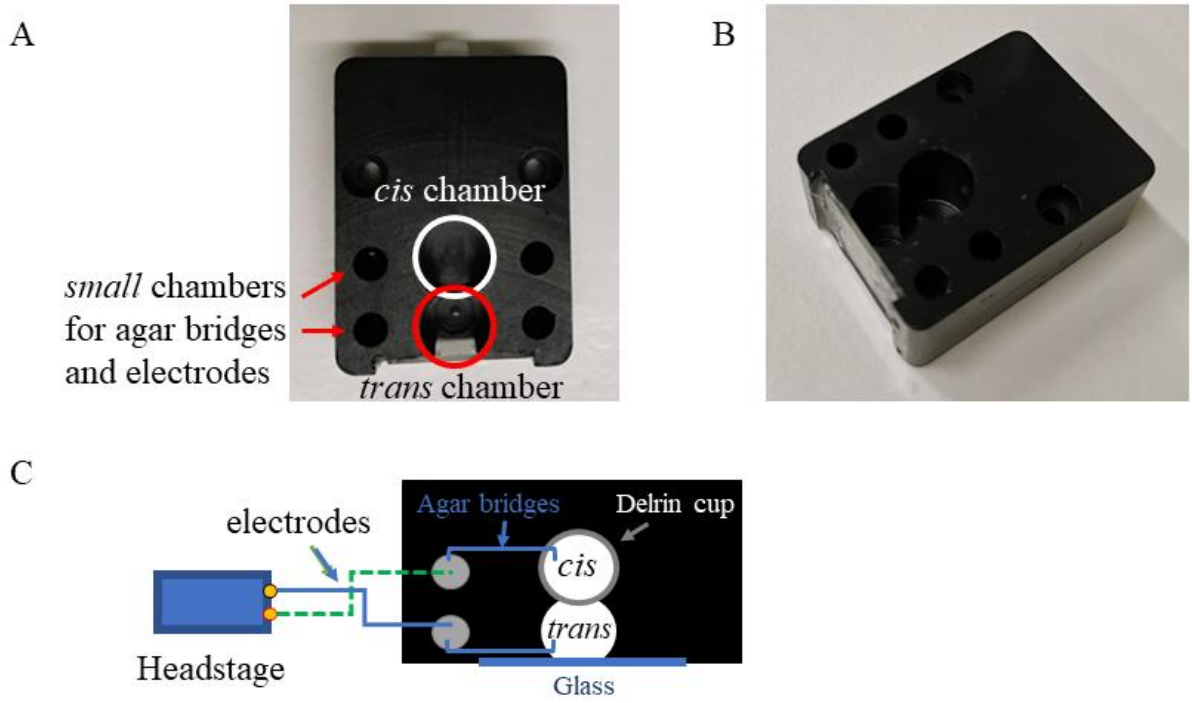



**Figure 2.1 A diagram of the lipid bilayer experimental block**

(A) Aerial view of the block with *cis* and *trans* chamber position labelled. (B) Overall view of the whole block. (C) A schematic of the headstage and block set up and connections: The *cis* chamber is indicated within the Delrin cup (150-200 μm aperture). The agar bridges connect the small chamber with 3M LiCl and *cis*/*trans* chambers. AgCl electrodes connect the headstage with the small chambers in the block.

### 2.2.3 Electrical equipment set up for measurement and acquisition

The electrical equipment was composed of the following parts: A block with Delrin cup (Warner instruments, Harvard Bioscience, USA), a headstage with electrodes, a stir-plate, a Faraday cage, an amplifier, a filter, an oscilloscope, an A/D interface, and a computer. The equipment was carefully grounded to avoid electrical noise caused by

ground loops. The grounding point was connected to the amplifier, which was connected to the Faraday cage, stir plate and head stage. The connections between the different parts are shown in the diagram below (Figure 2.2).

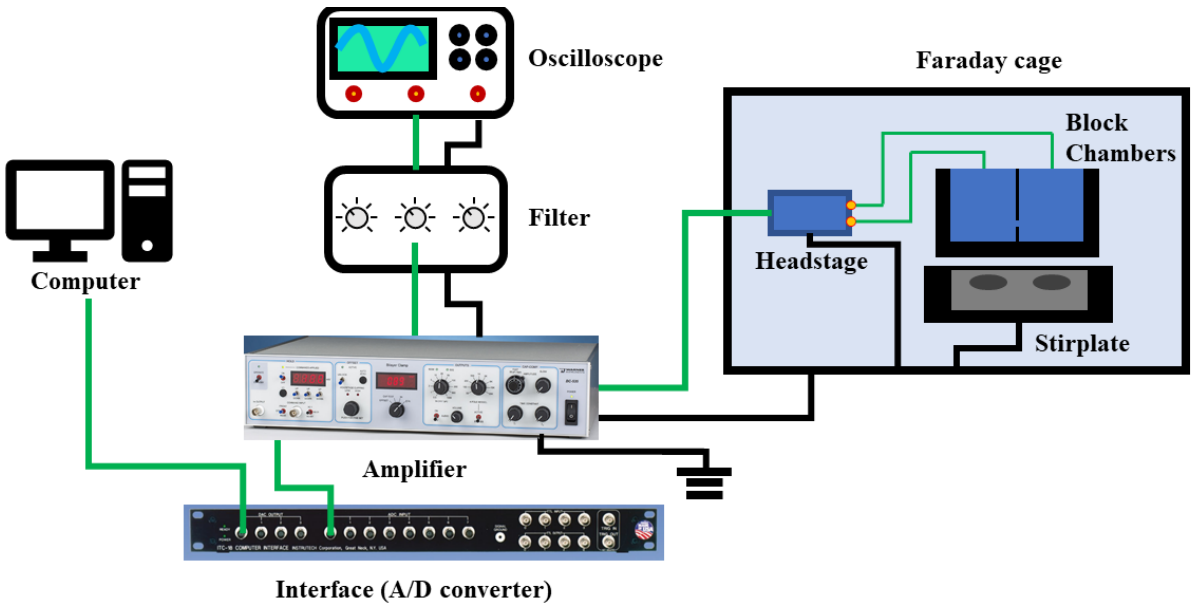



**Figure 2.2 A diagram of electrical equipment for single channel recording**

Electrical currents caused by ions passing through the bilayer aperture were recorded by the headstage in the Faraday cage and passed to the amplifier. The amplified signals passed through a 600Hz filter and were shown on the oscilloscope. At the same time, the unfiltered signals were converted to digital signals via the interface and recorded by the relevant software on the computer.

The cups, blocks, magnetic stirring system and BC-535 Bilayer Clamp Amplifier were obtained from Warner Instruments LLC (Hamden, USA); The low-pass 8 pole Bessel filter was from Frequency Devices Inc (Ottawa, Canada). The oscilloscope TDS 1012C-EDU was from Tektronix (Oregen, USA). The A/D converters InstruTECH ITC-18 were from HEKA Elektronik (Lambrecht/Pfalz, Germany) or Digidata 1440A Digitizer

Acquisition System from Molecular Devices LLC (California, United States) and a computer with Microsoft Windows system (Viglen Ltd, Hertfordshire, UK).

### 2.2.4 Voltage-clamp approach

After the lipid bilayer is painted on the aperture of the cup, the set-up constitutes a simplified circuit, where the head stage is connected to the amplifier and the two chambers are filled with salt solutions and connect to the head stage with two electrodes as indicated in Figure 2.3. The artificial phospholipid bilayer membrane behaves as a capacitor ($C_b$), which can store the electrical charges on two sides of the membrane. Any ion channel that incorporates into the bilayer plays the role of a resistor. Ions can pass through the ion channel under certain driving forces, including chemical driving force (concentration gradient of ions across the membrane) and electrical driving force (an applied voltage difference across the membrane), when the ion channel is in an open state.

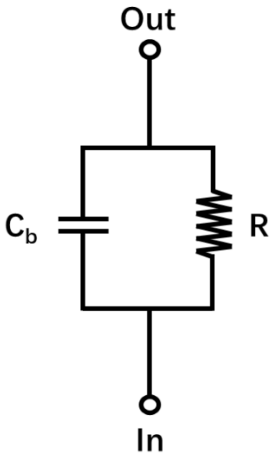



**Figure 2.3 A diagram of a simplified circuit of an ion channel in a bilayer**

$C_b$ is the bilayer capacitor and R is the ion channel as a resistor. 'In' and 'Out' are the holding

potential across the membrane

We can measure the current through the bilayer ($I_b$) using our equipment (described previously), where $I_b$ is composed of two components: (i) An ionic current ($I_i$) flowing through the ion channel; (ii) A current through the capacitor ($C_b$) due to charging and discharging of the membrane caused by the voltage ($V$) changes over time ($t$). The total current ($I_b$), thus, can be expressed using the following equation:

$$I_b = I_i + C_b \frac{dV}{dt}$$

During our single-channel experiments, the $I_b$ is measured by the voltage-clamp technique (Hodgkin and Huxley 1952). When we voltage-clamp the bilayer, the voltage across the membrane is held at a constant, in which case dV/dt equals 0 and the obtained current, $I_b$, equals the ionic current through the incorporated ion channel with a conductance limit.

## 2.3 Fusion of vesicles with the lipid bilayer

Incorporation of ion channels from the various membrane vesicle preparations was performed as follows: A salt gradient condition between the cytosolic and luminal chambers was created by adding 200 µL of 3 M KCl to the cytosolic chamber to provide a driving force from the osmotic gradient for the incorporation. The addition of 200 µL 3 M KCl was performed as follows: 100 µL of solution was removed from the cytosolic chamber and 100 µL 3 M KCl was added with stirring. Another 100 µL solution was removed from the cytosolic chamber and replaced by another 100 µL 3 M KCl with stirring. Then, 1-2 µL of the relevant membrane vesicles were added to the cytosolic

chamber while stirring. Figure 2.4 shows the osmotic gradient causing swelling of vesicles in contact with the bilayer, which eventually burst and fuse with the bilayer (Cohen, 1986). This process can be monitored by oscilloscope as gating ion channels from the fused vesicles cause significant currents to pass through the bilayer and these are detected by the amplifier. Incorporation of ion channels selective to cations cause a positive current fluctuation and incorporation of ion channels selective to anions cause a negative current fluctuation.

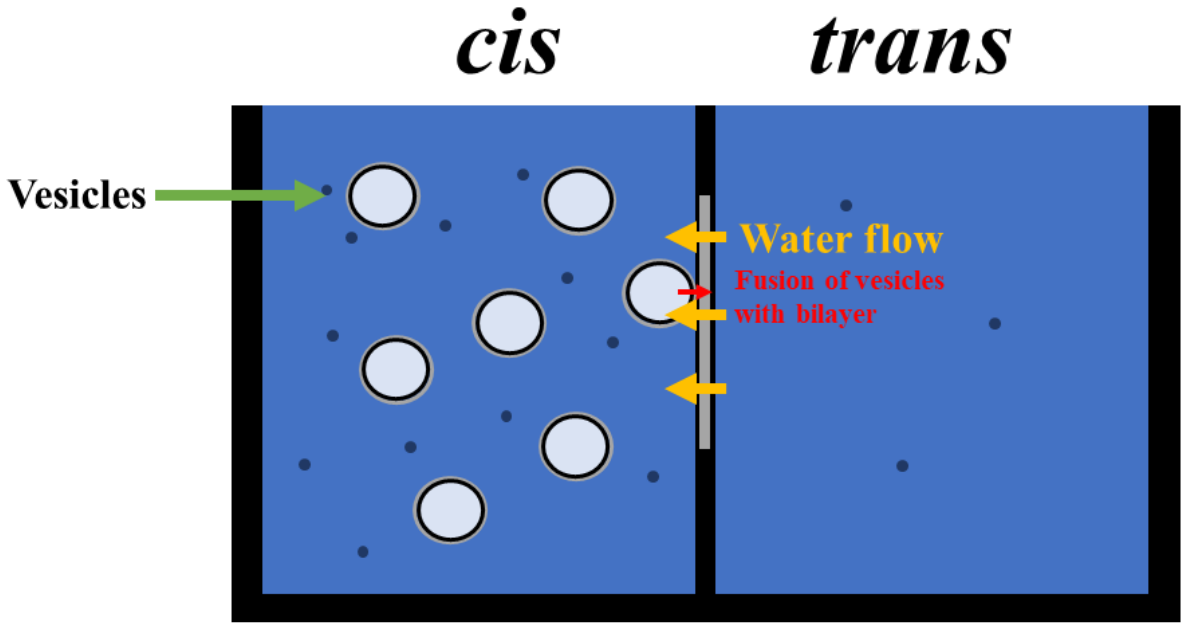



**Figure 2.4 Fusion of vesicles under the osmotic gradient across the bilayer membrane.**

An osmotic gradient (dark blue dots represent ions in the solutions) between the solutions contained in the *cis* (left) and *trans* (right) chamber. Water flows (orange arrows) across the bilayer from the *trans* to the *cis* chamber causing the swelling of the vesicles lined up along the bilayer and finally fusion of these vesicles with the bilayer as indicated by the red arrow.

After fusion of vesicles with the bilayer, the chambers were perfused with the appropriate cytosolic recording solution to remove the rest of the vesicles and the salt gradient. The recording solutions for each experiment are described in the '**2.3.2 Experimental solutions and choice of permeant ion**' section. Perfusion of the chambers was performed using a peristaltic pump with inflow and outflow polyethylene tubing. The recording solutions were perfused into the cytosolic and luminal chambers through the inflow tubing while the gradient solution was removed from the *cis* chamber through the outflow tubing. The perfusion of the chamber was complete after 10 volumes of the chamber (10 mL) had been replaced.

## 2.3.1 Bilayer detection and estimation of the area

The bilayer clamp amplifier, BC-535, measures the capacitance of the bilayer membrane under the capacitance test configuration ("CAPTEST"). We detect the formation of the bilayer membrane and estimate the bilayer area by the membrane capacitance. The capacity ($C_b$) of the bilayer membrane can be estimated by the following equation, where $C_b$ is proportional to the membrane surface area ($A$) and inversely proportional to the thickness of the membrane ($d$) while $\varepsilon$ is the dielectric constant:

$$C_b = \varepsilon \frac{A}{d}$$

As the current ($I_c$) through the bilayer capacitor follows the equation:

$$I_c = C_b \frac{dV}{dt}$$

where $C_b$ is the capacitance of the bilayer, $V$ is the potential across the membrane and $t$ is the time. Thus, we can combine the two equations to get the following:

$$I_c = \varepsilon \frac{A}{d} \frac{dV}{dt}$$

where dV/dt is a constant in the CAPTEST configuration as the amplifier applies a steady triangular wave to the membrane. Considering $d$ is the thickness of membrane that depends on the distance of the lipid tails of the bilayer and ε also depends on the type of lipid used, we can simplify these parameters to a constant and get the following equation:

$$I_c \propto A$$

which means that the amplitude of the square waveform detected by the amplifier is proportional to the area of the bilayer. The output scale is set to 1 mV/pF in the CAPTEST configuration, and the gain of amplifier is normally set at 10 mV/pA, which means that if the amplifier obtains a resulting square waveform, the capacitance of the bilayer is 100 pF. For the incorporation of channels for single-channel experiments, a capacitance of 80 to 120 pF gives stable and fusigenic bilayers.

## 2.3.2 Experimental solutions and choice of permeant ion

SR membranes contain many ion channels including RyR channels, the SR $K^+$ channel and a variety of other poorly characterized ion channels that are permeable to anions. Thus, in order to observe single-channel currents through a specific SR ion channel, it is necessary to use recording solutions that do not allow current flow through the other SR ion channels. In this thesis, the SR $K^+$ channel was recorded under conditions in which $K^+$ was the permeant ion. Thus, 210 mM KPIPES solution, free $Ca^{2+}$ 2 μM, pH 7.2 with KOH, was used in the experiments since the anion PIPES is impermeant in SR $Cl^-$

channels. RyR channels are also permeable to $K^+$ but as most of the RyR are in the heavy SR, I used light SR when experimenting on the SR $K^+$ channel. It is also simple to distinguish RyR and SR $K^+$ channels by the large difference in single-channel $K^+$ conductance and gating behaviour.

For RyR2 channel experiments from the TRIC-A or TRIC-B co-expressed RyR2 induced HEK293 cell vesicle preparations, 210 mM KPIPES solution, free $Ca^{2+}$ 2 μM, pH 7.2 with KOH was also used as the recording solution for monitoring RyR2 channel function. 1 M $CaCl_2$ solution was added to the cytosolic chamber to increase cytosolic [$Ca^{2+}$].

To investigate the relative permeability of ion channels to $K^+$ and $Cl^-$ ($P_K/P_{Cl}$), a symmetrical solution of 210 KCl, free $Ca^{2+}$ 2 μM, pH 7.2 with KOH, was used as the recording solution. 200 μL 3 M KCl was added to the cytosolic chamber to introduce the gradient.

## 2.4 Data acquisition and analysis process

### 2.4.1 Data acquisition

During the single-channel experiments, single-channel currents were filtered at 800 Hz by the filter (Figure 2.2) and displayed on the oscilloscope for real-time visualization of the currents. At the same time, the single-channel currents were also digitized by the Digidata and transferred to the computer. On the computer, we used WinEDR or Clampex software to record and store the digitized signal onto the hard drive. To avoid aliasing and distortion of the signal, the sampling frequency, which is the number of recorded data points every second, should be at least twice the frequency of the filtering

rate (Nyquist, 1928). In this case, we set sampling frequency at 20 kHz to prevent aliasing of the signal due to the 5 kHz frequency of the amplifier's internal filter.

For further single-channel analysis, we filtered the recording with a Gaussian low-pass filter at frequencies depending on the specific experimental conditions. During this low-pass filtering step, the background noise was reduced to as low a level possible so that the single-channel current fluctuations could be observed. The optimum frequency of low-pass filtering for each type of experiment was chosen according to the signal-to-noise ratio in order to omit as few as possible opening and closing events of the channels.

For experiments with the SR $K^+$ channel from sheep skeletal muscle in 210 mM KPIPES, the recording was filtered at 1 kHz using Clampfit (v 11.1, pCLAMP, Molecular Devices, USA) to remove the background noise. For voltage-clamp experiments with RyR2 channels from TRIC-A or TRIC-B co-expressed RyR2 induced HEK293 cells, the filtering of the recording was set at 4 kHz. For voltage ramp experiments with incorporated ion channels from TRIC-A/TRIC-B co-expressed RyR2 HEK 293 cells, the filter was set at 600 Hz, to prevent the bilayer noise from interfering with the accuracy of the reversal potential measurement.

### 2.4.2 Analysis of the single-channel recordings

The function of ion channel activity can be assessed by two aspects, single-channel conductance and the open probability (Po). We therefore measure these two parameters to study each channel.

### 2.4.2.1 Conductance and Po analysis of single-channel recording

As described previously in the Figure 2.3, the ion channel behaves as a resistor, where we can measure the conductance ($G$) of an ion channel according to its resistance. The following equation is used:

$$G = \frac{1}{R}$$

where $G$ is the conductance of the ion channel, and $R$ is the resistance of the ion channel.

During the voltage-clamp experiments, we can measure the voltage ($V$) across the membrane and the current ($I$) passing between the chambers by the amplifier. In this case, we can calculate the resistance using Ohm's law as following:

$$V = IR$$

The previous equation can be substituted with Ohm's law and we get the following equation:

$$G = \frac{I}{V}$$

Therefore, when the current-voltage relationship of the measured data is plotted where $V$ forming the x-axis and $I$ forming the y-axis, the gradient of the linear fitting regression ($dI/dV$) gives the conductance of the channel.

In our voltage-clamp experiments, we obtained the voltage in mV, which equals to the holding potential applied to the bilayer membrane, and measured the current from the

signal for each holding potential. In the pCLAMP software, we manually set one curser on the baseline of the signal (closed level), and another curser on an apparent single-channel open signal (open level). The software will give the current difference in pA between the two levels indicated by cursers.

To analyse the single-channel gating events, estimation of the time point and amplitude of each transition of channels between open and closed states is needed. We perform idealisation of the recording using a 50% threshold method (Colquhoun and Sigworth, 1995). We manually set two cursors on the open and closed states in the filtered recording. The closed state is defined as the state in which the ion channel does not conduct ions and is thus the baseline level (no current). When current amplitude crossed the 50% threshold level between open and closed states, the transitions between the two states are identified as gating events. This method is normally applied to ion channels that gate between the closed and fully open states with rare gating to sub-conductance levels.

The durations in which the ion channel dwells in open ($t_{open}$) or closed ($t_{closed}$) states are used to calculate the Po. Po is calculated by the following equation:

$$Po = \frac{t_{open}}{t_{open} + t_{closed}}$$

If there are multiple channels incorporated into the bilayer, each level of the fully open states is defined and the following equation is used to determine the *N Po*:

$$NPo = \frac{T_{open1} + 2(T_{open2}) + 3(T_{open3}) + \cdots + n(T_{openN})}{T_{total}}$$

where *NPo* is the sum of the *Po* of multiple channels, N is the total number of gating

channels incorporated into the bilayer, $T_{openN}$ is the duration of N channels gating at open levels and $T_{total}$ is the total time of the recording. The average Po for the channels is calculated by dividing the *NPo* value by the total number of channels *N*. Combining the two equations, we can get the following equation:

$$Po_{average} = \frac{NPo}{N} = \frac{\frac{T_{open1}}{T_{total}} + 2\frac{T_{open2}}{T_{total}} + 3\frac{T_{open3}}{T_{total}} + \cdots + n\frac{T_{openN}}{T_{total}}}{N}$$
$$= \frac{Po_1 + 2Po_2 + 3Po_3 + \cdots + nPo_n}{N}$$

where the $Po_n$ is the Po of n channel gating at the same time and thus this equation is a weighted average of Po of N channels with the number of opening channels as the weight. During the single-channel experiments, we can measure the Po of each gating level ($Po_n$) and thus calculate the average Po of multiple channels.

#### 2.4.2.2 Sub-conductance state analysis

For single-channel recording of SR $K^+$ channels, the channel gating in the recordings revealed three conductance states: a closed state, a sub-conductance state and an open state (Matyjaszkiewicz et al. 2015). There is no current passing through the channel during the closed state. When the channel gates to the sub-conductance state and open state, ions flow through the SR $K^+$ channel and thus produce current. The duration of time that the channel stays in either state is called the 'dwell time'. Some of the sub-conductance level gating observed fell below the 50% threshold for Po analysis described previously and, thus, would not be included in the Po measurement. Therefore, to adequately analyse sub-conductance levels, we instead used the segmental k-means (SKM)

algorithm which can be performed using the Quantify Unknown Biophysics (QuB) software (by Christopher Nicolai and Frederick Sachs, University of Buffalo, described below). The SKM algorithm uses a hidden Markov model to deduce state transitions of the signal. A Markov model was therefore created for each SR $K^+$ channel to calculate Po of each gating state.

#### 2.4.2.3 Modelling and idealization of the SR $K^+$ channel

The Markov models used in Prof. Sitsapesan's laboratory for the SR $K^+$ channel are as described in Matyjaszkiewicz (Matyjaszkiewicz et al. 2015). A three-state model consisting of a closed level, a single 'merged' conductance level, and a fully open level is used to idealize the current-fluctuations from the SR $K^+$ channel opening as follows:

$$\boldsymbol{Closed} \leftrightarrow \boldsymbol{Open_{sub}} \leftrightarrow \boldsymbol{Open_{full}}$$

This is a three-state linear model, in which most of the fully open or closed states (>97%) gated through the sub-conductance level (Matyjaszkiewicz et al. 2015).

#### 2.4.2.4 (Quantify Unknown Biophysics) QuB Data Pre-processing

The software, QuB (University of Buffalo, NY, USA), used here for analysis was developed by Christopher Nicolai and Frederick Sachs. The recordings were re-sampled in QuB at 10 kHz and a 1 kHz Gaussian digital filter was applied to the recording to remove high frequency noise. A dead time of 0.6 ms was also applied as, at this filtering

frequency, events shorter than this duration were not properly resolved. The electrical noise and/or capacitance spikes were visually inspected and manually removed before analysis.

We built the three-state linear Markov model mentioned previously in QuB with arbitrary rate constants of 10 $s^{-1}$. The closed and full conductance levels were identified visually and manually from the filtered recording in QuB. The sub-conductance level was then assigned at 50% between the fully open level and closed level with a large standard deviation to represent the noise of the state.

Once we built the model, the inbuilt idealization was performed. The Viterbi algorithm was firstly used to assess the most likely sequence of hidden states, the Viterbi path. This Viterbi path was then used to determine the parameters of the model in an iterative procedure called 'maximum likelihood' to reach the optimum likelihood. The conductance levels were represented by Gaussian fits to single-channel current amplitude following the following distribution:

$$f(I) = \frac{Po}{\sqrt{2\pi\sigma^2}} e^{\frac{-(I-\mu)^2}{2\sigma^2}}$$

where $I$ is the current amplitude in the recording, $Po$ is the Po of a given state in the model, $\mu$ is the mean current amplitude for this given state, and $\sigma$ is the standard deviation of the current amplitude for the given state, which represents the noise of the channel.

The Gaussian curves for each state were plotted according to the above equation alongside a histogram of the current amplitude in the recording as shown in Figure 2.5.

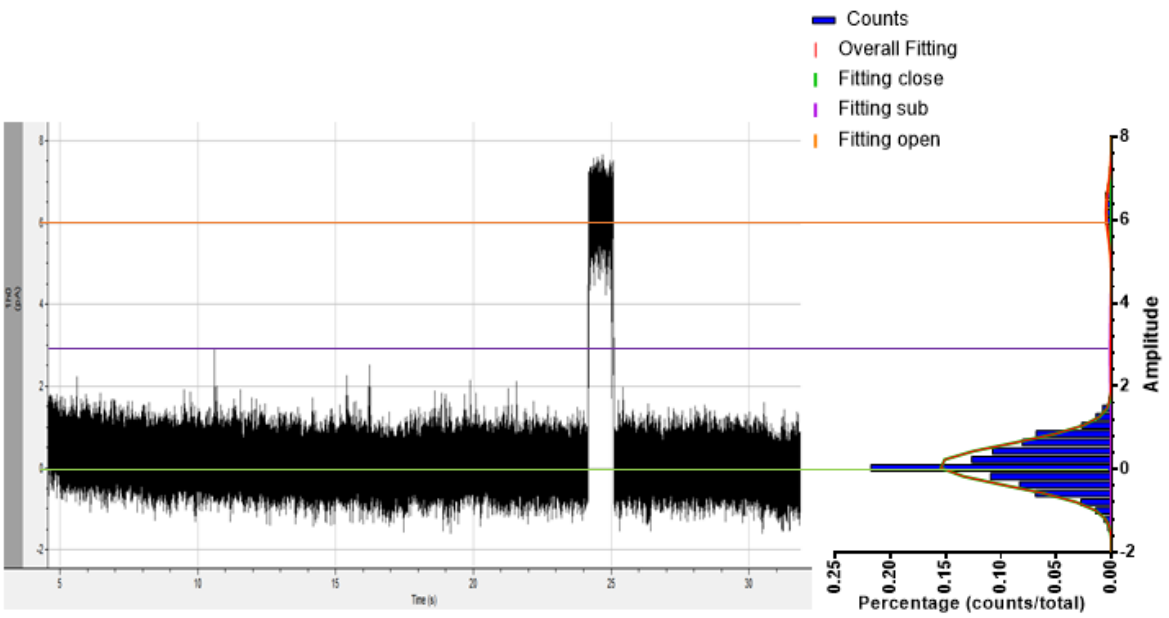



**Figure 2.5 Gaussian curve fitting to current amplitude and compiling the amplitude histogram in QuB.**

An example of a current amplitude histogram (right) based on a 30s recording of a single SR $K^+$ channel at +30 mV (left). Each state of the channel is fitted by a Gaussian curve, closed state in green, sub-conductance state in purple, full open state in orange and the overall Gaussian curve fitting in red.

In the QuB software, the recording was idealized using the following parameters: 'Histogram bin count 100' gives the bins of the histogram that determines the intervals of the histogram. The SKM algorithm is applied as described previously. 'Max iteration 10 without re-estimate' decides the iteration process in the Viterbi algorithm, in which QuB software will follow the state we specified without re-estimation. The $P_O$ was calculated according to the formula below by the software, and lifetime and event frequency were also calculated for the analysis.

$$Po = \frac{t_{in-state}}{t_{total}}$$

where $t_{in\text{-}state}$ is the dwell time of channel gating in each state and $t_{total}$ is the total time of the analysed recording. We therefore assessed the Po for closed state, sub-conductance state and fully open state as $Po_{closed}$, $Po_{sub}$ and $Po_{full}$, respectively. We can calculate the percentage of Po of each state in the overall Po to represent how long the SR $K^+$ channel gates to each state relatively. To express the Po of multiple channels, the following equations were used:

$$Po_{total} = \frac{\sum_{i=1}^{n} n \times \left(Po_{full\,n} + Po_{sub\,n}\right)}{n}$$

$$Po_{sub} = \frac{\sum_{i=1}^{n} Po_{sub\,n}}{n}$$

$$Po_{full} = Po_{total} - Po_{sub}$$

where n is the number of incorporated channels and $Po_{total}$, $Po_{sub}$ and $Po_{full}$ represent the overall Po for all channels, sub-conductance states of all channels and fully open state of all channels, respectively.

### 2.4.2.5 Relative permeability

When we plot the current-voltage data of the single-channel recordings under asymmetrical solution conditions, the regression line crosses the *x*-axis at a point known as the reversal potential ($E_{rev}$). The $E_{rev}$ reflects the relative permeability of ions depending on the type of ions in the solution. The calculation of $E_{rev}$ follows the Goldman-Hodgkin-Katz equation as follows:

$$E_{rev} = \frac{RT}{F} ln(\frac{P_{Na}[Na^+]_{out} + P_K[K^+]_{out} + P_{Cl}[Cl^-]_{in}}{P_{Na}[Na^+]_{in} + P_K[K^+]_{in} + P_{Cl}[Cl^-]_{out}})$$

where $E_{rev}$ is the reversal potential in V, $R$ is the ideal gas constant, ~8.314 J/K/mol, $T$ is the temperature in K, 295.15 K under experimental conditions, F is the Faraday constant, 96485.33289 C/mol, $P_{Na}$, $P_K$ and $P_{Cl}$ are the relative permeability (selectivity) values for $Na^+$, $K^+$, and $Cl^-$ ions, respectively; *in* and *out* of each ion concentrations indicate cytosolic and luminal sides of membrane, respectively. In single-channel experiments under KCl gradient solutions (740 mM KCl cytosolic: 210 mM KCl luminal), there are only $K^+$ and $Cl^-$ ions present in the solutions, so $Na^+$ can be discounted. The re-arranged equation is shown as follows:

$$Exp\left(\frac{E_{rev}F}{RT}\right) = \frac{P_K[K^+]_{luminal} + P_{Cl}[Cl^-]_{cytosolic}}{P_K[K^+]_{cytosolic} + P_{Cl}[Cl^-]_{luminal}}$$

which then gives the following equation:

$$\frac{P_K}{P_{Cl}} = \frac{[Cl^-]_{cytosolic} - Exp\left(\frac{E_{rev}F}{RT}\right)[Cl^-]_{luminal}}{Exp\left(\frac{E_{rev}F}{RT}\right)[K^+]_{cytosolic} - [K^+]_{luminal}}$$

We can calculate the relative permeability based on the above equation and substitute the $K^+$ and $Cl^-$ with other monovalent cation or anion in the experimental solutions from other experiments, respectively.

### 2.4.2.6 Liquid junction potentials

Two different solutions at any place in the experimental set up will result in a liquid

junction potential (LJP) at the interface of the solutions. It is therefore important to correct the $E_{rev}$ for any LJP that is present during the relative permeability measurement (Tinker and Williams, 1992). To measure the LJP, the amplifier offset was firstly set at 0 mV. After painting a bilayer, we perfused the chambers to recording solution conditions in the experiments. We broke the bilayer and the offset potential readout on the amplifier gives the LJP of this solution condition.

## 2.5 Cardiac TRIC-A KO mouse colony

### 2.5.1 Genotyping via Polymerase chain reaction (PCR):

**Table 2-1 Primers of Flox pairs and Cre pairs**

| | |
|---|---|
| Tm38a-Forward (Flox) | TCCTGCACATGTCCTTGTGAGT |
| Tm38a-Reverse (Flox) | ACTGAGAGACCCTGCCTCAAAA |
| Cre-Forward (Cre) | GTTCGCAAGAACCTGATGGACA |
| Cre-Reverse (Cre) | CTAGAGCCTGTTTTGCACGTTC |

To prepare samples for PCR, each mouse ear-clip was lysed in 300 µL lysis buffer (100 mM Tris, 250 mM NaCl, 5 mM EDTA, 0.2% SDS at pH 8.5) with 3 µL Proteinase K and then heated at 56°C overnight. The samples were then centrifuged at 16,000 x g (Rotor: microlitre rotor 7055-3328, Biofuge Fresco, Heraeus, Germany) at 20°C for 3 minutes. 10 µL of the supernatant was then diluted 5 times with 40 µL molecular biology grade water (UltraPure, Invitrogen, UK). 1 µL of each DNA sample was then placed in

a small tube, mixed with 1 µL of forward and reverse primers and 12.5 µL Master Mix (M750B, Promega, Madison, Wisconsin, USA) and diluted to a total volume of 25 µL with molecular biology grade water. All the samples were kept on ice and the PCR protocol was followed:

A 5 min initialization step was applied at 94°C followed by 30 cycles of denaturation at 94 °C for 45 s, annealing at 57 °C/54 °C (for Flox/Cre respectively) for 45 s and extension at 72 °C for 30 s. The final elongation step was applied at 72 °C for 7 min, followed by a holding temperature at 4 °C. The PCR product was checked and determined by running a 1.5% agarose gel with ethidium bromide.

### 2.5.2 mRNA level validation with real-time polymerase chain reaction (RT-qPCR) protocol

We measured the mRNA expression level by real-time polymerase chain reaction (RT-qPCR) protocol. RNA extraction from mouse hearts proceeded using the RNeasy Mini Kit (QIAGEN, Hilden, Germany) and was reverse transcripted to cDNA using high-capacity RNA-to-DNA kit (Thermo Fisher Scientific, UK), where the procedures used were according to the manual of each kit. We then quantified gene expression levels of target genes using RT-qPCR based on the cDNA samples. The details of protocol of qPCR were as following:

**Table 2-2 Target gene and corresponding *Taqman* assay (Thermo Fisher Scientific, UK)**

| Target gene | *Taqman* Assay ID | Catalogue Number | Probe Type |
|---|---|---|---|
| Hypoxanthine-guanine phosphoribosyltransferase (*Hprt*, housekeeping gene as endogenous control) | Mm03024075_m1 | 4448484 | VIC-MGB primer limited |
| *Tric-a* | Mm00507437_m1 | 4331182 | FAM-MGB |
| *Tric-b* | Mm00518471_m1 | 4331182 | FAM-MGB |
| *Ryr2* | Mm00465877_m1 | 4331182 | FAM-MGB |

Using Master Mix, a mixture was made up as shown in the following table:

**Table 2-3 Master Mix table**

| Component | Volume for each well (μL) |
|---|---|
| 20X Gene Expression Assay (target gene) | 1.0 |
| Taqman® Gene Expression Endogenous Control (HPRT) | 1.0 |
| 2X Master Mix | 10.0 |
| RNase free water | 4.0 |
| Total (not including cDNA) | 16.0 |

The mixture was then vortexed and briefly centrifuged for 10 s (SN0712 microfuge). The Master Mix Mixture (16 µL/well) was loaded in each well of the plate. The cDNA was diluted with RNase free water at 1:10 dilution and 4 µL of diluted cDNA (~1 pg-100 ng) of each sample or RNase free water for non-template control (NTC) was added to each well (triplicate for each sample). After spinning down the solution in the plate at 1000 g for 1 min, we performed real-time PCR using the LightCycler 480 PCR platform under dual colour hydrolysis probe configuration (Roche Life Science, Penzberg, Germany). For RT-qPCR, the enzyme activation step was set at 95 °C for 10 min, with 40 cycles of denaturation at 95 °C for 15s and annealing/extension at 60°C for 1 min. The data was acquired and stored on the computer.

### 2.5.3 Delta-delta cycle threshold (Ct) method (ΔΔCt method) analysis

To analyse the data, we use the delta-delta cycle threshold (Ct) method (ΔΔCt method) to calculate the relative fold of mRNA expression level in RT-qPCR (Livak and Schmittgen 2001). The Ct of each well is given after the qPCR programme is using the PCR platform, which is the cycle number of each well where the fluorescence signal from the PCR product can be distinguished from the background noise. We calculated the average Ct for each sample from the triplicate technical repeats and then calculated the delta-Ct (ΔCt), the difference of Ct values, using the following equation:

$$\Delta Ct = Ct_{target-gene} - Ct_{housekeeping-gene}$$

where the $Ct_{target\text{-}gene}$ is the average Ct value of target gene, e.g., *Tric-a* gene, in each

sample, and $Ct_{housekeeping\text{-}gene}$ is the average Ct value of housekeeping gene, *Hprt* gene in our experiments. We then calculated the arithmetic mean of ΔCt of control and treated sample groups in the experiments, respectively. ΔΔCt was then calculated by the following equation:

$$\Delta\Delta Ct = \Delta Ct_{treated} - \Delta Ct_{control-average}$$

where $\Delta Ct_{treated}$ is ΔCt of treated samples and $\Delta Ct_{control}$ is the arithmetic mean of ΔCt of control samples. Finally, we obtained the gene expression level from performing 2 to the power of negative ΔΔCt of each sample by the following equation:

$$Gene\ expression\ in\ fold = 2^{-\Delta\Delta Ct}$$

## 2.6 Homology modelling method

A work-flow diagram is presented in Figure 2.6. Homology modelling of the HD1 of RyR2 was performed using MODELLER (Šali and Blundell 1993) through the Chimera (UCSF) software (Pettersen et al. 2004). The amino acid sequences of pig and human RyR2 were obtained and extracted from RCSB PDB (Berman et al. 2000) and UniProt (UniProt 2021) (PDB ID: 5GOA; UniProt entry: Q92736), respectively, and residues corresponding to human residues 2111-2679 (the HD1 region, 2112-2680 in pig numbering) were used for further modelling. The HD1 of two wild-type (WT) pig RyR2 structures, open and closed states (PDB ID: 5GOA and 5GO9 (Peng et al. 2016); chain A in both cases), were used as templates for the modelling.

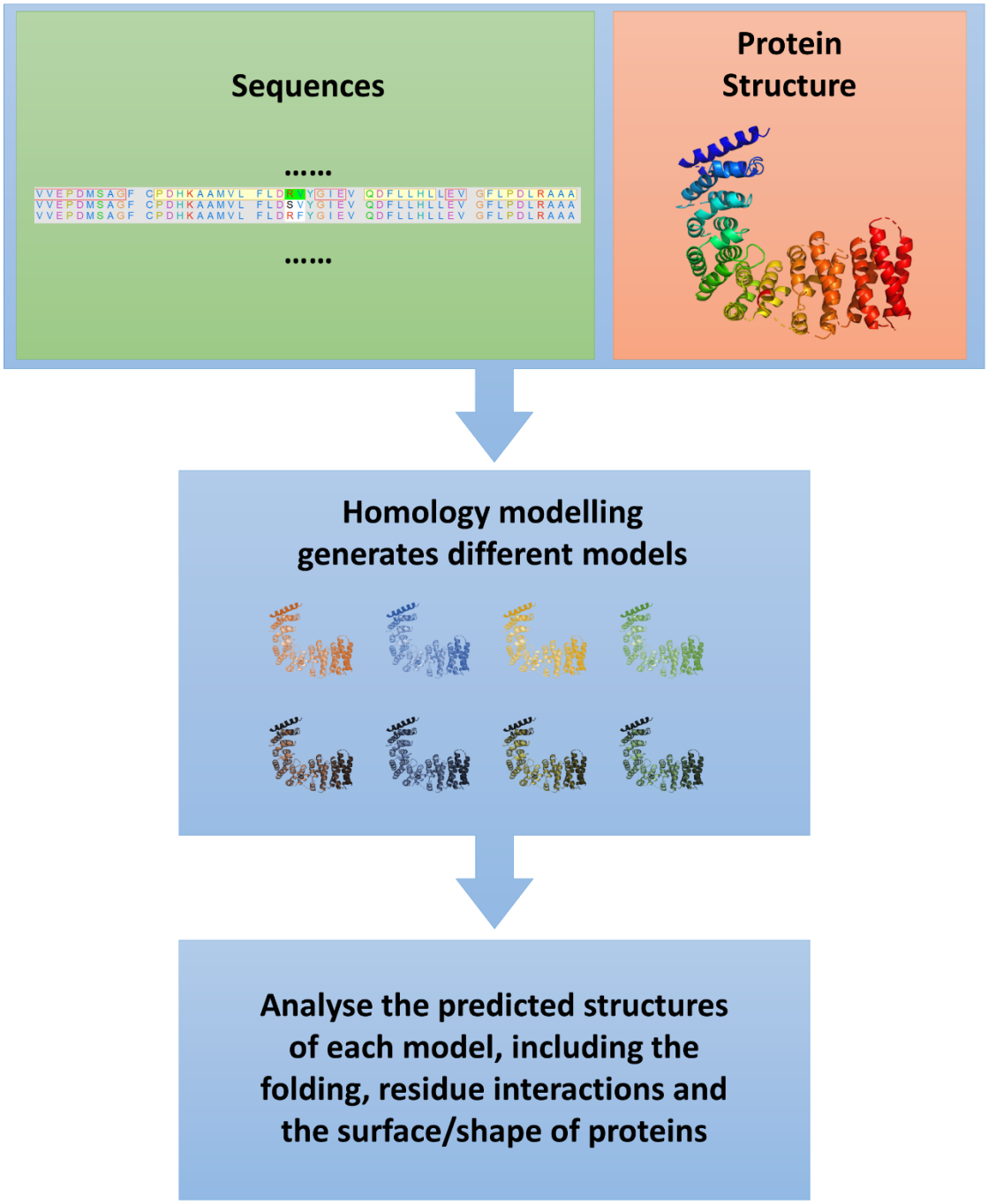



Figure 2.6 A diagram of work-flow of the homology modelling method

Using Chimera, irrelevant small molecules, like solvent molecules, were deleted from the template files. PDB files of just HD1 of chain A were saved separately, followed by alignment of the sequences of HD1 for pig, human wild-type as well as human with either of the two mutations. There are some residues missing in the secondary structure information in the PDB template file. We thus also performed a check to investigate whether the amino-acid sequence information was correct before performing homology modelling during the alignment. Homology models were generated using the default parameters for MODELLER in Chimera except those 50 models that were generated for each round of modelling and that the "thorough optimization" procedure was applied.

To optimize the conformation of the model structure, "thorough optimization" via molecular dynamics performed an equilibration and then a sampling using the following default parameters: (1) The cap of atom shift along the axis: 0.39 Å; Time step: 4.0 fs/step; (2) Equilibration (maximal 200 iterations for each temperature): Rescale the velocities every 20 steps; Equilibration temperatures: 150K, 250K, 400K, 700K, 1000K. (3) Sampling (maximal 600 iterations for each temperature): Rescale the velocities every 200 steps; Sampling temperatures: 1000 K, 800K, 600K, 500K, 400K, 300K.

The resulting HD1 homology models included a total of 300 structural models of six different constructs: human WT, the V2475F mutant and the R2474S mutant, each modelled on both open and closed state pRyR2 template structures. Two lobes were defined for HD1: lobe A (residues 2111-2473) and lobe B (residues 2476-2679) and the mutation sites made up the hinge between these lobes. The angle between these lobes

was calculated by defining two vectors, both originating from the centre of mass of the mutation site: with one of them going to the centre of mass of lobe A and the other one to the centre of mass of lobe B. The angle between these vectors was considered the hinge angle. One-way ANOVA was applied to access the significant differences between the different groups of the models.

## 2.7 Statistics

### 2.7.1 Statistical test

The unpaired Student's t-test was used to determine statistically significant differences when comparing numerical data between two groups within one independent variable. For comparisons of numerical data from more than two groups within one independent variable, the parametric one-way analysis of variance (ANOVA) or the non-parametric Kruskal-Wallis test was performed for datasets that followed or did not follow a normal distribution, respectively. The normality of datasets was assessed by using Kolmogorov-Smirnov and Shapiro-Wilk tests. Following a statistically significant result in one-way ANOVA or Kruskal-Wallis test, the differences between groups were determined by post-hoc multiple comparisons. However, multiple pairwise comparisons with a fixed level of statistical inference (which was set to $p<0.05$) can raise the rate of Type I error, also known as a false positive error. To reduce the error caused by multiple comparisons, the $p$-values were adjusted using Tukey's correction for the one-way ANOVA or Dunn's correction for the Kruskal-Wallis test.

For comparisons of numerical data between groups within two independent variables,

two-way ANOVA was performed to determine statistically significant interaction effects. In other words, to assess if the effect of one independent variable on the dependent variable is the same for all levels of the other independent variable. This factorial model allows partitioning the variance between the two independent variables, providing more accurate results than the one-way ANOVA (Krzywinski and Altman 2014). This model was also used to determine statistically significant differences in the main effects of each of the two independent variables, however, these were only considered when the interaction effects were not statistically significant. For example, the results from a two-way ANOVA comparing Po values between the independent variables "$[Ca^{2+}]$" and "type of HEK293 cells" will be reported as follows:

- "$[Ca^{2+}]$" by "type of HEK293 cells" interaction, $p$ = x.
- main effect of "$[Ca^{2+}]$", $p$ = y.
- main effect of "type of HEK293 cells", $p$ = z.

where x, y and z are probability values.

In this example, the $p$-value from the interaction effect "$[Ca^{2+}]$" by "type of HEK293 cells" informs how ion-channel Po in different $[Ca^{2+}]$ is affected by the different types of HEK293 cells and vice versa. The main effect of "$[Ca^{2+}]$" informs how different $[Ca^{2+}]$ affect the Po value irrespective of the type of HEK293 cells, and the main effect of "type of HEK293 cells" reports how different types of HEK293 cells affect Po, irrespective of $[Ca^{2+}]$. When the interaction effects were significant, the simple main effects (or simple effects) were assessed to identify the source of the interaction between the two independent variables. When assessing main or simple effects, multiple pairwise

comparisons were performed (as stated per case), and the *p*-values were adjusted using Tukey's correction.

The *p*-values from each statistical test are stated in the respective figure legends, together with adjusted *p*-values obtained from post-hoc tests in one- or two-way ANOVA tests and a description of the independent variables in two-way ANOVA tests. The data are shown as mean±SEM, n⩾4 unless otherwise stated. The differences were considered statistically significant when *p*-value $< 0.05$. Asterisks were used to indicate the *p*-value between the groups as follows: * $p < 0.05$, ** $p < 0.01$, *** $p < 0.001$, and **** $p < 0.0001$.

## 2.7.2 Models for linear and non-linear regression

The linear and non-linear fitting was performed in Prism 6 by the least square fit. For linear regression, the fitting lines used the following equation:

$$Y = aX + b$$

where a is the slope of the line and b is the Y-intercept.

For a biphasic log[ligand]-response curve, a bell-shaped curve fitting was performed used the following equations:

$$Span1 = Plateau1 - Peak$$

$$Span2 = Plateau2 - Peak$$

$$Y = \frac{Span1}{1 + 10^{(LogEC_{50} - X) \times nH}} + \frac{Span2}{1 + 10^{(X - LogIC_{50}) \times \times nH}} + Peak$$

where *Plateau1* and *Plaeau2* are the plateaus at left and right ends of the curve in the units of *Y*, *Peak* is the plateau in the middle of the curve in the units of *Y*, *nH* is the

unitless slope factor, and where $EC_{50}$ and $IC_{50}$ are the concentrations of half of the maximal stimulatory and inhibitory effect in the units of $X$, respectively.

# Chapter 3 The effects of ebselen on the SR $K^+$ channel

# 3.1 Introduction

The SR $K^+$ channel plays an important role in the release of $Ca^{2+}$ from the SR. However, the identity of the channel remains elusive since the protein has been searched for a long time but has not been confirmed yet. One main challenge is that there is no specific ligand identified for the SR $K^+$ channel to use for protein isolation. Based on previous research, we speculate that ebselen, a selenium compound, could be a unique ligand for the SR $K^+$ channel. In this chapter, I used single-channel recordings to investigate the effects of ebselen on the SR $K^+$ channel from sheep skeletal muscle. To explore the mechanism of the effect of ebselen, I designed a series of experiments to explore this mechanism of ebselen's effect on the SR $K^+$ channel. These results provide further insight in the properties of the SR $K^+$ channel, such as its gating behaviour and a ligand that could potentially be used to identify the protein.

# 3.2 Results

## 3.2.1 Effects of ebselen on SR $K^+$ channel gating

Vesicles from light SR membrane fractions (LSR) from sheep skeletal muscle have a high concentration of the SR $K^+$ channel as shown on a previous electrophysiology study while vesicles from heavy SR membrane fractions contain a high proportion of RyR proteins according to western-blot results (David Eberhardt, PhD thesis, (Eberhardt 2018)). Vesicles of LSR were thus incorporated into bilayers as described in the Methods and recordings were obtained in the presence of symmetrical 210 mM KPIPES solution, pH

7.2. Figure 3.1 shows the typical gating characteristics of the SR $K^+$ channels at the holding potentials of ±30 mV. Multiple channels usually incorporated into the bilayer. The SR $K^+$ channel is voltage-dependent (Coronado, Rosenberg, and Miller 1980; Labarca and Miller 1981; Matyjaszkiewicz et al. 2015) and Po was always lower at -30 mV than at +30 mV. Figure 3.1 illustrates the typical effects of addition of 100 nM ebselen to the cytosolic side of the channels, showing a reduction in Po that was not reversed on removal of ebselen by perfusion of the cytosolic chamber with 210 KPIPES solution. It can be seen that gating of SR $K^+$ channel was inhibited irrespective of whether the holding potential was +30 mV or -30 mV. The SR $K^+$ channel gates into many sub-conductance levels that are not fully resolved (Matyjaszkiewicz et al. 2015) but, when filtered under the conditions of our experiments (800 Hz), often appears as a single sub-conductance state close to 40% of the full open state (Matyjaszkiewicz et al. 2015). Assuming the ion channels are independent from each other, at this high level of Po as shown in Figure 3.2, the amplitude will follow binomial distribution if there are more than one channels incorporated into the bilayer and we can confirm the number of ion channels incorporated in the bilayer by adding agonist of the channel to fully activate the channels if there is any known agonist. Figure 3.2 shows an experiment where only a single SR $K^+$ channel has incorporated into the bilayer in order to illustrate the sub-conductance states more clearly. As described more fully below, addition of ebselen tended to reduce the Po of the full open states more than the Po of the sub-conductance states.

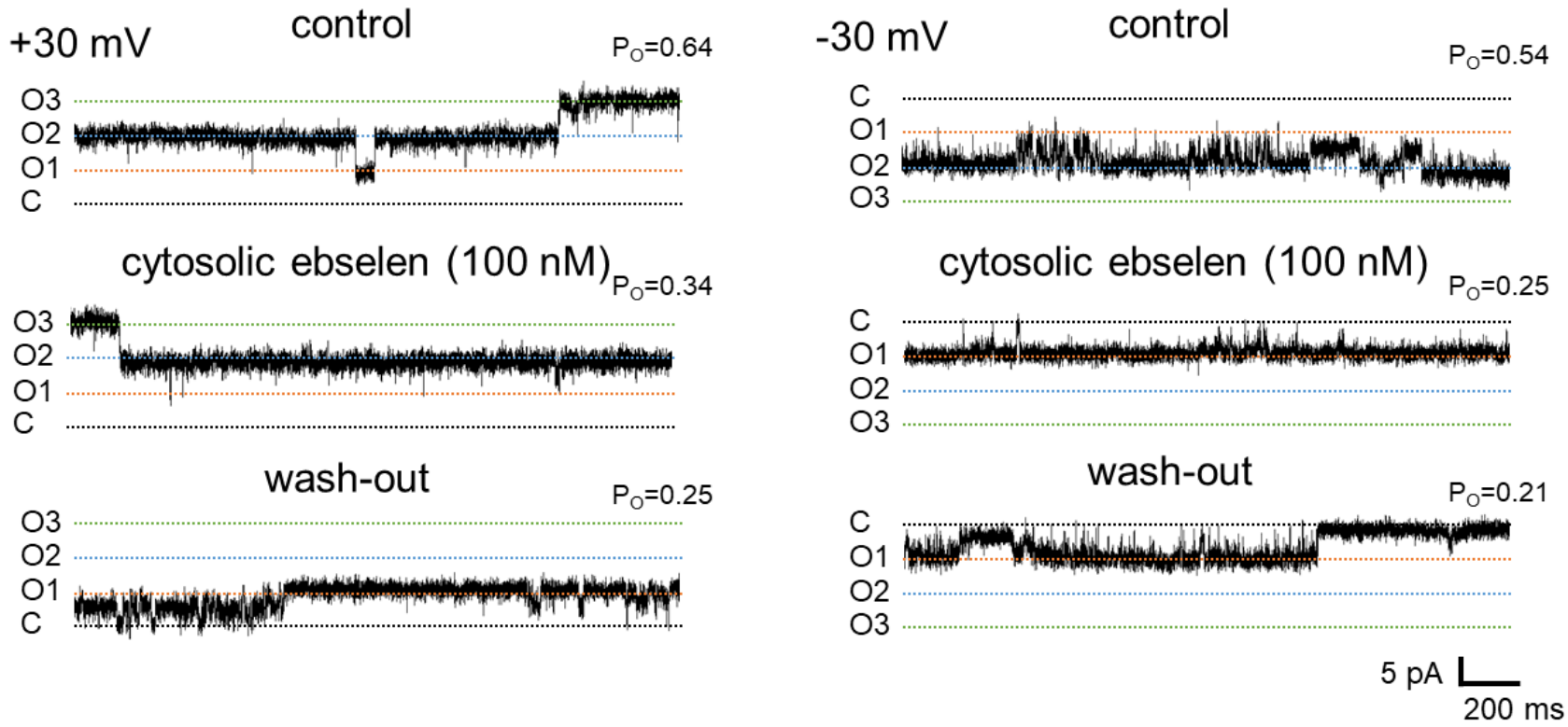



**Figure 3.1 The typical effects of ebselen on the gating of SR $K^+$ channels**

Representative current fluctuations from a single bilayer where 3 sheep skeletal SR $K^+$ channels have incorporated at the holding potentials of +30 mV (left) and -30 mV (right) in symmetrical 210 mM KPIPES solution. The total Po (full open state Po + sub-conductance state Po calculated from 1.5 min of recording at each potential (see Methods)) is shown above each trace. The zero current (fully closed channel level) is indicated by C and the different full open channel levels by O1, O2 and O3. The top traces illustrate the control conditions. 100 nM ebselen was then added to the cytosolic chamber (middle traces). The bottom traces show the gating of the channels after ebselen was washed out by perfusion with the 210 mM KPIPES solution back to control conditions.

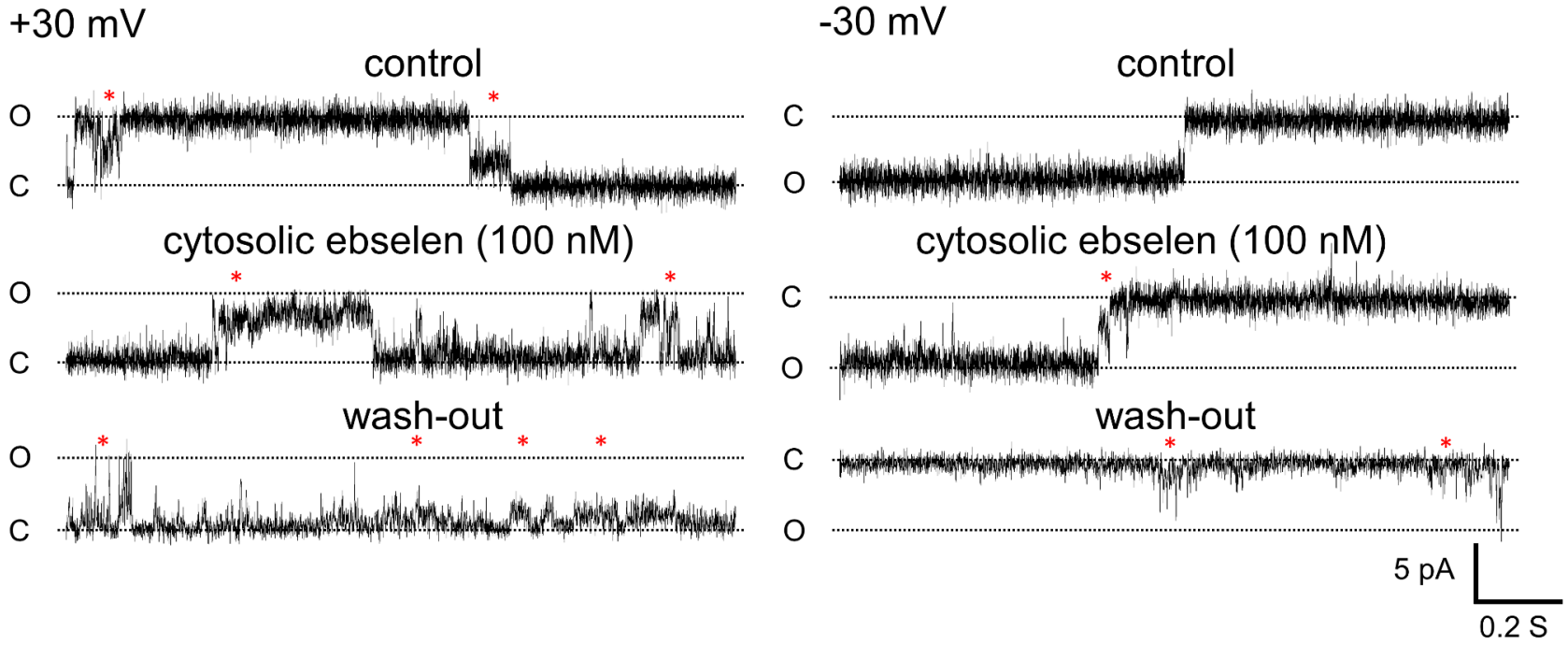



**Figure 3.2 Ebselen shows inhibitory effect in experiments where only one SR $K^+$ channel in the bilayer for visualisation of the full open and sub-conductance open states**

Typical examples of the full open events and sub-conductance gating states of the SR $K^+$ channel are shown at +30 mV (left) and -30 mV (right). The total Po (full open state Po and sub-conductance state Po calculated from 1.5 min of recording at each potential (see Methods)) is shown above each trace. Note that the short stretches of trace are chosen to illustrate the full open and sub-conductance states clearly rather than being representative of the overall Po at each intervention. The red asterisks indicate sub-conductance states. O and C represent the fully open and closed levels, respectively. The top traces illustrate the control conditions (210 mM KPIPES solution). 100 nM ebselen was then added to the cytosolic chamber (middle traces). The bottom traces show the gating of the channels after ebselen was washed out by perfusion with the 210 mM KPIPES solution back to control conditions.

The above results suggest that 100 nM ebselen is affecting the gating of the SR $K^+$ channel but it is possible that ebselen may affect the pore region of the channel and alter the conduction of $K^+$ through the channel. We therefore investigated if the single-channel conductance of the full open state of the SR $K^+$ channel would be affected by ebselen. Current amplitude from -60 mV to +60 mV was therefore plotted and the current-voltage relationship of the SR $K^+$ channel before and after addition of 100 nM cytosolic ebselen is shown in Figure 3.3. There was no evidence that ebselen affected the single-channel conductance of the full open state and so we conclude that any effect of ebselen on the full open state is due purely to an effect on the gating of the channel. Note that it is not possible to accurately measure the current-voltage relationship of the sub-conductance states because of limited resolution of the single-channel events (Matyjaszkiewicz et al. 2015).

In an attempt to understand the observation that addition of ebselen tended to reduce the Po of the full open states more than the Po of the sub-conductance states, we calculated the Po of the channels in the full open state and the Po of the channels in the sub-conductance states separately (see Methods) and measured Po every 1 s so that we could plot the time course of the ebselen effect. Figure 3.4 shows a typical example where it can be seen that ebselen reduces the Po of the channel in the full open state immediately and this effect is not accompanied by any obvious effect on the Po in the sub-conductance states. It is also noteworthy that the effect of ebselen is irreversible after washout of ebselen.

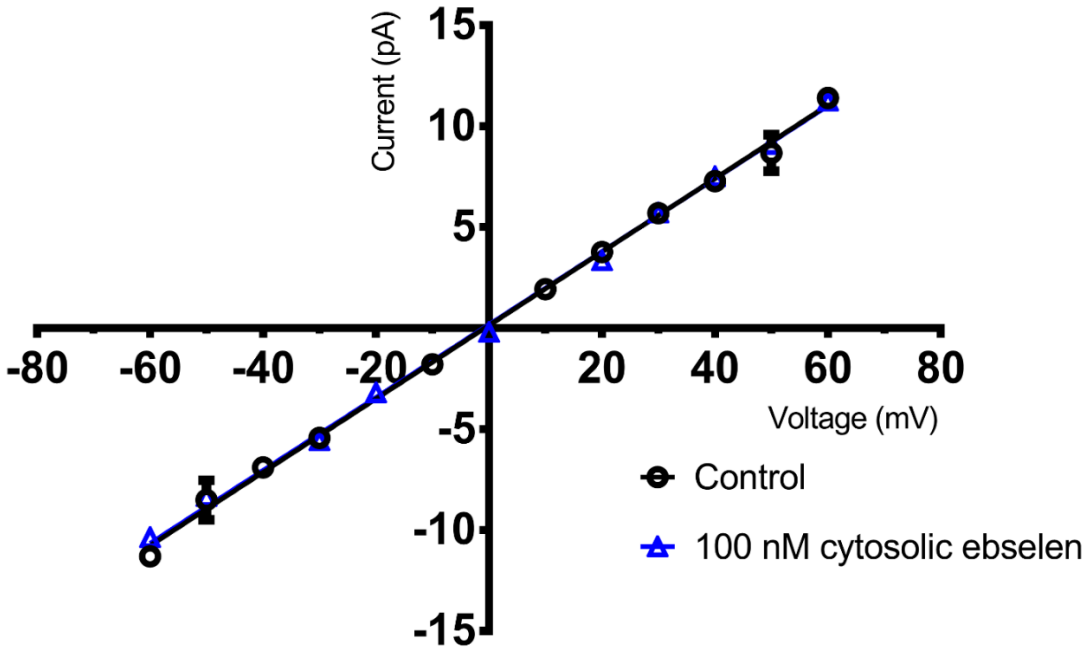



**Figure 3.3 The conductance of the SR $K^+$ single-channel full open state is not altered by ebselen**

The single-channel current-voltage relationship for SR $K^+$ channels from sheep skeletal muscle preparations in symmetrical 210 mM KPIPES, pH 7.2 is shown. The single-channel conductance of the full open state obtained from linear fitting was 181.8±2.0 pS and 180.6±2.3 pS for control and 100 nM cytosolic ebselen, respectively. Values are mean ± SD (n ≥ 3).

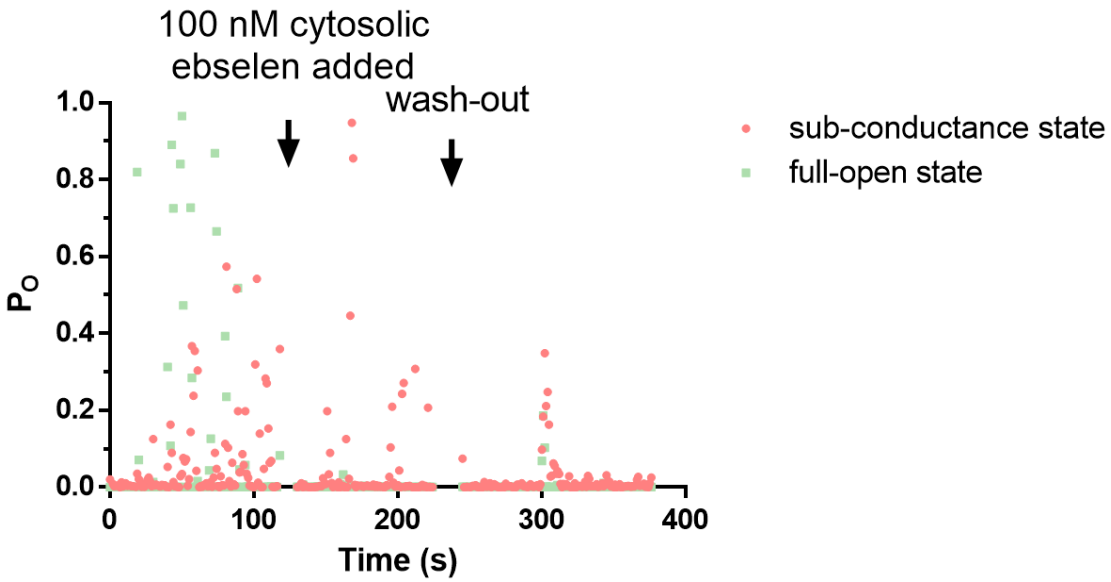



**Figure 3.4 Time-dependent effects of ebselen on the Po of the full open state and sub-conductance open states of the SR $K^+$ single-channel**

A typical experiment is shown to illustrate the effects of adding 100 nM cytosolic ebselen on the Po of the full open state (green) and the Po of the sub-conductance state (red) of a single SR $K^+$ channel. The addition of ebselen and washout of ebselen (by perfusion with control solution) are indicated by the black arrows. Po was calculated every 1 s and each 1 s Po measurement is shown by the points.

In Figure 3.5, a bar chart showing the mean ebselen-induced changes to full and sub-conductance state Po is shown, demonstrating that ebselen significantly reduces the Po of the full open state at both ±30 mV without significant change to sub-conductance state Po. This effect was irreversible. Figure 3.6 shows the mean Po of the full and sub-conductance open states of the SR $K^+$ channel expressed as a percentage of the total Po at both ±30 mV. As expected from the results shown in the previous figures, after ebselen treatment, it can be seen that the channels spend an increased proportion of time gating in the sub-conductance open states.

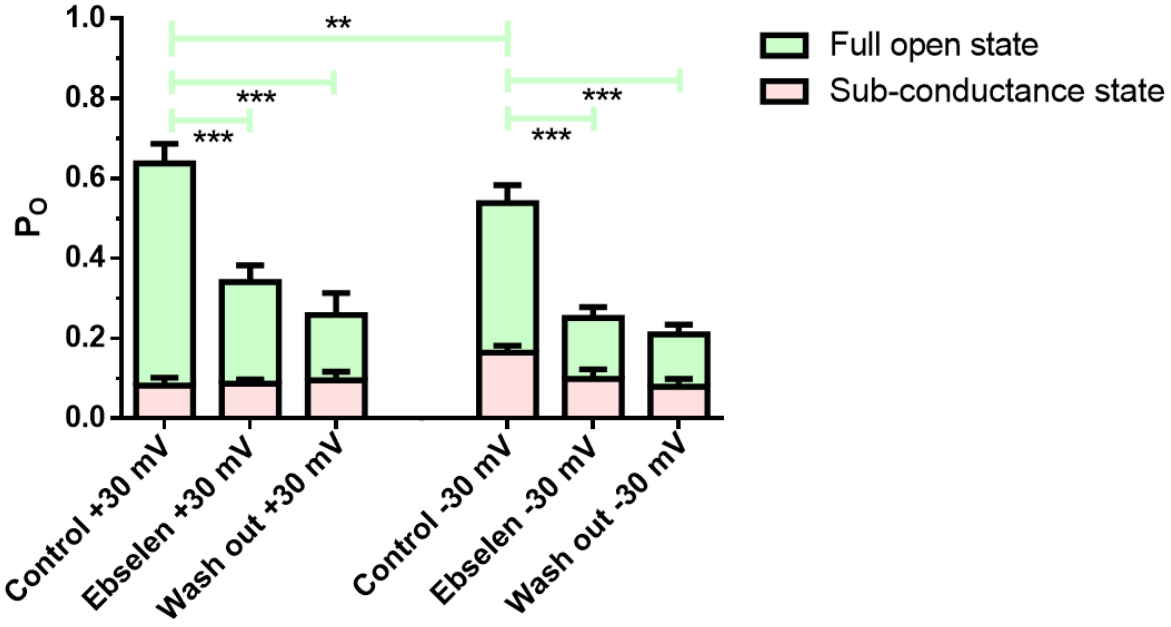



**Figure 3.5 The irreversible inhibitory effects of ebselen on the Po of the full and sub-conductance open states of the SR $K^+$ channel**

The bar chart shows the mean Po of the full and sub-conductance open states of the SR $K^+$ channel at ±30 mV in control conditions, after addition of cytosolic 100 nM ebselen and following washout of ebselen. Two-way ANOVA for two independent variables: (1) open state of SR $K^+$ channel; (2) treatment of ebselen and wash-out process. Interaction effect of the two variables $p < 0.0001$; main effect of each variables $p<0.0001$. Adjusted $p$-values (Tukey's correction) for simple effect comparing the effect of ebselen treatment are labelled by asterisks (*: $p< 0.05$; **: $p < 0.01$; ***: $p < 0.001$). Values are mean ± SEM (n=5-7).

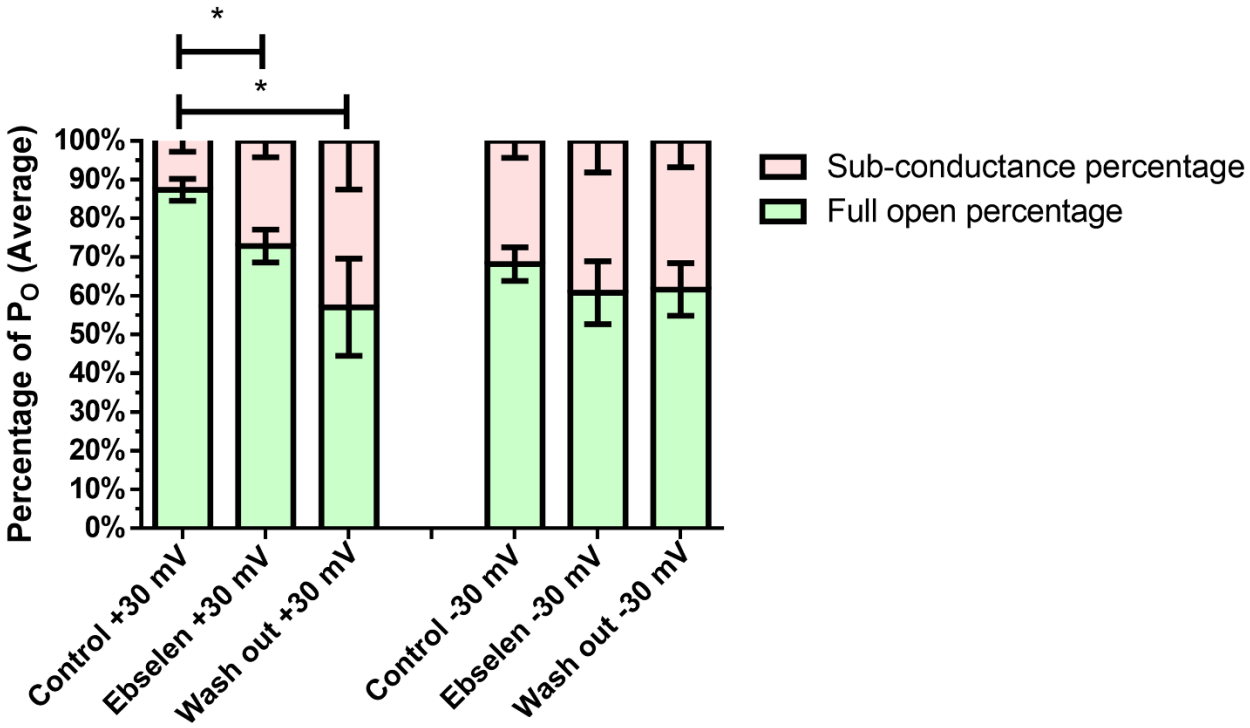



**Figure 3.6 The effects of ebselen on the Po of the full and sub-conductance open states of the SR $K^+$ channel expressed as a percentage of the total Po**

The bar chart shows the mean Po of the full and sub-conductance open states of the SR $K^+$ channel expressed as a percentage of the total Po at ±30 mV in control conditions, after addition of cytosolic 100 nM ebselen and following washout of ebselen. Two-way ANOVA for two independent variables: (1) open state of SR $K^+$ channel; (2) treatment of ebselen and wash-out process. Interaction effect of the two variables $p = 0.0002$; main effect of ebselen treatment and wash-out $p < 0.0001$. Adjusted $p$-values (Tukey's correction) for simple effect comparing the effect of ebselen treatment: $p = 0.0415$ between control and ebselen treatment under +30 mV; $p = 0.0298$ between control and wash-out step under +30 mV; Adjusted p-values (Tukey's correction) for simple effect comparing the effect of ebselen treatment are labelled by asterisks (*: $p< 0.05$; **: $p < 0.01$; ***: $p < 0.001$). Values are mean ± SEM (n = 5-7).

### 3.2.2 Investigation into the mechanism of the inhibitory effect of ebselen on SR $K^+$ channel gating

We referred to previous articles regarding the relationship between selenium compounds and proteins to investigate the mechanism of ebselen's inhibitory effect on the SR $K^+$ channel. A reasonable mechanism for this irreversible inhibitory effect appears to be that the selenium compound, ebselen in this case, formed a Se-S bond with a thiol group from a cysteine residue/s in the channel. The cysteine residue/s would be converted into an oxidized state by ebselen and lose conformation flexibility and the ability to form certain interactions, and which could therefore result in the dysfunctional gating behaviour of the SR $K^+$ channel. Figure 3.7.1 illustrates the proposed mechanism of formation of the Se-S covalent bond between ebselen and the cysteine residue. It is clear that the covalent bond would make ebselen molecule bind to the SR $K^+$ channel firmly. Thus, when ebselen inhibited the SR $K^+$ channel in an appropriate conformation and location, the inhibition would be irreversible, remaining even after wash-out of ebselen as evidenced in Figure 3.4 and Figure 3.5. We proposed a way to validate this hypothesis as shown in Figure 3.7.2. We can apply dithiothreitol (DTT) to the ebselen-modified SR $K^+$ channel, as DTT works as a common reducing agent and so it may have access to reduce the oxidized cysteine residues to the natural state. Figure 3.7.2 shows how the DTT molecule substitutes for the ebselen molecule on the cysteine residue and Figure 3.7.3 shows DTT leaves the cysteine residue and reduces the residue to the natural state. In this case, we would expect that there is a possibility that DTT may restore the gating of the ebselen-

inhibited SR $K^+$ channel.

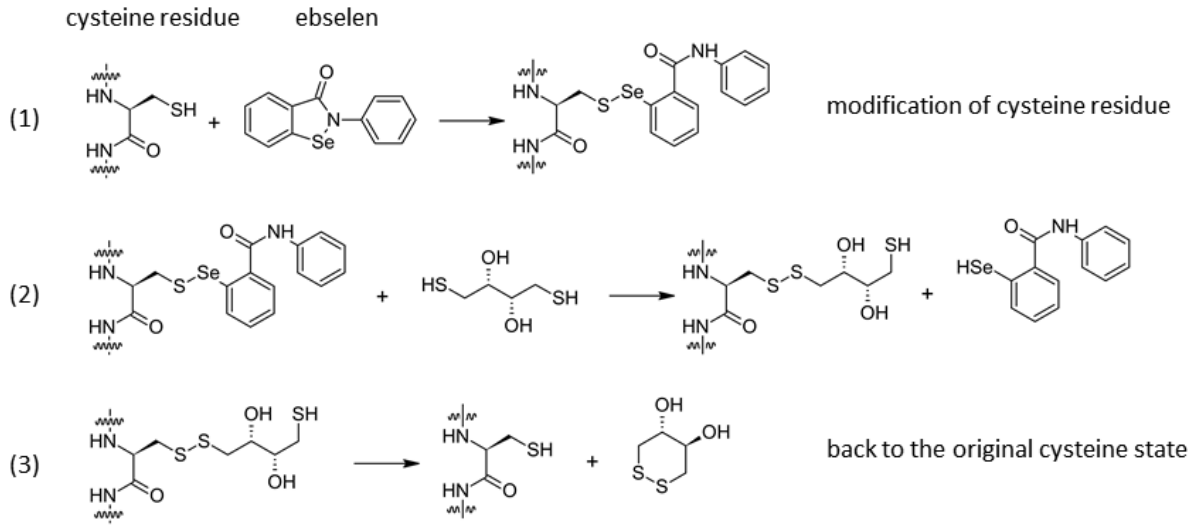



**Figure 3.7 Diagram of the proposed mechanism for ebselen's effect on the SR $K^+$ channel and the proposed validation method of the mechanism**

(1) The redox reaction between ebselen and a cysteine residue; other residues in the channel are omitted. The formation of the covalent S-Se bond is through this step.
(2) The substitution reaction between the ebselen modified cysteine residue and DTT. The DTT molecule takes the modification position from ebselen and a non-reactive selenium molecule is released.
(3) The cyclization reaction of the DTT molecule (also can be regarded as a substitution reaction of DTT itself. The cysteine residue is reduced to the normal state and, thus, the channel resumes normal function.

We then applied increasing concentrations of ebselen on the SR $K^+$ channel from the cytosolic and luminal sides followed by application of DTT. Figure 3.8 shows the effect of increasing concentrations (100 nM to 1 μM) of ebselen on SR $K^+$ channel function at a holding potential of +30 mV, followed by a treatment of 10 mM DTT. It shows that there was a reduction of Po with both cytosolic and luminal addition, the effect of which appeared to be partially reversed by subsequent of DTT.

Figure 3.9 shows the mean data for ebselen inhibition on full and sub-conductance state Po and the reversible effect of DTT. Figure 3.9 shows that (i) ebselen significantly reduces the Po of the full open state at all concentrations from the cytosolic side and can even significantly reduce sub-conductance state Po at high concentration (1 μM) from both cytosolic and luminal sides. (ii) The addition of cytosolic DTT can significantly restore the Po but not fully reverse it to the original level. We also measured Po every 1 s to plot the time course of the effect of ebselen and DTT from the cytosolic and luminal sides as shown in Figure 3.10. Figure 3.10A shows an example where it can be seen that 100 nM cytosolic ebselen reduces the Po of the channel as expected and increasing ebselen to a higher concentration (500 nM) displays a further inhibition on Po of the channel. Figure 3.10A also shows when 10 mM DTT was applied to the cytosolic side, the Po of the channel was restored to a significantly higher level thus the inhibitory effect was partially reversed. Figure 3.10B shows the addition of ebselen and DTT to the luminal side of the SR $K^+$ channels, and in this experiment, ebselen didn't reduce the Po of channels significantly until the concentration of ebselen was raised to a

higher level (1 μM). This indicated that the inhibitory effect of ebselen from luminal side was not as efficient as that from the cytosolic side. Figure 3.10B also shows that the addition of DTT seemed to have a trend to re-open the channel but did not significantly reverse the inhibitory effect. Figure 3.11 shows the mean Po of the full and sub-conductance open states of the SR $K^+$ channel in these ebselen and DTT treatments expressed as a percentage of the total Po at +30 mV.

The results above show that the addition of ebselen on either the cytosolic or the luminal side of the channel significantly reduced the Po. This effect could be partially reversed by the subsequent application of DTT but not back to the original gating levels. Furthermore, these results showed that the inhibitory effect of ebselen was greater when added to the luminal side than when added to the cytosolic side.

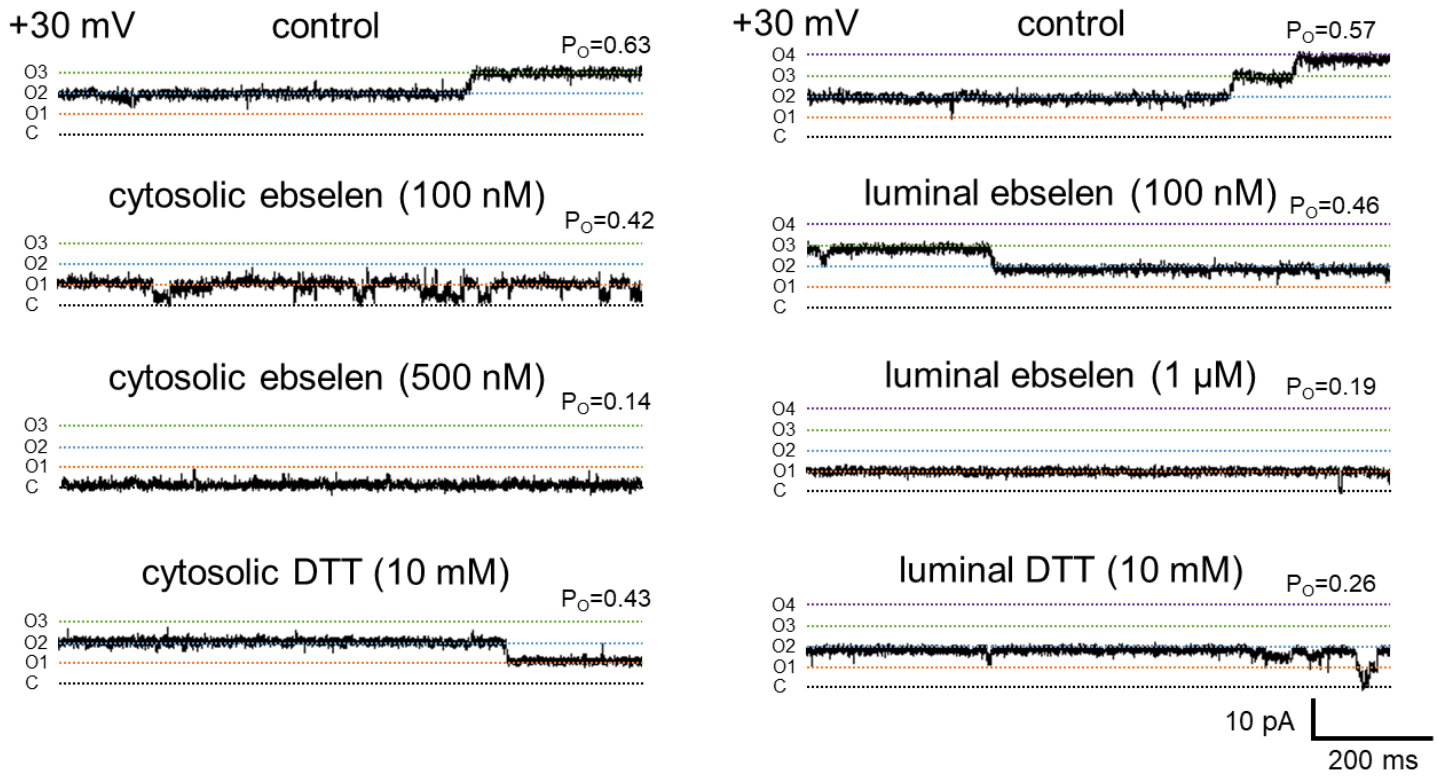



**Figure 3.8 Effects of cytosolic and luminal ebselen and DTT treatments on the gating of SR $K^+$ channels, showing a recovery of channel gating from the inhibitory effect of ebselen when treated with DTT**

Representative current fluctuations from two representative experiments where multiple sheep skeletal SR $K^+$ channels have incorporated into the bilayers. The holding potential was +30 mV. Treatments to the cytosolic (left) and luminal (right) side are labelled above each trace. The total Po (full open state Po + sub-conductance state Po calculated from 1.5 min of recording at each potential (see Methods)) is shown above each trace. The zero current (fully closed channel level) is indicated by C and the different full open channel levels by O1, O2, O3 and O4.

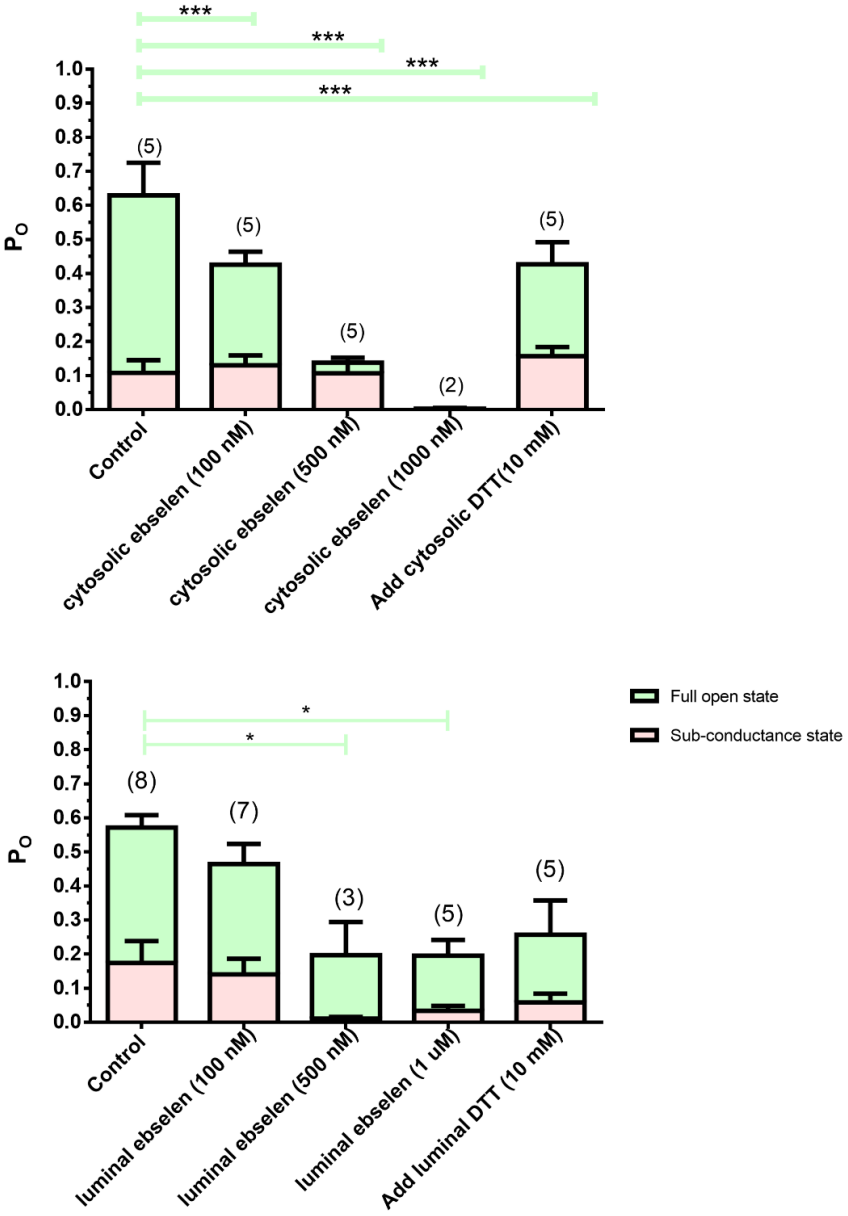



**Figure 3.9 Effects of a range of ebselen concentrations followed by DTT treatment on the Po of SR $K^+$ channel from cytosolic and luminal side.**

Effect of increasing concentrations of cytosolic (top) or luminal (bottom) ebselen followed by DTT treatment on the SR $K^+$ channel. Two-way ANOVA for two independent variables: (1) open state of SR $K^+$ channel; (2) treatment of different concentration of ebselen and DTT steps. For cytosolic side treatment (top), interaction effect of the two variables $p = 0.0002$; main effect of ebselen and DTT treatment $p < 0.0001$; main effect of open states of SR $K^+$ channel $p = 0.0010$. For luminal side treatment (bottom), main effect of ebselen and DTT treatment $p = 0.0033$; main effect of open states of SR $K^+$ channel $p < 0.0001$. Adjusted $p$-values (Tukey's correction) for simple effect comparing the effect of ebselen treatment are labelled by asterisks (*: $p< 0.05$; **: $p < 0.01$; ***: $p < 0.001$). Values are mean ± SEM where n ≥ 3.

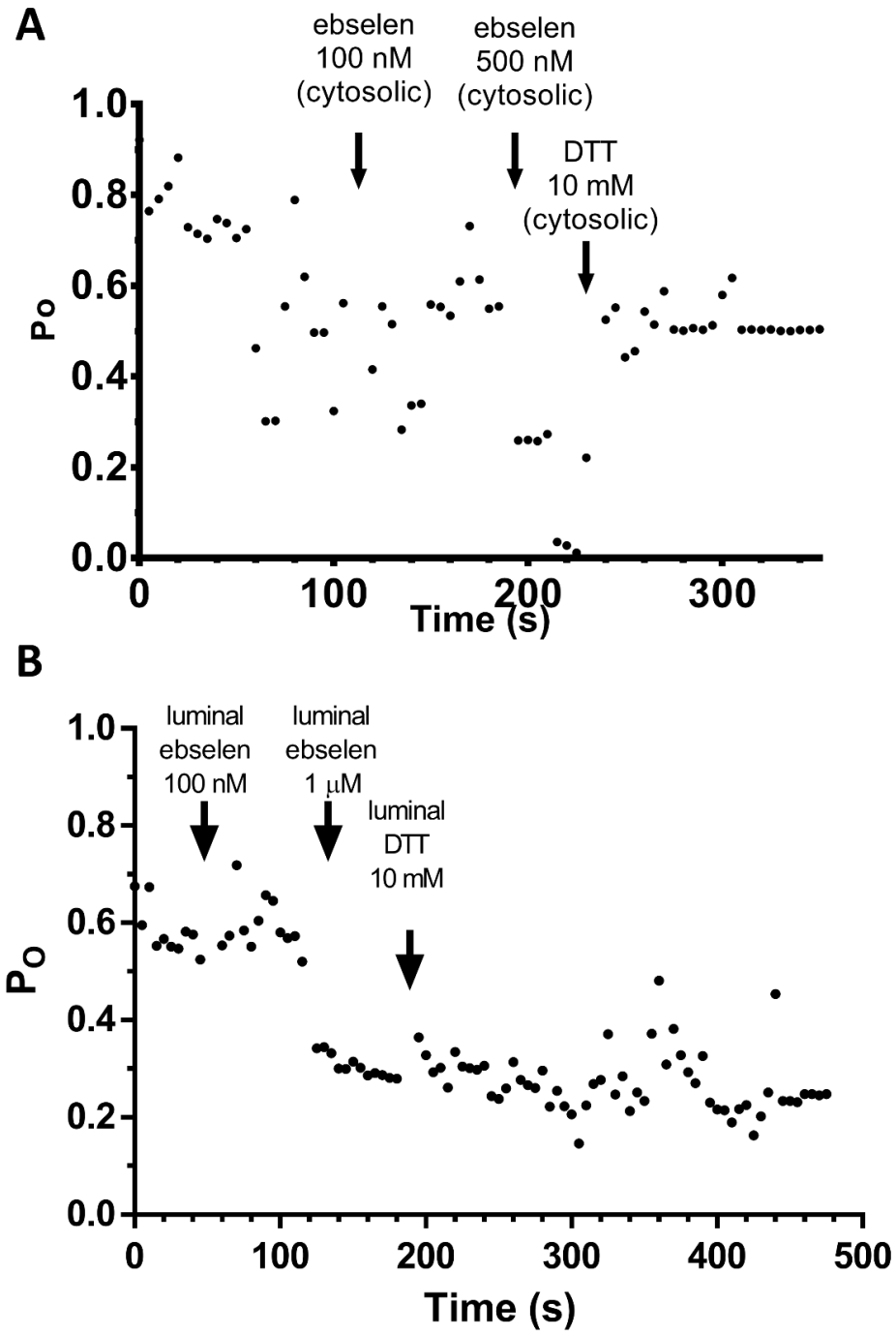



**Figure 3.10 Time-dependent effects on the Po of the SR $K^+$ channel showing the inhibition by ebselen and the partial recovery by DTT.**

The results of a typical experiment are shown for a single SR $K^+$ single-channel to illustrate the time dependence of the effects of ebselen and DTT on the total Po of the channel. Addition of different concentrations of ebselen and DTT treatment to the cytosolic (A) and luminal (B) side are indicated by the black arrows. Po was calculated every 5s and the points indicates the Po for each 5s period.

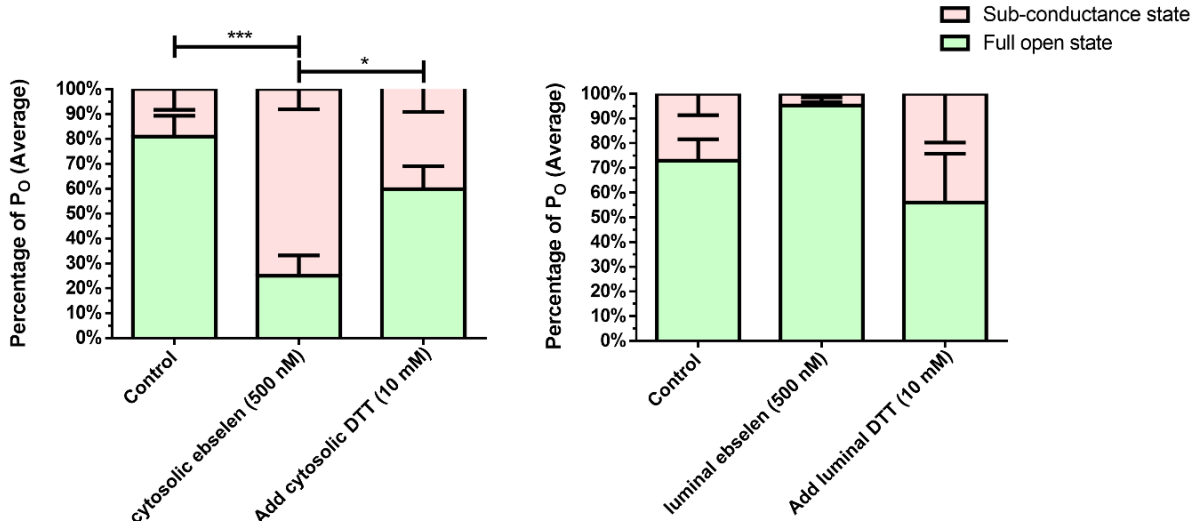



**Figure 3.11 Comparison of cytosolic and luminal additions of ebselen and DTT on the Po of the full and sub-conductance open states of the SR $K^+$ channel expressed as a percentage of the total Po**

The bar chart shows the mean Po of the full and sub-conductance open states of the SR K+ channel expressed as a percentage of the total Po at ±30 mV in control conditions, after addition of cytosolic 500 nM ebselen and following DTT treatment.

Two-way ANOVA for two independent variables: (1) open state of SR $K^+$ channel; (2) treatment of ebselen and DTT process. For cytosolic ebselen and DTT treatments, interaction effect of the two variables $p < 0.0002$. For luminal ebselen and DTT treatments, no significant differences between the variable groups. Adjusted $p$-values (Tukey's correction) for simple effect comparing the effect of ebselen treatment: $p = 0.0003$ between control and cytosolic ebselen treatment; $p = 0.0214$ between cytosolic ebselen and DTT step; Adjusted $p$-values (Tukey's correction) for simple effect comparing the effect of ebselen treatment are labelled by asterisks (*: $p< 0.05$; **: $p < 0.01$; ***: $p < 0.001$). Values are of mean ± SEM (n=4).

## 3.3 Discussion

My results suggest that ebselen can irreversibly inhibit the gating of SR $K^+$ channel from both cytosolic and luminal sides. The inhibitory effect of ebselen is induced by a S-Se covalent bond between ebselen and the channel, as validated by the effect of subsequent DTT addition. The mechanism of the inhibitory effect also implies that ebselen changes the gating behaviour of SR $K^+$ channel in a manner affecting more on the full open state of the channel.

In Figure 3.3, it can be seen that ebselen didn't affect the conductance of SR $K^+$ channel at a concentration causing the inhibitory effect, thereby indicated that ebselen does not physically block the channel pore or chemically modify the pore structure. Regarding the cytosolic and luminal ebselen effects at 100 nM concentration, Figure 3.4 and Figure 3.9 indicate that ebselen is more efficient at inhibiting the SR $K^+$ channel from the cytosolic side. The Po of the channel was further reduced by high concentrations (1 μM) of cytosolic ebselen, as expected, and was also reduced to a significantly low level with luminal side treatment. There are two possible explanations for ebselen's luminal effects on the channel: (i) ebselen may irreversibly inhibit SR $K^+$ channel by interacting with the channel from both cytosolic and luminal sides but it requires a higher concentration for the luminal effect. (ii) Considering that ebselen is a polar molecule without charge, it is possible that some ebselen molecules diffused from the luminal to the cytosolic side and, thus, caused inhibition by interacting with residues on the cytosolic face of the channels. Further investigation into this can be conducted if we can find an analogue of

ebselen that is not permeable to the membrane.

In Figure 3.4, we can observe that the full open state SR $K^+$ channel shuts down as soon as the ebselen (100 nM) is applied to the cytosolic side. This indicates that the rate constant of ebselen association is quite high. When the SR $K^+$ channel opens to the full open state, it does so by passing through a sub-conductance state in 99.99% of events (Matyjaszkiewicz et al. 2015). Thus, when ebselen is bound to the channel, it appears not efficient at fully opening from the sub-conductance state. This is because the sub-conductance state Po was not significantly affected, leading to the channel spending an increased percentage of time in sub-conductance states (Figure 3.6). We assume that the binding of ebselen doesn't affect the process of the channel opening to the sub-conductance states from the closed state since the Po in the sub-conductance states was not significantly altered at this concentration of ebselen. In the example experiment shown in Figure 3.10A, showing the time-course of the ebselen effect, the total Po was reduced with 100 nM cytosolic ebselen but this effect was much greater with 500 nM ebselen and was an immediate effect on openings to the fully open state without openings to the sub-conductance state being affected (the mean data is shown in Figure 3.9). In contrast, when the very high concentration of 1000 nM cytosolic ebselen was added, sub-conductance openings were virtually abolished and therefore full openings were also abolished because 99.99% of full openings occur via openings to the sub-conductance states 9Antos paper).

Figure 3.9 and Figure 3.10 suggest that DTT can partially reverse the inhibitory effect

of cytosolic ebselen. This supports the hypothesis that ebselen forms a Se-S covalent bond with a cysteine residue/s on the SR $K^+$ channel. It is apparent that ebselen quickly and efficiently inhibited the SR $K^+$ channel from the cytosolic side and that the addition of DTT (Figure 3.9A and Figure 3.10A) reversed the effect of high concentrations of ebselen back to the Po of the channels observed at 100 nM ebselen but did not fully reverse Po back to control levels. The luminal response of ebselen appeared more variable and weaker, requiring higher concentrations of ebselen for an effect on Po and DTT only exhibited a non-significant trend towards reopening the channel (Figure 3.9B and Figure 3.10B). I therefore suggest that it is more likely that the critical cysteine residue/s affected by ebselen that are involved in the channel gating mechanism is located on the cytosolic side of the SR $K^+$ channel. In this regard, the process of the inhibitory effect of ebselen and DTT treatment may go through several steps: (i) The ebselen molecule binds to a specific position on the cytosolic surface of the SR $K^+$ channel. (ii) The selenium atom in the ebselen locates close to a cysteine residue/s, reacts and forms a Se-Se bond as a result of a certain orientation of ebselen molecule on the channel (Figure 3.7.1). (iii) The binding of ebselen and the oxidation of a cysteine residue/s causes an alteration to the channel conformation and subsequently inhibits channel opening. (iv) The addition of DTT brings a reducing agent to the ebselen-modified cysteine residue/s and reduces at least some of the cysteine residues to their original state (Figure 3.7.2-3). (v) The cleaved ebselen molecule, which is no longer reactive to cysteine, leaves the surface of the channel, allowing that cysteine residue to rotate back to its normal conformation, resulting in the partial restoration of channel gating.

In summary, my results suggest that ebselen may act as an irreversible inhibitor of the SR $K^+$ channel. They suggest that ebselen is binding to the SR $K^+$ channel through a Se-S covalent bond. Though we haven't confirmed the exact binding site, it appears that ebselen can influence the SR $K^+$ channel from both cytosolic and luminal sides but that the cytosolic ebselen treatment is more efficient than that from the luminal side. My results are important because I have found the first ligand that can influence the gating of the SR $K^+$ channel without affecting conductance. All other known agents that affect the SR $K^+$ channel function is voltage-dependent, positively charged pore blockers; they enter the pore under the influence of voltage, thus blocking current flow. Future experiments should build on my results to try to find an agent similar to ebselen but which is more selective for the SR $K^+$ channel over other proteins. This would be a useful tool for investigating the identity of the SR $K^+$ channel and for causing selective block of counter-ion $K^+$ current across the SR which would improve our understanding of the physiology of SR ionic currents. There is also a need for further detailed experiments to investigate the binding site of ebselen on the SR $K^+$ channel. Our DTT experiment results suggest that a reducing agent can partially reverse the inhibition due to ebselen. This provides us with new basis for exploring the mechanisms underlying SR $K^+$ channel gating properties.

# Chapter 4 Effect of co-expressing TRIC-channels on RyR2 in HEK293 cells

## 4.1 Introduction

TRIC channels play an important role in the SR $Ca^{2+}$ release in cardiac and skeletal muscle cells as evidenced in pathology studies using *Tric* knock-out channel mouse models (Yamazaki et al. 2011; Zhao et al. 2010). It is believed that TRIC channels provide a cation flux through the SR to act as a counter-current during SR $Ca^{2+}$-release by RyRs. However, an additional role for TRIC channels has been recently proposed based on previous reports that have suggested a functional interaction between RyRs and TRIC channels (Zhou et al. 2020). To obtain a better understanding of the relationship between the activity of RyR and TRIC channels, I performed single-channel experiments in RyR2 channels obtained from HEK293 cells that had been previously transfected with RyR2 only, RyR2 and TRIC-A or RyR2 and TRIC-B. HEK293 cells have been previously shown to contain no endogenous RyR2 or TRIC channels. Therefore, the SR vesicles isolated from the 3 aforementioned cell types of transfected HEK293 cells will contain either: 1) RyR2, 2) RyR2 + TRIC-A or 3) RyR2 + TRIC-B. Consequently, when these SR vesicles are incorporated in artificial lipid bilayers, we can observe any changes induced in RyR2 activity by the co-expression of TRIC-A or TRIC-B. This approach will therefore help us understand the effect of TRIC-A or TRIC-B channels on the gating behaviour of RyR2.

While previous studies have always reported $K^+$ as the main SR ion that gates through TRIC channels, a detailed examination of their permeability properties has not been

performed to date. The SR vesicles from the three types of transfected HEK293 cells offer the possibility to explore the permeability properties of the TRIC-A and TRIC-B channels without undergoing an extensive detergent-based purification process that can disrupt channel function. Therefore, I performed additional experiments to measure the relative permeability between $K^+$ and $Cl^-$ ions of incorporated channels from each type of cell. My results suggest that TRIC channels may be permeable to both cation and anion rather than only permeable to monovalent cation. This reveals further attributes of the interaction between TRIC and RyR channels and how TRIC channels regulate SR $Ca^{2+}$-release.

## 4.2 Result

### 4.2.1 Effect of co-expressing TRIC-channels with RyR2 in HEK293 cells on RyR2 single-channel function

To investigate the influence of TRIC-A and TRIC-B on the single-channel conductance and gating properties of RyR2 channels, we used RyR2 over-expressing HEK293 cells transfected with TRIC-A or TRIC-B. The cell pellets were supplied by our Japan collaborators (Dr Hiroshi Takeshima, Dr Takashi Murayama, Dr Miyuki Nishi) to enable us to isolate three different membrane preparations containing: (1) vesicles from cells expressing only RyR2. (2) vesicles from cells co-expressing RyR2 and TRIC-A. (3) vesicles from cells co-expressing RyR2 and TRIC-B. The validation of these different transfected HEK293 cells were performed by Dr Takashi Murayama's group via western blot as shown in Figure 4.1.

Vesicles were incorporated into planar phospholipid bilayers in symmetrical solutions of 210 mM KPIPES, 2 μM free $Ca^{2+}$, pH 7.2, with an addition of 600 mM cytosolic KCl gradient as described in Methods. Figure 4.2 shows examples of typical current fluctuations that we observed in the bilayers after fusion of membrane vesicles from RyR2 only, RyR2 + TRIC-A or RyR2 + TRIC-B cells and after the cytosolic chamber was perfused with 210 mM KPIPES solution to remove excess vesicles and at holding potentials of ±30 mV. It can be seen that the gating of RyR2 appeared similar irrespective of whether TRIC-A or TRIC-B was co-expressed with RyR2. And with 2 μM cytosolic $Ca^{2+}$ as the activator, Po was low in all three groups. However, close inspection of the recordings revealed that RyR2 occasionally gated to a sub-conductance state, and this appeared more obvious in those experiments where TRIC-A and TRIC-B had been co-expressed with RyR2.

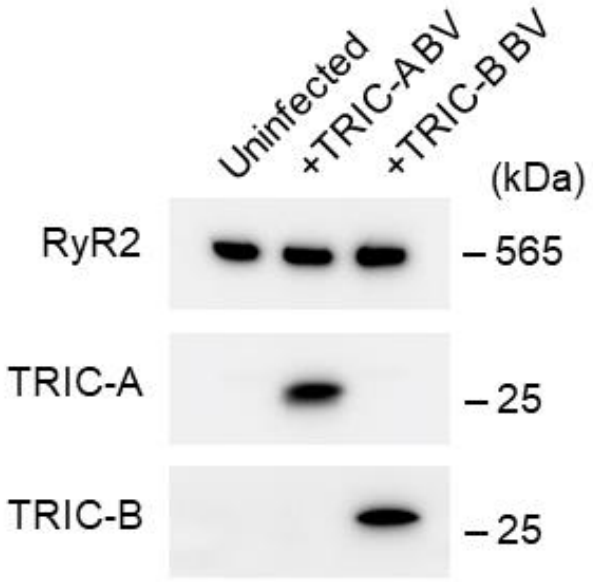



**Figure 4.1 Western blot of RyR2 over-expressing HEK293 cells transfected with TRIC-A or TRIC-B by Dr Takashi Murayama's group**

Western blots of the microsomal membrane vesicles isolated from RyR2 over-expressing HEK293 cells that were either uninfected (left), infected with TRIC-A baculovirus (BV) (center) or TRIC-B BV (right). The loading of samples is normalized to total protein. Bands for RyR2 (565 kDa), TRIC-A (25 kDa) and TRIC-B (25 kDa) are labelled.

### 4.2.2 Effect of co-expression of TRIC channels on RyR2 single-channel conductance

To investigate whether RyR2 would exhibit a different $K^+$ conductance when co-expressed with TRIC-A or TRIC-B, we measured the current amplitude at ±30 mV and 0 mV and plotted the relationship between current amplitude and voltage for the three different RyR2 groups. Figure 4.3A illustrates current-voltage relationships of RyR2 channels from three experimental groups and demonstrates that co-expression of TRIC-A or TRIC-B did not affect single-channel $K^+$ conductance. RyR2 is approximately 7 times more permeable to $Ca^{2+}$ than to $K^+$ (Tinker and Williams 1992) and because the $Ca^{2+}$ single-channel conductance of RyR2 is much lower than that of $K^+$, addition of a relatively small amount of $Ca^{2+}$ (1 mM) to 210 mM $K^+$ solutions cause a significant decrease in conductance (Tinker, Lindsay, and Williams 1992). Figure 4.3B demonstrates how addition of 1 mM cytosolic $Ca^{2+}$ to symmetrical 210 mM $K^+$ solutions reduces single-channel conductance as expected therefore suggesting that co-expression of TRIC-A or TRIC-B does not alter RyR2 $Ca^{2+}$ conductance or the relative permeability of $K^+$: $Ca^{2+}$.

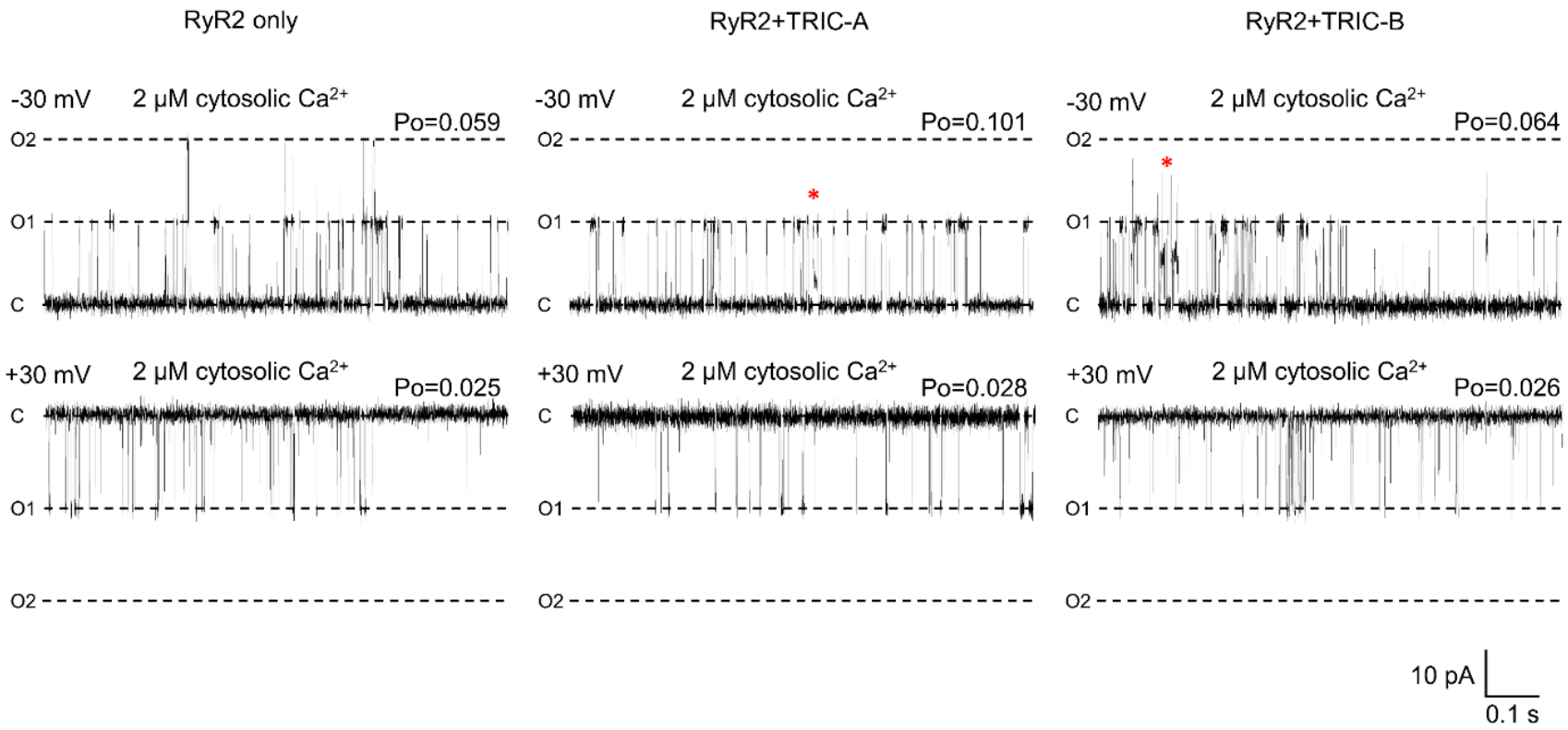



**Figure 4.2 Effects of co-expressing TRIC-A or TRIC-B with RyR2 on the gating of RyR2 channels incorporated into bilayers at 2 μM free $Ca^{2+}$**

Representative current fluctuations of incorporated RyR2 channels from HEK293 cells expressing RyR2-only (left traces), RyR2+TRIC-A (middle traces) and RyR2+TRIC-B (right traces) at holding potentials of ±30 mV in symmetrical 210 mM KPIPES, 2 μM free $Ca^{2+}$. The Po (calculated from 1.5 min of recording) is shown above each trace. The zero current level is indicated by C and different fully open channel levels by O1 and O2. Red stars indicate the observed sub-conductance levels in the traces.

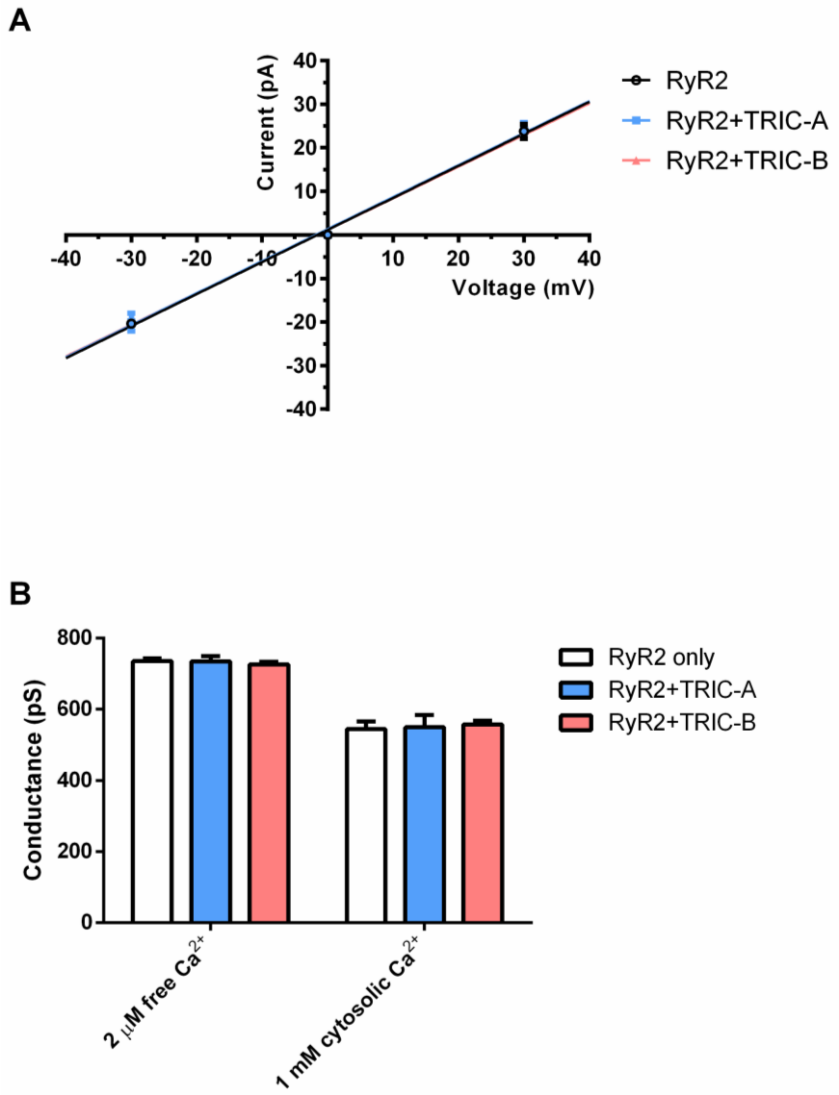



**Figure 4.3 The co-expression of TRIC-A or TRIC-B with RyR2 does not affect RyR2 single-channel conductance**

(A) The single-channel current-voltage relationship for RyR2 channels from HEK293 cells expressing only RyR2, RyR2+TRIC-A and RyR2+TRIC-B are shown. Solutions were symmetrical 210 mM KPIPES, pH 7.2 with 2 μM free $Ca^{2+}$. Values are mean ± SEM (n=5-8). (B) The bar chart shows effect of increasing cytosolic free [$Ca^{2+}$] from 2 μM to 1 mM on RyR2 single-channel conductance in the same symmetrical 210 mM KPIPES solution as in (A). Mean conductance values ± SEM (n = 4~8) are shown for RyR2 channels from HEK293 cells expressing only RyR2, RyR2+TRIC-A and RyR2+TRIC-B. Two-way ANOVA for the independent variable, type of HEK293 cells, is not significant with p = 0.7200. Values are of mean ± SEM.

### 4.2.3 Effect of TRIC-A and TRIC-B on the response of RyR2 to changes in cytosolic $Ca^{2+}$

$CaCl_2$ was added to the cytosolic side to increase $Ca^{2+}$ concentration from 2 μM free $Ca^{2+}$ to 10 μM, 100 μM, 1 mM, and 2 mM in all experimental groups. Figure 4.4 shows representative examples of RyR2 current fluctuations observed at the holding potential of -30 mV. Notice how RyR2 channel openings were very brief for RyR2 only and RyR2+TRIC-B experiments, whereas in RyR2+TRIC-A experiments, longer openings were observed. Unfortunately, we were not able to investigate this apparent change in gating mechanism because study of the open and closed lifetime durations requires that only one channel is present in the bilayer and we rarely observed any bilayers where only one RyR2 channel had incorporated. We also observed some sub-conductance state gating in the recordings with higher Po (see Figure 4.4) and our analysis of this is described later in more detail. The traces show that Po changes driven by the increases in cytosolic [$Ca^{2+}$] was different depending on whether RyR2 had been co-expressed in HEK293 cells with TRIC-A or TRIC-B. This can be observed more clearly in Figure 4.5A where the relationships between Po and [$Ca^{2+}$] are illustrated for the mean data. All RyR2 channels exhibited a biphasic response to cytosolic $Ca^{2+}$, consistent with previous research (Sitsapesan, Montgomery, and Williams 1995; Hill and Sitsapesan 2002) but co-expression of TRIC-A or TRIC-B affected both the activation and inactivation arms of the relationship. The $IC_{50}$ values for RyR2-only, RyR2+TRIC-A and RyR2+TRIC-B experiments were 87.5 μM, 1.08 mM and 843.3 μM, respectively. The

co-expression of TRIC-A led to an obvious increase in the maximum level to which $Ca^{2+}$ increased Po from approximately 0.2 to 0.5. Also marked, was the reduced ability of cytosolic $Ca^{2+}$ to cause inactivation if RyR2 was co-expressed with TRIC-A or TRIC-B.

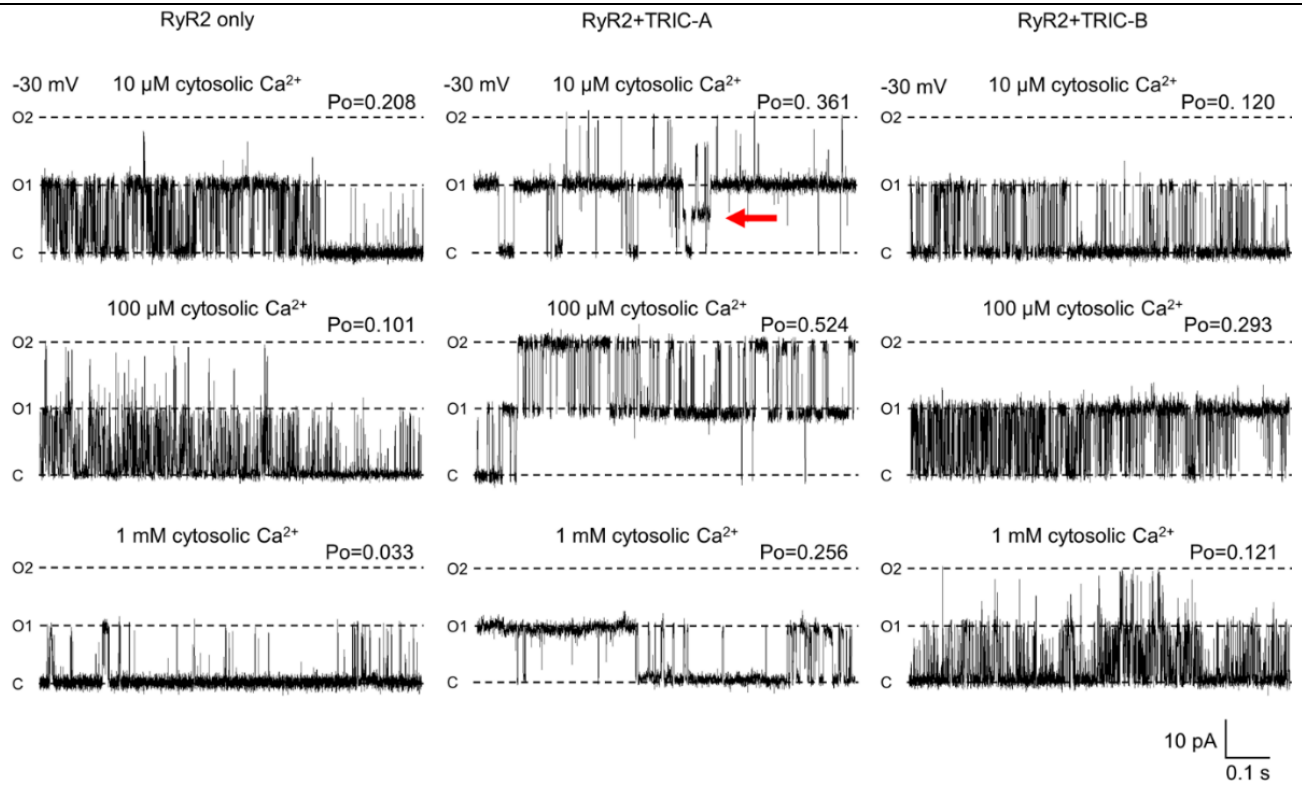



**Figure 4.4 Effect of co-expressing TRIC-A or TRIC-B with RyR2 on the gating of incorporated RyR2 channels at increased cytosolic [$Ca^{2+}$]**

Representative current fluctuations of incorporated RyR2 channels from HEK293 cells expressing RyR2 only (left traces), RyR2+TRIC-A (middle traces) and RyR2+TRIC-B (right traces) at the holding potential of -30 mV in symmetrical 210 mM KPIPES with 10 μM cytosolic $Ca^{2+}$ ($1^{st}$ row traces), 100 μM cytosolic $Ca^{2+}$($2^{nd}$ row traces), and 1 mM cytosolic $Ca^{2+}$ ($3^{rd}$ row traces). The free [$Ca^{2+}$] was increased by additions of $CaCl^2$ to the cytosolic chamber. The Po (calculated from 1.5 min of recording) is shown above each trace. The zero current level is indicated by C and different fully open channel levels by O1 and O2. A red arrow indicates the observed sub-conductance state at 10 μM cytosolic $Ca^{2+}$ in RyR+TRIC-A group.

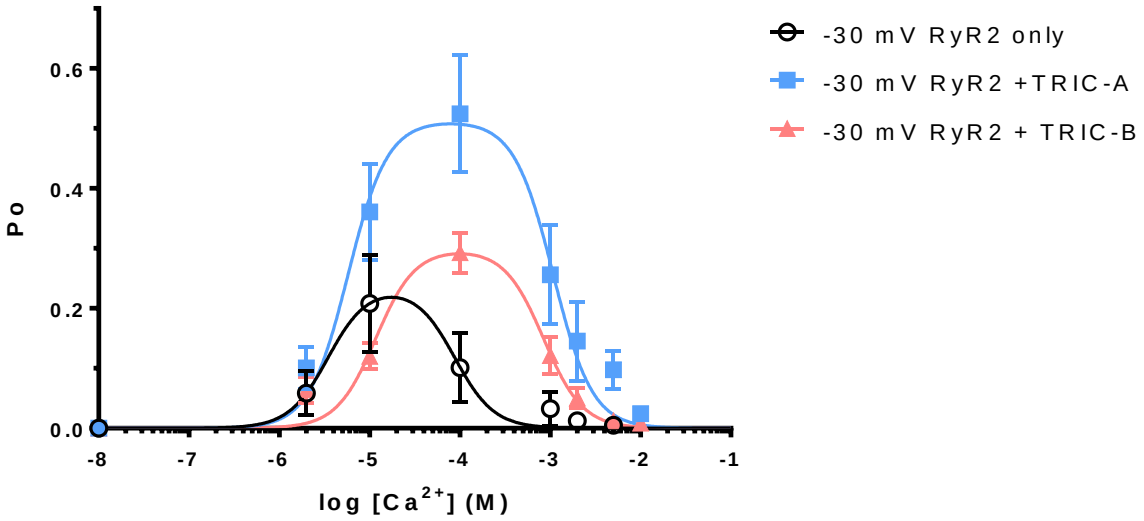



**Figure 4.5 Effect of co-expressing TRIC-A or TRIC-B with RyR2 on the response of RyR2 to increasing cytosolic [$Ca^{2+}$]**

The relationship between cytosolic [$Ca^{2+}$] and the Po of RyR2 channels from HEK293 cells expressing only RyR2 (black), RyR2+TRIC-A (blue), and RyR2+TRIC-B (red) in symmetrical 210 mM KPIPES at the holding potential of -30 mV. Lines display non-linear bell-shaped fitted curves. The $EC_{50}$ values for RyR2 only, RyR2+TRIC-A and RyR2+TRIC-B are 3.6 µM, 5.8 µM and 11.7 µM, respectively and $IC_{50}$ values for these three groups are 87.5 µM, 1.08 mM, and 843.3 µM, respectively. Values are mean ± SEM (n=6, 3-7, 12 for RyR2 only, RyR2+TRIC-A and RyR2+TRIC-B, respectively).

### 4.2.4 Effect of co-expression of TRIC-A and TRIC-B on the voltage-dependence of RyR2 gating

To fully investigate the influence of co-expressing TRIC-A or TRIC-B on the gating behaviour of RyR2, we also measured RyR2 Po at the holding potential of +30 mV. The relationship between cytosolic $Ca^{2+}$ and Po was compiled for all three experimental groups at -30 mV and +30 mV and is shown in Figure 4.6. After switching to +30 mV, we observed inactivation and this markedly affected the measurement of Po as shown in Figure 4.4B. The voltage-dependent inactivation did not significantly affect overall Po measurements of RyR2-only channels but it can be seen that in the experiments where TRIC-channels were co-expressed, average steady-state Po was reduced to near zero. It can be seen that the Po in RyR2-only experiments was similar at both +30 mV and -30 mV with only a trend towards lower Po values at +30 mV. However, it can be seen that in the experiments where TRIC-channels were co-expressed, average steady-state Po was reduced to near zero across all concentrations of $Ca^{2+}$ at +30 mV. This was not totally unexpected as RyR2 is known to undergo voltage-dependent inactivation in a manner that is dependent on the activating ligands (Sitsapesan, Montgomery, and Williams 1995; Hill and Sitsapesan 2002). We therefore investigated the gating behaviour of the channels in more detail after the voltage switch to +30 mV. We found that many channels shut down soon after the voltage switch to +30 mV and did not reopen again until voltage was switched back to -30 mV similar to behaviour previously observed with RyR2 (Sitsapesan, Montgomery, and Williams 1995; Hill and Sitsapesan 2002).

**A**

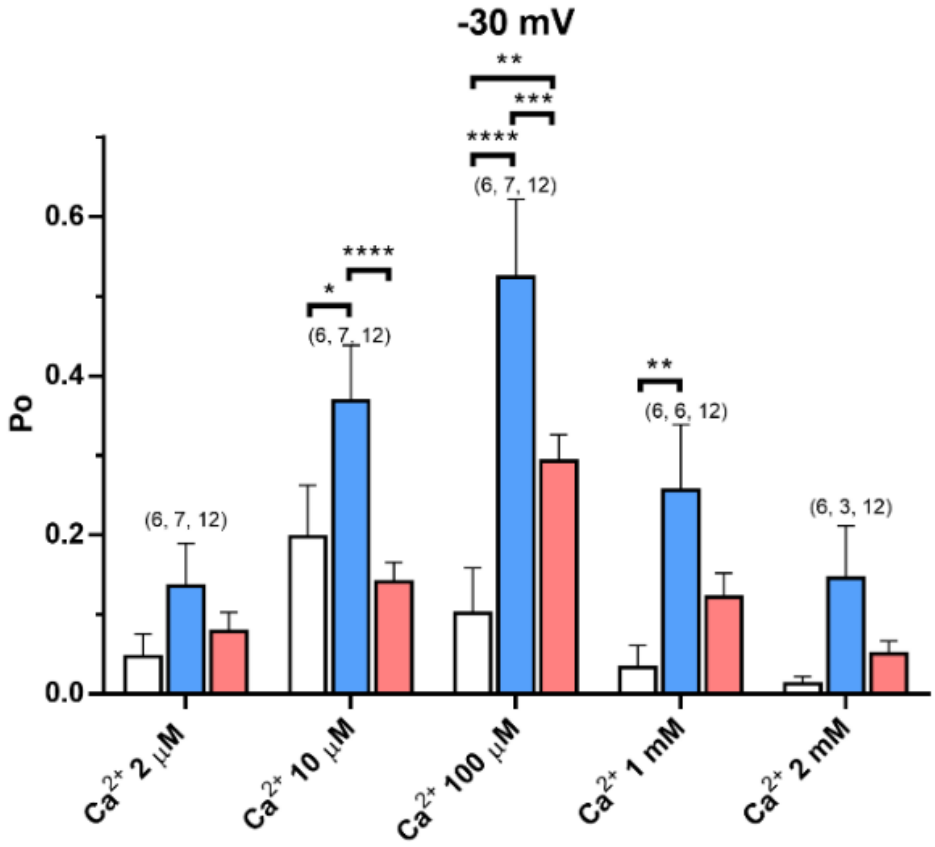



**Figure 4.6 The co-expression of TRIC-A or TRIC-B with RyR2 affects RyR2 Po over a range of cytosolic [$Ca^{2+}$] at -30 mV**

Effect of holding potential ((A) -30 mV; (B)+30 mV) on the relationship between [$Ca^{2+}$] and Po for RyR2 derived from HEK293 cells expressing RyR2-only (black), RyR2+TRIC-A (blue) and RyR2+TRIC-B (red). Two-way ANOVA for with two independent variables: 1) "cytosolic [$Ca^{2+}$]", and 2) "type of HEK293 cells". For the -30 mV on the left: interaction effect for "cytosolic [$Ca^{2+}$]" by "type of HEK293 cells" p =0.0035; main effect of "cytosolic [$Ca^{2+}$]", $p < 0.0001$; main effect of "type of HEK293 cells", $p < 0.0001$. Adjusted p-values (Tukey's correction) for simple effects are listed in Tables 1 and 2 in the Appendix. For the +30 on the right: interaction effect for "cytosolic [$Ca^{2+}$]" by "type of HEK293 cells", p = 0.1222; main effect of "cytosolic [$Ca^{2+}$]", p =0.0394; main effect of "type of HEK293 cells"; p = 0.0028. Adjusted p-values (Tukey's correction) for simple effects are listed in Tables 3 and 4 in the Appendix. Simple effects tests for "type of HEK293 cells" comparing (i) RyR2 only, (ii) RyR2 + TRIC-A, and (iii) RyR2 + TRIC-B are indicated by asterisks (*: $p < 0.05$; **: $p < 0.01$; ***: $p<0.001$; ****: $p<0.0001$). Values are of the mean ± SEM, N was labelled above each group RyR2 gating.

B

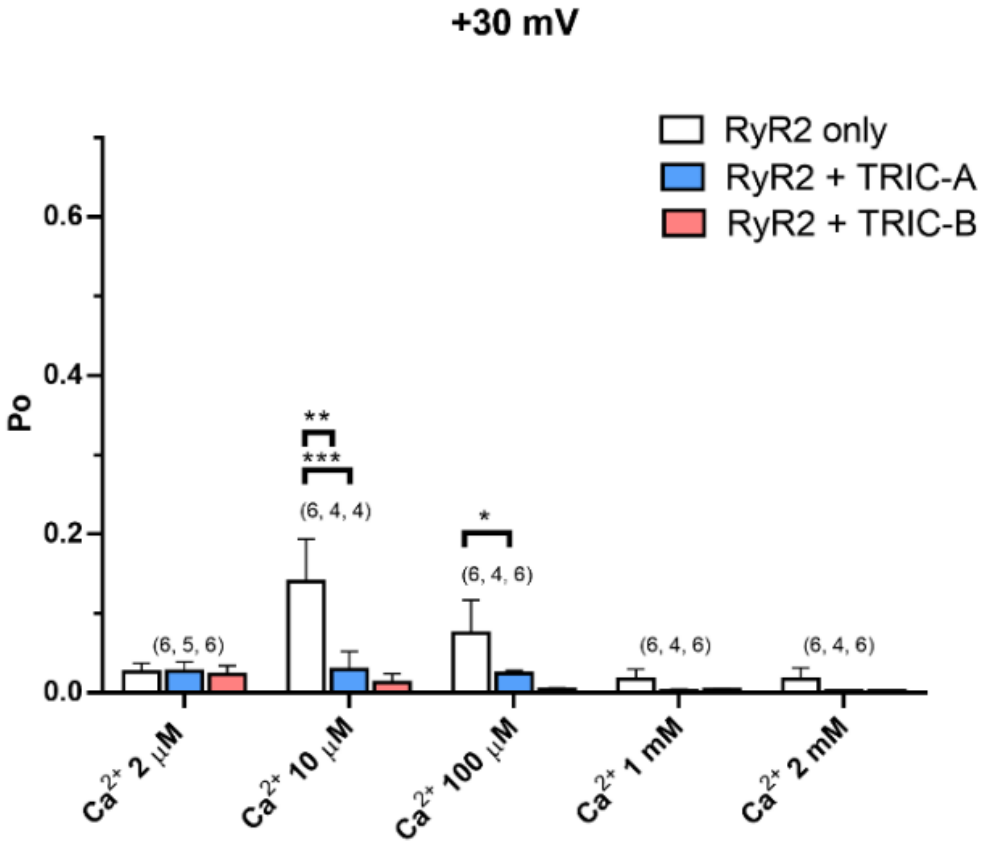



**Figure 4.6 The co-expression of TRIC-A or TRIC-B with RyR2 affects RyR2 Po over a range of cytosolic [$Ca^{2+}$] at +30 mV**

Effect of holding potential (-30 mV on the top; +30 mV on the bottom) on the relationship between [$Ca^{2+}$] and Po for RyR2 derived from HEK293 cells expressing RyR2-only (black), RyR2+TRIC-A (blue) and RyR2+TRIC-B (red). Two-way ANOVA for with two independent variables: 1) "cytosolic [$Ca^{2+}$]", and 2) "type of HEK293 cells". For the -30 mV on the left: interaction effect for "cytosolic [$Ca^{2+}$]" by "type of HEK293 cells" p =0.0035; main effect of "cytosolic [$Ca^{2+}$]", $p < 0.0001$; main effect of "type of HEK293 cells", $p < 0.0001$. Adjusted p-values (Tukey's correction) for simple effects are listed in Tables 1 and 2 in the Appendix. For the +30 on the right: interaction effect for "cytosolic [$Ca^{2+}$]" by "type of HEK293 cells", p = 0.1222; main effect of"cytosolic [$Ca^{2+}$]", p =0.0394; main effect of "type of HEK293 cells"; p = 0.0028. Adjusted p-values (Tukey's correction) for simple effects are listed in Tables 3 and 4 in the Appendix. Simple effects tests for "type of HEK293 cells" comparing (i) RyR2 only, (ii) RyR2 + TRIC-A, and (iii) RyR2 + TRIC-B are indicated by asterisks (*: $p < 0.05$; **: $p < 0.01$; ***: $p<0.001$; ****: $p<0.0001$). Values are of the mean ± SEM, N was labelled above each group RyR2 gating.

Figure 4.7 shows a typical example of this voltage-dependent inactivation in a bilayer where vesicles from cells co-expressing RyR2+TRIC-B had been incorporated. In this experiment, seven RyR2 channels were incorporated into the bilayer and the steady-state gating of the channels can be observed at -30 mV. After the holding potential was changed to +30 mV, the individual channels were inactivated one by one as indicated by orange arrows. These channels did not open again until the voltage was switched back to -30 mV when Po reverted back to the usual gating at -30 mV.

Observation of individual RyR2 channel inactivation events could not always be monitored. This is because when vesicles from cells co-expressing TRIC-A or TRIC-B were fused with the bilayers, there were often non-RyR2 current fluctuations that interfered with our measurements and obscuring inactivation events. However, in those traces where RyR2 gating was clear, we measured the time for each channel in the bilayer to inactivate in all three experimental groups. Not all RyR2 channels in each bilayer inactivated at +30 mV, so we also counted the number of channels in each bilayer that inactivated and the number that did not inactivate. Only 54% (15 of 28 channels) of channels in RyR2-only group inactivated following the voltage-switch in comparison to 79% (15 of 19 channels) of channels in RyR+TRIC-A group and 69% (18 of 26 channels) of channels in RyR2+TRIC-B group. For those channels that did inactivate, a cumulative plot of the number of inactivated channels against the time to the inactivation was constructed as shown in Figure 4.8.

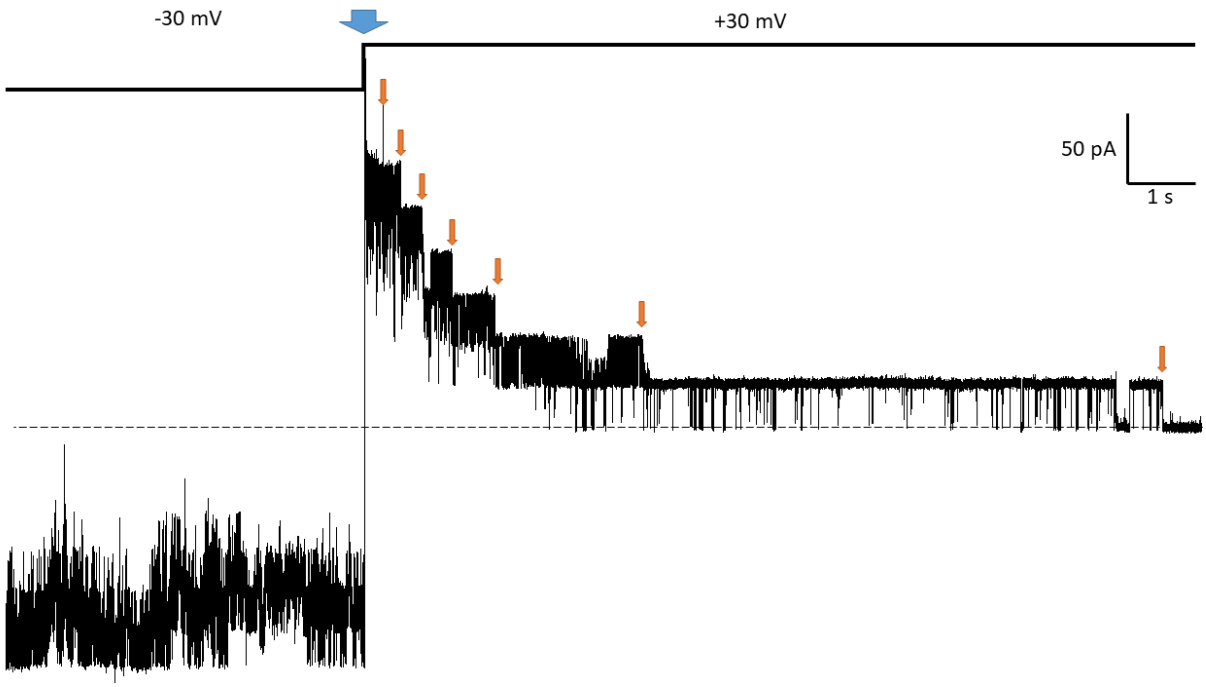



**Figure 4.7 Voltage-dependent inactivation of multiple RyR2 channels at +30 mV**

Example of the voltage-dependent inactivation of RyR2 channels that results from switching the holding potential from -30 mV to +30 mV in a bilayer where multiple RyR2 channels were gating prior to the voltage change. The blue arrow indicates the time of voltage change and the orange arrows indicate the times of individual channel inactivation. The dashed line indicates 0 pA. Solutions were symmetrical 210 mM KPIPES solutions with 100 µM cytosolic [$Ca^{2+}$]. This is an example of RyR2 channels from HEK293 cells expressing RyR2 + TRIC-B.

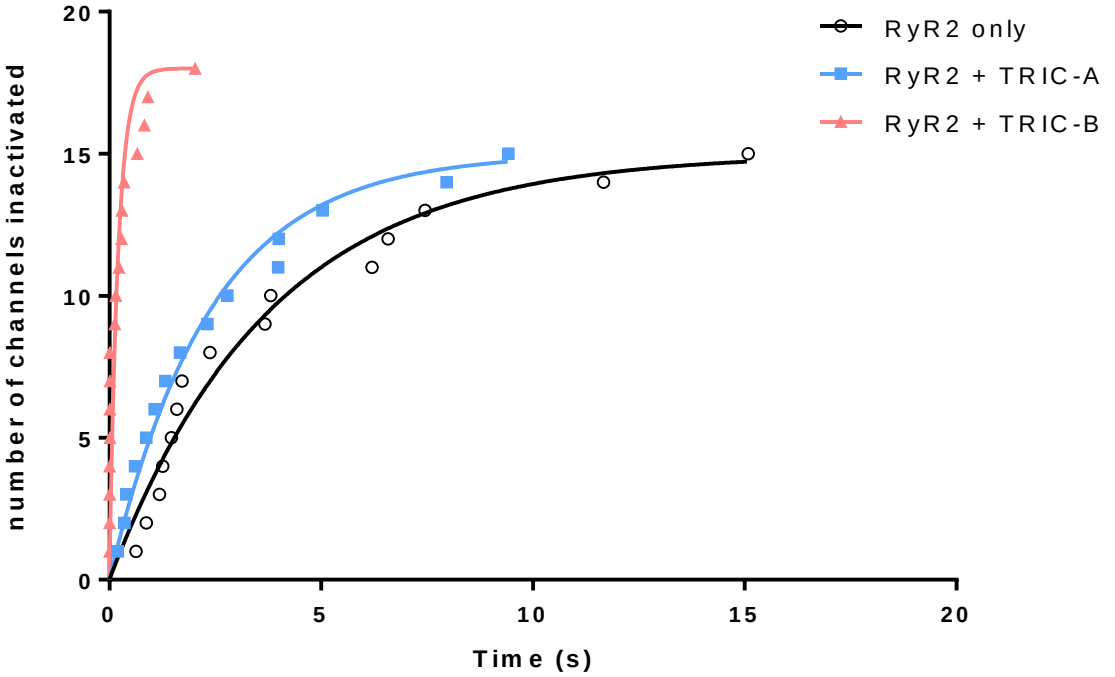



**Figure 4.8 Co-expressing TRIC-A or TRIC-B with RyR2 increases the rate of voltage-dependent inactivation of RyR2 channels**

The time at which RyR2 channels were inactivated after changing holding potential from -30 mV to +30 mV is shown for experiments where RyR2-only (black), RyR2+TRIC-A (blue) and RyR2+TRIC-B (red) co-expressed in HEK cells. The curves were fitted according to the equation: $y = n(1 - e^{-kt})$ where t=time in s, n is the number of channels and k is the rate constant. n and k were 15 and 0.264 for RyR2-only, 15 and 0.422 for RyR2+TRIC-A and 18 and 4.89 for RyR2+TRIC-B. The time for half channels to become inactivated ($t_{1/2}$) was 2.62 s, 1.64 s and 0.14 s for RyR2-only, RyR2+TRIC-A and RyR2+TRIC-B, respectively.

Data points of each RyR2 group in the plot was fitted by a one-phase-decay curve fitting. The fitting equations of curves in these three different RyR2 groups were as following:

RyR2 group $y = 15(1 - e^{-0.264t})$;

RyR2 + TRIC-A group $y = 15(1 - e^{-0.422t})$;

RyR2 + TRIC-B group $y = 18(1 - e^{-4.89t})$.

According to the non-linear fitting, the half-life of RyR2, RyR2 + TRIC-A and RyR2 + TRIC-B groups is 2.62 s, 1.64 s, 0.14 s, respectively. It can be noted that the rate of RyR2 inactivation would be higher while the half-life of inactivation becomes lower when TRIC-A and TRIC-B are co-expressed with RyR2.

### 4.2.5 Sub-conductance state of RyR channels with TRIC-A or TRIC-B co-expressed

In a close inspection of the single-channel traces (Figure 4.2), we observed occasional gating into sub-conductance states in Figure 4.2A at -30 mV (2 μM cytosolic $Ca^{2+}$ in the RyR2+TRIC-A and RyR2+TRIC-B traces) and in Figure 4.4 at -30 mV (10 μM $Ca^{2+}$ in the RyR2+TRIC-A trace). There are very brief gating events for RyR2 channels and the duration of the majority of events is close to the minimum resolvable sub-conductance events. We therefore investigated if co-expression of TRIC channels was associated with an alteration in frequency of sub-conductance states by counting only those sub-conductance states that were ≥2 ms to avoid misclassifying rapid gating as sub-conductance events. We chose to count the events under a suitable cytosolic $Ca^{2+}$ concentration where Po was high enough and single-channel traces were clean to observe

sub-conductance events. After comparing the traces in different cytosolic $Ca^{2+}$ groups, we found 10 μM cytosolic $Ca^{2+}$ to fit our aims since there were too many channels in the bilayer with cytosolic [$Ca^{2+}$] higher than 10 μM and also there were not enough sub-conductance events with cytosolic [$Ca^{2+}$] lower than 10 μM. Figure 4.9 shows that the frequency of sub-conductance events was lower than 1 event per min on average in the RyR2-only channel group. Although there was a trend towards more sub-conductance events when either TRIC-A or TRIC-B was co-expressed, it was statistically significant only when TRIC-A was co-expressed.

### 4.2.6 Investigation into the ion permeability of channels from the HEK cell preparations of co-expressed TRIC-A or TRIC-B

To investigate the permeability properties of the incorporated TRIC channels from our HEK cell membrane preparations, we fused as many vesicles as possible into each bilayer in an attempt to incorporate a lot of channels in gradient solutions of 740 mM KCl cytosolic:210 mM KCl luminal. The sub-conductance and rapid gating behaviour of the TRIC channels makes it impossible to measure the $E_{rev}$ of a single channel, hence we reasoned that the Erev of multiple channels would be more a more accurate estimation. To each bilayer, we applied a voltage ramp from -50 mV to +50 mV to determine the $E_{rev}$ of each bilayer. Figure 4.10 shows representative examples of the different ramp currents obtained from vesicles of the HEK cell preparations with RyR2 only, RyR2+TRIC-A and RyR2+TRIC-B. In each experiment, we performed triplicate ramps

and averaged the $E_{rev}$ values and these are shown in Figure 4.11. As we observed little current that was not due to RyR2 in the RyR2-only preparations, $E_{rev}$ was very dependent on whether the RyR2 channels in the bilayer were opening during the ramp (Figure 4.10). If they were open, $E_{rev}$ was close to the calculated $E_{rev}$ for $K^+$ (-32 mV in the 740/210 mM cytosolic/luminal KCl), as RyR2 is ideally selective for cations (Lindsay, Manning, and Williams 1991). If the RyR2 channels were closed, the small residual currents exhibited $E_{rev}$s that suggested that the HEK membranes also contain other ion channels that have permeability to $Cl^-$ and to $K^+$ or to both.

RyR2 made a smaller contribution to the overall currents when vesicles from HEK cells expressing RyR2+TRIC-A or RyR2+TRIC-B were fused with the bilayer as can be seen in the example ramp currents in Figure 4.10. Figure 4.11 shows that $E_{rev}$ was usually not near the calculated $E_{rev}$ for an ideally selective $K^+$ channel (-32 mV) or $Cl^-$ channel (+32 mV) indicating that the extra type of channel (TRIC-A or TRIC-B) that incorporated into the bilayer along with RyR2 was one that was permeable to both $K^+$ and $Cl^-$. It was especially apparent that the bilayers containing RyR2+TRIC-B exhibited an $E_{REV}$ that was closer to the calculated $E_{rev}$ for ideally selective $Cl^-$ channels than for $K^+$ channels suggesting that TRIC-B may be more permeable to $Cl^-$ than $K^+$.

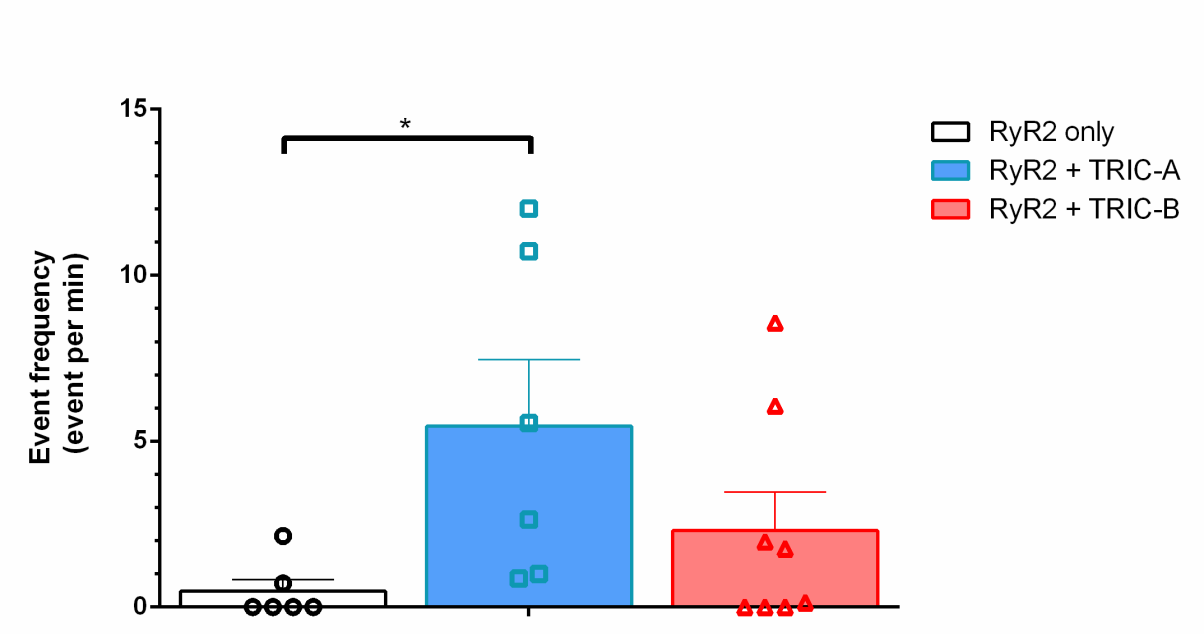



**Figure 4.9 Effect of co-expressing TRIC-A or TRIC-B with RyR2 on sub-conductance frequency**

Bar chart showing the frequency of sub-conductance open events >2 ms in duration at 10 µM cytosolic free [$Ca^{2+}$] at -30 mV, in the same solutions as in Figure 2, for RyR2 derived from HEK293 cells expressing RyR2-only (black), RyR2+TRIC-A (blue) and RyR2+TRIC-B (red). The Kruskal-Wallis test for one independent variable, type of HEK293 cell, $p = 0.0271$. Post-hoc multiple comparison with Dunn's correction: Significant difference between the event frequency of RyR2 derived from HEK293 cells expressing RyR2-only or cells expressing RyR2 + TRIC-A is indicated by * for $p = 0.0287$. Symbols indicate values from individual experiments and bars show mean ± SEM.

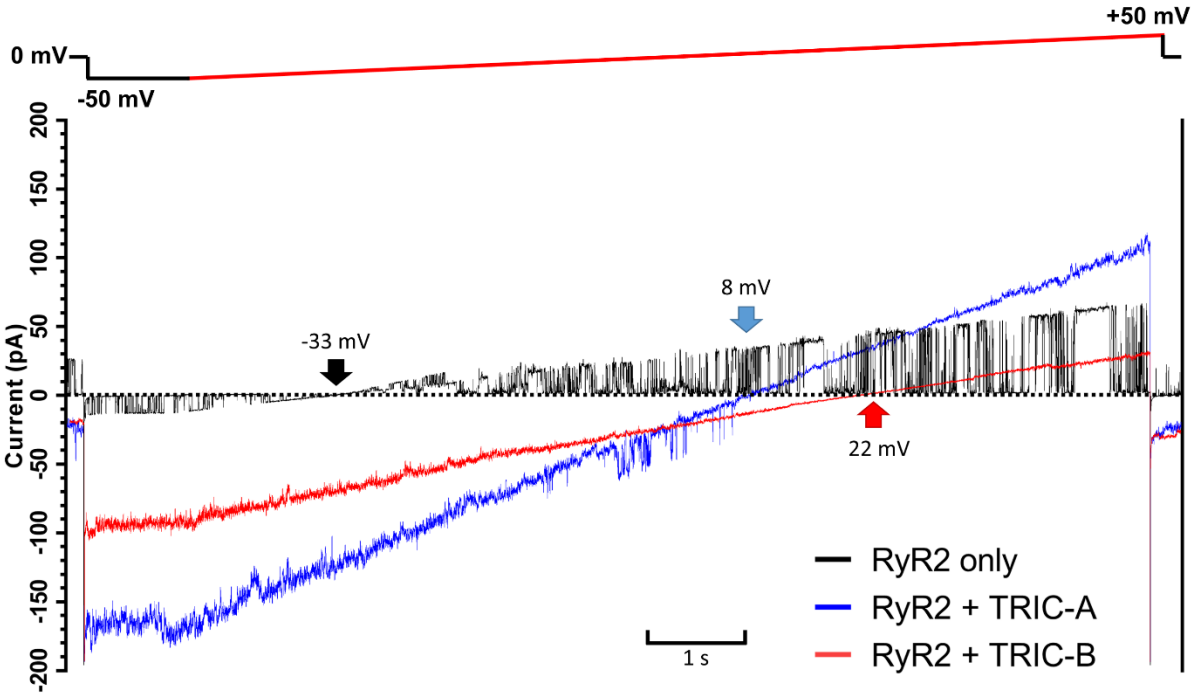



**Figure 4.10 Typical current fluctuation of channels from HEK cell preparations co-expressing TRIC-A or TRIC-B with RyR2 by voltage ramps**

Representative currents from individual bilayer experiments after incorporating vesicles from HEK293 cells expressing only RyR2 (black), co-expressing RyR2+TRIC-A (blue) or co-expressing RyR2+TRIC-B (red) into the bilayer. Vesicles were incubated with the bilayer for 5-10 min in 740 mM cytosolic :210 luminal mM KCl gradient to allow many fusion events (evidenced by step changes in conductance) to occur. Vesicle fusion was halted by perfusing the cytosolic chamber with 210 mM KCl. The 740 mM cytosolic :210 mM luminal KCl gradient was then reapplied. The bilayers were held at 0 mV and then switched to -50 mV for 1 s before applying the voltage ramp (red) from -50 mV to +50 mV. The black (RyR2-only), blue (RyR2+TRIC-A) and red (RyR2+TRIC-B) arrows indicate the $E_{rev}$ for that bilayer.

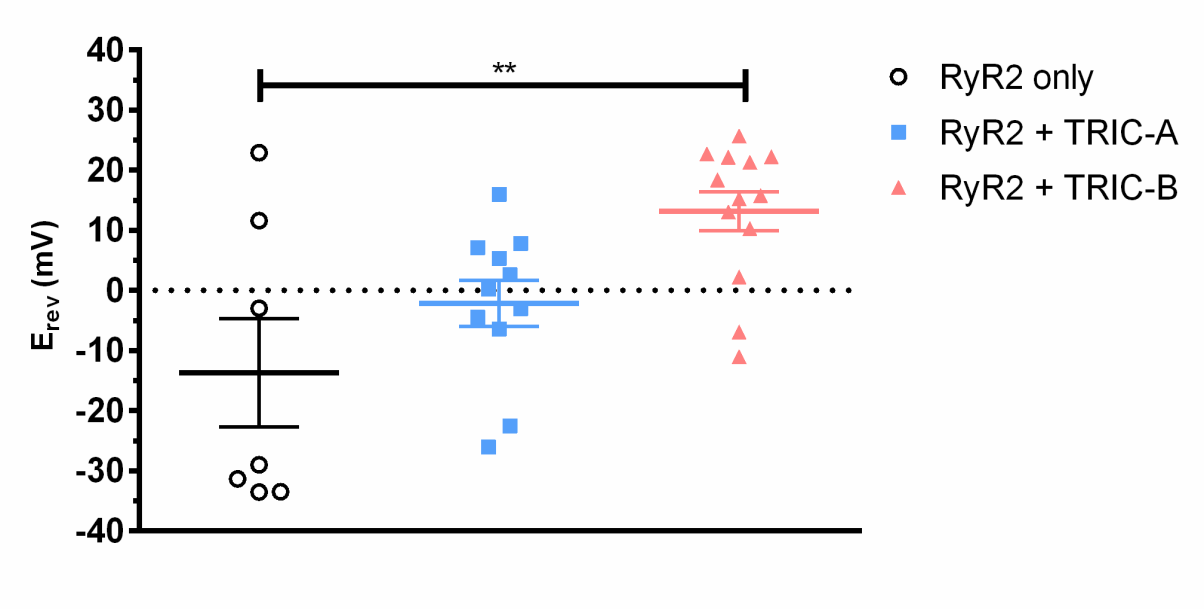



**Figure 4.11 Effects of co-expressing TRIC-A or TRIC-B with RyR2 on the Erev of the currents elicited by voltage ramps**

Ramp currents were obtained in triplicate for each bilayer and the mean $E_{rev}$ values for each bilayer are shown for RyR2-only (black circles; $n = 7$), RyR2+TRIC-A (blue squares; $n = 11$) and RyR2+TRIC-B (red triangles; $n = 13$) vesicle preparations. One-way ANOVA: $p = 0.0026$. Post-hoc multiple comparison with Tukey's correction: significant differences between RyR2 only and RyR2 + TRIC-B vesicle preparations are indicated by ** for $p = 0.0025$. No significant difference between the RyR2 only and RyR2 + TRIC-A, $p = 0.2840$, and between the RyR2 + TRIC-A and RyR2 + TRIC-B vesicle preparations, $p = 0.0561$. Symbols indicate values from individual experiments and bars indicate mean ± SEM.

### 4.2.7 Current fluctuation comparison between the channels incorporated from TRIC-A/TRIC-B co-expressed RyR2 HEK293 cells and normal SR $K^+$ channel

As mentioned in the introduction, it was suggested that TRIC-A or TRIC-B played the role of SR $K^+$ channel on SR to provide counter currents with $K^+$ ions. To compare these channels, Figure 4.12 showed representative traces of single-channel gating that were observed when TRIC-A (Figure 4.12B) or TRIC-B (Figure 4.12C) were co-expressed with RyR2 and when previous SR $K^+$ channel were incorporated under identical experimental conditions. Figure 6A shows a typical example of SR $K^+$ channel gating from mouse skeletal muscle at +30 mV in symmetrical solutions of 210 mM KPIPES, 2 μM free [$Ca^{2+}$], at pH 7.2, where the recording conditions are the same for Figure 4.12B and Figure 4.12C. It can be seen that these single-channel gating events bear little resemblance to the full opening of the SR $K^+$ channel. In the current study, incorporation of vesicles from the HEK293 cells into bilayers were performed without use of detergents or lengthy, harsh purification procedures, there was still no observation of any channel events similar to the full opening events of the mouse SR $K^+$ channel exemplified in Figure 4.12. These data, coupled with the data suggesting that TRIC channels are non-selective ion channels, support the idea that neither TRIC-A nor TRIC-B is the SR $K^+$ channel.

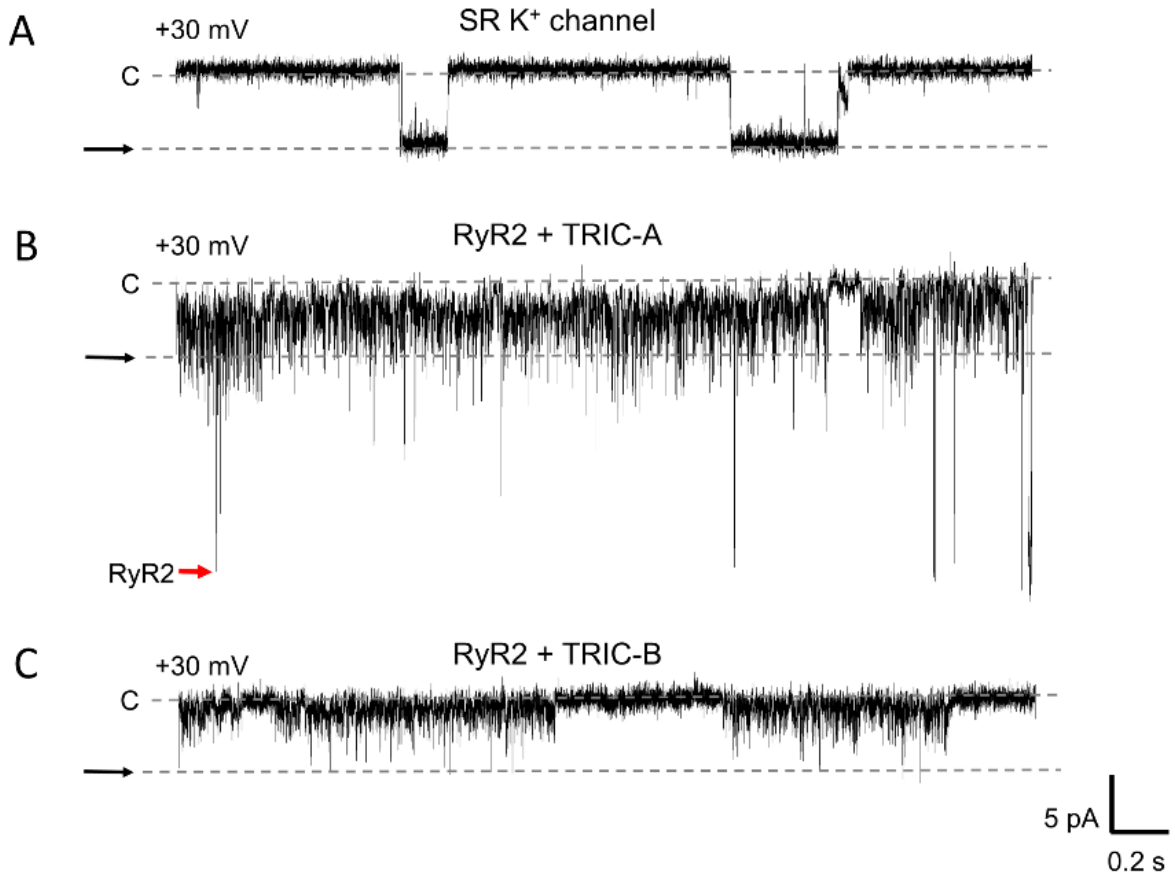



**Figure 4.12 Comparison of mouse skeletal SR $K^+$ single-channel events with those derived from HEK293 cell vesicles co-expressing TRIC-A or TRIC-B with RyR2**

(A) Typical SR $K^+$ channel openings observed after incorporating mouse skeletal muscle SR vesicles into bilayers in 210 mM KPIPES, 2 µM free [$Ca^{2+}$] at the holding potential of +30 mV. (B) Example of the variable and erratic currents observed after incorporating vesicles from HEK293 cells co-expressing RyR2+TRIC-A under the same experimental conditions as in (A). Note that a RyR2 channel is also incorporated into this bilayer (indicated by red arrows). (C) Example of one of the types of currents observed after incorporating vesicles from HEK293 cells co-expressing RyR2+TRIC-B under the same experimental conditions as in (A). RyR2 channel gating can also be observed. C represents the zero current level. The black arrows and dashed line indicate the current amplitude of a fully open mouse SR $K^+$ channel for comparative purposes.

## 4.3 Discussion

The results from our experiments provide new information that suggest (i) that TRIC-A and TRIC-B alter RyR2 gating by somehow interacting directly with the channels or via a protein tightly bound to RyR2 and (ii) suggest that TRIC channels may be non-selective ion channels, permeable to both anions and cations.

In Figure 4.3, it can be seen that co-expression of TRIC-A or TRIC-B together with RyR2 in HEK293 cells does not influence the single-channel conductance of RyR2 when monitored after incorporation into bilayers but it does affect channel gating suggesting that both TRIC-A and TRIC-B interact with RyR2. It is important to notice that the co-expression of TRIC channels altered voltage-dependence of RyR2 gating. Although channel inactivation of RyR2 does take place at +30 mV in those experiments where TRIC channels are absent, this does not significantly reduce steady-state RyR2 Po at any cytosolic [$Ca^{2+}$] (Figure 4.6). In contrast, steady-state RyR2 Po at +30 mV is lower than that at -30 mV at all cytosolic [$Ca^{2+}$] if TRIC-A or TRIC-B is present. This voltage-dependence of Po is particularly obvious at 10, 100 and 1000 µM $Ca^{2+}$ and, notably, the inactivation of RyR2 by TRIC-B is very rapid (Figure 4.6). At these [$Ca^{2+}$], TRIC-A stimulation of RyR2 at -30 mV is very marked and is significantly more effective than TRIC-B stimulation. Overall, therefore, the presence of TRIC-A may be expected to potentiate RyR2 activity, whereas it is more difficult to determine the effect of TRIC-B. These results are thus consistent with those of a report (Zhou et al. 2020), where $Ca^{2+}$ spark frequency was shown to be reduced in cardiomyocytes from *Tric-a* KO mice, and

delayed onset of $Ca^{2+}$ transients and time-to-peak amplitude of the transients were also observed.

It is well-known that RyR channels exhibit voltage-dependent inactivation (Percival et al. 1994; Ma and Zhao 1994; Sitsapesan, Montgomery, and Williams 1995; Laver and Lamb 1998; Hill and Sitsapesan 2002). It is, however, not understood how this inactivation contributes to the physiological regulation of $Ca^{2+}$ release during EC-coupling. It has always been assumed, since the Garcia & Miller report (1984) (Garcia and Miller 1984), that there will be no large potential change across the SR during the $Ca^{2+}$ release process because of the rapid flux of counter ions, and more recent experimentation has not contradicted this (e.g Sanchez-Fernandez et al. 2018 (Sanchez-Fernandez et al. 2018)). We cannot, however, rule out the possibility that very brief potential changes do occur and that the voltage-sensing RyR2 channels respond with a change in gating. The physiological relevance of this intrinsic property of RyR2 is therefore likely to be important for controlling the time to inactivation of the $Ca^{2+}$ transient so that the SR can refill during diastole. Further experiments needed to explore how this particular property of RyR2 channels is integrated with the other gating characteristics of RyR2 to provide an efficient $Ca^{2+}$-release process from the SR in the heart.

If the single-channel properties of RyR2 can be regulated by the physical interaction with TRIC-A or B, one might expect a reciprocal effect on the TRIC channels such that their correct functioning as ion channels depends on the presence of a $Ca^{2+}$-release

channel. Hence the co-expressing of RyR2 with TRIC channels in HEK293 cells may provide a necessary stabilising effect for TRIC channel function. Bilayer incorporation of membrane vesicles from HEK293 cells co-expressing TRIC-A or TRIC-B with RyR2 generally resulted in bilayers conducting more current than those where vesicles from HEK293 cells expressing only RyR2 were incorporated, as shown in the representative traces in Figure 4.10. These currents were not due to RyR2 and were difficult to characterise. This is because the current amplitudes of the individual channel openings were small and difficult to accurately monitor because of the large noise of the bilayer system and because open and closing events were brief and hence not fully resolved. Recordings from previous reports of purified TRIC channel conductance and gating behaviour also reveal these problems (Yazawa et al. 2007; Pitt et al. 2010; Su et al. 2017). Moreover, if TRIC channels gate into sub-conductance open states as these reports also suggest, then the reliable characterisation of the gating and conductance properties of single TRIC channels becomes more problematic. Hence our aim of incorporating multiple channels into bilayers in order to investigate if TRIC channels are selectively permeable to cations.

According to Figure 4.10 and Figure 4.11, variable $E_{rev}$ was obtained for the bilayers where RyR2 channels were closed, suggesting that the HEK membranes also contain other ion channels that have permeability to $Cl^-$ and to $K^+$ or to both. RyR2 made a smaller contribution to the overall currents when vesicles from HEK cells expressing RyR2+TRIC-A or RyR2+TRIC-B were fused with the bilayer as can be seen in the example ramp currents in Figure 4.10. Figure 4.11 shows that $E_{rev}$ was usually not near

the calculated $E_{rev}$ for an ideally selective $K^+$ channel (-32 mV) or $Cl^-$ channel (+32 mV). $E_{rev}$ of bilayers containing TRIC-A or TRIC-B was far from the $E_{rev}$ expected for cation-selective channels (without counting the contribution of $E_{rev}$ from the gating of RyR2 channels to the total current), and suggests that the TRIC channels may be permeable to both $K^+$ and $Cl^-$. It was especially apparent that the bilayers containing RyR2+TRIC-B exhibited an $E_{rev}$ that was closer to the calculated $E_{rev}$ for ideally selective $Cl^-$ channels than for $K^+$ channels suggesting that TRIC-B may be more permeable to $Cl^-$ than $K^+$. The results also suggest that TRIC-B channels may be more permeable to $Cl^-$ than TRIC-A. These properties will still enable TRIC channels to be efficient pathways for counter-ion current across the SR. In fact, the ability to act as a pathway for both anions and cations would be expected to provide a more flexible counter-ion current that is suitable for a wider variety of cell types. In this regard, it is interesting that TRIC-B is present in many cell types (Yazawa et al. 2007) where perhaps the need for $Cl^-$ flux is greater than that for $K^+$ flux, whereas excitable cells tend to have high quantities of TRIC-A to support the larger SR $Ca^{2+}$ release events that occur predominantly via RyR channels.

In conclusion, our results suggest that TRIC-A and TRIC-B may exert complementary roles in directly regulating RyR2 gating during EC-coupling. It also suggests that TRIC-A and TRIC-B bind to RyR2 channels and subsequently alter gating. TRIC-A, however, appears to play a greater stimulatory role than TRIC-B. There is also the need for further detailed biophysical examination of the gating and conductance properties of purified TRIC channels and identification of the unknown $Cl^-$ channels in muscle SR. If

TRIC channels are indeed permeable to both $K^+$ and $Cl^-$ as our results suggest, this property will bring the possibility that both TRIC-A and TRIC-B provide counter-ion currents of $K^+$ and $Cl^-$ to balance $Ca^{2+}$ movements across the SR while TRIC-A provides a greater proportion of $K^+$ current than TRIC-B. We will explore the effect of TRIC channel expression on the RyR2 in the next chapter. We hope that our study will direct further effort into the difficult task of characterising the biophysical properties of TRIC channels in more detail and the mechanisms of how they affect RyR2 gating.

# Chapter 5 Development of a cardiac-specific *Tric-a* knock out mice colony

## 5.1 Introduction

Apart from their role in cardiac myocytes (as previously discussed), TRIC channels regulate ER/SR $Ca^{2+}$-release in other tissues where they are expressed (Yamazaki et al. 2009; Zhou et al. 2020; Shaheen et al. 2012; Rubinato et al. 2014; Zhao et al. 2010). For example, TRIC-A is expressed in vascular cells in the heart and a *Tric-a* KO mouse was found to exhibit hypertension due to insufficient RyR-mediated $Ca^{2+}$ sparks that led to $Ca^{2+}$-signaling dysregulation in these cells (Yamazaki et al. 2011; Zhao et al. 2010). Consequently, knocking out TRIC-A can cause secondary effects to the cardiac function, rendering experiments on such tissue difficult to interpret. Therefore, I established a cardiac-specific *Tric-a* knock-out (*Tric-a*-cKO) mouse colony to investigate the role of TRIC-A in cardiac function while avoiding any secondary effects due to TRIC-A mediated effects in blood vessels.

In this chapter, I am responsible for the mouse colony breeding design starting from the $tmem38a^{tm1.1}$ (Flox/+) and $A1cf^{Tg(Myh6\text{-}cre/Esr1*)1Jmk}$ (Tg(Cre)/+) colony, genotyping of different mouse genotypes during the breeding, inducing the specific knock-out after establishing the colony, optimization of the inducing protocol, collecting tissues for further experiments, and the RT-qPCR session in the validation of *Tric-a*-cKO colony.

## 5.2 Methods & Results

### 5.2.1 Breeding mouse colony with Cre-Lox recombination system

To investigate the physiological role of TRIC-A in the heart, we aimed to develop a mouse colony with the *Tric-a* gene knocked out (KO) only in hearts. We planned to use the Cre-Lox system to produce inducible cardiac-specific *Tric-a* KO mice. In this system, we introduced two LoxP sites sandwiching the target gene, *Tmem38a* allele (*Tric-a* gene), known as "flanking/flanked by LoxP" (flox) (Hoess, Wierzbicki, and Abremski 1986; Sauer 2002). Then, the floxed gene can be deleted (knock-out) by Cre recombinase, leaving only one LoxP in the original site. The whole process is called Cre-Lox recombination (Sternberg and Hamilton 1981).

Initially, the *Tmem38a*$^{tm1.1}$(Flox/+) mouse colony was generated at the Wellcome Centre for Human Genetics, University of Oxford by Dr Ben Davies' group. This is a service provided by the University of Oxford and was paid for by a grant to R Sitsapesan by the Oxford BHF CRE. Figure 5.1A illustrates the structure of the *Tmem38a* gene, the protein-coding region for TRIC-A channel and the position where two LoxP sites were introduced. Figure 5.1B shows the details of the target insertion region and a schematic of the vector used to insert the LoxP sites. Here, Dr Ben Davies' group used CRISPR/Cas9 technology (Jinek et al. 2012) to achieve the insertion of the vector. To remove the selection cassette introduced together with the vector (FRT flanked neomycin (NEO) selection cassette in Figure 5.1B), mice with the targeted *Tmem38a* allele were

then bred with a Flp recombinase delete strain Tg(ACTB-*Flpe*)9205Dym (Jax stock 005703) to get floxed *Tmem38a*. To obtain the Flox/+ colony, the floxed *Tmem38a* colony with the floxed *Tmem38a* was then bred with the WT C57BL/6J colony to segregate transgene of the Flp recombinase away. This gene-editing process is shown in Figure 5.2A and the validation of floxed mice via gel genotyping is shown in Figure 5.2B.

We then crossed the Flox/+ colony with *A1cf*$^{Tg(Myh6\text{-}cre/Esr1^{*})1Jmk}$ (Tg(Cre)/+) mice from Professor Paul Riley's colony, Department of Physiology, Anatomy & Genetics, University of Oxford. In the Tg(Cre)/+ colony, mice have the cardiac-specific alpha-myosin heavy chain promoter (Myh6) controlling the expression of a tamoxifen-inducible Cre recombinase in the myocyte (Yan et al. 2015). As mentioned, Cre recombinase will knock out the floxed targeted gene, *Tmem38a,* in this case. Figure 5.3 illustrates how we bred the colony and approached the Tg(Cre)/+; Flox/Flox colony. Since a Tg(Cre)/+ mouse will only express Cre recombinase in the cardiac myocytes, we achieved the cardiac-specific *Tric-a* KO (*Tric-a*-cKO) colony genotype. Figure 5.3 shows that we need to breed 3 generations to have a colony that has inducible *Tric-a*-cKO. Then, we bred 8 generations (321 mice) to get enough mice to optimize and validate the induction of the *Tric-a*-cKO phenotype and to collect hearts for further physiological experiments.

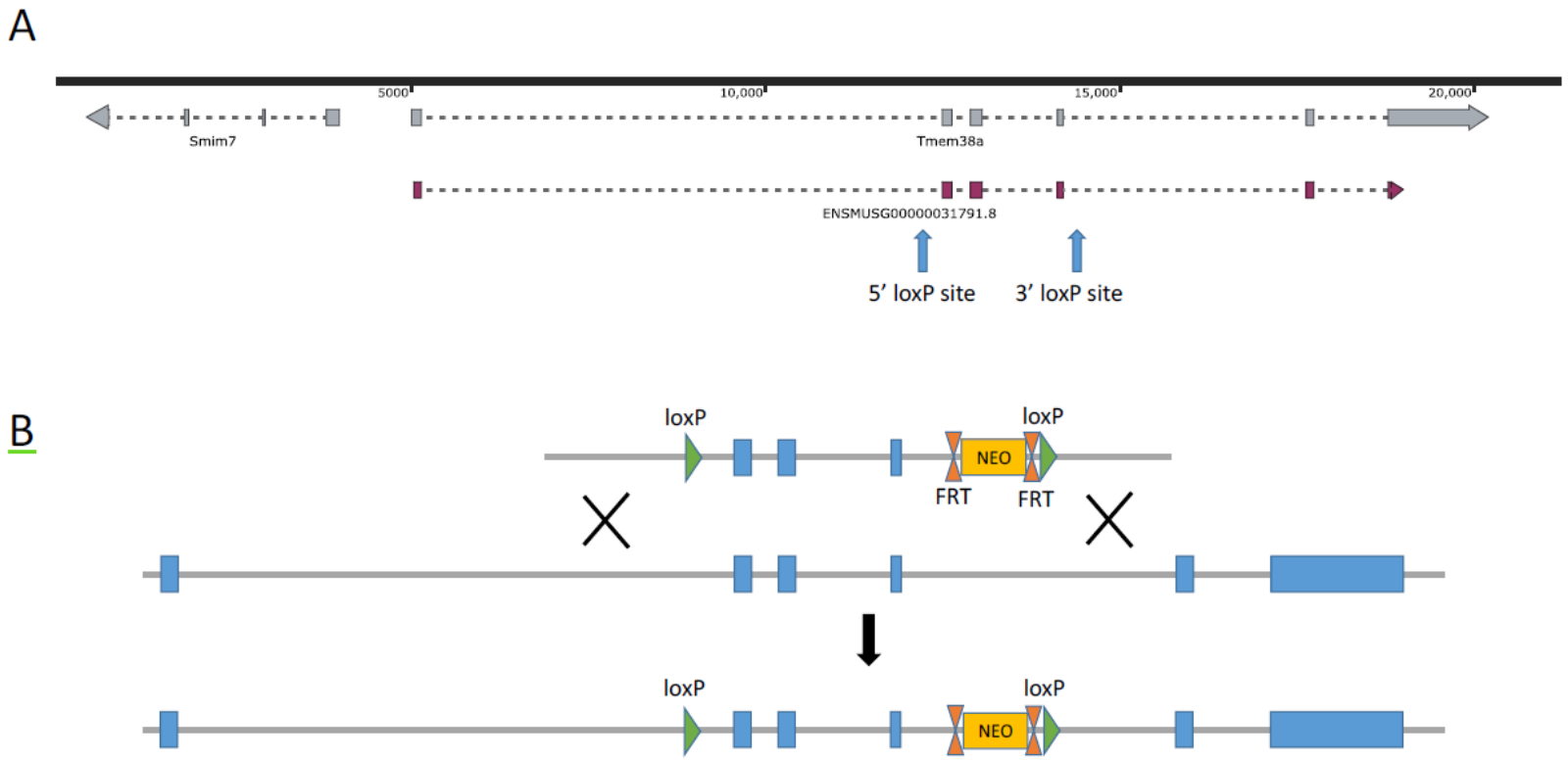



**Figure 5.1 Structure of the *Tric-a* gene coding, *Tmem38a*, and a schematic of gene editing on the gene**

(A) The structure of the *Tmem38a* gene, showing the transcript (in grey) and the protein-coding region (in purple). The positions of the two loxP sites are indicated by blue arrows.

(B) A schematic of the targeting vector used to insert loxP sites within intron 1 and 4. The downstream loxP is associated with an FRT flanked Neomycin selection cassette to allow selection of recombinant clones. This FRT flanked selection cassette can be deleted by the application of Flp recombinase.

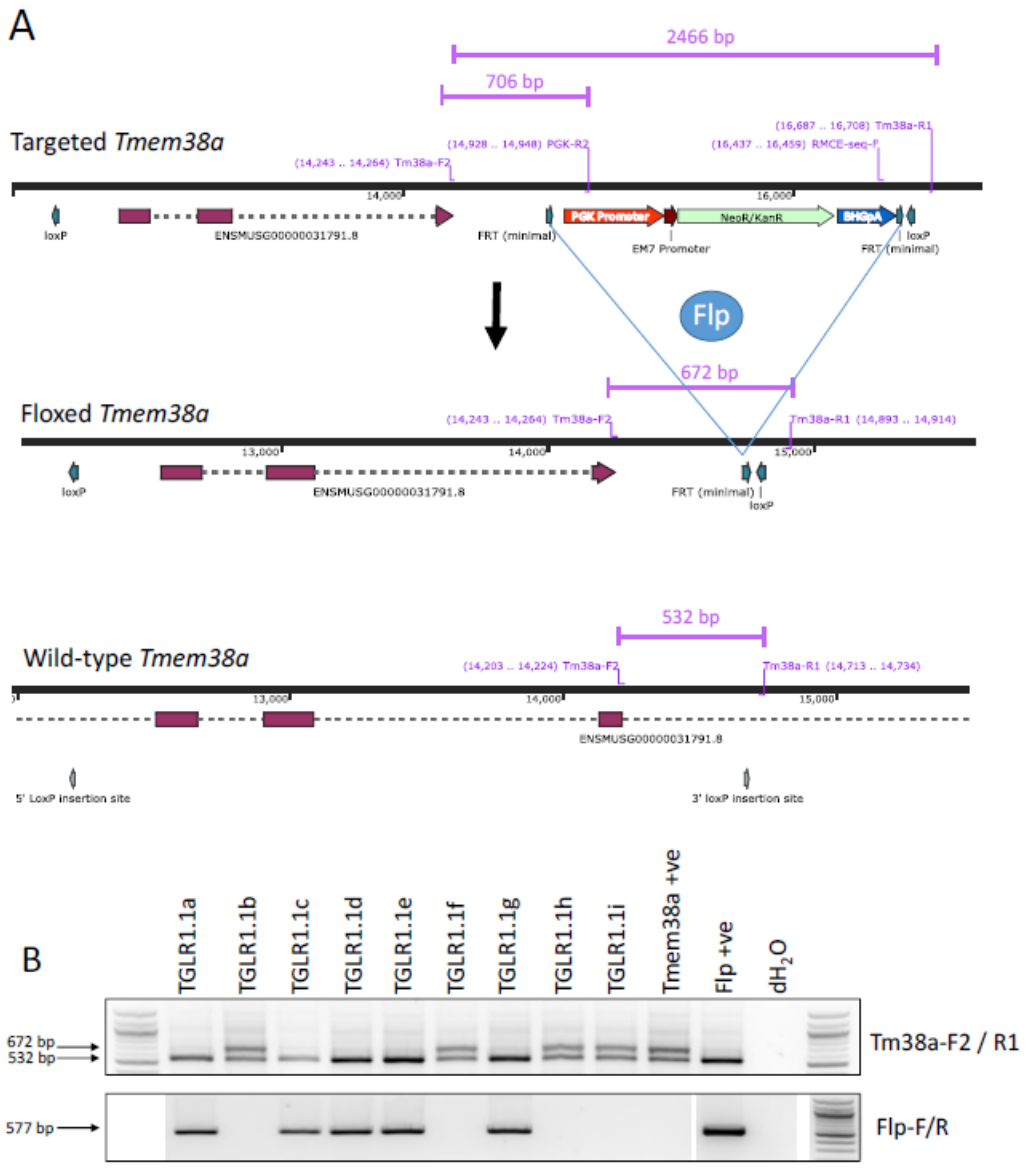



**Figure 5.2 Genotyping of the targeted, Flp deleted, and wild-type gene.**

(A) The 3 types of alleles: (top) the targeting *Tmem38a* with the neomycin selection cassette still present, (middle) the floxed *Tmem38a* allele, with the selection cassette deleted and (bottom) the wild-type *Tmem38a* – are shown, together with the primers used for genotyping.
(B) An example of the genotyping gels obtained showing the generation of multiple floxed mice (top panel) without the inheritance of the Flp recombinase transgene (bottom panel). The example shown is from the mating of a mouse with the correct deletion but harbouring the Flp transgene. All mice were also checked for the presence of the non-deleted *Tmem38a* and all mice were negative for this PCR as expected.

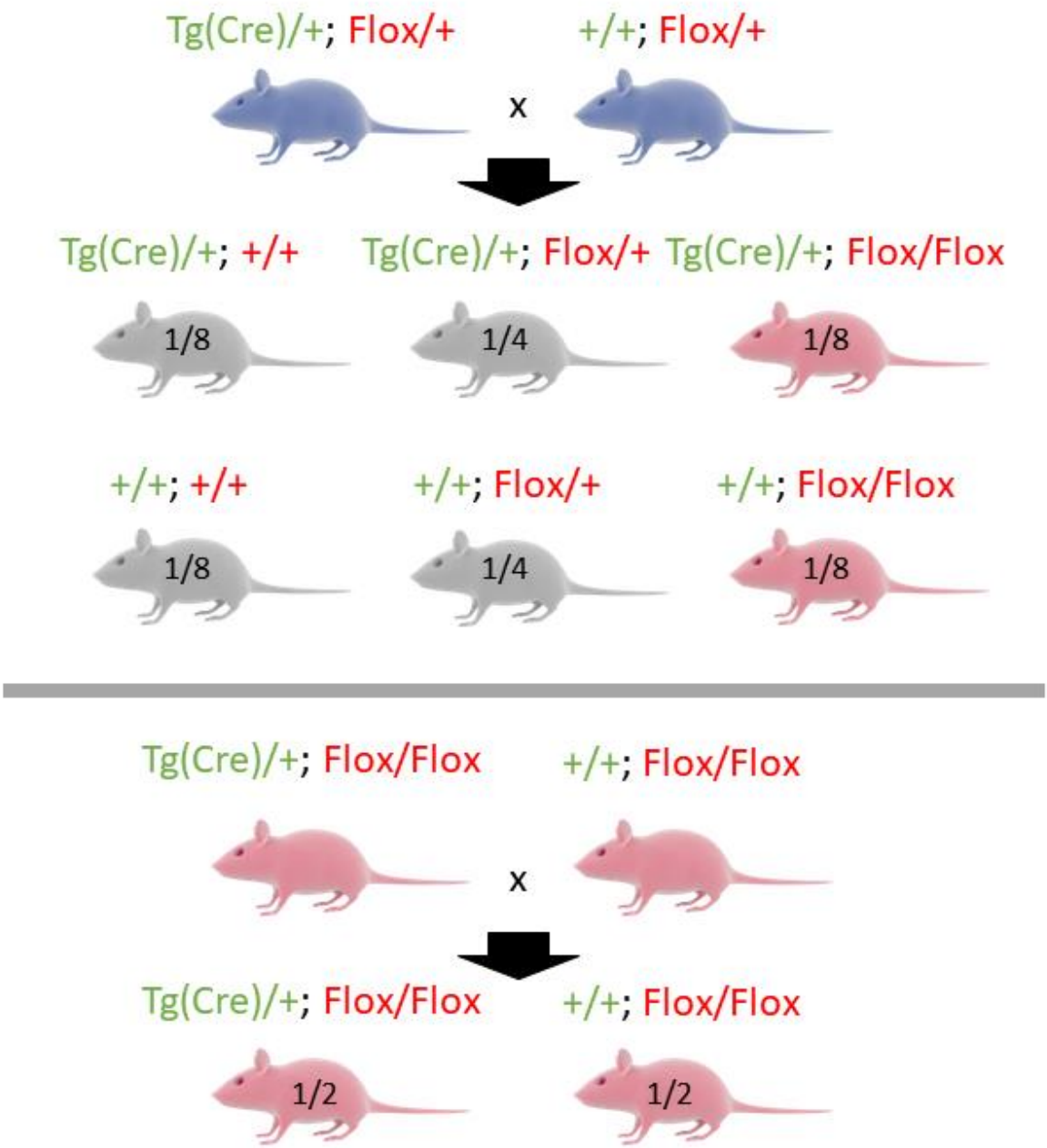



**Figure 5.3 Schematic diagram of the breeding strategy for the cardiac-specific *Tric-a* KO mouse**

The parent colonies with Tg(Cre)/+; Flox/+ (blue) and +/+; Flox/+ (blue) genotype are crossed. The offspring colony is drawn as grey mice (not needed for further breeding) and red mice (needed for further breeding). The second breeding using Tg(Cre)/+; Flox/Flox and +/+; Flox/Flox can continuously give offspring that can induce *Tric-a*-cKO (Tg(Cre)/+; Flox/Flox genotype) as well as mice for the next round of breeding. The genotypes of different mice are labelled above each mouse and the probability of each genotype is labelled on the mice.

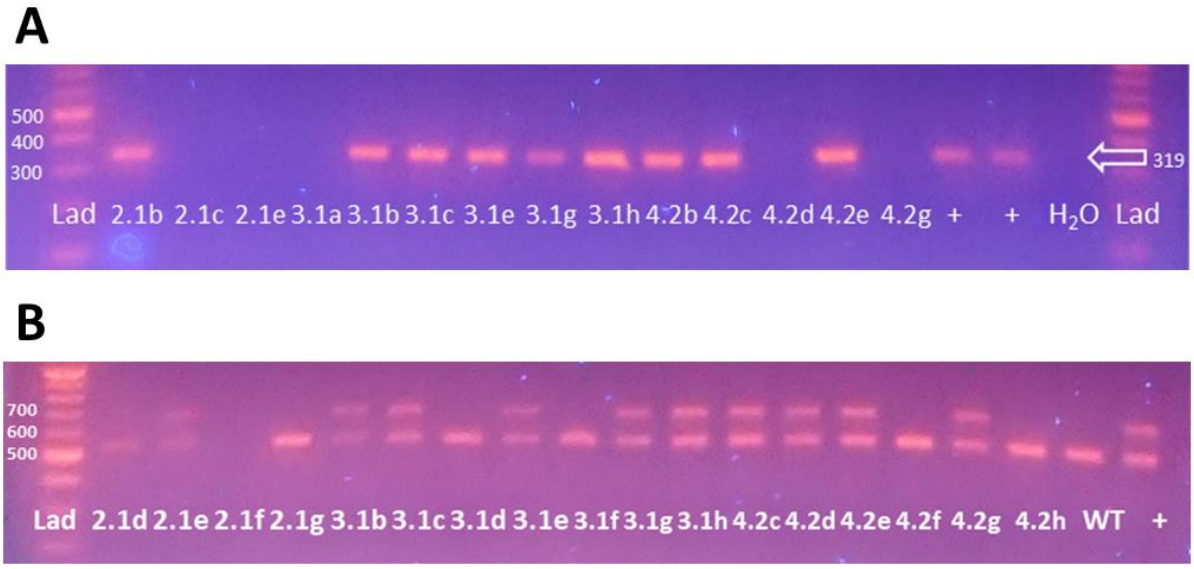



**Figure 5.4 Genotyping gel of Cre and Flox on the colony**

(A) An example of the genotyping gel of Cre gene on the colony by DNA gel electrophoresis. In this case, 14 mice are genotyped for Cre gene by PCR. The gel shows ladders (left and right indicated by Lad), mouse samples (indicated by the code of each mouse under each lane), positive control (mouse with Cre gene and indicated by +) and blank (molecular biology grade DNA-free $H_2O$) in the lanes. The molecular weight of the Cre gene PCR product (319 bp) is indicated by the white arrow.

(B) An example of the genotyping gel of the Flox gene on the same colony by DNA gel electrophoresis. 17 mouse samples are genotyped for the Flox gene by PCR and lanes of DNA gel are loaded with ladders (left, indicated by Lad), mouse samples (indicated by the code of each mouse under each lane), wild-type control (indicated by WT) and positive control (mouse with Flox/+ genotype and indicated by +). The lower band (532 bp) is the molecular-weight size of the wild-type gene PCR product and the upper band (672 bp) is the molecular size of the Flox gene PCR product.

### 5.2.2 Tamoxifen induced knock-out (KO) in the mouse heart

To induce the KO of *Tric-a* in the heart, we injected tamoxifen into the Tg(Cre)/+; Flox/Flox colony. We referred to previous articles before deciding on the concentration of tamoxifen (Bersell et al. 2013) and adopted a tamoxifen concentration that was suggested to induce significant KO in the heart while not developing other cardiac symptoms. To find the lowest effective concentration of tamoxifen for cardiac KO of *Tric-a*, we chose to inject 10-week-old mice with 40 mg/kg tamoxifen for 1 or 4 continuous days. We sacrificed the injected mice at 14 weeks and collected hearts for validation of the degree of *Tric-a* KO. Figure 5.5 shows the *Tric-a* mRNA expression level obtained while Figure 5.6 shows a typical Western blot of TRIC-A protein expression level in the same mouse group. It can be seen that with 4 days of 40 mg/kg tamoxifen, the protein expression level of TRIC-A has been decreased to a significantly low level (~5%) while mRNA expression level is reduced to $< 25\%$. We deduced from these results that the 4x40 mg/kg tamoxifen injection regimen provides a good level of deletion of TRIC-A channel in the heart.

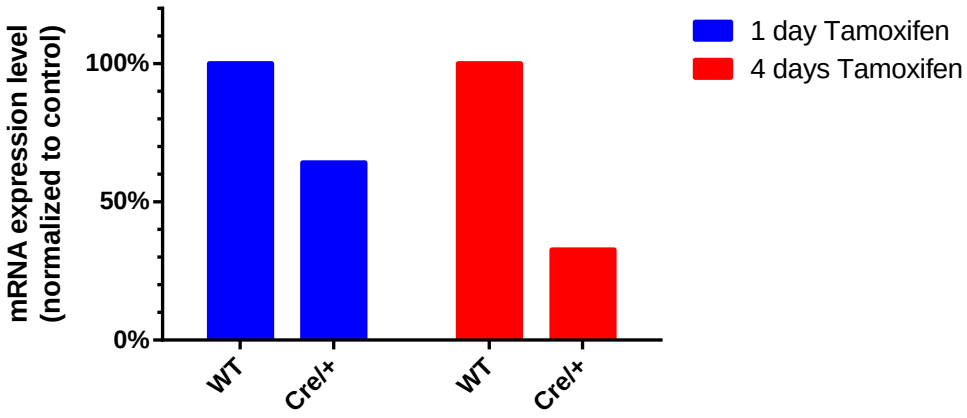



**Figure 5.5 RT-qPCR result of TRIC-A mRNA expression level**

The RT-qPCR result for the level of *Tric-a* mRNA expression in WT and Tg(Cre)/+; Flox/Flox mouse hearts treated with two different concentrations of tamoxifen, 1 day with 40 mg/kg and 4 days with 40 mg/kg tamoxifen. The assay result is based on 3 repeat values and mean value was calculated by the $\Delta\Delta$Ct method, in order to analyse the relative changes in gene expression from RT-qPCR and normalized according to the expression level of the control group (WT).

We then decided to apply 30 mg/kg tamoxifen for 3 continuous days on 10-week mice. To confirm the expression level of *Tric-a* and related pathways, we measured the mRNA expression level of *Tric-a*, *Tric-b*, *RyR2* in *Tric-a*-cKO mouse hearts as shown in Figure 5.7. It can be seen that the mRNA expression level of *Tric-a* was significantly reduced while that of *Tric-b* was not affected. The mRNA level of *RyR2* showed a decreasing trend but the effect was not statistically significant.

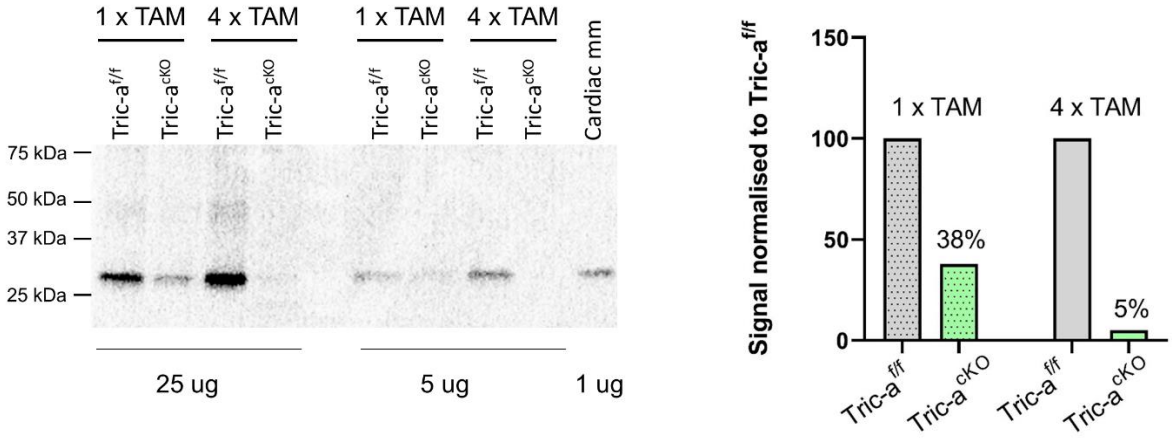



**Figure 5.6 Western-blot of TRIC-A protein expression level (from Dr E. Venturi)**

Western blot result for TRIC-A protein expression level (left) shows the band of TRIC-A (molecular weight~27kDa) with 1-day or 4-day tamoxifen (TAM) injections between control (*Tric-a*$^{f/f}$), Tg(Cre)/+; Flox/Flox (*Tric-a*$^{cKO}$) and wild-type (Cardiac mm) groups. The loading amount of samples are labelled under the lanes. Analysis of TRIC-A protein expression level is shown in a bar chart for control (*Tric-a*$^{f/f}$, grey) and tamoxifen-induced (*Tric-a*$^{cKO}$, green) mouse hearts in two different concentrations of tamoxifen. The values are normalized to the control group (100%). The experiments and figures are contributed by Dr E. Venturi (Sitsapesan lab)

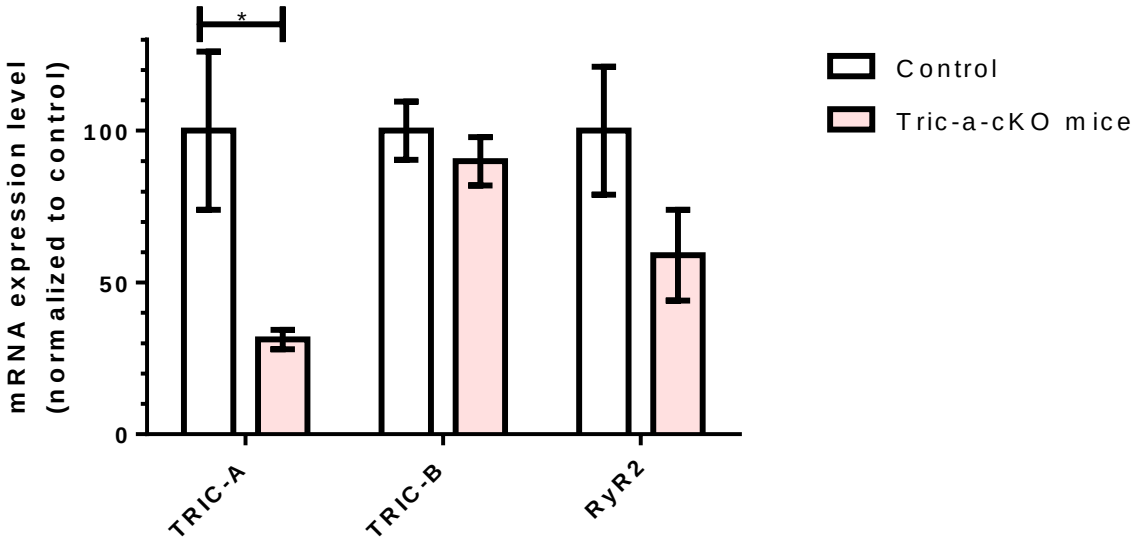



**Figure 5.7 RT-qPCR analysis of Tric-a, Tric-b, and RyR2 mRNA expression level**

RT-qPCR analysis of *Tric-a*, *Tric-b* and *Ryr2* mRNA expression level in WT and *Tric-a*-cKO mouse hearts treated with two concentrations of tamoxifen. Results were obtained in triplicate and were calculated by $\Delta\Delta$Ct method and normalized to the control group (WT). Two-way ANOVA on two variables: (1) individual genes for proteins TRIC-A, TRIC-B and RyR2; (2) tamoxifen treatment. Main effect of tamoxifen is significant different $p = 0.0063$. With simple effect comparison with Bonferroni's correction, TRIC-A mRNA level gives $p = 0.0199$ between control and *Tric-a*-cKO. Values are of mean±SEM, n=7, 5 for control and *Tric-a*-cKO, respectively.

## 5.3 Discussion

In the future, we would like to use the *Tric-a*-cKO colony as a platform to investigate any possible abnormalities to cardiac morphology and function caused by the reduction in TRIC-A protein. Biochemical measurements suggest an approximate ratio of 10 TRIC-A: 2 RyR1: 1 TRIC-B in mouse skeletal muscle SR (Pitt et al. 2010; Zhao et al. 2010). There is 4 times less TRIC-A and TRIC-B in mouse cardiac muscle (Pitt et al. 2010) and [$^3$H]ryanodine binding indicates approximately 8 times less RyR (Witschas et al. 2016) suggesting an approximate ratio of 10 TRIC-A: 1 RyR2: 1 TRIC-B in cardiac muscle. This indicates an especially important role for TRIC in cardiac muscle. Western blot analysis demonstrates that TRIC accumulates more densely in junctional SR so it can be envisaged that RyR2 channels in the dyad are closely positioned near many TRIC-proteins. Thus, the *Tric-a*-cKO colony also provides the opportunity to investigate the biophysical properties of native RyR2 and TRIC-B from mouse hearts after incorporation into bilayers when TRIC-A is no longer the most populous SR cation channel. The *Tric-a*-cKO colony also does not suffer from any possible secondary cardiac changes caused by the vascular problems of knocking out TRIC-A (Yamazaki et al. 2011; Zhou et al. 2020).

To explore the role of RyR2 and TRIC-A in the EC-coupling process, I would like to further assess the protein expression profile in the *Tric-a*-cKO hearts. As shown in Figure 5.5 to Figure 5.7, we can measure and track the protein and mRNA expression level of specific targets by Western blot and RT-qPCR, respectively. Thus, we will probe for

TRIC-A, TRIC-B, RyR2, IP3R, SERCA, PLB, L-type $Ca^{2+}$ channel, CaM, CASQ and NCX1. After the measurement of these targets, we can apply a pathway analysis of these genes/proteins (Kanehisa 2000; von Mering et al. 2005). We can therefore begin to assess how these targets will be affected in genomic and proteomic aspects.

Regarding *Tric-a*-cKO mouse cardiac morphology and function, I would measure end-systolic and end-diastolic pressure and average to calculate parameters of end-diastolic left ventricular posterior wall thickness, left ventricular mass, and fractional shortening. Meanwhile, I will apply *in-vivo* ECG recordings during echocardiographic measurements to monitor cardiac rhythms, RR interval, P wave duration, PR interval, QRS, JT and QT durations both in the basal condition and upon beta-adrenergic stimulation.

To investigate the effect of *Tric-a*-cKO on cardiac physiological properties, I will isolate ventricular cardiac myocytes from *Tric-a*$^{f/f}$ and *Tric-a*$^{cKO}$ hearts using a Langendorff-free method (Ackers-Johnson et al. 2016) with a field stimulation to pace at 1-3 Hz. Whole-cell $Ca^{2+}$ transients will be compared using Fluo-4-AM, a $Ca^{2+}$ fluorescent dye (Liu et al. 2011). In order to assess changes in the SR $Ca^{2+}$-cycling properties, I will monitor spontaneous $Ca^{2+}$-wave characteristics (frequency, propagation velocity and $\tau$ decay) in permeabilised ventricular myocytes isolated from Tric-a $^{f/f}$ and *Tric-a* $^{cKO}$ hearts. To investigate the responses of *Tric-a*$^{cKO}$ myocytes to stress and the incidence of diastolic $Ca^{2+}$ events, isoprenaline will be applied to the myocytes to provide the $\beta$-adrenergic stimulation.

The next steps would be to examine if RyR2 single-channel function is affected in *Tric-a* $^{cKO}$ mice, after incorporating SR vesicles from the hearts of *Tric-a* $^{f/f}$ and *Tric-a* $^{cKO}$

mice into planar lipid bilayers under voltage-clamp conditions as previously described (see Methods and (El-Ajouz, Venturi, and Sitsapesan 2016)). It will also be important to measure and compare the single-channel conductance and gating of other ion channels from the *Tric-a*$^{cKO}$ heart, to understand the single-channel conductance and gating of TRIC-B channels. It may of course be necessary to perform experiments where large quantities of SR vesicles are incorporated into the bilayer if multiple channels are required to calculate Erev (as described in chapter 4 using material from HEK293 cells). Here, investigation of conductance in solutions where $K^+$, $Ca^{2+}$, $Mg^{2+}$ or $Cl^-$ are the only permeant ion will be important and also the use of bionic conditions so that the relative permeability of these ions in the TRIC-B channels can be calculated (Lindsay, Tinker, and Williams 1994; Tinker and Williams 1992; Tinker and Williams 1993).

In summary, we developed a colony with inducible cardiac-specific TRIC-A KO mice using the Cre-Lox recombination approach (Hoess, Wierzbicki, and Abremski 1986; Sauer 2002; Sternberg and Hamilton 1981). We validated the *Tric-a*-cKO expression level using mRNA and protein techniques and we successfully knocked out the TRIC-A channel specifically in the heart. We bred the colony for several generations to collect some hearts for determining the biophysical properties of the channels from *Tric-a*-cKO mouse hearts in further experiments. Further grant funding is now required to pursue these experiments.

# Chapter 6 Homology modelling of RyR2 CPVT1 mutations

## 6.1 Introduction

RyR2 channels in the heart play a crucial role in EC-coupling, as discussed previously. Mutations to the *RyR2* gene can have dramatic consequences for cardiac function. For example, more than 160 RyR2 mutations have been linked to a lethal arrhythmogenic cardiac disease called CPVT1 (Priori et al. 2001). The vast majority of these mutations are gain-of-function, i.e., they induce conformational changes to the structure of RyR2 that increase the activity of the channel leading to $Ca^{2+}$ leak through the SR that can give rise delayed after-depolarisations and ultimately arrhythmias (Napolitano, Priori, and Bloise 2016; Priori et al. 2001). The exact mechanism these conformational changes lead to enhanced RyR2 activity remains elusive to date. To obtain a better understanding I used homology modelling to explore the potential structural changes to RyR2 induced by the V2475F and the neighbouring residue R2474S. Both of these mutations have been linked to CPVT1 (Tester et al. 2005). Further studies in animal models have shown that they are gain-of-function mutations (Loaiza et al. 2013; Wilson et al, 2021). For example, single-channel recordings using native SR vesicles from mice heterozygous to the V2475F mice showed increased activity to low concentrations of cytosolic $Ca^{2+}$ and increased activation by luminal $Ca^{2+}$ (Wilson et al, 2021).

It is important to study the structural changes caused by CPVT1 mutations and link them with the channel-gating behaviour of RyR2 (Loaiza et al. 2013; Wilson

et al. 2021). We recently showed that single-channel recordings using native SR vesicles from heterozygous V2475F mice displayed increased activity to low concentrations of cytosolic $Ca^{2+}$ and increased activation by luminal $Ca^{2+}$ (Wilson et al 2021). In this chapter, I centred on investigating the potential structural changes to RyR2 from the V2475F CPVT mutation and compared it with another CPVT next to it, R2474S. I applied a homology modelling of the RyR2-CPVT mutation using the available resolved structure of pig RyR2 and sequences of human RyR2. The models predicted the structural and conformational changes to the RyR2 HD1 region caused by these two CPVT mutations. The homology modelling is based on the sequences of proteins and the solved structure of the proteins. Thus, the resolution and accuracy of the structure are important for this approaching and the reliability of the analysis result. Due to limit of the missing residues in other region and enormous residues in the full length RyR2 structure, I choose to only perform modelling on part of the important region, HD1 in this case. The modelling result helps us understand the relationships between structure and function of RyR2 in CPVT.

## 6.2 Results

### 6.2.1 Homology modelling models on RyR2 CPVT1 mutations

We used structures of the pig RyR2 in open and closed states as templates for our homology modelling (PDB ID: 5GOA, 5GO9 (Peng et al., 2016)) and our models

were restricted to the HD (residues 2111 to 2679). In the two wild-type (WT) pig RyR2 structures, the open and closed states, the solved pig HD1 was used as template in the modelling. Figure 6.1A illustrates the amino acid sequences and domain organization of RyR2 and the ribbon diagram in Figure 6.1B and 6.1C shows the 3D structure of RyR2 in the open state in side- and cytosolic views to illustrate the overall structure of RyR2. In Figure 6.1B and 6.1C, the HD1 containing the two different mutation sites is highlighted. We then performed a 'clean-up' process on the template files by deleting the small molecules (for example, $H_2O$ molecules), and checking the amino acid sequences. Figure 6.2A illustrates the extracted HD1s of chain A after the clean-up process and the mutation site in the HD1 is circled. Figure 6.2B shows the alignment of all sequences of HD1s from pig, wild-type human as well as human with either of the R2474S and V2475F mutations. The sequences of RyR2 from human and pig have a conserved identity of 98.21% and a conserved identity of 98.95% specifically for HD1 region. For the mutated sites, R2474 and V2475, both human and pig RyR2 have exactly the same residues.

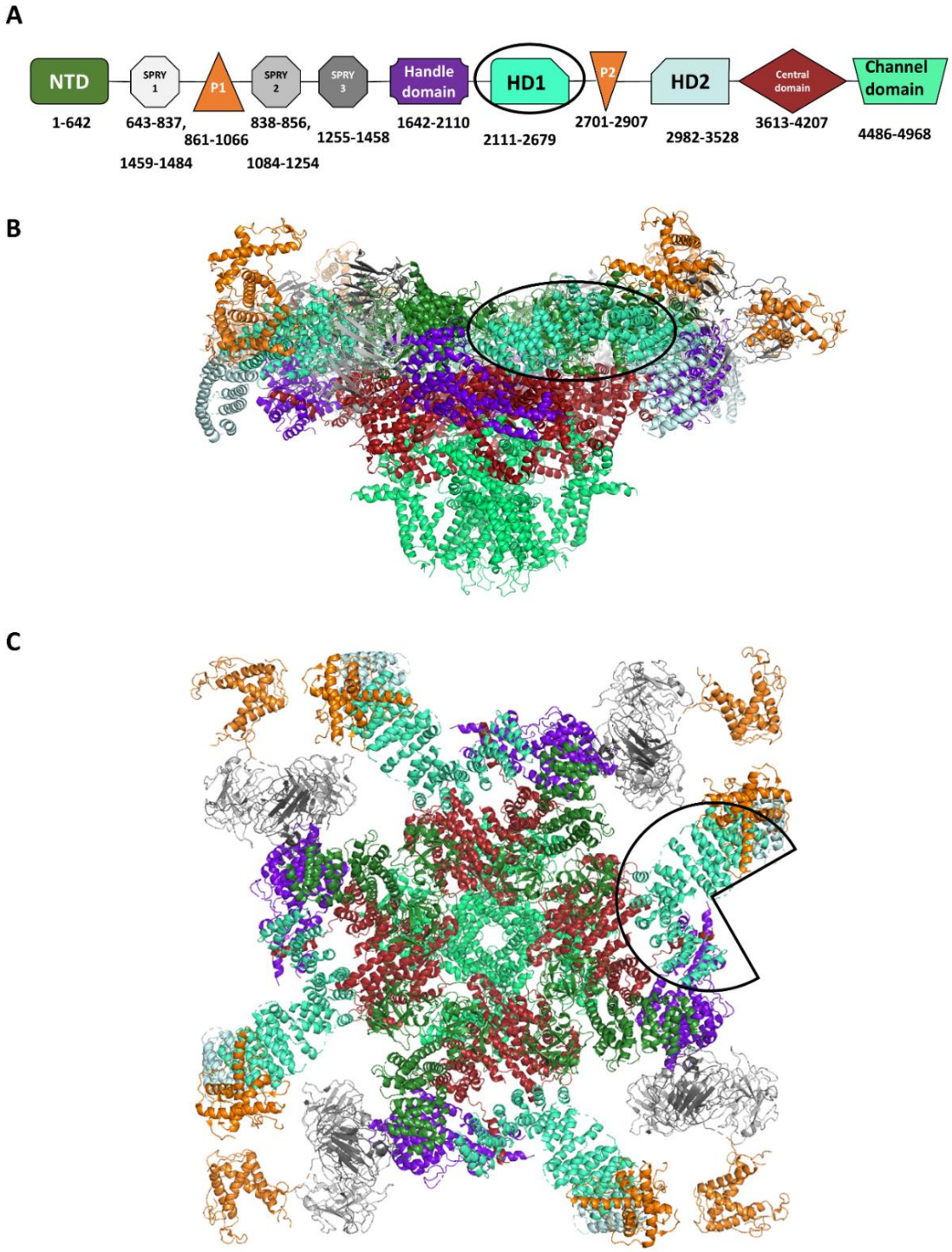



**Figure 6.1 Sequences and structures of the RyR2 channel**

**(A)** Domain organisation of the RyR2 channel and **(B)** Side-view of the cryo-EM RyR2 structure (PDB ID: 5GOA as a demonstration). The helical domain-1 (HD1) is circled by black lines. **(C)** Cytosolic-view of the cryo-EM RyR2 structure. HD1 is circled by black lines.

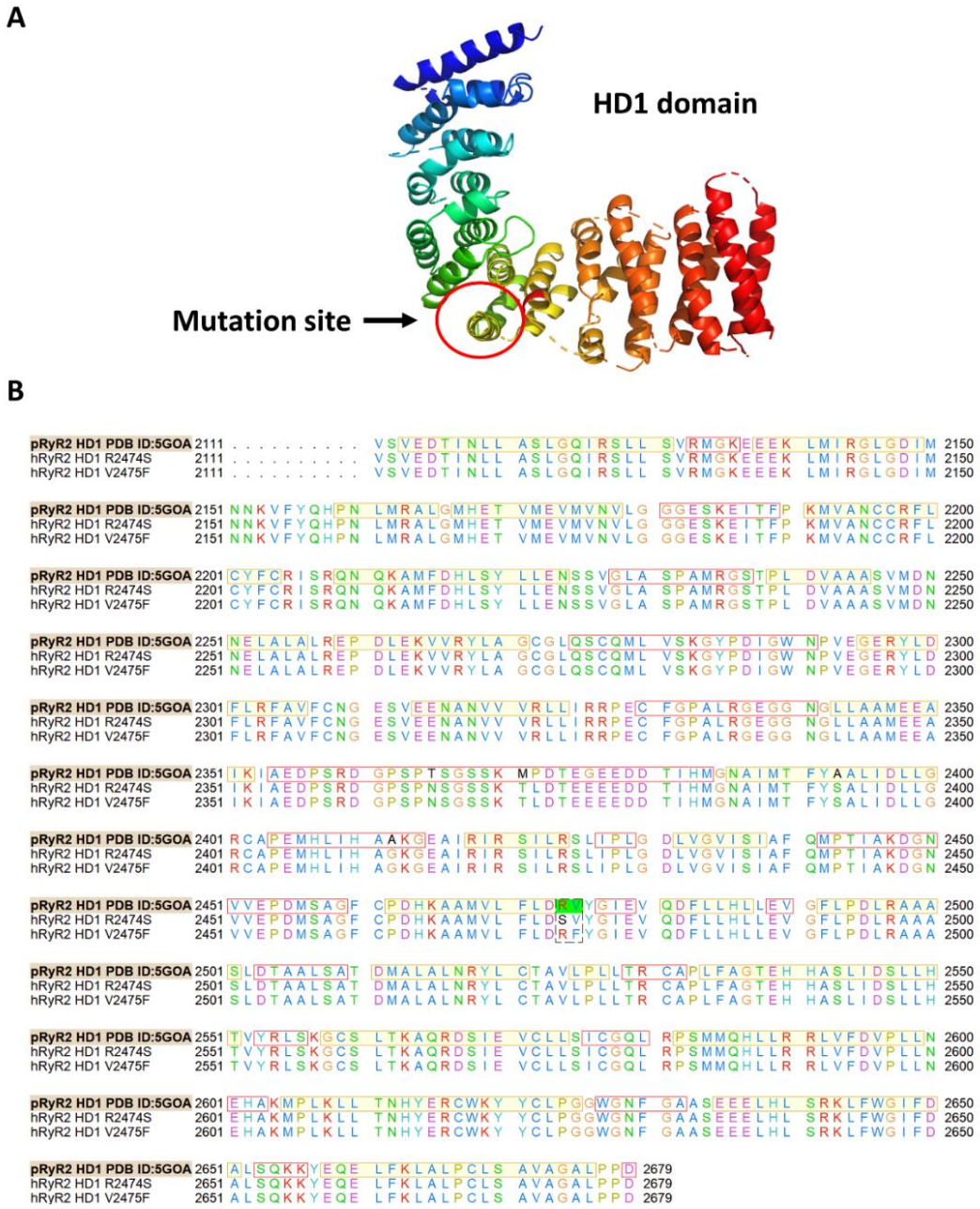



**Figure 6.2 Structure of the HD1 and alignment of the corresponding wild-type and mutated HD1 amino acid sequences of RyR2 from pig and human**

(A) Ribbon diagram of the HD1 structure. The mutation sites of R2474 and V2475 are circled in red.

(B) WT (pig) sequence alignment showing the R2474S (human) and V2475F (human) mutations. The mutant sites, R2474 and V2475, are conserved between pig and human sequences. The mutation sites are highlighted within the green background and the secondary structure (alpha-helices) associated with the WT sequence is highlighted in yellow.

### 6.2.2 Clustering and structural analysis of homology modelling results

Models for human WT, human R2474S and human V2475F were constructed for both the open and the closed states, to give six groups of models in total. 50 models were generated for each of these six groups, and the five best models from each group, based on their MODELLER scores, were chosen for analysis. We calculated the root mean square deviation (RMSD) between each pair of the total 30 models (five best models from six groups) and compiled a distance matrix from the RMSD values. We applied a hierarchical clustering method on the distance matrix to categorize the models into several groups based the similarity. Figure 6.3 shows the RMSD matrix of the models before and after the hierarchical clustering (plotted by Morpheus, https://software.broadinstitute.org/morpheus). It can be seen that the wild-type models were similar to each other, highlighted by the green box. Figure 6.3 illustrates that the R2474S and V2475F open models (clustered in the blue box) are similar to each other but markedly different to all the other models (red clustering areas), suggesting that the mutations may cause changes in this region.

**A**

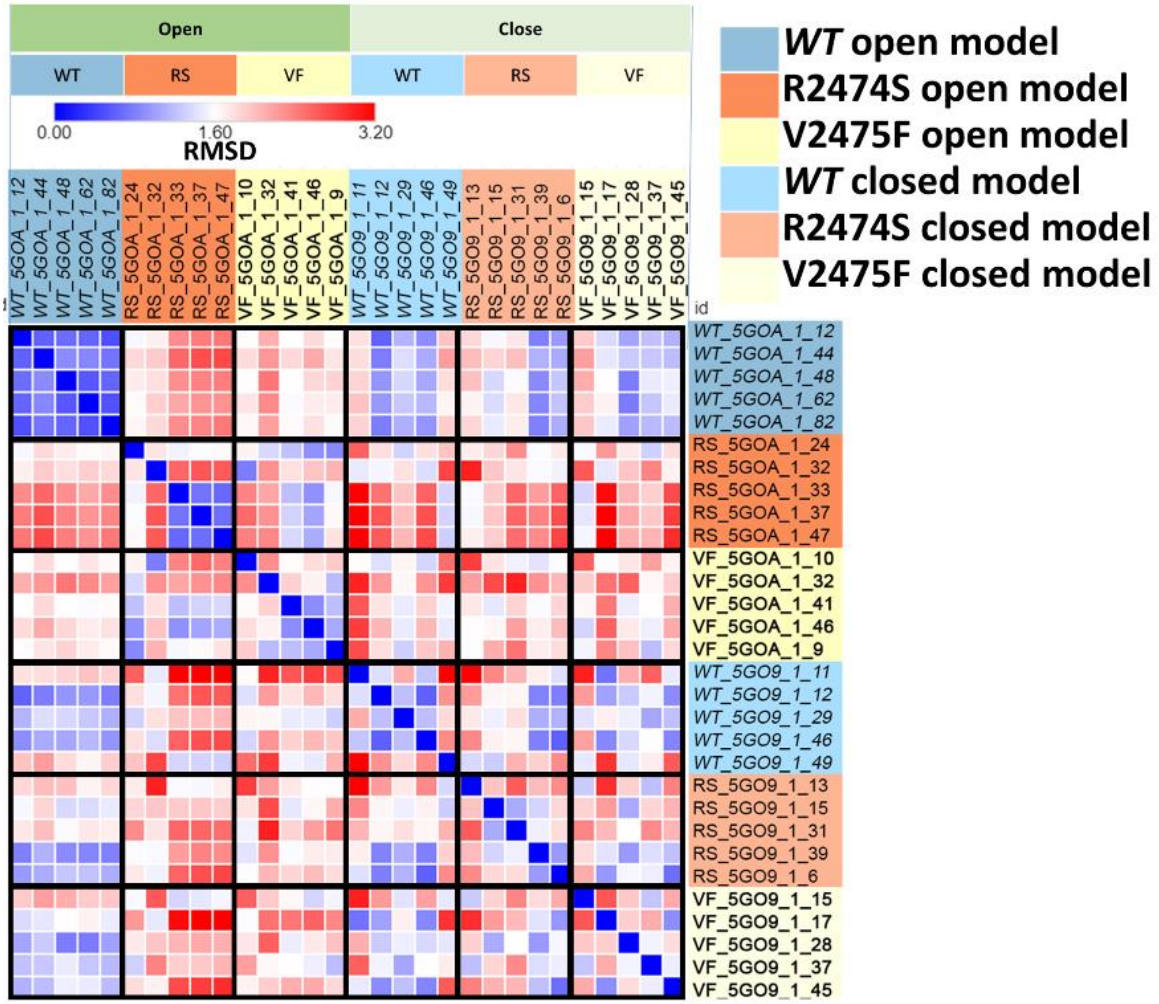



**Figure 6.3 Using root-mean-square deviation (RMSD) to quantify structural similarities between WT and mutant models**

(A) Heatmap of the RMSD matrix comparing the five best models of WT, R2474S and V2475F in open and closed RyR2 structures. The RMSD between each model pair is mapped such that blue represents maximum similarity (0 Å) and red represents minimum similarity (3.2 Å).
(B) Hierarchical clustering applied to the RMSD matrix. Large clusters with the closest similarity are enclosed in blue and green boxes. The template and the sequence used for the different models are indicated by different colour bands. The clustering shows that the WT open and closed models (green box) are quite similar, indicating that in the wildtype RyR2 channel, there are minor structural changes in this region as the channel opens and closes.

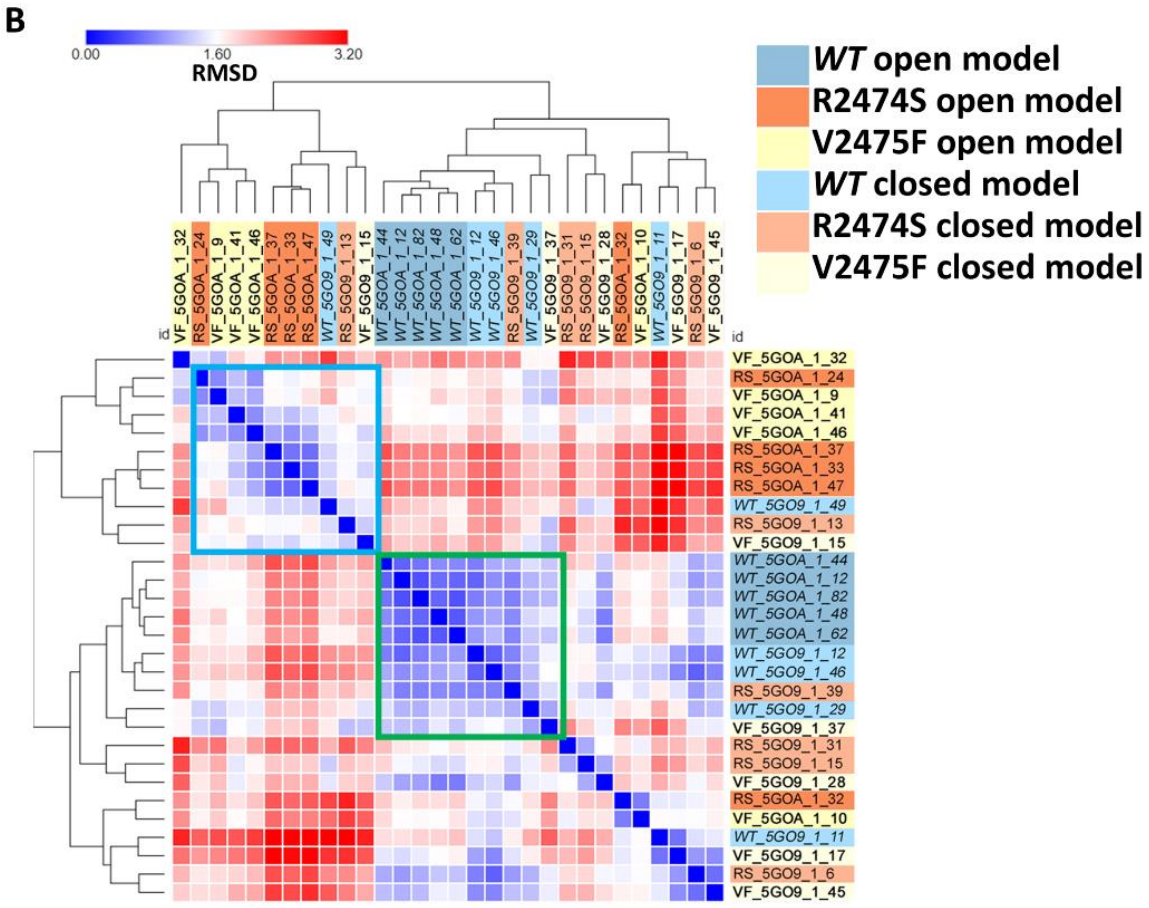



**Figure 6.3 Using root-mean-square deviation (RMSD) to quantify structural similarities between WT and mutant models**

(A) Heatmap of the RMSD matrix comparing the five best models of WT, R2474S and V2475F in open and closed RyR2 structures. The RMSD between each model pair is mapped such that blue represents maximum similarity (0 Å) and red represents minimum similarity (3.2 Å).
(B) Hierarchical clustering applied to the RMSD matrix. Large clusters with the closest similarity are enclosed in blue and green boxes. The template and the sequence used for the different models are indicated by different colour bands. The clustering shows that the WT open and closed models (green box) are quite similar, indicating that in the wildtype RyR2 channel, there are minor structural changes in this region as the channel opens and closes.

We applied the 'thorough optimization' protocol described in Methods. This allowed for some flexibility in the structure and brought unexpected conformational changes in this homology modelling approach. When comparing the models, we noticed what appeared to be different hinge motions in the HD1. Figure 6.4A shows two defined lobes for HD and that the two lobes are connected by the mutation site. The hinge angle between these lobes was calculated. As the data illustrated in Figure 6.4B shows, the hinge angle was significantly reduced for both V2475F and R2474S mutations relative to the WT models and was especially decreased when the channel was in the open state. Figure 6.5 shows a cartoon illustrating the structural changes.

The details of the predicted residue interactions are shown in Figure 6.6. Both mutations appear to increase the distance between the helix containing the mutated residue and the helix containing R2424 within HD1 by reducing the interactions between residues V2475 and R2424. This may lead to the increased bending of the whole HD1 seen in the two mutant structures and which appears to be more pronounced in the R2474S mutant.

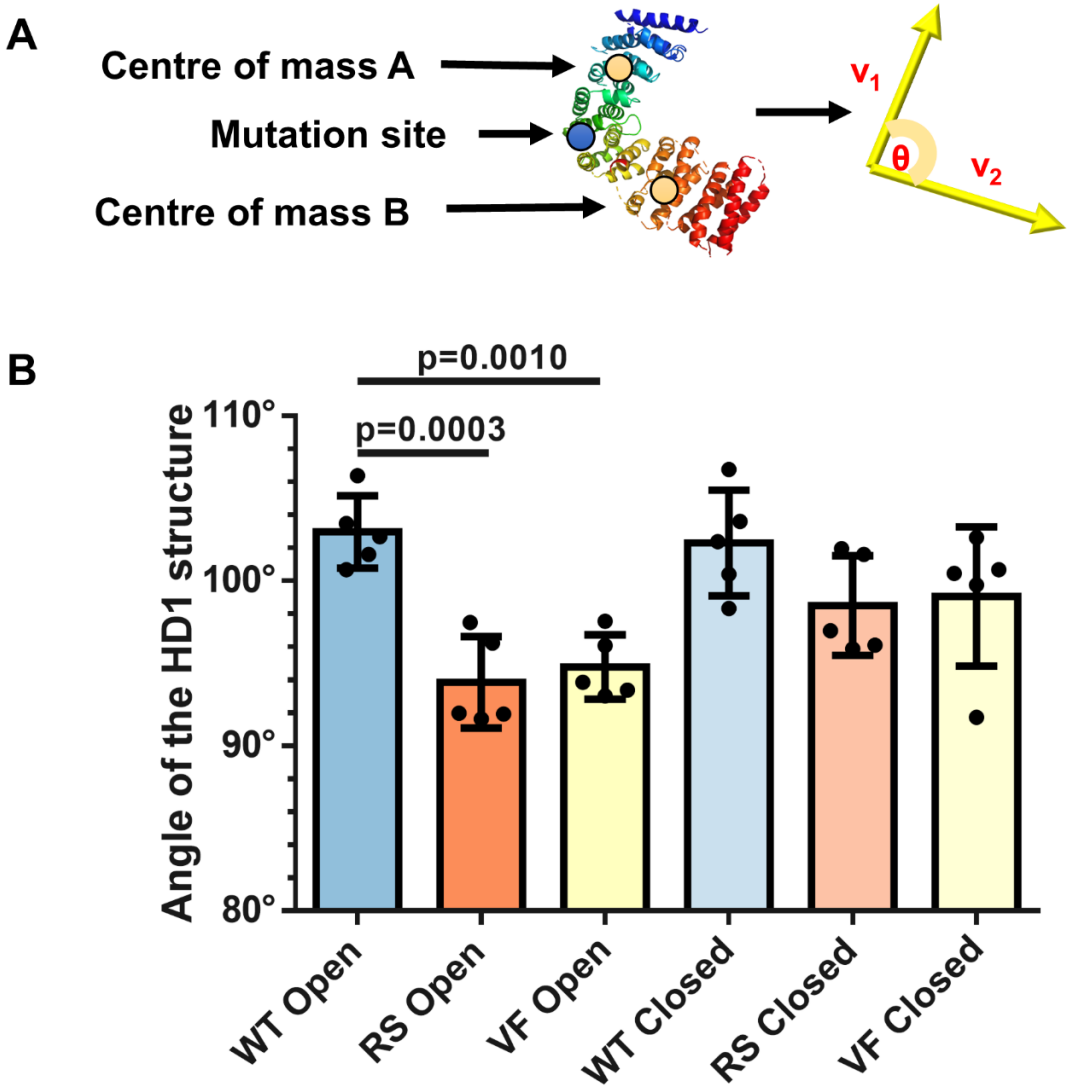



**Figure 6.4 Effects of the R2474S and V2475F mutations on the structure of the HD1**

**(A)** The angle between the two vectors originating from the mutation site was calculated by dividing the HD1 into two parts, lobe A (residues 2111-2473) and lobe B (residues 2476-2679), connected by the mutation site (blue spot). The centre of mass was calculated for each lobe as well as for the mutation site. **(B)** Bar chart illustrating the hinge angles for V2475F and R2474S compared with WT in both open and closed state models. Values are of mean±SEM (n=5).

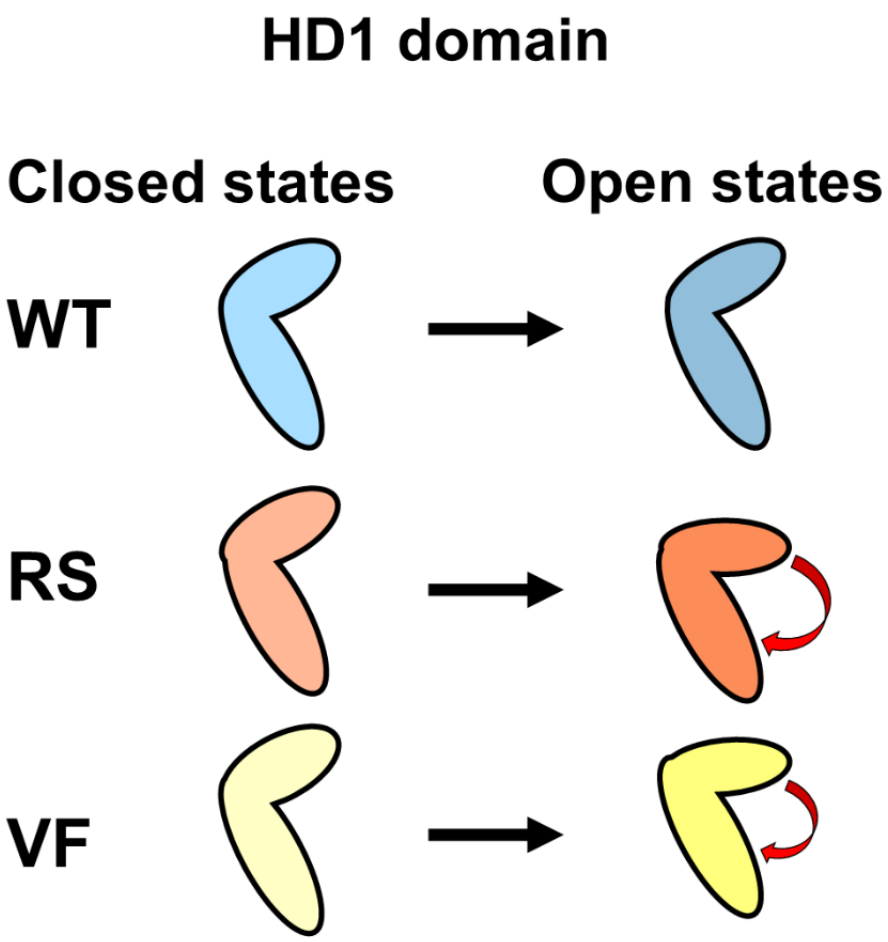



**Figure 6.5 Cartoon of effects of the R2474S and V2475F mutations on the HD1 conformation**

Cartoon illustrating the reduction in the angle between lobes A and B of the RyR2 HD1 caused by the mutations. The curved red arrows symbolise the amount of reduction in the angles between the two lobes. Wild-type (blue), R2474 (orange) and V2475F (yellow). Open states are represented by the darker colours and closed states by the lighter colours.

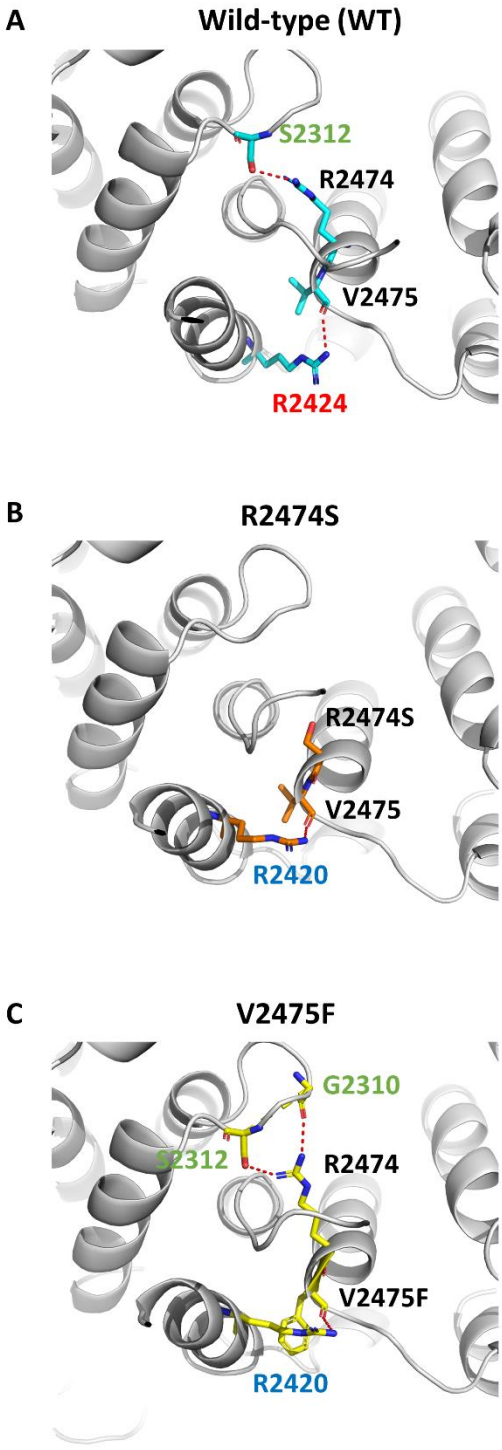



**Figure 6.6 Structural details of the interactions around the mutation site**

(A) WT, (B) R2474S mutation and (C) V2475F mutation. The polar interactions are shown with red dashed lines and the corresponding residues involved in the interactions are shown as sticks.

## 6.3 Discussion

My HD1 models suggest that both the V2475F and R2474S mutations reduce the angle between the two lobe regions (Figure 6.7). It was found that this angle was especially decreased for both mutations in the open state. Residue interaction results also indicate that both mutations may increase the distance between the helix containing the mutated residue and the helix containing R2424 within HD1 (Figure 6.6). In Figure 6.6A, it can be seen that there are two direct interactions between S2312/R2474 and R2424/V2475, respectively, in WT model. Figure 6.6B shows that there is no long interaction between S2312 and R2474 when R2474 is mutated to a serine residue (S) and that the side-chain of the mutated residue becomes much shorter. It can also be seen that the R2424/V2475 interaction was altered to a new similar interaction between R2420 and V2475. Interestingly, when V2475 is mutated to phenylalanine (F), the interaction between R2424 and V2475 is also altered to the same interaction between R2420 and V2475 and the S2312/R2474 residue interaction remains the same as WT. We speculate that these reduced interactions between the helix regions result in the observed reduction of the hinge angle in the mutated models. This may lead to the increased bending of the whole HD1 seen in the two mutant structures with the larger conformational change occurring in the R2474S mutant.

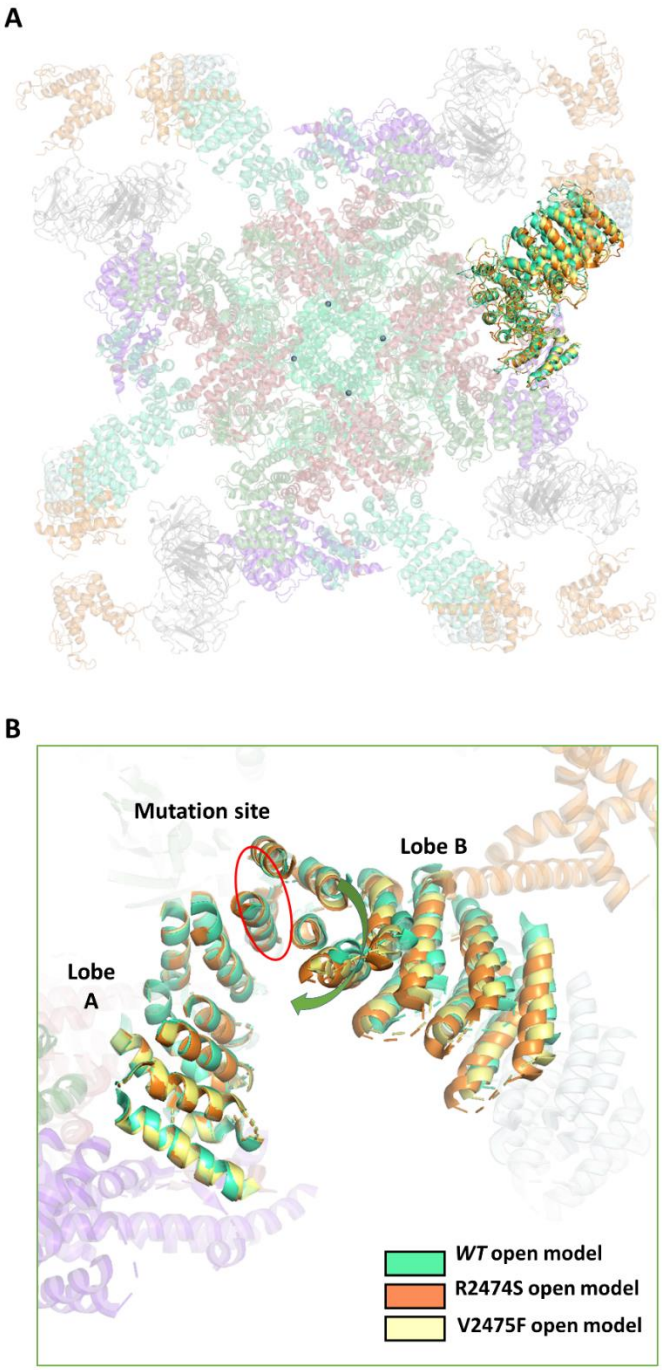



**Figure 6.7 Overall view of the homology modelling results aligned with the original cryo-EM pRyR2 structure.**

**(A)** WT (green), R2474S mutation (orange) and V2475F mutation (yellow) aligned onto the pRyR2 open state structure (5GOA, the semi-transparent structure) with the short-arm lobe A (residues 2111-2473) of HD1 overlapped. **(B)** Detailed HD1 area with the random coil structures are hidden.

In parallel with my structural investigations of the V2475F CPVT1 mutation, Abigail Wilson (AW), in the Sitsapesan group, investigated the changes in RyR2 single-channel function that occur with the V2475F mutation in a mouse model of this human disease (Loaiza et al. 2013). Our joint results have recently been published in the Journal of Physiology (Wilson et al. 2021) and I am the second author. Figures 6.8-6.10 and the legends are taken from the paper with minor modifications and are the work of AW. It is instructive to consider the structural and functional changes together with the aim of finding important relationships between these two types of data as this will not only provide a greater understanding of CPVT1 as a disease but may provide clues about basic RyR2 function.

When examining the single-channel data, it is important to be aware that, as described in the introduction, CPVT1 is an autosomal dominant disease and that patients are heterozygous for the mutation. RyR2 is a tetrameric protein with the potential to be expressed in the heart and other tissues with different numbers of mutated monomers as shown in Figure 6.1. The mouse model of CPVT1-V2475F was developed by Hector Valdivia's group (Loaiza et al. 2013). As in the human, only mice heterozygous for V2475F (V2475F(+/-) survive (Loaiza et al. 2013). Loaiza *et al.* found no evidence that any of the possible combinations of WT or mutated monomers were not expressed as functional ion channels or trafficked to the correct organelle although this was not rigorously investigated. We also found no loss of RyR2 protein in the hearts of the V2475F$^{(+/-)}$ mice (Wilson et al. 2021).

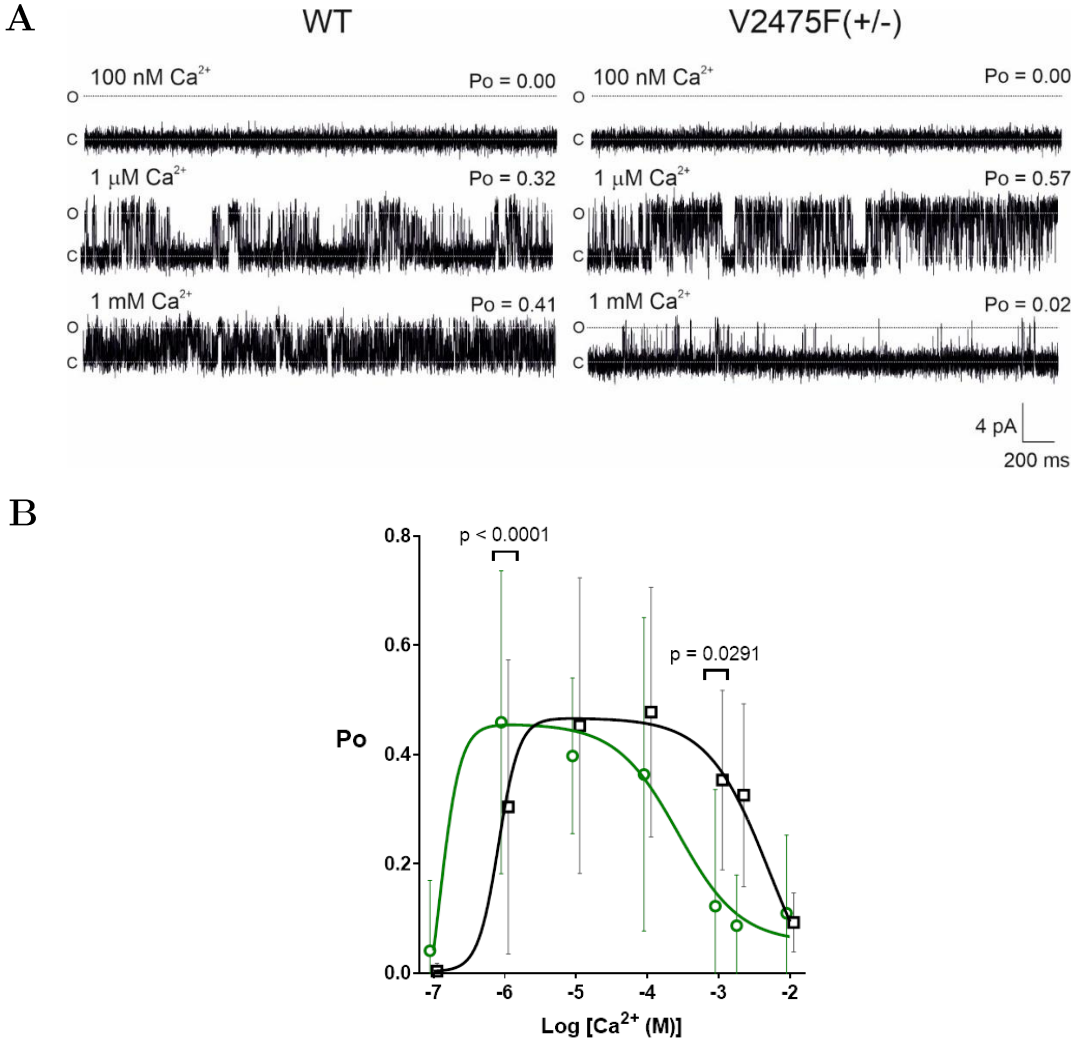



**Figure 6.8 Typical gating of native RyR2 channels derived from the hearts of WT and V2475F(+/-) mice and effects of the V2475F mutation on the response of RyR2 channels to cytosolic $Ca^{2+}$**

(A) Representative single-channel traces in Tris/HEPES, $Ca^{2+}$ glutamate solutions, illustrating the effects of varying cytosolic [$Ca^{2+}$] on gating and conductance for WT (left panel) and V2475F(+/-) (right panel) channels . Luminal [$Ca^{2+}$] is approximately 50 mM and the cytosolic free [$Ca^{2+}$] is indicated above each trace along with the average Po (measured over 3 min). O and C represent the fully open and closed levels, respectively. (B) Relationship between [$Ca^{2+}$] and Po values for RyR2 derived from WT (black) and V2475F(+/-) (green) mice. Two-way ANOVA: $Ca^{2+}$-by-genotype interaction, $p < 0.0001$; main effect of $Ca^{2+}$, $p < 0.0001$; main effect of genotype $p = 0.0325$. Post-hoc multiple comparisons with Sidak's correction comparing WT and V2475F(+/-): $p < 0.0001$ at 1 µM, $p = 0.0291$ at 1 mM $Ca^{2+}$. Mean ± SD; n for WT = 8 – 110, n for VF = 5 – 95. Lines display non-linear bell-shaped fitted curves. $EC_{50}$ values are 0.82 µM for WT and 0.12 µM for V2475F, and $IC_{50}$ values are 5.18 mM for WT and 0.27 mM for V2475F. Experiments and analysis performed by Dr Wilson (Wilson et al. 2021).

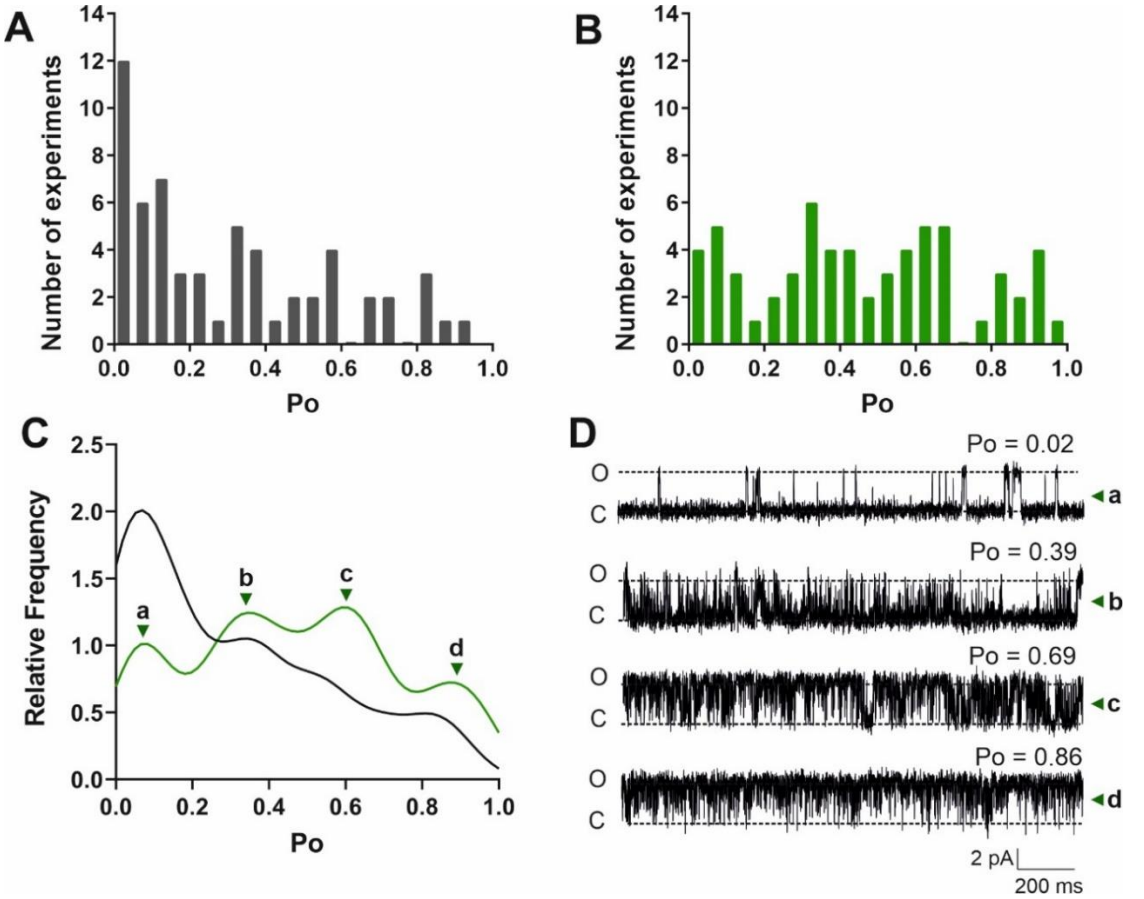



**Figure 6.9 Effects of the V2475F mutation on the population frequency of high Po RyR2 channels in mouse cardiac muscle.**

The Po values from individual experiments are plotted as frequency distributions for (A) WT (n = 59) and (B) V2475F(+/-) (n = 62) experiments in the presence of 1 μM cytosolic $Ca^{2+}$. (C) A Kernel Density Estimate (KDE) was fit to the WT and V2475F(+/-) Po values. For the V2475F(+/-) Po values, the KDE estimated 4 peaks and therefore suggests the presence of at least four different populations of activity at Po values of 0.08, 0.34, 0.59 and 0.87. (D) The gating behaviour of typical V2475F(+/-) channels drawn from these populations peaks are shown in the four traces labelled for the corresponding component. Experiments and analysis performed by Dr Wilson (Wilson et al. 2021).

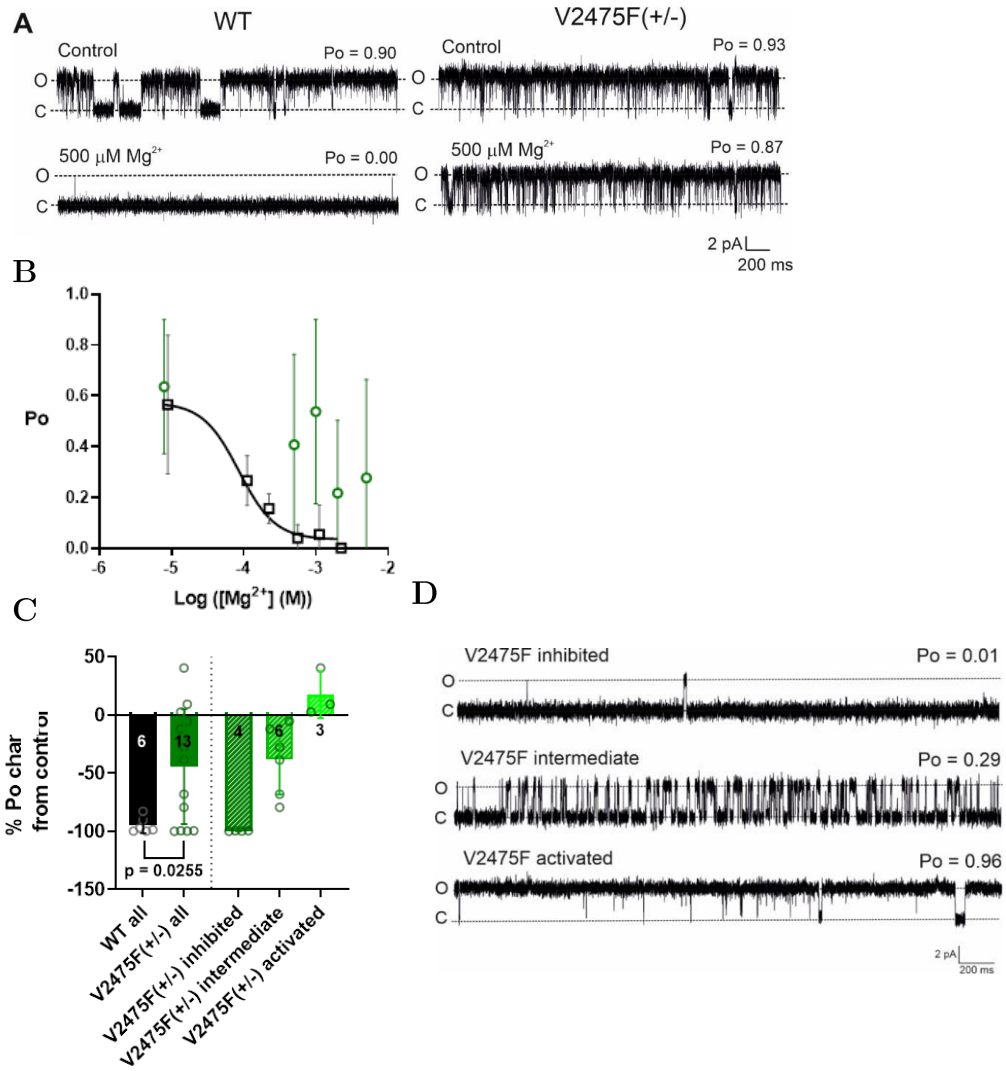



**Figure 6.10 Effect of cytosolic $Mg^{2+}$ on WT and V2475F channels**

(A) Recordings from WT (left) and V2475F (right) channels before and after adding 500 μM free cytosolic [$Mg^{2+}$] in the presence of 1 mM adenosine and a maintained 1 μM free cytosolic [$Ca^{2+}$] (control). In order to directly compare the ability of $Mg^{2+}$ to inhibit WT and V2475F channels, recordings from channels with a similar Po under control conditions were chosen. O and C indicate the open and closed states, respectively. (B) Relationship between Po and free [$Mg^{2+}$] for WT (black) and V2475F (green) channels in the presence of 1 μM free $Ca^{2+}$ and 1 mM adenosine. Mean ± SD, n ≥ 5. (C) Left of the dashed line: comparison of the percentage inhibition of Po induced by 500 μM $Mg^{2+}$ in all WT (black) and all V2475F (green) channels. Unpaired t-test, p = 0.0255. Right of the dashed line: percentage change in Po of V2475F channels after the channels are separated into 3 groups: those channels inhibited to within the range of inhibition expected for WT channels (>80% inhibition, n = 4), those channels inhibited to a reduced or intermediate extent (<80% inhibition, n = 6) and those channels that were activated (increase in Po, n = 3) by $Mg^{2+}$. Mean ± SD, n numbers for each group are indicated on the bars. (D) Typical examples of the gating behaviour of V2475F channels showing WT-like inhibition (top trace), intermediate inhibition (middle trace) and activation (bottom trace) in response to 500 μM $Mg^{2+}$. Experiments and analysis performed by Dr Wilson (Wilson et al. 2021).

Figure 6.8A shows the typical single-channel current fluctuations of the RyR2 channels derived from the hearts of WT or V2475F(+/-) mice at three key cytosolic [$Ca^{2+}$]. Single channel $Ca^{2+}$ conductance was reduced in some V2475F(+/-) channels, the first time a change in the ion conducting properties of RyR2 has been reported in CPVT, but for comparative purposes, channels exhibiting similar $Ca^{2+}$ conductances are compared in the figure. In Figure 6.8B, the full relationship between cytosolic $Ca^{2+}$ and Po is shown and the important changes caused by the V2475F mutation can be seen. The V2475F(+/-) channels are much more sensitive to cytosolic $Ca^{2+}$ at nanomolar [$Ca^{2+}$]. This includes a subset of channels that open at the resting free cytosolic [$Ca^{2+}$] that is present in cardiac cells during diastole (100 nM). The V2475F(+/-) channels are also inactivated by lower concentrations of $Ca^{2+}$ than WT channels. It is interesting that in a previous study of RyR2 single-channel behaviour of the mouse model of CPVT1-R2474S(+/-), the mutated channels are reported to be 'hypersensitive to cytosolic $Ca^{2+}$' (Lehnart et al. 2008). Our homology modelling (Figure 6.5) proposes that both R2474S and V2475F would lead to similar structural alterations to the HD1 of the RyR2 channel and so we speculate that that the bending of the HD1 may be correlated with an increased sensitivity of RyR2 to cytosolic $Ca^{2+}$.

As reported in our publication (Wilson et al. 2021), extremely large Po data sets were obtained and this allowed Po frequency histograms to be plotted for WT and V2475F(+/-) channels at the cytosolic [$Ca^{2+}$] of 1 μM (Figure 6.9). Kernel density estimation (KDE) was used to highlight the possible Po populations of the WT and

V2475F(+/-) channels. While WT channels exhibited a single population of channels, the KDE suggested that V2475F(+/-) mutated channels were best described by at least four different populations of channels identified by four peak Po values of 0.08, 0.34, 0.59 and 0.87. Examples of the type of gating exhibited by the V2475F(+/-) channels at these activity levels are shown in Figure 6.9D. For V2475F(+/-) channels, the lowest Po component (0.08) occurs at a similar Po to that of the WT channels but three other higher Po components make up the bulk of the distribution. We suggested that the different populations of V2475F(+/-) RyR2 channels result because different compositions of mutated and non-mutated monomers in an RyR2 tetramer may lead to differences in the degree to which the $Ca^{2+}$ sensitivity of the RyR2 channels is altered. In this regard, it is also interesting, that $Ca^{2+}$ conductance was only reduced in some V2475F(+/-) channels.

As $Mg^{2+}$ competes with cytosolic $Ca^{2+}$ at both the activation and inhibition sites (Meissner, Darling, and Eveleth 1986; Ashley and Williams 1990; Laver, Baynes, and Dulhunty 1997), we postulated that the $Mg^{2+}$ regulation of the V2475F(+/-) channels might also be altered. Figure 6.10 shows that $Mg^{2+}$ regulation was strongly affected, and again, there was evidence for populations of channels with different degrees of dysfunction. It was found that some V2475F(+/-) channels behaved like WT channels in respect to $Mg^{2+}$ inhibition, whereas some channels were only partially inhibited by $Mg^{2+}$ and some channels were actually activated by $Mg^{2+}$. Although not shown at the single channel level, it is noteworthy that the R2474S mutation decreases the ability of $Mg^{2+}$ to inhibit ryanodine binding (Uehara et al.

2017), suggesting that consistent functional changes are associated with similar structural abnormalities. Homology modelling suggests that both of these CPVT1 mutations would have similar structural effects, which is in line with the defects from the two mutations in $Mg^{2+}$ regulation of RyR2 channels.

Both the increase in sensitivity to nanomolar concentrations of cytosolic $Ca^{2+}$ and the strong reduction in the ability of $Mg^{2+}$ to inhibit V2475F(+/-) RyR2 channel opening would be expected to increase the likelihood of RyR2 channel opening during diastole to give rise to the waves of CICR and DADs that are characteristic of CPVT1. It is interesting that the alterations to the single-channel function of V2475F(+/-) RyR2 appeared to be specific to particular aspects of channel function in that only regulation via the $Ca^{2+}$ activation and inhibition sites was altered together with a change in $Ca^{2+}$ conductance. Activation of the channel by adenosine, ATP or luminal $Ca^{2+}$ were not affected (Wilson et al. 2021), nor was the response of the channel to phosphorylation (Dr Abigail D. Wilson PhD thesis, (Wilson 2020)).

The RyR2 HD1 is located far away from the pore region (55~80 angstroms) and from regions of the channel known to move during gating, so it is fascinating that a structural alteration to this region might somehow be transduced into specific functional changes. From the structures of pig RyR2 in open and closed states, it has previously been suggested that the motions of the helical domain and the central domain (including the pore region) are coupled and, therefore, that shifts in the helical domain may be translated into changes in the central domain (Peng

et al. 2016). Obviously, much further work is required to understand these processes but my molecular modelling investigations will hopefully provide a useful basis for further studies aimed at investigating how structural changes in distinct domains of RyR2 can be translated into dynamic changes in RyR2 protein movements in the pore region and gating machinery.

The HD1 of RyR2 may be involved in many regulatory processes that eventually lead to changes in gating or conductance of RyR2 channels. It is therefore interesting that calmodulin (CaM), a $Ca^{2+}$ binding protein that is tightly bound to RyR2, appears to interact with RyR2 in this region. In a recently solved RyR2 structure, CaM was solved together with RyR2 (Gong et al. 2019). The structure reveals the surface of RyR2 interacting with the non-$Ca^{2+}$ bound form of CaM (apo-CaM). On close inspection of the interactions, the N-lobe of apo-CaM interacts with RyR2 through three interfaces located in the HD1 (Figure 6.11b). The main interactions between residues of apo-CaM and HD1 are between the extensive hydrophobic residues. One of the involved interacting residues is Y2156; in the human, the Y2156C variant is linked to CPVT1 (Gong et al. 2019; Medeiros-Domingo et al. 2009). Another interface is formed between a region in apo-CaM rich in acidic residues and Lys2558 in HD1. Although we did not include CaM in our homology modelling, it is possible that the interactions between CaM and the HD1 contribute to the mechanisms that bring about the changes in RyR2 $Ca^{2+}$ sensitivity observed in CPVT1 mutations located in HD1 of RyR2. As the binding of CaM to RyR2 is a $Ca^{2+}$-dependent process that regulates the gating of RyR2

(Tripathy et al. 1995; Sigalas, Bent, et al. 2009; Sigalas, Mayo-Martin, et al. 2009) important future investigations include investigation of possible links between the $Ca^{2+}$-CaM/apo-CaM binding interactions with RyR2 and the structural changes that occur in RyR2 to alter the cytosolic $Ca^{2+}$ regulation of RyR2 gating in CPVT1 mutations in the HD1.

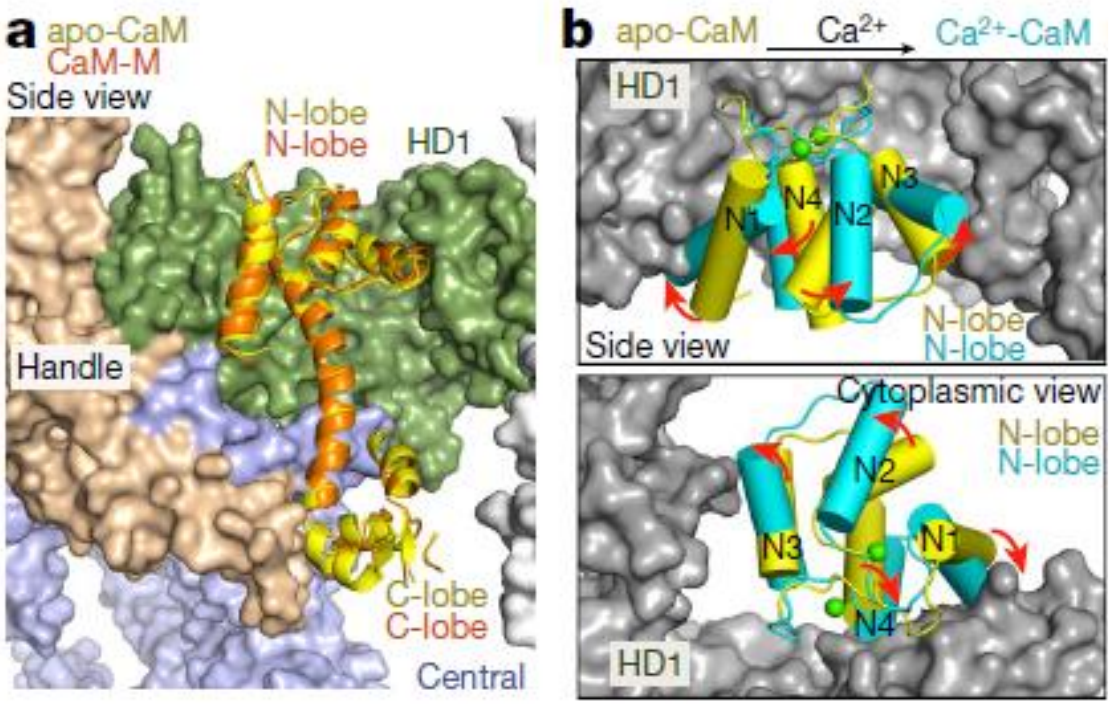



**Figure 6.11 CaM-RyR2 domain interactions illustrating the shift of the RyR2 binding site for CaM at different $Ca^{2+}$ concentrations from (Gong et al. 2019)**

a. At 20 μM $Ca^{2+}$, the binding site for CaM-M is the same as for apo-CaM. The two structures are superimposed relative to CaM.
b. With increased [$Ca^{2+}$], the conformational changes of the CaM structure may cause steric block between the N-lobe and HD1 of RyR2. The N-lobes of CaM are shown and superimposed. Red arrows indicate directions of conformational changes from apo-CaM to $Ca^{2+}$-CaM.

# Chapter 7 Conclusions

In summary, my thesis has centred on investigating certain structural and biophysical properties of several SR ion channels via artificial phospholipid bilayer techniques including the SR $K^+$ channel, RyR and TRIC channels. RyR channels are essential to the SR $Ca^{2+}$-release process during EC-coupling but the physiological roles of the SR $K^+$ channel and TRIC channels are not established.

In Chapter 3 of my thesis, I demonstrated a novel binding ligand, ebselen, for the SR $K^+$ channel from sheep skeletal muscle. I found that cytosolic ebselen irreversibly altered the gating of the channel reducing Po and causing it to predominantly open into sub-conductance states. Ebselen didn't alter the full open conductance of the SR $K^+$ channel, suggesting that the channel pore was unaffected. The cysteine reducing agent, DTT partly reversed the effects of ebselen and so I hypothesized that the selenium atom in ebselen forms a covalent bond with cysteine residue/s on the SR $K^+$ channel. When ebselen followed by DTT was added to the luminal side of the bilayer, the effects were not so clear. Higher concentrations of ebselen were required to affect channel gating and the actions of DTT were not significant. It is therefore likely that ebselen interacts with cysteine residues on the cytosolic side of the SR $K^+$ channel as indicated in Figure 7.1. Ebselen may also bind to different sites on the luminal side of the channel but further work is required to establish this. Ebselen is the first compound to be found that can bind tightly to the SR $K^+$ channel causing a distinctive function change. It may now be possible to design a ligand based on ebselen that is more selective for the SR $K^+$ channel to

aid purification and identification of the channel and to further examine the physiological roles of this channel.

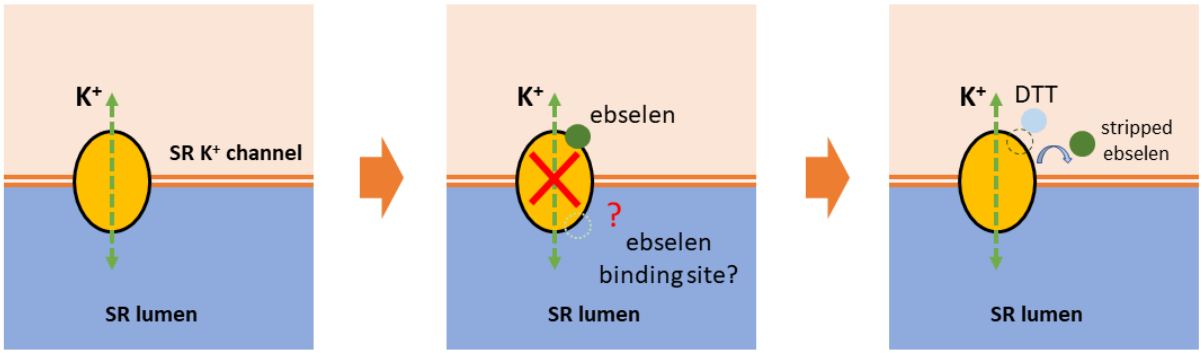



**Figure 7.1 Schematic showing the effects of ebselen and DTT on the SR $K^+$ channel**

Ebselen reduces the Po of the SR $K^+$ channel by binding to a site/s on the cytosolic side of the channel (dark green spot). There may also be a site/s on the luminal side of the channel (pale green dashed circle). DTT (light blue spot) can partly reverse the effect on gating.

In Chapter 4 of my thesis, I found that co-expression of TRIC-A or TRIC-B together with RyR2 in HEK293 cells markedly altered the gating of RyR2 after incorporation into bilayers, suggesting that both TRIC-A and TRIC-B physically interacted with RyR2 (see Figure 7.2). The effects of TRIC-A and TRIC-B were different with TRIC-A showing more ability to increase the Po of RyR2. My results also indicated that TRIC channels are permeable to both $K^+$ and $Cl^-$ therefore suggesting that neither TRIC-A nor TRIC- B is the SR $K^+$ channel because the SR $K^+$ channel is highly selective for monovalent cations. My results suggest that both TRIC-A and TRIC-B would be highly efficient providers of counter-ion currents of $K^+$ and $Cl^-$ to balance $Ca^{2+}$ movements across the SR (see Figure 7.2) with TRIC-A providing a greater proportion of $K^+$ current than TRIC-B.

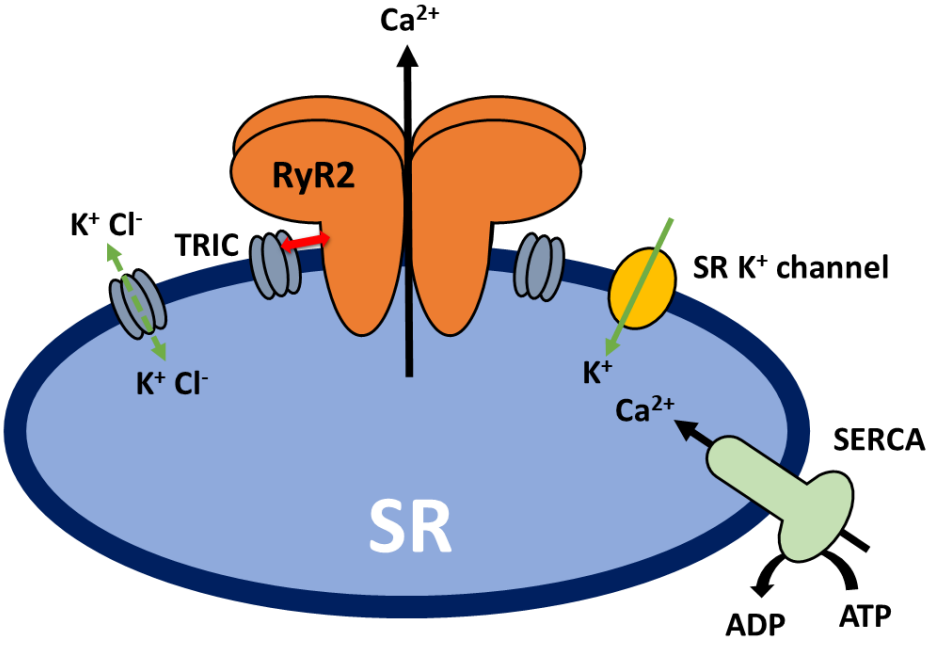



**Figure 7.2 $Ca^{2+}$-release-related ion pathways on the SR**

The $Ca^{2+}$-release through RyR channels (black arrows) will develop a negatively charged SR lumen. Counter currents through TRIC-A and/or TRIC-B could compensate the charge asymmetry across the membrane by allowing $K^+$ to flow into the SR or $Cl^-$ flow into cytosol (green arrows). TRIC channels may also bind to RyR2 to directly regulate gating (red arrow).

I also developed a cardiac-specific *Tric-a* knock-out (*Tric-a*-cKO) mouse colony as described in Chapter 5. We validated the mRNA and protein expression levels in *Tric-a*-cKO mice, showing successful knock out of the TRIC-A channel specifically in the heart. We bred the colony for several generations to collect hearts for determining the biophysical properties of the channels from *Tric-a*-cKO mouse hearts in future experiments.

In Chapter 6 of the thesis, I studied the RyR2 CPVT1 mutations, V2475F and R2474S, by performing a homology modelling on the RyR2 HD1 structure. The predicted models suggested that there were significant conformation changes to the RyR2 HD1 region, where the hinge angle of HD1 region was especially decreased

for both mutations in the open state models. We inspected the residue interaction changes in the models caused by the CPVT mutations, providing the possible structural changes to the conformation of RyR2. These results have now been published in a paper describing both these molecular modelling predictions together with the actual single-channel conductance and gating changes to RyR2 that can be observed due to the V2475F mutation (Wilson et al. 2021). These results thus provide clues as to the relationships between structure and function of RyR2 plus a greater understanding of CPVT1 as a disease.

# References

Ackers-Johnson, Matthew, Peter Yiqing Li, Andrew P Holmes, Sian-Marie O'Brien, Davor Pavlovic, and Roger S Foo. (2016). 'A simplified, Langendorff-free method for concomitant isolation of viable cardiac myocytes and nonmyocytes from the adult mouse heart', *Circulation research*, 119: 909-20.

Ahern, Gerard P, Pauline R Junankar, and Angela F Dulhunty. (1997). 'Ryanodine receptors from rabbit skeletal muscle are reversibly activated by rapamycin', *Neuroscience letters*, 225: 81-84.

Aizenman, Elias, Stuart A Lipton, and Ralph H Loring. (1989). 'Selective modulation of NMDA responses by reduction and oxidation', *Neuron*, 2: 1257-63.

Alvarez, Osvaldo. (1986). 'How to set up a bilayer system.' in, *Ion channel reconstitution* (Springer).

Armstrong, CM, FM Bezanilla, and P Horowicz. (1972). 'Twitches in the presence of ethylene glycol bis (β-aminoethyl ether)-N, N′-tetraacetic acid', *Biochimica et Biophysica Acta (BBA)-Bioenergetics*, 267: 605-08.

Ashley, RH, and AJ Williams. (1990). 'Divalent cation activation and inhibition of single calcium release channels from sheep cardiac sarcoplasmic reticulum', *The Journal of general physiology*, 95: 981-1005.

Bassani, JW, Rosana A Bassani, and Donald M Bers. (1994). 'Relaxation in rabbit and rat cardiac cells: species-dependent differences in cellular mechanisms', *The Journal of physiology*, 476: 279-93.

Bassani, JW, Weilong Yuan, and Donald M Bers. (1995). 'Fractional SR Ca release is regulated by trigger Ca and SR Ca content in cardiac myocytes', *American Journal of Physiology-Cell Physiology*, 268: C1313-C19.

Bassani, Rosana A, JW Bassani, and Donald M Bers. (1992). 'Mitochondrial and sarcolemmal $Ca^{2+}$ transport reduce $[Ca^{2+}]$ i during caffeine contractures in rabbit cardiac myocytes', *The Journal of physiology*, 453: 591-608.

Bean, Bruce P. (1985). 'Two kinds of calcium channels in canine atrial cells. Differences in kinetics, selectivity, and pharmacology', *The Journal of general physiology*, 86: 1-30.

Berman, Helen M, John Westbrook, Zukang Feng, Gary Gilliland, Talapady N Bhat, Helge Weissig, Ilya N Shindyalov, and Philip E Bourne. (2000). 'The protein data bank', *Nucleic acids research*, 28: 235-42.

Bers, Donald. (2001). *Excitation-contraction coupling and cardiac contractile force* (Springer Science & Business Media).

Bers, Donald M. (2002). 'Cardiac excitation–contraction coupling', *Nature*, 415: 198-205.

———. (2008). 'Calcium cycling and signaling in cardiac myocytes', *Annu. Rev. Physiol.*, 70: 23-49.

Bers, Donald M, and JH Bridge. (1989). 'Relaxation of rabbit ventricular muscle by Na-Ca exchange and sarcoplasmic reticulum calcium pump. Ryanodine and voltage sensitivity', *Circulation research*, 65: 334-42.

Bersell, Kevin, Sangita Choudhury, Mariya Mollova, Brian D Polizzotti, Balakrishnan Ganapathy, Stuart Walsh, Brian Wadugu, Shima Arab, and Bernhard Kühn. (2013). 'Moderate and

high amounts of tamoxifen in αMHC-MerCreMer mice induce a DNA damage response, leading to heart failure and death', *Disease models & mechanisms*, 6: 1459-69.

Block, Barbara A, Toshiaki Imagawa, Kevin P Campbell, and Clara Franzini-Armstrong. (1988). 'Structural evidence for direct interaction between the molecular components of the transverse tubule/sarcoplasmic reticulum junction in skeletal muscle', *The Journal of cell biology*, 107: 2587-600.

Camors, Emmanuel, and Héctor H Valdivia. (2014). 'CaMKII regulation of cardiac ryanodine receptors and inositol triphosphate receptors', *Frontiers in pharmacology*, 5: 101.

Carl, S Lewis, Kelly Felix, Anthony H Caswell, Neff R Brandt, W James Ball, Pol L Vaghy, Gerhard Meissner, and Donald G Ferguson. (1995). 'Immunolocalization of sarcolemmal dihydropyridine receptor and sarcoplasmic reticular triadin and ryanodine receptor in rabbit ventricle and atrium', *Journal of Cell Biology*, 129: 673-82.

Carter, Simon, John Colyer, and Rebecca Sitsapesan. (2006). 'Maximum phosphorylation of the cardiac ryanodine receptor at serine-2809 by protein kinase a produces unique modifications to channel gating and conductance not observed at lower levels of phosphorylation', *Circulation research*, 98: 1506-13.

Carter, Simon, Samantha J Pitt, John Colyer, and Rebecca Sitsapesan. (2011). 'Ca 2+-dependent phosphorylation of RyR2 can uncouple channel gating from direct cytosolic Ca 2+ regulation', *The Journal of membrane biology*, 240: 21-33.

Castro-Lopes, JM, M Malcangio, BH Pan, and NG Bowery. (1995). 'Complex changes of GABAA and GABAB receptor binding in the spinal cord dorsal horn following peripheral inflammation or neurectomy', *Brain research*, 679: 289-97.

Cheung, Wai Yiu. (1980). 'Calmodulin plays a pivotal role in cellular regulation', *Science*, 207: 19-27.

Ching, Li Lien, Alan J Williams, and Rebecca Sitsapesan. (2000). 'Evidence for $Ca^{2+}$ activation and inactivation sites on the luminal side of the cardiac ryanodine receptor complex', *Circulation research*, 87: 201-06.

Chu, A, M Fill, E Stefani, and ML Entman. (1993). 'Cytoplasmic $Ca^{2+}$ does not inhibit the cardiac muscle sarcoplasmic reticulum ryanodine receptor $Ca^{2+}$ channel, although $Ca^{2+}$-induced Ca $^{2+}$ inactivation of $Ca^{2+}$ release is observed in native vesicles', *The Journal of membrane biology*, 135: 49-59.

Copello, Julio A, Sebastian Barg, Hitoshi Onoue, and Sidney Fleischer. (1997). 'Heterogeneity of $Ca^{2+}$ gating of skeletal muscle and cardiac ryanodine receptors', *Biophysical journal*, 73: 141-56.

Coronado, Roberto, and Christopher Miller. (1980). 'Decamethonium and hexamethonium block $K^+$ channels of sarcoplasmic reticulum', *Nature*, 288: 495-97.

———. (1982). 'Conduction and block by organic cations in a $K^+$-selective channel from sarcoplasmic reticulum incorporated into planar phospholipid bilayers', *The Journal of general physiology*, 79: 529-47.

Coronado, Roberto, Robert L Rosenberg, and Christopher Miller. (1980). 'Ionic selectivity, saturation, and block in a $K^+$-selective channel from sarcoplasmic reticulum', *The Journal of general physiology*, 76: 425-46.

Costello, Brian, Christopher Chadwick, Akitsugu Saito, Alice Chu, Andreas Maurer, and Sidney Fleischer. (1986). 'Characterization of the junctional face membrane from terminal cisternae

of sarcoplasmic reticulum', *The Journal of cell biology*, 103: 741-53.

Denniss, Amanda, Angela F Dulhunty, and Nicole A Beard. (2018). 'Ryanodine receptor $Ca^{2+}$ release channel post-translational modification: Central player in cardiac and skeletal muscle disease', *The international journal of biochemistry & cell biology*, 101: 49-53.

Despa, Sanda, Bo Shui, Julie Bossuyt, Di Lang, Michael I Kotlikoff, and Donald M Bers. (2014). 'Junctional cleft $[Ca^{2+}]_i$ measurements using novel cleft-targeted $Ca^{2+}$ sensors', *Circulation research*, 115: 339-47.

Dimmeler, Stefanie, Bernhard Brüne, and Volker Ullrich. (1991). 'Ebselen prevents inositol (1, 4, 5)-trisphosphate binding to its receptor', *Biochemical pharmacology*, 42: 1151-53.

Eberhardt, David Richard. (2018). "Characterisation of novel cardiac and skeletal ion channels on intracellular $Ca^{2+}$ stores." , University of Oxfrod.

El-Ajouz, Sam, Elisa Venturi, and Rebecca Sitsapesan. (2016). 'Differential Effects of Temperature and Lipids on the Gating of RyR and SR K+ Channels', *Biophysical journal*, 110: 266a.

El-Ajouz, Sam, Elisa Venturi, Katja Witschas, Matthew Beech, Abigail D Wilson, Chris Lindsay, David Eberhardt, Fiona O'Brien, Tsunaki Iida, and Miyuki Nishi. (2017). 'Dampened activity of ryanodine receptor channels in mutant skeletal muscle lacking TRIC-A', *The Journal of physiology*, 595: 4769-84.

Elison, C, and DJ Jenden. (1967). 'The effects of ryanodine on model systems derived from muscle—II: Myofibrils and natural actomyosin', *Biochemical pharmacology*, 16: 1347-54.

Fabiato, Alexandre. (1985). 'Time and calcium dependence of activation and inactivation of calcium-induced release of calcium from the sarcoplasmic reticulum of a skinned canine cardiac Purkinje cell', *The Journal of general physiology*, 85: 247-89.

Flucher, Bernhard E, Hiroaki Takekura, and Clara Franzini-Armstrong. (1993). 'Development of the excitation-contraction coupling apparatus in skeletal muscle: association of sarcoplasmic reticulum and transverse tubules with myofibrils', *Developmental biology*, 160: 135-47.

Fox, James A. (1985). 'Conductance and selectivity properties of a substate of the rabbit sarcoplasmic reticulum channel', *Biophysical journal*, 47: 573-76.

Franzini-Armstrong, Clara, and Annelise O Jorgensen. (1994). 'Structure and development of EC coupling units in skeletal muscle', *Annual review of physiology*, 56: 509-34.

Franzini-Armstrong, Clara, and Feliciano Protasi. (1997). 'Ryanodine receptors of striated muscles: a complex channel capable of multiple interactions', *Physiological reviews*, 77: 699-729.

Galfre, Elena, Samantha J Pitt, Elisa Venturi, Mano Sitsapesan, Nathan R Zaccai, Krasimira Tsaneva-Atanasova, Stephen O'Neill, and Rebecca Sitsapesan. (2012). 'FKBP12 activates the cardiac ryanodine receptor $Ca^{2+}$-release channel and is antagonised by FKBP12. 6', *PloS one*, 7: e31956.

Garcia, Ann Maria, and Christopher Miller. (1984). 'Channel-mediated monovalent cation fluxes in isolated sarcoplasmic reticulum vesicles', *The Journal of general physiology*, 83: 819-39.

Ghoshal, Kalpana, Yijie Wang, John F Sheridan, and Samson T Jacob. (1998). 'Metallothionein induction in response to restraint stress: transcriptional control, adaptation to stress, and role of glucocorticoid', *Journal of Biological Chemistry*, 273: 27904-10.

Gong, Deshun, Ximin Chi, Jinhong Wei, Gewei Zhou, Gaoxingyu Huang, Lin Zhang, Ruiwu Wang, Jianlin Lei, SR Wayne Chen, and Nieng Yan. (2019). 'Modulation of cardiac ryanodine receptor 2 by calmodulin', *Nature*, 572: 347-51.

Györke, Inna, Nichole Hester, Larry R Jones, and Sandor Györke. (2004). 'The role of calsequestrin,

triadin, and junctin in conferring cardiac ryanodine receptor responsiveness to luminal calcium', *Biophysical journal*, 86: 2121-28.

Hill, Adam Parker, and Rebecca Sitsapesan. (2002). 'DIDS modifies the conductance, gating, and inactivation mechanisms of the cardiac ryanodine receptor', *Biophysical journal*, 82: 3037-47.

Hill Jr, JA, R Coronado, and HC Strauss. (1990). 'Open-channel subconductance state of $K^+$ channel from cardiac sarcoplasmic reticulum', *American Journal of Physiology-Heart and Circulatory Physiology*, 258: H159-H64.

Hodgkin, Alan L, and Andrew F Huxley. (1952). 'A quantitative description of membrane current and its application to conduction and excitation in nerve', *The Journal of physiology*, 117: 500-44.

Hoess, Ronald H, Anna Wierzbicki, and Kenneth Abremski. (1986). 'The role of the loxP spacer region in PI site-specific recombination', *Nucleic acids research*, 14: 2287-300.

Jeyakumar, Loice H, Leomar Ballester, Dong S Cheng, James O McIntyre, Paul Chang, Harold E Olivey, Louise Rollins-Smith, Joey V Barnett, Katherine Murray, and Hong-Bo Xin. (2001). 'FKBP binding characteristics of cardiac microsomes from diverse vertebrates', *Biochemical and biophysical research communications*, 281: 979-86.

Jiang, Dawei, Ruiwu Wang, Bailong Xiao, Huihui Kong, Donald J Hunt, Philip Choi, Lin Zhang, and SR Wayne Chen. (2005). 'Enhanced store overload–induced $Ca^{2+}$ release and channel sensitivity to luminal $Ca^{2+}$ activation are common defects of RyR2 mutations linked to ventricular tachycardia and sudden death', *Circulation research*, 97: 1173-81.

Jiang, Dawei, Bailong Xiao, Dongmei Yang, Ruiwu Wang, Philip Choi, Lin Zhang, Heping Cheng, and SR Wayne Chen. (2004). 'RyR2 mutations linked to ventricular tachycardia and sudden death reduce the threshold for store-overload-induced $Ca^{2+}$ release (SOICR)', *Proceedings of the National Academy of Sciences*, 101: 13062-67.

Jinek, Martin, Krzysztof Chylinski, Ines Fonfara, Michael Hauer, Jennifer A Doudna, and Emmanuelle Charpentier. (2012). 'A programmable dual-RNA–guided DNA endonuclease in adaptive bacterial immunity', *Science*, 337: 816-21.

Jones, Larry R, Henry R Besch Jr, John W Fleming, Mona M McConnaughey, and August M Watanabe. (1979). 'Separation of vesicles of cardiac sarcolemma from vesicles of cardiac sarcoplasmic reticulum. Comparative biochemical analysis of component activities', *Journal of Biological Chemistry*, 254: 530-39.

Kanehisa, Minoru. (2000). *Post-genome informatics* (OUP Oxford).

Kapiloff, Michael S, Nicole Jackson, and Nathan Airhart. (2001). 'mAKAP and the ryanodine receptor are part of a multi-component signaling complex on the cardiomyocyte nuclear envelope', *Journal of cell science*, 114: 3167-76.

Karlin, Arthur, and Eva Bartels. (1966). 'Effects of blocking sulfhydryl groups and of reducing disulfide bonds on the acetylcholine-activated permeability system of the electroplax', *Biochimica et Biophysica Acta (BBA)-Biophysics including Photosynthesis*, 126: 525-35.

Kasuya, Go, Masahiro Hiraizumi, Andrés D Maturana, Kaoru Kumazaki, Yuichiro Fujiwara, Keihong Liu, Yoshiko Nakada-Nakura, So Iwata, Keisuke Tsukada, and Tomotaka Komori. (2016). 'Crystal structures of the TRIC trimeric intracellular cation channel orthologues', *Cell research*, 26: 1288-301.

Kawamoto, Richard M, J-P Brunschwig, and Anthony H Caswell. (1988). 'Localization by

immunoelectron microscopy of spanning protein of triad junction in terminal cisternae/triad vesicles', *Journal of Muscle Research & Cell Motility*, 9: 334-43.

Kermode, Helen, Wei Mun Chan, Alan J Williams, and Rebecca Sitsapesan. (1998). 'Glycolytic pathway intermediates activate cardiac ryanodine receptors', *FEBS letters*, 431: 59-62.

Kermode, Helen, Alan J Williams, and Rebecca Sitsapesan. (1998). 'The interactions of ATP, ADP, and inorganic phosphate with the sheep cardiac ryanodine receptor', *Biophysical journal*, 74: 1296-304.

Kil, Jonathan, E Emily Harruff, and Ryan J Longenecker. (2022). 'Development of ebselen for the treatment of sensorineural hearing loss and tinnitus', Hearing Research, 413: 108209.Krzywinski, Martin, and Naomi Altman. (2014). 'Points of significance: two-factor designs', Nature methods, 11: 1187-88.

Labarca, Pedro P, and Christopher Miller. (1981). 'A $K^+$-selective, three-state channel from fragmented sarcoplasmic reticulum of frog leg muscle', *The Journal of membrane biology*, 61: 31-38.

Lai, F Anthony, Harold P Erickson, Eric Rousseau, Qi-Yi Liu, and Gerhard Meissner. (1988). 'Purification and reconstitution of the calcium release channel from skeletal muscle', *Nature*, 331: 315-19.

Laver, DR, TM Baynes, and AF Dulhunty. (1997). 'Magnesium inhibition of ryanodine-receptor calcium channels: evidence for two independent mechanisms', *The Journal of membrane biology*, 156: 213-29.

Laver, DR, and GD Lamb. (1998). 'Inactivation of $Ca^{2+}$ release channels (ryanodine receptors RyR1 and RyR2) with rapid steps in $[Ca^{2+}]$ and voltage', *Biophysical journal*, 74: 2352-64.

Laver, DR, LD Roden, GP Ahern, KR Eager, PR Junankar, and AF Dulhunty. (1995). 'Cytoplasmic $Ca^{2+}$ inhibits the ryanodine receptor from cardiac muscle', *The Journal of membrane biology*, 147: 7-22.

Lehnart, Stephan E, Marco Mongillo, Andrew Bellinger, Nicolas Lindegger, Bi-Xing Chen, William Hsueh, Steven Reiken, Anetta Wronska, Liam J Drew, and Chris W Ward. (2008). 'Leaky $Ca^{2+}$ release channel/ryanodine receptor 2 causes seizures and sudden cardiac death in mice', *The Journal of clinical investigation*, 118: 2230-45.

Lindsay, A. R., A. Tinker, and A. J. Williams. (1994). 'How does ryanodine modify ion handling in the sheep cardiac sarcoplasmic-reticulum $Ca^{2+}$-release channel', *Journal of General Physiology*, 104: 425-47.

Lindsay, A. R., S. D. Manning, and A. J. Williams. (1991). 'Monovalent cation conductance in the ryanodine receptor-channel of sheep cardiac muscle sarcoplasmic reticulum', *The Journal of physiology*, 439: 463-80.

Liu, Nian, Barbara Colombi, Mirella Memmi, Spyros Zissimopoulos, Nicoletta Rizzi, Sara Negri, Marcello Imbriani, Carlo Napolitano, F Anthony Lai, and Silvia G Priori. (2006). 'Arrhythmogenesis in catecholaminergic polymorphic ventricular tachycardia: insights from a RyR2 R4496C knock-in mouse model', *Circulation research*, 99: 292-98.

Liu, Wei, Min Zi, Ronald Naumann, Susanne Ulm, Jiawei Jin, Domenico M Taglieri, Sukhpal Prehar, Junhong Gui, Hoyee Tsui, and Rui-Ping Xiao. (2011). 'Pak1 as a novel therapeutic target for antihypertrophic treatment in the heart', *Circulation*, 124: 2702-15.

Livak, Kenneth J, and Thomas D Schmittgen. (2001). 'Analysis of relative gene expression data using real-time quantitative PCR and the 2− ΔΔCT method', *methods*, 25: 402-08.

*References*

Loaiza, Randall, Nancy A Benkusky, Patricia P Powers, Timothy Hacker, Sami Noujaim, Michael J Ackerman, José Jalife, and Héctor H Valdivia. (2013). 'Heterogeneity of ryanodine receptor dysfunction in a mouse model of catecholaminergic polymorphic ventricular tachycardia', *Circulation research*, 112: 298-308.

Lukyanenko, Valeriy, Inna Györke, and Sandor Györke. (1996). 'Regulation of calcium release by calcium inside the sarcoplasmic reticulum in ventricular myocytes', *Pflügers Archiv-European Journal of Physiology*, 432: 1047-54.

Ma, Jianjie, and Jiying Zhao. (1994). 'Highly cooperative and hysteretic response of the skeletal muscle ryanodine receptor to changes in proton concentrations', *Biophysical journal*, 67: 626-33.

Mak, Don-On Daniel, Horia Vais, King-Ho Cheung, and J Kevin Foskett. (2013). 'Nuclear patch-clamp electrophysiology of $Ca^{2+}$ channels', *Cold Spring Harbor Protocols*, 2013: pdb. prot073064.

Marban, Eduardo, Shawn W Robinson, and W Gil Wier. (1986). 'Mechanisms of arrhythmogenic delayed and early afterdepolarizations in ferret ventricular muscle', *The Journal of clinical investigation*, 78: 1185-92.

Marx, Steven O, Steven Reiken, Yuji Hisamatsu, Thotalla Jayaraman, Daniel Burkhoff, Nora Rosemblit, and Andrew R Marks. (2000). 'PKA phosphorylation dissociates FKBP12. 6 from the calcium release channel (ryanodine receptor): defective regulation in failing hearts', *Cell*, 101: 365-76.

Matyjaszkiewicz, Antoni, Elisa Venturi, Fiona O'Brien, Tsunaki Iida, Miyuki Nishi, Hiroshi Takeshima, Krasimira Tsaneva-Atanasova, and Rebecca Sitsapesan. (2015). 'Subconductance gating and voltage sensitivity of sarcoplasmic reticulum $K^+$ channels: a modeling approach', *Biophysical journal*, 109: 265-76.

McGarry, SJ, and AJ Williams. (1994). 'Adenosine discriminates between the caffeine and adenine nucleotide sites on the sheep cardiac sarcoplasmic reticulum calcium-release channel', *The Journal of membrane biology*, 137: 169-77.

McKinley, D., and G. Meissner. (1978). 'Evidence for a $K^+$, $Na^+$ permeable channel in sarcoplasmic reticulum', *J Membr Biol*, 44: 159-86.

Medeiros-Domingo, Argelia, Zahurul A Bhuiyan, David J Tester, Nynke Hofman, Hennie Bikker, J Peter van Tintelen, Marcel MAM Mannens, Arthur AM Wilde, and Michael J Ackerman. (2009). 'The RYR2-encoded ryanodine receptor/calcium release channel in patients diagnosed previously with either catecholaminergic polymorphic ventricular tachycardia or genotype negative, exercise-induced long QT syndrome: a comprehensive open reading frame mutational analysis', *Journal of the American College of Cardiology*, 54: 2065-74.

Meissner, G, E Darling, and J Eveleth. (1986). "Kinetics of rapid $Ca^{2+}$ release by sarcoplasmic reticulum. Effects of $Ca^{2+}$, $Mg^{2+}$ and adenine nucleotides." In.: Biochem.

Meissner, Gerhard. (1975). 'Isolation and characterization of two types of sarcoplasmic reticulum vesicles', *Biochimica et Biophysica Acta (BBA)-Biomembranes*, 389: 51-68.

———. (2017). 'The structural basis of ryanodine receptor ion channel function', *Journal of General Physiology*, 149: 1065-89.

Miller, Christopher. (1978). 'Voltage-gated cation conductance channel from fragmented sarcoplasmic reticulum: steady-state electrical properties', *The Journal of membrane biology*, 40: 1-23.

———. (1982). 'Bis-quaternary ammonium blockers as structural probes of the sarcoplasmic reticulum $K^+$ channel', *The Journal of general physiology*, 79: 869-91.

———. (1992). 'Ion channel structure and function', *Science*, 258: 240-42.

Miller, Christopher, and Robert L Rosenberg. (1979). 'A voltage-gated cation conductance channel from fragmented sarcoplasmic reticulum. Effects of transition metal ions', *Biochemistry*, 18: 1138-45.

Mohamed, Uwais, Carlo Napolitano, and Silvia G Priori. (2007). 'Molecular and electrophysiological bases of catecholaminergic polymorphic ventricular tachycardia', *Journal of cardiovascular electrophysiology*, 18: 791-97.

Müller, Armin, Enrique Cadenas, Peter Graf, and Helmut Sies. (1984). 'A novel biologically active seleno-organic compound—1: Glutathione peroxidase-like activity in vitro and antioxidant capacity of PZ 51 (Ebselen)', *Biochemical pharmacology*, 33: 3235-39.

Munro, Michelle L, Isuru D Jayasinghe, Qiongling Wang, Ann Quick, Wei Wang, David Baddeley, Xander HT Wehrens, and Christian Soeller. (2016). 'Junctophilin-2 in the nanoscale organisation and functional signalling of ryanodine receptor clusters in cardiomyocytes', *Journal of cell science*, 129: 4388-98.

Murayama, Takashi, and Yasuo Ogawa. (1996). 'Properties of Ryr3 Ryanodine Receptor Isoform in Mammalian Brain (∗)', *Journal of Biological Chemistry*, 271: 5079-84.

Nabauer, Michael, GC Ellis-Davies, Jack H Kaplan, and Martin Morad. (1989). 'Modulation of $Ca^{2+}$ channel selectivity and cardiac contraction by photorelease of $Ca^{2+}$', *American Journal of Physiology-Heart and Circulatory Physiology*, 256: H916-H20.

Nakamura, Yoshimasa, Qing Feng, Takeshi Kumagai, Koji Torikai, Hajime Ohigashi, Toshihiko Osawa, Noriko Noguchi, Etsuo Niki, and Koji Uchida. (2002). 'Ebselen, a glutathione peroxidase mimetic seleno-organic compound, as a multifunctional antioxidant: implication for inflammation-associated carcinogenesis', *Journal of Biological Chemistry*, 277: 2687-94.

Napolitano, Carlo, Silvia G Priori, and Raffaella Bloise. (2016). 'Catecholaminergic polymorphic ventricular tachycardia'.

Nikawa, Takeshi, Gunter Schuch, Gunter Wagner, and Helmut Sies. (1994). 'Interaction of ebselen with glutathione S-transferase and papain in vitro', *Biochemical pharmacology*, 47: 1007-12.

Otsu, K, HF Willard, VK Khanna, Francesco Zorzato, NM Green, and DH MacLennan. (1990). 'Molecular cloning of cDNA encoding the $Ca^{2+}$ release channel (ryanodine receptor) of rabbit cardiac muscle sarcoplasmic reticulum', *Journal of Biological Chemistry*, 265: 13472-83.

Ou, Xiaomin, Jianli Guo, Longfei Wang, Hanting Yang, Xiuying Liu, Jianyuan Sun, and Zhenfeng Liu. (2017). 'Ion-and water-binding sites inside an occluded hourglass pore of a trimeric intracellular cation (TRIC) channel', *BMC biology*, 15: 1-17.

Parsegian, V Adrian. (1975). 'Ion-membrane interactions as structural forces', *Annals of the New York Academy of Sciences*, 264: 161-74.

Peachey, Lee D. (1965). 'The sarcoplasmic reticulum and transverse tubules of the frog's sartorius', *The Journal of cell biology*, 25: 209-31.

Peng, Wei, Huaizong Shen, Jianping Wu, Wenting Guo, Xiaojing Pan, Ruiwu Wang, SR Wayne Chen, and Nieng Yan. (2016). 'Structural basis for the gating mechanism of the type 2 ryanodine receptor RyR2', *Science*, 354.

Percival, Ann L, Alan J Williams, James L Kenyon, Matthew M Grinsell, Judith A Airey, and John

L Sutko. (1994). 'Chicken skeletal muscle ryanodine receptor isoforms: ion channel properties', *Biophysical journal*, 67: 1834-50.

Perez, Claudio F, José R López, and Paul D Allen. (2005). 'Expression levels of RyR1 and RyR3 control resting free $Ca^{2+}$ in skeletal muscle', *American Journal of Physiology-Cell Physiology*, 288: C640-C49.

Pessah, Isaac N, Gennady Cherednichenko, and Pamela J Lein. (2010). 'Minding the calcium store: Ryanodine receptor activation as a convergent mechanism of PCB toxicity', *Pharmacology & therapeutics*, 125: 260-85.

Pettersen, Eric F, Thomas D Goddard, Conrad C Huang, Gregory S Couch, Daniel M Greenblatt, Elaine C Meng, and Thomas E Ferrin. (2004). 'UCSF Chimera—a visualization system for exploratory research and analysis', *Journal of computational chemistry*, 25: 1605-12.

Pitt, Samantha J, Ki-Ho Park, Miyuki Nishi, Toshiki Urashima, Sae Aoki, Daijyu Yamazaki, Jianjie Ma, Hiroshi Takeshima, and Rebecca Sitsapesan. (2010). 'Charade of the SR K+-channel: two ion-channels, TRIC-A and TRIC-B, masquerade as a single $K^+$-channel', *Biophysical journal*, 99: 417-26.

Priori, Silvia G, and SR Wayne Chen. (2011). 'Inherited dysfunction of sarcoplasmic reticulum $Ca^{2+}$ handling and arrhythmogenesis', *Circulation research*, 108: 871-83.

Priori, Silvia G, Carlo Napolitano, Natascia Tiso, Mirella Memmi, Gabriele Vignati, Raffaella Bloise, Vincenzo Sorrentino, and Gian Antonio Danieli. (2001). 'Mutations in the cardiac ryanodine receptor gene (hRyR2) underlie catecholaminergic polymorphic ventricular tachycardia', *Circulation*, 103: 196-200.

Qin, Jia, Giorgia Valle, Alma Nani, Alessandra Nori, Nicoletta Rizzi, Silvia G Priori, Pompeo Volpe, and Michael Fill. (2008). 'Luminal $Ca^{2+}$ regulation of single cardiac ryanodine receptors: insights provided by calsequestrin and its mutants', *The Journal of general physiology*, 131: 325-34.

Ringer, Sydney. (1883). 'A further contribution regarding the influence of the different constituents of the blood on the contraction of the heart', *The Journal of physiology*, 4: 29-42.

Ríos, Eduardo, Jianjie Ma, and Adom González. (1991). 'The mechanical hypothesis of excitation—contraction (EC) coupling in skeletal muscle', *Journal of Muscle Research & Cell Motility*, 12: 127-35.

Ríos, Eduardo, and Gonzalo Pizarro. (1991). 'Voltage sensor of excitation-contraction coupling in skeletal muscle', *Physiological reviews*, 71: 849-908.

Rodriguez, Patricia, Moninder S Bhogal, and John Colyer. (2003). 'Stoichiometric phosphorylation of cardiac ryanodine receptor on serine 2809 by calmodulin-dependent kinase II and protein kinase A', *Journal of Biological Chemistry*, 278: 38593-600.

Rousseau, Eric, Jeffrey S Smith, and Gerhard Meissner. (1987). 'Ryanodine modifies conductance and gating behavior of single $Ca^{2+}$ release channel', *American Journal of Physiology-Cell Physiology*, 253: C364-C68.

Ruan, Yanfei, Nian Liu, and Silvia G Priori. (2009). 'Sodium channel mutations and arrhythmias', *Nature Reviews Cardiology*, 6: 337-48.

Rubinato, Elisa, Anna Morgan, Angela D'Eustacchio, Vanna Pecile, Giulia Gortani, Paolo Gasparini, and Flavio Faletra. (2014). 'A novel deletion mutation involving TMEM38B in a patient with autosomal recessive osteogenesis imperfecta', *Gene*, 545: 290-92.

Saftenku, E, AJ Williams, and R Sitsapesan. (2000). "$Ca^{2+}$-dependence of low and high activity

levels of cardiac ryanodine receptor channels." In *Biophysical journal*, 312A-12A.

Šali, Andrej, and Tom L Blundell. (1993). 'Comparative protein modelling by satisfaction of spatial restraints', *Journal of molecular biology*, 234: 779-815.

Salvage, Samantha C, Esther M Gallant, Nicole A Beard, Shiraz Ahmad, Haseeb Valli, James A Fraser, Christopher L-H Huang, and Angela F Dulhunty. (2019). 'Ion channel gating in cardiac ryanodine receptors from the arrhythmic RyR2-P2328S mouse', *Journal of cell science*, 132: jcs229039.

Sanchez-Fernandez, A, OS Hammond, KJ Edler, T Arnold, J Doutch, RM Dalgliesh, P Li, K Ma, and AJ Jackson. (2018). 'Counterion binding alters surfactant self-assembly in deep eutectic solvents', *Physical Chemistry Chemical Physics*, 20: 13952-61.

Sauer, Brian. (2002). 'Chromosome manipulation by Cre-lox recombination.' in, *Mobile DNA II* 38-58.

Schneider, Martin F. (1994). 'Control of calcium release in functioning skeletal muscle fibers', *Annual review of physiology*, 56: 463-84.

Shaheen, Ranad, Anas M Alazami, Muneera J Alshammari, Eissa Faqeih, Nadia Alhashmi, Noon Mousa, Aisha Alsinani, Shinu Ansari, Fatema Alzahrani, and Mohammed Al-Owain. (2012). 'Study of autosomal recessive osteogenesis imperfecta in Arabia reveals a novel locus defined by TMEM38B mutation', *Journal of medical genetics*, 49: 630-35.

Shannon, Thomas R, Kenneth S Ginsburg, and Donald M Bers. (2000). 'Potentiation of fractional sarcoplasmic reticulum calcium release by total and free intra-sarcoplasmic reticulum calcium concentration', *Biophysical journal*, 78: 334-43.

Sharpley, Ann L, Clare Williams, Adele A Holder, Beata R Godlewska, Nisha Singh, Milensu Shanyinde, Orla MacDonald, and Philip J Cowen. (2020). 'A phase 2a randomised, double-blind, placebo-controlled, parallel-group, add-on clinical trial of ebselen (SPI-1005) as a novel treatment for mania or hypomania', *Psychopharmacology*, 237: 3773-82.

Sigalas, C, S Bent, A Kitmitto, S O'neill, and R Sitsapesan. (2009). '$Ca^{2+}$-calmodulin can activate and inactivate cardiac ryanodine receptors', *British journal of pharmacology*, 156: 794-806.

Sigalas, Charalambos, Maria Belen Mayo-Martin, David E Jane, and Rebecca Sitsapesan. (2009). '$Ca^{2+}$-calmodulin increases RyR2 open probability yet reduces ryanoid association with RyR2', *Biophysical journal*, 97: 1907-16.

Sitsapesan, Rebecca, and Alan J Williams. (1994a). 'Regulation of the gating of the sheep cardiac sarcoplasmic reticulum Ca 2+-release channel by luminal $Ca^{2+}$', *The Journal of membrane biology*, 137: 215-26.

Sitsapesan, Rebecca, RA Montgomery, KT MacLeod, and Alan J Williams. (1991). 'Sheep cardiac sarcoplasmic reticulum calcium-release channels: modification of conductance and gating by temperature', *The Journal of physiology*, 434: 469-88.

Sitsapesan, Rebecca, Richard AP Montgomery, and Alan J Williams. (1995). 'New insights into the gating mechanisms of cardiac ryanodine receptors revealed by rapid changes in ligand concentration', *Circulation research*, 77: 765-72.

Sitsapesan, Rebecca, and Alan J Williams. (1994b). 'Gating of the native and purified cardiac SR $Ca^{2+}$-release channel with monovalent cations as permeant species', *Biophysical journal*, 67: 1484-94.

Smith, Jeffrey S, Roberto Coronado, and Gerhard Meissner. (1986). 'Single channel measurements of the calcium release channel from skeletal muscle sarcoplasmic reticulum. Activation by

$Ca^{2+}$ and ATP and modulation by $Mg^{2+}$', *The Journal of general physiology*, 88: 573-88.

Sternberg, Nat, and Daniel Hamilton. (1981). 'Bacteriophage P1 site-specific recombination: I. Recombination between loxP sites', *Journal of molecular biology*, 150: 467-86.

Su, Min, Feng Gao, Qi Yuan, Yang Mao, De-lin Li, Youzhong Guo, Cheng Yang, Xiao-hui Wang, Renato Bruni, and Brian Kloss. (2017). 'Structural basis for conductance through TRIC cation channels', *Nature communications*, 8: 1-13.

Sun, Xin-Hui, Feliciano Protasi, Masami Takahashi, Hiroshi Takeshima, Donald G Ferguson, and Clara Franzini-Armstrong. (1995). 'Molecular architecture of membranes involved in excitation-contraction coupling of cardiac muscle', *The Journal of cell biology*, 129: 659-71.

Sy, Raymond W, Michael H Gollob, George J Klein, Raymond Yee, Allan C Skanes, Lorne J Gula, Peter Leong-Sit, Robert M Gow, Martin S Green, and David H Birnie. (2011). 'Arrhythmia characterization and long-term outcomes in catecholaminergic polymorphic ventricular tachycardia', *Heart Rhythm*, 8: 864-71.

Takeshima, Hiroshi, Seiichiro Nishimura, Takeshi Matsumoto, Hiroyuki Ishida, Kenji Kangawa, Naoto Minamino, Hisayuki Matsuo, Masamichi Ueda, Masao Hanaoka, and Tadaaki Hirose. (1989). 'Primary structure and expression from complementary DNA of skeletal muscle ryanodine receptor', *Nature*, 339: 439-45.

Takeshima, Hiroshi, Hiroaki Takekura, Miyuki Nishi, Junko Kuno, Osamu Minowa, Hiroshi Takano, and Tetsuo Noda. (1994). 'Excitation-contraction uncoupling and muscular degeneration in mice lacking functional skeletal muscle ryanodine-receptor gene', *Nature*, 369: 556-59.

Takeshima, Hiroshi, Elisa Venturi, and Rebecca Sitsapesan. (2015). 'New and notable ion-channels in the sarcoplasmic/endoplasmic reticulum: do they support the process of intracellular Ca2+ release?', *The Journal of physiology*, 593: 3241-51.

Tanabe, Tsutomu, Kurt G Beam, Brett A Adams, Tetsuhiro Niidome, and Shosaku Numa. (1990). 'Regions of the skeletal muscle dihydropyridine receptor critical for excitation–contraction coupling', *Nature*, 346: 567-69.

Tanabe, Tsutomu, Kurt G Beam, Jeanne A Powell, and Shosaku Numa. (1988). 'Restoration of excitation—contraction coupling and slow calcium current in dysgenic muscle by dihydropyridine receptor complementary DNA', *Nature*, 336: 134-39.

Tang, Lian-Hong, and Elias Aizenman. (1993). 'Allosteric modulation of the NMDA receptor by dihydrolipoic and lipoic acid in rat cortical neurons in vitro', *Neuron*, 11: 857-63.

Tester, David J, Laura J Kopplin, Wendy Creighton, Allen P Burke, and Michael J Ackerman. (2005). "Pathogenesis of unexplained drowning: new insights from a molecular autopsy." In *Mayo Clinic Proceedings*, 596-600. Elsevier.

Timerman, Anthony P, Hitoshi Onoue, Hong-Bo Xin, Sebastian Barg, Julio Copello, Greg Wiederrecht, and Sidney Fleischer. (1996). 'Selective binding of FKBP12. 6 by the cardiac ryanodine receptor', *Journal of Biological Chemistry*, 271: 20385-91.

Tinker, A., and Alan J. Williams. (1993). 'Probing the structure of the conduction pathway of the sheep cardiact sarcoplasmic-reticulum calcium-release channel with permeant and impermeant organic cations', *Journal of General Physiology*, 102: 1107-29.

Tinker, Andrew, AR Lindsay, and Alan J Williams. (1992). 'A model for ionic conduction in the ryanodine receptor channel of sheep cardiac muscle sarcoplasmic reticulum', *The Journal of general physiology*, 100: 495-517.

Tinker, Andrew, and Alan J Williams. (1992). 'Divalent cation conduction in the ryanodine receptor

channel of sheep cardiac muscle sarcoplasmic reticulum', *The Journal of general physiology*, 100: 479-93.

Tomlins, Barbara, and Alan J Williams. (1986). 'Solubilisation and reconstitution of the rabbit skeletal muscle sarcoplasmic reticulum $K^+$ channel into liposomes suitable for patch clamp studies', *Pflügers Archiv*, 407: 341-47.

Tripathy, Ashutosh, Le Xu, Geoffrey Mann, and Gerhard Meissner. (1995). 'Calmodulin activation and inhibition of skeletal muscle $Ca^{2+}$ release channel (ryanodine receptor)', *Biophysical journal*, 69: 106-19.

Uehara, Akira, Takashi Murayama, Midori Yasukochi, Michael Fill, Minoru Horie, Toru Okamoto, Yoshiharu Matsuura, Kiyoko Uehara, Takahiro Fujimoto, and Takashi Sakurai. (2017). 'Extensive $Ca^{2+}$ leak through K4750Q cardiac ryanodine receptors caused by cytosolic and luminal $Ca^{2+}$ hypersensitivity', *Journal of General Physiology*, 149: 199-218.

Uehara, Akira, Midori Yasukochi, and Issei Imanaga. (1994). 'Calcium modulation of single SR potassium channel currents in heart muscle', *Journal of molecular and cellular cardiology*, 26: 195-202.

UniProt, Consortium. (2021). 'UniProt: the universal protein knowledgebase in 2021', *Nucleic acids research*, 49: D480-D89.

Valdeolmillos, Miguel, Rosa M Santos, Diego Contreras, Bernat Soria, and Luis M Rosario. (1989). 'Glucose-induced oscillations of intracellular $Ca^{2+}$ concentration resembling bursting electrical activity in single mouse islets of Langerhans', *FEBS letters*, 259: 19-23.

Venturi, Elisa, Elena Galfré, Fiona O'Brien, Samantha J Pitt, Stuart Bellamy, Richard B Sessions, and Rebecca Sitsapesan. (2014). 'FKBP12. 6 activates RyR1: investigating the amino acid residues critical for channel modulation', *Biophysical journal*, 106: 824-33.

Venturi, Elisa, Antoni Matyjaszkiewicz, Samantha J Pitt, Krasimira Tsaneva-Atanasova, Miyuki Nishi, Daiju Yamazaki, Hiroshi Takeshima, and Rebecca Sitsapesan. (2013). 'TRIC-B channels display labile gating: evidence from the TRIC-A knockout mouse model', *Pflügers Archiv-European Journal of Physiology*, 465: 1135-48.

von Mering, C., L. J. Jensen, B. Snel, S. D. Hooper, M. Krupp, M. Foglierini, N. Jouffre, M. A. Huynen, and P. Bork. (2005). 'STRING: known and predicted protein-protein associations, integrated and transferred across organisms', *Nucleic Acids Res*, 33: D433-7.

Wang, Xiao-hui, Min Su, Feng Gao, Wenjun Xie, Yang Zeng, De-lin Li, Xue-lei Liu, Hong Zhao, Li Qin, and Fei Li. (2019). 'Structural basis for activity of TRIC counter-ion channels in calcium release', *Proceedings of the National Academy of Sciences*, 116: 4238-43.

Wehrens, Xander HT, Stephan E Lehnart, Steven R Reiken, and Andrew R Marks. (2004). '$Ca^{2+}$/calmodulin-dependent protein kinase II phosphorylation regulates the cardiac ryanodine receptor', *Circulation research*, 94: e61-e70.

White, Stephen H. (1986). 'The physical nature of planar bilayer membranes.' in, *Ion Channel Reconstitution* (Springer).

Wilson, Abigail D.. (2020). "Investigation into pathophysiological mechanisms that alter ryanodine receptor function in cardiovascular disease.", University of Oxfrod.

Wilson, Abigail D., Jianshu Hu, Charalampos Sigalas, Elisa Venturi, Héctor H. Valdivia, Carmen R. Valdivia, Ming Lei, Maria Musgaard, and Rebecca Sitsapesan. (2021). 'The V2475F CPVT1 mutation yields distinct RyR2 channel populations that differ in their responses to cytosolic $Ca^{2+}$ and $Mg^{2+}$', *The Journal of physiology*, 599(23), 5179-5201.

Witschas, Katja, Fiona O'Brien, Elisa Venturi, Sam El-Ajouz, Matthew Beech, David Eberhardt, Tsunaki Iida, Miyuki Nishi, Hiroshi Takeshima, and Rebecca Sitsapesan. (2016). 'Dampened Activity of Single Ryanodine Receptor Channels in Mice Devoid of TRIC-A', *Biophysical journal*, 110: 266a.

Xiao, Bailong, Guofeng Zhong, Masakazu Obayashi, Dongmei Yang, Keyun Chen, Michael P Walsh, Yakhin Shimoni, Heping Cheng, Henk Ter Keurs, and SR Wayne Chen. (2006). 'Ser-2030, but not Ser-2808, is the major phosphorylation site in cardiac ryanodine receptors responding to protein kinase A activation upon β-adrenergic stimulation in normal and failing hearts', *Biochemical Journal*, 396: 7-16.

Yamaguchi, Takenori, Keiji Sano, Kintomo Takakura, Isamu Saito, Yukito Shinohara, Takao Asano, and Hajime Yasuhara. (1998). 'Ebselen in acute ischemic stroke: a placebo-controlled, double-blind clinical trial', *Stroke*, 29: 12-17.

Yamazaki, Daiju, Shinji Komazaki, Hiroki Nakanishi, Aya Mishima, Miyuki Nishi, Masayuki Yazawa, Tetsuo Yamazaki, Ryo Taguchi, and Hiroshi Takeshima. (2009). 'Essential role of the TRIC-B channel in $Ca^{2+}$ handling of alveolar epithelial cells and in perinatal lung maturation', *Development*, 136: 2355-61.

Yamazaki, Daiju, Yasuharu Tabara, Satomi Kita, Hironori Hanada, Shinji Komazaki, Daisuke Naitou, Aya Mishima, Miyuki Nishi, Hisao Yamamura, and Shinichiro Yamamoto. (2011). 'TRIC-A channels in vascular smooth muscle contribute to blood pressure maintenance', *Cell metabolism*, 14: 231-41.

Yan, Jianyun, Lu Zhang, Nishat Sultana, David S Park, Akshay Shekhar, Lei Bu, Jun Hu, Shegufta Razzaque, and Chen-Leng Cai. (2015). 'A murine Myh6MerCreMer Knock-in allele specifically mediates temporal genetic deletion in Cardiomyocytes after Tamoxifen induction', *PloS one*, 10: e0133472.

Yang, Hanting, Miaohui Hu, Jianli Guo, Xiaomin Ou, Tanxi Cai, and Zhenfeng Liu. (2016). 'Pore architecture of TRIC channels and insights into their gating mechanism', *Nature*, 538: 537-41.

Yarotskyy, Viktor, and Robert T Dirksen. (2014). 'Monovalent cationic channel activity in the inner membrane of nuclei from skeletal muscle fibers', *Biophysical journal*, 107: 2027-36.

———. (2016). 'Manual Patch-Clamp Recording for Medium-Throughput Ion Channel Drug Screening: Assay Validation by Searching for a Blocker of Nuclear Monovalent Cationic Channel', *Biophysical journal*, 110: 527a.

Yazawa, Masayuki, Christopher Ferrante, Jue Feng, Kazuhiro Mio, Toshihiko Ogura, Miao Zhang, Pei-Hui Lin, Zui Pan, Shinji Komazaki, and Kazuhiro Kato. (2007). 'TRIC channels are essential for $Ca^{2+}$ handling in intracellular stores', *Nature*, 448: 78-82.

Zhao, Xiaoli, Daiju Yamazaki, Ki Ho Park, Shinji Komazaki, Andoria Tjondrokoesoemo, Miyuki Nishi, Peihui Lin, Yutaka Hirata, Marco Brotto, and Hiroshi Takeshima. (2010). '$Ca^{2+}$ overload and sarcoplasmic reticulum instability in tric-a null skeletal muscle', *Journal of Biological Chemistry*, 285: 37370-76.

Zhou, Xinyu, Ki Ho Park, Daiju Yamazaki, Pei-hui Lin, Miyuki Nishi, Zhiwei Ma, Liming Qiu, Takashi Murayama, Xiaoqin Zou, and Hiroshi Takeshima. (2020). 'TRIC-A channel maintains store calcium handling by interacting with type 2 ryanodine receptor in cardiac muscle', *Circulation research*, 126: 417-35.

Zsolnay, Vilmos, Michael Fill, and Dirk Gillespie. (2018). 'Sarcoplasmic reticulum $Ca^{2+}$ release uses

a cascading network of intra-SR and channel countercurrents', *Biophysical journal*, 114: 462-73.

# Appendix

Raw western blot data from Dr Takashima's group

